Beyond pilot wave dynamics : non-linearity and non-equilibrium in quantum mechanics

Mohamed Hatifi

ECOLE CENTRALE MARSEILLE - INSTITUT FRESNEL

THÈSE PRÉSENTÉE À
L'ECOLE CENTRALE DE MARSEILLE
POUR OBTENIR LE GRADE DE DOCTEUR

Beyond pilot wave dynamics: non-linearity and non-equilibrium in quantum mechanics

---

Autheur:
Mohamed HATIFI

Directeur de thèse:
Pr. Thomas DURT

Spécialité: Physique Théorique
Ecole Doctorale 352 - Physique et Sciences de la Matière

Soutenue le 24 septembre 2019 devant le jury composé de :

M. Christos EFTHYMIOPOULOS	Research Center for Astronomy and Applied Mathematics	Rapporteur
M. Jacques ROBERT	Laboratoire de Physique des Gaz et des Plasmas (LPGP)	Rapporteur
M. Alexandre MATZKIN	Laboratoire de Physique Théorique et Modélisation (LPTM)	Examinateur
Mme Fabienne MICHELINI	Institut Matériaux Microélectronique Nanosciences de Provence (IM2NP)	Examinatrice
M. Thomas DURT	Institut Fresnel	Directeur de thèse

"L'existence du quantum d'action (...) implique une sorte d'incompatibilité entre le point de vue de la localisation dans l'espace et dans le temps et le point de vue de l'évolution dynamique (...) La localisation exacte dans l'espace et le temps est une sorte d'idéalisation statique qui exclut toute évolution et toute dynamique. (...) Dans la mécanique classique, il était permis d'étudier pour eux-mêmes les déplacements dans l'espace et de définir ainsi les vitesses, les accélérations sans s'occuper de la façon dont sont matériellement réalisés ces déplacements : de cette étude abstraite des mouvements, on s'élevait ensuite à la dynamique en introduisant quelques principes physiques nouveaux. Dans la mécanique quantique, une semblable division de l'exposé n'est plus en principe admissible puisque la localisation spacio-temporelle qui est à la base de la cinématique est acceptable seulement dans une mesure qui dépend des conditions dynamiques du mouvement..."

Louis de Broglie - « La physique nouvelle et les quanta » - (1937)

ECOLE CENTRALE MARSEILLE - INSTITUT FRESNEL

Abstract (French)

Institut Fresnel
Ecole Doctorale 352 - Physique et Sciences de la Matière

Doctor of Philosophy

Beyond pilot wave dynamics: non-linearity and non-equilibrium in quantum mechanics

by Mohamed HATIFI

La mécanique quantique a modifié notre façon d'interpréter ce que jadis l'on appelait communément "réalité physique". A titre d'exemple, selon l'interprétation standard de la mécanique quantique (dite interprétation probabiliste de Copenhague) les propriétés d'un objet quantique n'ont pas de réalité physique, du moins, pas avant que l'observateur ne les mesure. De plus, tout semble se passer comme s'il y avait un indéterminisme intrinsèque à la dynamique quantique qui ne permettrait pas de prédire avec certitude le résultat d'une mesure. Dès lors, plusieurs interprétations physiques et philosophiques ont vu naissance afin de décrire (notre connaissance de) cette réalité.

C'est au cours de la conférence de Solvay en 1927 que Louis de Broglie, un opposant à l'interprétation probabiliste, proposa une solution alternative qui permettait d'une part de restaurer le déterminisme (ainsi que le réalisme) et d'autre part de remettre au premier plan la notion de trajectoire. Par la suite cette théorie fut redécouverte et complétée par David Bohm pour donner naissance à la théorie connue aujourd'hui sous l'appellation de théorie de l'onde pilote. John Bell a dit[1] à propos de cette interprétation : " En 1952, l'impossible a été rendu possible. C'était dans l'article de David Bohm. Bohm a montré explicitement comment une description indéterministe pouvait être transformée en théorie déterministe."

Les travaux présentés dans ce manuscrit de thèse s'inscrivent dans la continuité de la vision de de Broglie et consistent en deux parties, chacune d'elles ayant pour but de répondre à une problématique particulière. Dans la première, on considère deux formalismes du type onde pilote, une version déterministe (dynamique de de Broglie-Bohm chapitre 2) ainsi qu'une de ses extensions stochastiques (dynamique de Bohm-Hiley-Nelson chapitre 3). On s'attardera notamment sur l'émergence de la probabilité quantique $|\Psi(\mathbf{x},\mathbf{t})|^2$ à partir de ces dynamiques dans l' approche dite du "Quantum Non-Equilibrium". Cette approche permet entre autres de s'affranchir du statut axiomatique de la distribution de probabilité $|\Psi(\mathbf{x},\mathbf{t})|^2$ mais aussi de la justifier par des arguments similaires à ceux que l'on retrouve en mécanique statistique. Parmi ces arguments on retrouvera à titre d'exemple la notion d'ergodicité, de chaos, de mixing ainsi que d'autres propriétés qui feront l'objet d'une étude approfondie (chapitre 4). En particulier, l' émergence de l' équilibre s'accompagne d'un processus de relaxation que nous allons caractériser dans chacune de ces dynamiques (dans le chapitre 3 nous dériverons un théorème H qui décrit quantitativement ce processus dans le cas stochastique). Par ailleurs, nous nous efforcerons, dans une approche phénoménologique, d'appliquer ces théories quantiques d'onde pilote à la dynamique macroscopique des gouttes d'huile rebondissantes dans un bain (chapitre 5).

La deuxième problématique quant à elle, repose sur une hypothétique généralisation non-linéaire de la mécanique quantique. En particulier, nous considérerons l'équation de Schrodinger Newton comme une première proposition a cette généralisation. Cette équation non-linéaire découle d'une approximation semi-classique de la gravité et a été entre autres proposée par Roger Penrose pour expliquer le collapse de la fonction d'onde. Nous montrerons dans un premier temps comment le programme de la double solution de Louis de Broglie se développe dans ce contexte (chapitre 6). Par la suite nous verrons comment tester cette généralisation non-linéaire par deux propositions expérimentales (chapitre 7). En particulier, l'une de ces propositions nous conduira à étudier des effets de décohérence lors du refroidissement laser (Doppler cooling, chapitre 8). Pour cela on utilisera le modèle de Ghirardi–Rimini–Weber (GRW) comme modèle de décohérence. Ce qui nous permettra par la suite de généraliser les résultats obtenus auparavant par GRW dans leur modèle.

[1] "*On the impossible pilot wave*" -1982

ECOLE CENTRALE MARSEILLE - INSTITUT FRESNEL

Abstract (English)

Institut Fresnel
Ecole Doctorale 352 - Physique et Sciences de la Matière

Doctor of Philosophy

Beyond pilot wave dynamics: non-linearity and non-equilibrium in quantum mechanics

by Mohamed HATIFI

The quantum theory has modified the way we interpret what in the past was commonly called "physical reality". As an example, according to the standard interpretation of quantum mechanics (the so-called probabilistic interpretation of Copenhagen), the properties of a quantum object have no physical reality, at least not before the observer measures them. Moreover, everything seems to happen as if there was an intrinsic indeterminism in the quantum dynamics that forbids to predict with certainty the result of a measurement. From then, several physical and philosophical interpretations were born to describe (our knowledge of) this reality.

It is in 1927, during the Solvay conference, that Louis de Broglie, an opponent of the probabilistic interpretation, proposed an alternative solution to that problem. He proposed on the one hand to restore determinism (as well as realism) and on the other hand to bring back the notion of trajectory to the foreground. Subsequently this theory was rediscovered and supplemented by David Bohm to give birth to the theory known today as pilot wave theory. John Bell said[2] about this interpretation: " In 1952, I saw the impossible done. It was in papers by David Bohm. Bohm showed explicitly how .... the indeterministic description could be transformed into a deterministic one."

The works carried out in this manuscript are in continuity with de Broglie's view and can be summed up in two main parts, each of them having the aim of answering a particular problem. In the first part, we consider two versions of the pilot wave theory: a deterministic version (de Broglie-Bohm dynamics in chapter 2) as well as one of its stochastic extensions (Bohm-Hiley-Nelson dynamics in chapter 3). In the framework of what is called the "Quantum non-equilibrium" approach we shall see how the quantum probability $|\Psi(\mathbf{x},\mathbf{t})|^2$ emerges from those dynamics. This approach makes it possible to get rid of the axiomatic status of the probability distribution $|\Psi(\mathbf{x},\mathbf{t})|^2$ but also to justify it by arguments similar to those found in statistical mechanics. Among these arguments we shall for instance find ergodicity, chaos, mixing and other properties that will be studied in depth (chapter 4). In particular, the emergence of the quantum probability is accompanied by a relaxation process that will be characterized for both dynamics (in chapter 3 we derive a strong H-theorem for the stochastic dynamics which quantitatively describes how this process occurs). In addition, we will try in a phenomenological approach to apply these quantum pilot wave theories to the macroscopic dynamics of bouncing oil droplets (chapter 5).

The second problem is linked to a hypothetical nonlinear generalization of the quantum theory. In particular, we considered the Schrodinger Newton equation as a first proposal to this generalization. In a nutshell, this non-linear equation derives from a semi-classical approximation of gravity and has been proposed by Roger Penrose among others to explain the collapse of the wave function. We shall first show how it is related to the double solution program of Louis de Broglie (chapter 6). Subsequently we will see how to test this nonlinear generalization by considering two experimental proposals (chapter 7). In particular, one of these proposals will lead us to study the interplay between decoherence and Doppler cooling (chapter 8). To do this we shall use the model of Ghirardi-Rimini and Weber (GRW) as a decoherence model, which will allow us to generalize their original results.

[2] "*On the impossible pilot wave*" -1982

Acknowledgements

Au nom de Dieu.

Papa, je me souviens encore de ce jour, ce jour où tes dernières paroles ont résonné à travers mon cœur et mon âme. Ce jour-là, je t'ai fait entre autres la promesse de faire des études. Me voilà aujourd'hui en train de concrétiser cette promesse. Le chemin a été long et difficile, les rencontres nombreuses et marquantes. Un point d'honneur est donné à cette section finale dans laquelle je suis plongé dans une douce nostalgie.

Avant de me perdre dans la nostalgie de ces remerciements, je souhaiterais tout d'abord remercier mon "mentor" et directeur de thèse, Thomas. Je suis très heureux d'avoir fait ta rencontre, tant sur le plan professionnel que sur le plan humain, vraiment je te remercie pour la liberté dont j'ai pu jouir pendant ma recherche, je n'oublierai jamais cette aventure. Ralph, un grand merci à toi, domo arigato gozaimasu Willox sensei. En travaillant à tes cotés j'ai énormément appris et j'espère avoir encore l'occasion de travailler avec toi. Merci pour l'accueil chaleureux à Tokyo. Je remercie bien évidemment, Samuel Colin. Ces deux mois à Rio ont été très formateurs pour moi. J'ai vraiment apprécié de travailler avec toi ainsi que les pauses café au "Katz" (c.a.d. là où j'ai enfin appris à aimer le café). Je te remercie d'avoir partagé avec moi ton savoir sur la théorie du quantum non-equilibrium mais aussi pour la formation en fortran.

Je remercie l'ensemble des membres du Jury d'avoir accepté d'en faire partie. Je les remercie pour leur temps ainsi que pour leur disponibilité. Je souhaiterais aussi remercier Nelly Bardet et Sarah Mostefa pour leur aide en ce qui concerne les tâches administratives. Tête en l'air que je suis, sans vous ça aurait été très compliqué. Un grand merci à Samia pour sa bonne humeur et sa gentillesse.

Je remercie bien évidemment l'ensemble des membres de l'institut Fresnel, il m'était vraiment agréable de vous côtoyer chaque jour. En particulier je tiens à remercier Nicolas Bonod pour sa disponibilité. Merci Brian pour nos diverses discussions; Redha pour ta "bonne" humeur; Stefan pour ton soutien; Gilles pour tes précieux conseils et Frédéric Zolla pour tes suggestions musicales mais aussi pour les diverses discussions philosophiques sur le port de la casquette. De même, je remercie l'ensemble des doctorants de l'institut, en particulier: Manu pour ton soutien; "Rémy" pour ton fauteuil (depuis ton départ c'est game of thrones au 3ème); Georges pour ta gentillesse; Elena, pour nos discussions, c'était cool de partager le bureau avec toi; Aswani pour ta bonté d'âme; Duy, rends-moi ma balle en mouuuusse enfoirax; Faris, nos heures de ping-pong vont énormément me manquer; le joueur François, n'oublie jamais la citation de Voltaire ("Le matin, ..."); Kevin a.k.a. teckel furtif a.k.a. le roi des rageux, te voir rager pour moult raisons, je pense que c'est certainement ce qui va le plus me manquer; Cyprien, je n'oublierai pas le montage le plus drôle de l'histoire des JDD; Camille pour tes cookies maison que je quémandais à chacune des pauses de 16h; Marine, pour ton chocolat. Je remercie aussi François IV, qui m'a aidé à perfectionner mon Haki des rois. Une pensée aussi pour mes voisins et voisines de Marseille, spécialement à Lamine, Yacine, Kya, Pape, Bob mais aussi à Charlotte, Lise et Wines.

Un grand merci à mes amis de l'époque "Parisienne", en particulier à: Dassine, Sydney, Lyna, Nacim, Celia, Amina, Sofia, Magnus, Souad Namane et Walid. Je tiens aussi à remercier chaleureusement Marc-Etienne Brachet, Fabrice Debbash et Giusepe Di Molfetta.

De même, un grand merci à mes amis de l'époque "Valrose", en particulier à: Julien, Guillaume, Polo, Anais, Johan, Marwa, Souad, François, Nico, Darine, Fabien, Kozeta, Teddy et Cécile.

Je remercie ma très chère amie Alia qui m'a largement soutenu au cours de cette dernière année de thèse. A ce moment précis je veux écrire que j'ai vraiment une chance incroyable de te connaitre mais je suis vite rattrapé par ce souvenir amer. Je repense à ce jour où machiavéliquement tu m'avais envoyé par voie postale directement du Japon un unique emballage vide d'onigiri aux algues ... mon préféré ... Ceci étant dit, j'ai vraiment apprécié nos discussions, nos débats et anecdotes. Pour tout cela je t'en remercie infiniment.

En réalité j'ai découvert ma passion pour les sciences légèrement par hasard et tardivement après une adolescence mouvementée et un parcours scolaire initialement chaotique. Cependant, certaines rencontres m'ont orienté et guidé vers une destinée de scientifique.

En particulier, je remercie et dédie une part de cette thèse à mon ancien professeur de physique-chimie de seconde (au lycée Albert Calmette) qui dorénavant est un ami: Eric Bourroul. Tu as été l'un des premiers à déceler mon intérêt pour les sciences, je me souviens encore de tes encouragements qui à cette époque ont largement contribués à me pousser à faire ce choix pour la physique. J'en profite aussi pour remercier Mme Guilhot (professeure de mathématiques) mais aussi M. Abbes qui à l'époque m'a appris à réaliser mon premier circuit RLC.

Bien évidemment, impossible d'écrire ces remerciements sans penser à toi. Doriane, je te remercie du fond de mon cœur et je te serai à jamais reconnaissant. Tu as cru en moi avant même que je ne le fasse pour moi même à une époque qui, comme tu le sais, m'était très compliquée. Je remercie ta mère Marie mais aussi ton père Daniel à qui je dédie une part de ce manuscrit de thèse.

Bilel, mon frère et ami, cette thèse est aussi pour toi. Pratiquement 28 ans que l'on se côtoie, 28 ans sur 28 ans ça fait beaucoup. Je te remercie infiniment pour tellement de choses que je ne peux les énumérer ici de peur d'écrire l'équivalent d'une seconde thèse dans cette section de remerciements. Cependant, au moment où j'écris ces lignes, un souvenir particulier me vient en tête. Il remonte à l'époque très modeste du lycée où, je me souviens, nous nous cotisions pour partager des sandwichs triangles au saumon le midi.

Je remercie l'ensemble des mes frères et amis d'enfance. Aziz je te remercie pour ta présence, je n'oublierai jamais ces bons moments que nous partagions avec Bilel et toi. Tu ne peux imaginer à quel point ces moments ont été indispensables à mon équilibre mental haha. Karim, mon ami d'enfance je te remercie aussi. A mes grands frères de coeur Bader et Mounir qui m'ont soutenu avec amour et sagesse malgré la distance, je vous remercie. Merci également à mon autre grand frère de cœur Kader qui m'a beaucoup inspiré dans la vie.

A mon grand frère Hakim et mes deux grandes sœurs Raja et Nadia. Je vous remercie pour votre amour, votre gentillesse ainsi que pour vos encouragements. Vous avez été des exemples pour moi. Enfin, Papa, Maman, vous êtes la source de ma motivation, je vous aime de tout mon être et je vous serai à jamais reconnaissant. Papa, Maman cette thèse est pour vous ...

Contents

To my parents...

Chapter 1

Introduction

> "L'humanité ne peut rien obtenir sans donner quelque chose en retour. Pour chaque chose reçue, il faut en abandonner une autre de même valeur. En alchimie, c'est la loi fondamentale de l'échange équivalent. A cette époque, nous pensions que c'était la seule et unique vérité au monde. Nous nous trompions, mais il à fallu ceder quelque chose pour l'apprendre."
>
> Edward Elric

Many problems of interpretation of the quantum theory deal with the following question: "are quantum systems localized in 3D physical space"? Formulated in the words of John Bell [1], the question could read "is position a beable"? Or in EPR words [2, 3] "Is the position of a quantum system an element of reality"?

At the infamous Solvay conference Electrons and Photons held in Brussels in 1927 [4], Louis de Broglie proposed [5] to positively answer to this question. It appeared that some confusion surrounds this question; many particle physicists give a realistic description of their experiments, and at the same time are opposed to de Broglie's view. It is also commonly believed that the violation of Bell's inequalities means the death of realism, which is wrong. In the present thesis we aim at tackling two questions that naturally appear if, like de Broglie, we assume that quantum systems are localized at any time and undergo continuous trajectories. These questions were not mentioned by Louis de Broglie in 1927, but he addressed them in several books [6, 7] and papers [8] when he studied the problem again, after 25 years of silence (seemingly after the revival of these questions by David Bohm in 1952 [9, 10]). The first of these questions is congenital to the so-called de Broglie-Bohm (dBB) interpretation of the quantum theory. In this interpretation, a very precise statement is proposed concerning the trajectories of quantum systems which is: particles obey de Broglie's guidance equation [11, 12]. In other words, their velocity at any time is proportional to the gradient of the phase of the quantum wave function (called pilot-wave in this context). Sometimes the guidance condition is also called the Madelung condition [13], and it appears very naturally if we develop the analogy between the Born distribution $|\Psi(\mathbf{r}, t)|^2$ of a quantum system and the distribution of positions of a fluid of classical particles (material points).

If thus we impose that quantum trajectories obey the guidance equation, the first question that we shall tackle is the following:

1. DOES THE BORN RULE EMERGE AS A CONSEQUENCE OF THE DE BROGLIE-BOHM DYNAMICS?

This is a natural question to ask, because in nearly all interpretations where position is a beable, the Born rule is postulated to begin with, without clear motivation, which provides the uncomfortable feeling that the interpretation is ad hoc, a criticism recurrently formulated against de Broglie-Bohm's interpretation [14].
In the literature, this problem is referred to as the quantum equilibrium condition in analogy with classical statistical mechanics, where there exist numerous attempts to derive the thermal equilibrium condition as a consequence of the dynamics. Boltzmann for instance spent a lot of time and energy to demonstrate the so-called H-theorem according to which a large class of systems spontaneously and irreversibly tend to thermal equilibrium. Several chapters (2,3 and 4) of this work are devoted to the onset of quantum equilibrium and to the derivation of a quantum H-theorem. In particular we derive a quantum version of the H-theorem in the case where the guidance condition is supplemented with some Brownian motion, which fits into what de Broglie called the quantum thermostat hypothesis [15], a concept which is inspired by the work of Bohm and Vigier in the 50's [16], and also underlies the Nelson approach to quantum dynamics [17, 18].

A second question concerns the apparent dual nature of the de Broglie Bohm dynamics in which two objects coexist: the particle (represented by its point like position) and the pilot wave. There exist attempts, de Broglie essentially, to formulate a monistic version of this interpretation (see [7] and [19] for a review) in which the Schrodinger equation is replaced by a non-linear equation in such a way that the particle is a peaked wave packet, stabilized by a self-focusing non-linearity (what is commonly called a soliton or a solitary wave). We shall refer to this idea in what follows as de Broglie's double solution program (the soliton and the pilot wave being two solutions of a non-linear Schrodinger equation, the first one in the presence of a strong non-linearity and the second one in the linear regime). The second question that we shall tackle, in this context, is the following:

2. DOES THE DBB DYNAMICS EMERGE AS A CONSEQUENCE OF A NON-LINEAR (GENERALISATION OF) SCHRODINGER EQUATION?

One can find in the literature a few attempts to tackle this question, but none of them appeared to be fully convincing and satisfactory. More recently however a lot of attention was devoted to the so-called Schrodinger-Newton equation [20, 21, 22, 23] in which a non-linear and self-focusing interaction of gravitational nature is present. Several chapters (6 and 7) of this work are devoted to the study of the Schrodinger-Newton equation and to its interplay with de Broglie's double solution program [24].

Having in mind that in the last resort our conceptions about the laws of nature must agree with experimental facts we also tackled two questions (**3** and **4**, which are respectively related to the two questions above).

3. Is dBB dynamics relevant in order to describe the behavior of so-called droplets?

The droplets [25, 26] (sometimes called bouncers, sometimes walkers) can be considered to some extent as macroscopic realizations of de Broglie double solution programs. They consist of oil droplets bouncing at the surface of an oil vessel put into vibration by a shaker, nearly at the Faraday threshold. The dynamics of these droplets [27, 28, 29, 30] is influenced by the wave that they create in their vicinity at the surface of the oil, which in turn exerts a feedback on their trajectory, in analogy with the dBB pilot wave. In order to study in depth the analogy between droplets and dBB particles, we mimicked [31] the dynamics of the droplets in terms of dBB trajectories, and studied in this context several dynamical properties such as ergodicity, mixing, and so on.

The last question that we address in this work is question **4**:

4. Is it possible to experimentally put into evidence the existence of a non-linear self-interaction à la Newton-Schrodinger?

This question is challenging in relation with de Broglie's double solution program but it also opens the way to an entirely new class of experiments aimed at testing the role of gravity at the quantum scale.

The thesis is structured as follows:

The first part is devoted to the questions **1** and **3**. The chapter 2 deals with the onset of quantum equilibrium in the deterministic dB-B dynamics. The chapter 3 with the same problem in the case of a stochastic generalization of dB-B dynamics, essentially due to Nelson (called here the BHN dynamics, where we refer to a formulation of Nelson dynamics due to Bohm and Hiley [32]). The BHN dynamics encapsulates some ideas of de Broglie about what he called the quantum thermostat hypothesis, aimed at explaining the irreversible emergence of quantum equilibrium as a consequence of the "hidden" dynamics. We derive a quantum H-theorem for BHN dynamics. In chapter 4 we study the role of mixing in the dBB and BHN dynamics in relation with the onset of quantum equilibrium and emphasize the role played by the presence of microstructures in position distributions. We also show that mixing is extremely sensitive to noise (Brownian motion) in the case of BHN dynamics. In chapter 5 we apply our results to simulate the behavior of droplets, and propose experimental tests [31] aiming at checking whether pilot wave dynamics provides a good phenomenological model of the droplets dynamics.

The second part is devoted to questions **2** and **4**.
In chapter 6 we introduce the Schrodinger-Newton equation. In a first time we show that it provides a negative answer to the question **2**: the dBB dynamics does not emerge as a consequence of the Schrodinger-Newton equation. This is due to a generalized Ehrenfest theorem which we show to be valid in this context. However, this generalized Ehrenfest theorem shows that the quantum-classical transition appears to naturally emerge in the framework of the double solution program which constitutes an interesting result in itself. In chapter 7 we propose two experimental tests aiming at answering the question **4**. In order to study the realizability of our experimental proposals we were led to study the interplay between decoherence and cooling which constitutes the core of chapter 8. The last section is devoted to open questions and conclusions.

Bibliography

[1] John S Bell. The theory of local beables. Technical report, 1975.

[2] Albert Einstein, Boris Podolsky, and Nathan Rosen. Can quantum-mechanical description of physical reality be considered complete? *Physical review*, 47(10):777, 1935.

[3] J.S. Bell. On the EPR paradox. *Physics*, 1:165, 1964.

[4] G. Bacciagaluppi and A. Valentini. *Quantum Theory at the Crossroads: Reconsidering the 1927 Solvay Conference*. Cambridge University Press, Cambridge, 2010.

[5] Louis deBroglie. La mécanique ondulatoire et la structure atomique de la matière et du rayonnement. *J. Phys. Radium*, 8(5):225–241, 1927.

[6] Louis De Broglie. An introduction to the study of wave mechanics. 1930.

[7] Louis De Broglie. *Non-linear wave mechanics: A causal interpretation*. Elsevier Publishing Company, 1960.

[8] Louis de Broglie. Interpretation of quantum mechanics by the double solution theory. *Annales de la Fondation Louis de Broglie*, 12(4):1–23, 1987.

[9] David Bohm. A Suggested Interpretation of the Quantum Theory in Terms of "Hidden" Variables. I. *Phys. Rev.*, 85(2):166–179, 1952.

[10] David Bohm. A Suggested Interpretation of the Quantum Theory in Terms of "Hidden" Variables. II. *Phys. Rev.*, 85(2):180–193, 1952.

[11] Louis De Broglie. *Recherches sur la théorie des quanta*. PhD thesis, Migration-université en cours d'affectation, 1924.

[12] Louis De Broglie. The wave nature of the electron. *Nobel lecture*, 12:244–56, 1929.

[13] Erwin Madelung. Quantentheorie in hydrodynamischer form. *Zeitschrift für Physik A Hadrons and Nuclei*, 40(3):322–326, 1927.

[14] Travis Norsen. On the explanation of born-rule statistics in the de broglie-bohm pilot-wave theory. *Entropy*, 20(6):422, 2018.

[15] Louis De Broglie. La thermodynamique «cachée» des particules. In *Annales de l'IHP Physique théorique*, volume 1, pages 1–19, 1964.

[16] David Bohm and Jean-Pierre Vigier. Model of the causal interpretation of quantum theory in terms of a fluid with irregular fluctuations. *Phys. Rev.*, 96(1):208, 1954.

[17] Edward Nelson. Derivation of the schrödinger equation from newtonian mechanics. *Physical review*, 150(4):1079, 1966.

[18] Edward Nelson. Dynamical Theories of Brownian Motion. *Mathematical Notes*, 131(6):2381–2396, 1967.

[19] S. Colin, T. Durt, and R. Willox. L. de Broglie's double solution program: 90 years later. *Annales de la Fondation Louis de Broglie*, 42:19, 2017.

[20] L. Rosenfeld. On quantization of fields. *Nuclear Physics*, 40:353 – 356, 1963.

[21] L. Diósi. Gravitation and quantum-mechanical localization of macro-objects. *Physics Letters A*, 105(4):199 – 202, 1984.

[22] S. Colin, T. Durt, and R. Willox. Can quantum systems succumb to their own (gravitational) attraction? *Class. Quantum Grav.*, 31:245003, 2014.

[23] Samuel Colin, Thomas Durt, and Ralph Willox. Crucial tests of macrorealist and semiclassical gravity models with freely falling mesoscopic nanospheres. *Physical Review A*, 93(6):062102, 2016.

[24] M. Hatifi, C. Lopez-Fortin, and T. Durt. De Broglie's double solution: limitations of the self-gravity approach. *Annales de la Fondation Louis de Broglie*, 43:63, 2018.

[25] Y. Couder and E. Fort. Single-particle diffraction and interference at a macroscopic scale. *Phys. Rev. Lett.*, 97:15410, 2006.

[26] John W M Bush. Pilot-wave hydrodynamics. *Annu. Rev. Fluid Mech.*, 47:269–292, 2015.

[27] Y. Couder, S. Protière, E. Fort, and A. Boudaoud. Dynamical phenomena: walking and orbiting droplets. *Nature*, 437:208, 2005.

[28] Y. Couder, A. Boudaoud, S. Protière, and E. Fort. Walking droplets, a form of wave-particle duality at macroscopic scale? *Europhysics News*, 41(1):14–18, 2010.

[29] Daniel M Harris, Julien Moukhtar, Emmanuel Fort, Yves Couder, and John W.M. Bush. Wavelike statistics from pilot-wave dynamics in a circular corral. *Phys. Rev. E.*, 88:011001, 2013.

[30] Stéphane Perrard, Matthieu Labousse, Marc Miskin, Emmanuel Fort, and Yves Couder. Self-organization into quantized eigenstates of a classical wave-driven particle. *Nature communications*, 5:3219, 2014.

[31] Mohamed Hatifi, Ralph Willox, Samuel Colin, and Thomas Durt. Bouncing oil droplets, de broglie's quantum thermostat, and convergence to equilibrium. *Entropy*, 20(10):780, 2018.

[32] D. Bohm and B. Hiley. Non-locality and locality in the stochastic interpretation of quantum mechanics. *Physics Reports*, 172(3):93–122, 1989.

Part I

Part I: Non-Equilibrium in Pilot Wave Dynamics

Chapter 2

A deterministic pilot wave dynamics: the de Broglie-Bohm interpretation

"Is this the real life? Is this just fantasy?"

Queen - *Bohemian Rhapsody*

Summary In this chapter an overview of the de Broglie Bohm interpretation will be presented. According to the Copenhagen interpretation of quantum mechanics the wave function is sufficent to describe completely the evolution of a quantum system. However, according to bohmian mechanics the standard interpretation is incomplete and to complete it, one only needs to add to the wave function description, well defined positions for the particles. In section 2.1 we introduce the de Broglie Bohm (dBB) interpretation of quantum mechanics [1, 2, 3] and we use the double slit experiment as an example to illustrate its dynamics. We then present in section 2.2 the quantum non-equilibrium hypothesis. In particular, we show in a well chosen context, how the probability distribution $|\Psi|^2$ (Born rule) emerges from the dynamics. This chapter is adapted from [4].

2.1 An introduction to the de Broglie-Bohm theory

2.1.1 Short introduction

There exist many different interpretations of quantum mechanics. Here in this chapter we focus on one of those interpretations, the so-called de Broglie-Bohm (dBB) theory also known as the pilot wave formulation of quantum mechanics. The theory was first proposed by Louis de Broglie in 1927 [1] and revived by David Bohm, in 1952 [2, 3]. It is a hidden variables interpretation because according to the dBB theory, the wave function is not sufficient to describe fully a quantum system. To complete the description, one needs to specify the positions of the particles which are considered as hidden from the point of view of the observer. In the present formulation a particle has always a truly definite position and is guided by the Schrodinger wave Ψ justifying the name of pilot wave. This formulation applies for all non relativistic phenomenons [5] and gives a different way of interpreting [6] the quantum wave function Ψ. Moreover, the position is revealed in a quantum measurement instead of "originating" with the measurement itself as is the case according to the standard interpretation of quantum mechanics. Actually, the position has a privileged role in this approach.

According to John Bell[1] all the measurements reduce to position measurements. As a consequence of that, the important status of the observers in standard quantum mechanics becomes superfluous in this picture.

2.1.2 The de Broglie Bohm dynamics

Let us start the presentation of the dBB dynamics in the case of a single particle. In standard and non-relativistic quantum mechanics, if we have an ensemble of experiments, it is assumed that each element of the ensemble is described by the same wave function $\Psi(\mathbf{x},t)$ which obeys the Schrodinger equation:

$$i\hbar\frac{\partial\Psi(\mathbf{x},t)}{\partial t} = -\frac{\hbar^2}{2m}\Delta\Psi(\mathbf{x},t) + V(\mathbf{x},t)\Psi(\mathbf{x},t), \tag{2.1}$$

where $V(\mathbf{x},t)$ is an external potential, m the mass of the particle, *and* by a position $\mathbf{x}$. The wave function $\Psi(\mathbf{x},t)$ lives in the so called 3-dimensional configuration space[2]. If we were to measure the position of the particle on many elements of the ensemble, we would find that the results are distributed according to the Born's law, i.e. corresponding to the distribution $|\Psi(\mathbf{x},t)|^2$.

Consequently, in order to reproduce the predictions of standard quantum mechanics one must have that the positions are distributed according to the Born rule:

$$\mathcal{P}(\mathbf{x},t) = |\Psi(\mathbf{x},t)|^2, \tag{2.2}$$

where $\mathcal{P}(\mathbf{x},t)$ is the distribution of particle positions over an ensemble of trajectories. An ensemble satisfying condition (2.2) is said to be in ***quantum equilibrium***[3]. It is easy to show from the Schrodinger equation (2.1) that the probability density $|\Psi(\mathbf{x},t)|^2$ satisfies the following continuity equation:

$$\frac{\partial|\Psi(\mathbf{x},t)|^2}{\partial t} + \boldsymbol{\nabla}\cdot\boldsymbol{j}(\mathbf{x},t) = 0, \tag{2.3}$$

where

$$\boldsymbol{j} = \frac{\hbar}{m}\,\mathfrak{Im}\left(\,\Psi^*\,\boldsymbol{\nabla}\,\Psi\,\right), \tag{2.4}$$

is the (probability) current describing the flow of the probability due to (2.1). In order to have trajectories, one needs a velocity vector which can be deduced as in hydrodynamics by taking the ratio between the current and the density:

$$\mathbf{v}(\mathbf{x},t) = \frac{\mathbf{j}(\mathbf{x},t)}{|\Psi(\mathbf{x},t)|^2}. \tag{2.5}$$

Secondly, if one expresses the wave function in terms of its phase $S(\mathbf{x},t)$ and modulus $R(\mathbf{x},t) = \sqrt{|\Psi(\mathbf{x},t)|^2}$ as it was proposed by Bohm [2, 3],

$$\Psi(\mathbf{x},t) = R(\mathbf{x},t)e^{i\,S(\mathbf{x},t)/\hbar}, \tag{2.6}$$

[1] *"... in physics the only observations we must consider are position observations, if only positions of instrument pointers. It is a great merit of the de Broglie-Bohm picture to force us to consider this fact'..."* ([7], p. 166)

[2] Note that the wave function of a system consisting of N particles, is defined in a $3N$-dimensional configuration space.

[3] In section 2.2 we study the case in which this condition is not fulfilled.

one finds that

$$j = \frac{|\Psi(\mathbf{x},t)|^2}{m}\nabla S, \tag{2.7}$$

and that the velocity of the particle at time t is given by[4] :

$$\boxed{\frac{d\mathbf{x}(t)}{dt} = \mathbf{v}(\mathbf{x},t) = \frac{1}{m}\nabla S(\mathbf{x},t)\Big|_{\mathbf{x}=\mathbf{x}(t)}} \tag{2.8}$$

After integrating the equation (2.8) we recover the dBB trajectory. From the above it should be clear that the dBB interpretation is deterministic, knowing the initial position allows us to know where the particle will be at all later time. Therefore, because of the continuity equation (2.3), integrating (2.8) ensures that if initially $\mathcal{P}(\mathbf{x},t_i) = |\Psi(\mathbf{x},t_i)|^2$, then the equality $\mathcal{P}(\mathbf{x},t) = |\Psi(\mathbf{x},t)|^2$ will hold for all later times $t > t_i$. This is the ***equivariance theorem***. It should be stressed that any stochastic element here only comes from our lack of knowledge of the initial positions.

2.1.3 The quantum Hamilton-Jacobi equation

It is worth emphasizing that injecting the polar form of Ψ (2.6) into the Schrodinger equation leads to a quantum generalization of the Hamilton Jacobi equation:

$$\frac{\partial S(\mathbf{x},t)}{\partial t} = -\left(\frac{(\nabla S(\mathbf{x},t))^2}{2\,m} + V(\mathbf{x},t) + Q_\Psi(\mathbf{x},t)\right), \tag{2.9}$$

where

$$Q_\Psi = -\frac{\hbar^2}{2\,m}\frac{\nabla^2 R(\mathbf{x},t)}{R(\mathbf{x},t)} \tag{2.10}$$

is the so called Quantum potential (see [9] for a review). Notice that this term is proportional to $\hbar$ and in the classical limit ($\hbar \to 0$) the classical Hamilton Jacobi equation is recovered.

2.1.4 Application: the double slit experiment

Here we use the double slit experiment as an example to illustrate the de Broglie-Bohm dynamics. This is one of the most famous quantum experiments[5] making the departure from the classical world[6].

Briefly summarized, if one sends quantum objects (for example photons, electrons or small atoms) one at a time into a screen with two slits, interference patterns will emerge behind the slits on a back wall showing a wave like behavior. At first sight, the repartition of the spots positions seems to appear randomly on the screen.

[4] The expression (2.5) for the velocity field is of course not the only possible one: any solution of the form

$$\mathbf{v}'(\mathbf{x},t) = \mathbf{v}(\mathbf{x},t) + \frac{\nabla \times f(\mathbf{x},t)}{|\Psi(\mathbf{x},t)|^2},$$

where f is a scalar function, will also give rise to (2.2) (see Ref. [8] for more details).

[5] Richard Feynman said about this experiment *"We choose to examine a phenomenon which is impossible, absolutely impossible, to explain in any classical way, and which has in it the heart of quantum mechanics. In reality, it contains the only mystery. We cannot make the mystery go away by "explaining" how it works. We will just tell you how it works."*

[6] In section 5.3.3 we discut it in the framework of the bouncing oil droplets.

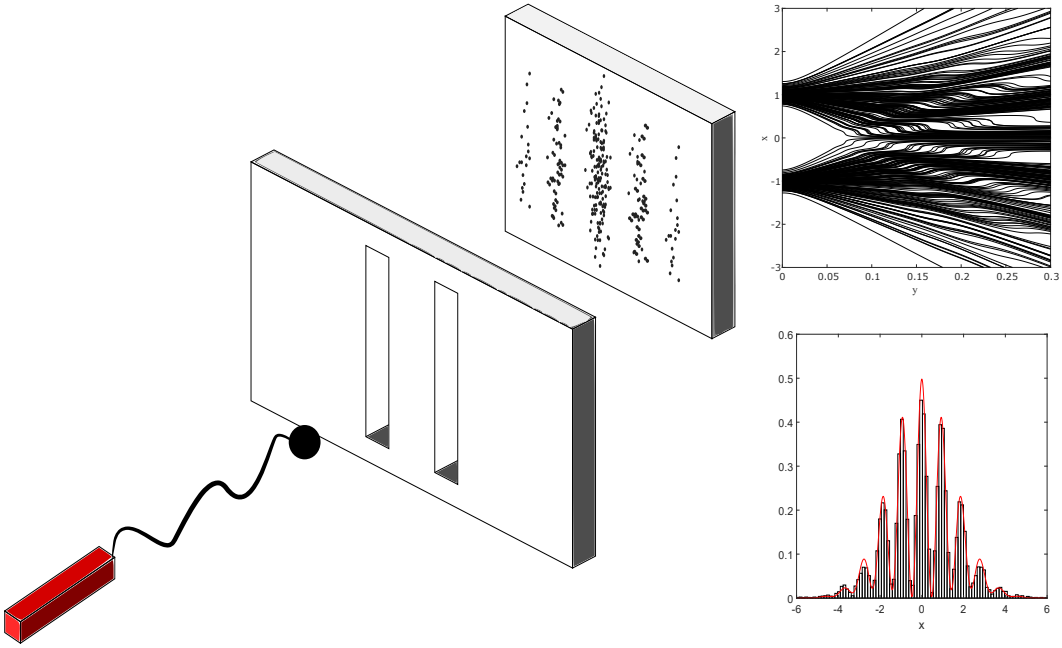

FIGURE 2.1: Illustration of the double-slit experiment on the left. On the right the de Broglie-Bohm trajectories in the top and in the bottom the corresponding histogram which is exactly fitted by the quantum probability in red.

By continuing to send quantum objects through the slits gradually reveal the interference patterns which emerge in the repartition of the spots positions. As an experimental fact, it turns out that the distribution of particle positions is in accordance with the Born rule $|\Psi|^2$. Several authors in the past have tried to explain how the Born rule emerges from individual trajectories which is a highly non-trivial problem. In the standard interpretation of quantum mechanics it is assumed that the interference patterns are a consequence of the superposition principle which is a cornerstone of the quantum theory which in turn is a consequence of the linearity of the Schrodinger equation. Because of that, it is impossible to separate different possible paths for a particle. One has to consider all the possibilities in a linear combination, i.e a linear superposition of paths.

On the other hand, in the pilot wave formulation of quantum mechanics, the particles follow a definite and continuous path from the source to the back-wall screen (see figure 2.1). Furthermore, the particle seems to be guided by "something" that we call pilot wave because the interference patterns suggests a wave like behavior. In this view, the particle goes into one slit and the interference patterns are simply due to the pilot wave interfering with itself. Because of that, opening one or the two slits will influence non-locally the trajectory of a particle through its pilot wave (2.8). Another strangeness of this experiment is that if one tries to know through which slit the particle went, for example by using a detector, it will irremediably destroy the interference patterns. In the Bohmian picture, if we try to interact with the particle, we change the Hamiltonian of the evolution, so that the wave function changes. Changing the wave function, changes also the trajectories[7]. Note that the wave function affects the trajectories but the trajectories have no influence on the wave function.

[7]We will come back to this point in section 5.3.3.

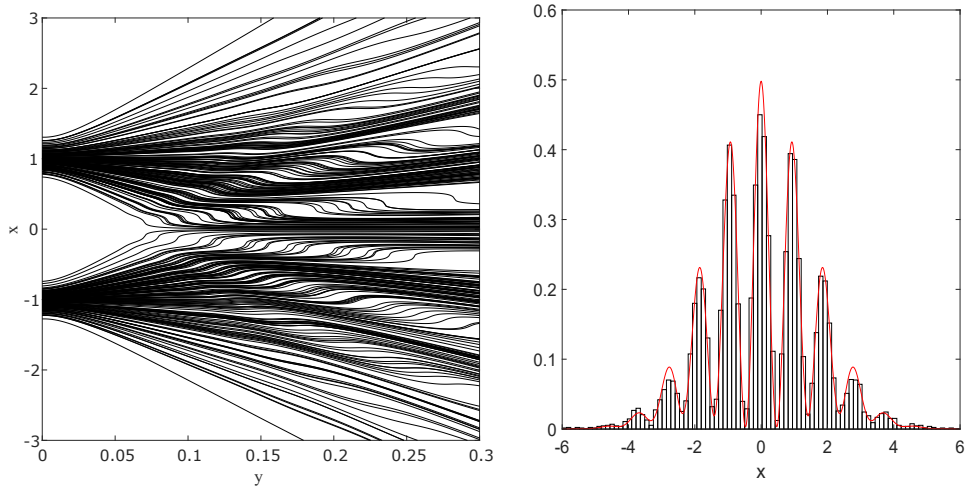

FIGURE 2.2: Left: dBB trajectories for the double-slit experiment. Right: Histogram of the positions and in red the quantum probability $|\Psi|^2$. The simulation was performed using (2.11) with $\sigma = 0.15$, $\frac{\hbar k}{m} = 1$, $x_s = 1$ and was sampled up to $t = 0.3$ with step $\Delta t = 0.01$.

Simulation In figure 2.1 and 2.2 we computed numerically the dBB trajectories for the double-slit experiment. As a consequence of the equivariance theorem it turns out that the histogram of the positions fits exactly with the quantum probability. We modeled the diffracted wave by using two identical gaussian profiles centered on each slits (at $t = y = 0$). The wave function is expressed in the coordinates (x, t):

$$\Psi(\mathbf{x},t) = \mathcal{N}\frac{exp\left(-\frac{\left(x-x_s+\frac{\hbar k}{m}t\right)^2}{2\sigma^2\left(1+\frac{it}{\sigma^2}\right)} - ik\left(x-x_s+\frac{\hbar k}{2m}t\right)\right)}{\sqrt{\sigma\left(1+\frac{it}{\sigma^2}\right)}} + \mathcal{N}\frac{exp\left(-\frac{\left(x+x_s-\frac{\hbar k}{m}t\right)^2}{2\sigma^2\left(1+\frac{it}{\sigma^2}\right)} + ik\left(x+x_s-\frac{\hbar k}{2m}t\right)\right)}{\sqrt{\sigma\left(1+\frac{it}{\sigma^2}\right)}} \tag{2.11}$$

where $\mathcal{N}$ is the normalization factor, $\pm xs$ and σ are the coordinate and the width of each slit. Solving equation (2.8) leads to the above figures. For more information, we refer the reader to the textbook of Peter R. Holland ([9], p.177).

2.1.5 The non locality in the pilot wave formulation

In the previous section, we were dealing with single particle wave functions. Note that for one particle, the wave function lives in the configuration space which coincides exactly with the classical space. It is possible to generalize this theory to a system of N particles [1]. In that case it is expressed in a $3N$-dimensional configuration space and, in the most general setting, the velocity of each particle is instantaneously influenced by the positions of the remaining $(N-1)$ particles. This instantaneous influence of one object on another wathever is the distance between them, is at the heart of the non-locality of quantum mechanics. Here we give a quick overview of the non-locality in the pilot wave formulation [10]. Let us illustrate this effect with a simple example involving two particles.

In this case, from the guidance equation (2.8) we deduce the velocities as :

$$\frac{d\mathbf{x_1}}{dt}(t) = \frac{\hbar}{m_1}\,\mathfrak{Im}\left(\frac{\boldsymbol{\nabla_1}\,\Psi(\mathbf{x_1},\mathbf{x_2},t)}{\Psi(\mathbf{x_1},\mathbf{x_2},t)}\right)\Bigg|_{\mathbf{x_1}=\mathbf{x_1}(t)} \quad \text{and} \quad \frac{d\mathbf{x_2}}{dt}(t) = \frac{\hbar}{m_2}\,\mathfrak{Im}\left(\frac{\boldsymbol{\nabla_2}\,\Psi(\mathbf{x_1},\mathbf{x_2},t)}{\Psi(\mathbf{x_1},\mathbf{x_2},t)}\right)\Bigg|_{\mathbf{x_2}=\mathbf{x_2}(t)} \tag{2.12}$$

- If the wave function $\Psi(\mathbf{x_1},\mathbf{x_2},t)$ is a product state of the form $\Psi(\mathbf{x_1},\mathbf{x_2},t) = \chi(\mathbf{x_1},t)\phi(\mathbf{x_2},t)$ the two velocities simplify to :

$$\frac{d\mathbf{x_1}}{dt}(t) = \frac{\hbar}{m_1}\,\mathfrak{Im}\left(\frac{\boldsymbol{\nabla_1}\,\chi(\mathbf{x_1},t)}{\chi(\mathbf{x_1},t)}\right)\Bigg|_{\mathbf{x_1}=\mathbf{x_1}(t)} \quad \text{and} \quad \frac{d\mathbf{x_2}}{dt}(t) = \frac{\hbar}{m_2}\,\mathfrak{Im}\left(\frac{\boldsymbol{\nabla_2}\,\phi(\mathbf{x_2},t)}{\phi(\mathbf{x_2},t)}\right)\Bigg|_{\mathbf{x_2}=\mathbf{x_2}(t)} \tag{2.13}$$

Everything simplifies so that each particle evolves independently from the other and is guided by its own local velocity field.

- Another feature of the quantum theory is the prediction of entanglement. In the case of entangled particles, the wave function is by definition not factorizable so that the simplification is not possible. In other words, the guidance equation:

$$\frac{d\mathbf{x_i}}{dt}(t) = \frac{\hbar}{m_i}\,\mathfrak{Im}\left(\frac{\boldsymbol{\nabla}_i\,\Psi(\mathbf{x_1},\mathbf{x_2},t)}{\Psi(\mathbf{x_1},\mathbf{x_2},t)}\right)\Bigg|_{\mathbf{x_i}=\mathbf{x_i}(t)}. \tag{2.14}$$

can not be simplified. In order to compute the velocity of one of the particles, we need to know the position of the other particle.

This is a highly non-local effect which has no classical equivalent. The dBB theory exposes with simplicity all the strangeness of quantum mechanics by also making explicit the quantum nonlocality. In fact, the dBB theory was the first interpretation that exposed the non locality in quantum mechanics, long before Bell inequalities. The violation of Bell inequalities in the experiment of Alain Aspect has shown the intrinsic non locality of the quantum theory and revealed the impossibility to build it from a local and classical description.

Let us now discuss the status of the quantum probability law in the context of the pilot wave formulation.

2.2 Relaxation to the quantum probability: the quantum equilibrium hypothesis

2.2.1 Discussion

In the standard interpretation of quantum mechanics, the probability $|\Psi(\mathbf{x},t)|^2$ has an axiomatic status. In our presentation of the dBB theory for a single particle, in section 2.1.1, we also assumed that the initial ensemble of particle positions (at $t = t_i$) is described by the Born's law

$$\boxed{\mathcal{P}(\mathbf{x},t_i) = |\Psi(\mathbf{x},t_i)|^2} \tag{2.15}$$

where $\mathcal{P}(\mathbf{x},t_i)$ is the statistical distribution of initial positions.

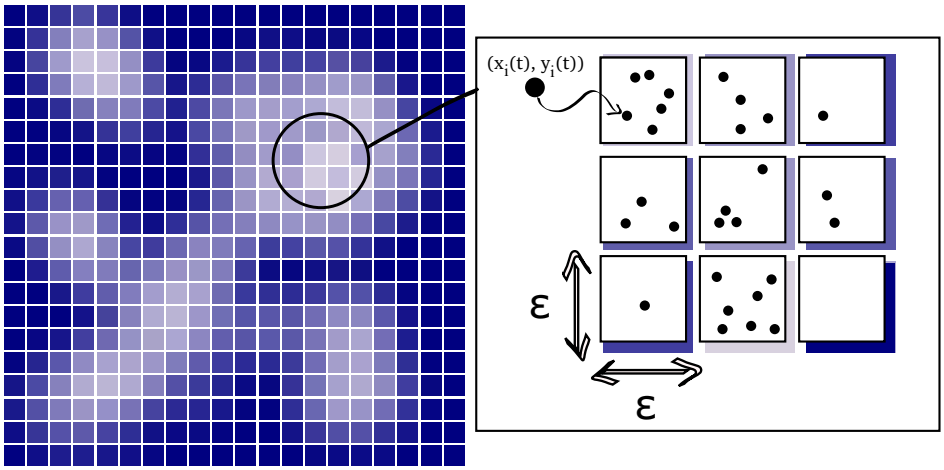

FIGURE 2.3: Illustration of the coarse graining procedure explained in the subsection 2.2.2.

The dynamics ensures that the same relation will hold for any later time because of equation (2.3); i.e because of the equivariance theorem which has been already discussed in the subsection 2.1.2. Louis de Broglie and David Bohm made the assumption (2.15) in their original papers [1, 2, 3], although Bohm tried, already in the 1950s (first on his own – see, e.g., sec. 9 in[2] – and later with Vigier [11]), to relax this assumption by modifying the dynamics. According to authors working today on the dBB theory [12, 6, 13], it is still an assumption which has to be made[8]. According to Valentini [14, 15, 16], however, there is no need to assume that the particle positions are initially distributed according to Born's law or to modify the dynamics.

His claim is that an ensemble $\mathcal{P}(\mathbf{x}, t_i)$ in which Born's law is not satisfied (this constitutes the so-called ***quantum non-equilibrium*** condition) will evolve spontaneously and irreversibly towards quantum equilibrium [13, 17], provided that the wave function leads to sufficiently complex dynamics. However, the relaxation process has to take place on a coarse-grained level.

2.2.2 The coarse grained hypothesis

To begin with, let us explain the need for coarse-graining by introducing the function $f = \mathcal{P}/|\Psi|^2$, as in [12]. The non equilibrium ensemble evolves according to a continuity equation:

$$\frac{\partial \mathcal{P}(\mathbf{x}, t)}{\partial t} + \boldsymbol{\nabla} \cdot \left(\mathcal{P}(\mathbf{x}, t) \frac{\boldsymbol{\nabla} S(\mathbf{x}, t)}{m} \right) = 0. \tag{2.16}$$

An important implication of (2.3) and (2.16) is that the function f is conserved along the dBB trajectories throught the Liouville's equation:

$$\frac{df(\mathbf{x}, t)}{dt} \equiv \frac{\partial f(\mathbf{x}, t)}{\partial t} + \dot{\mathbf{x}} \cdot \boldsymbol{\nabla} f(\mathbf{x}, t) = 0. \tag{2.17}$$

[8]The final objective of de Broglie, Bohm, Vigier, Nelson (and several other contributors to various realistic hidden variable interpretations in which quantum systems are assumed to be localized in space at any time) was to rationalize wave-like statistics in terms of individual trajectories. The same problem occurs when we deal with droplets phenomenology as we will see in chapter 5

Consequently,

$$f(\mathbf{x},t) = f(\mathbf{x}_i,t_i) \tag{2.18}$$

Hence we have that

$$\boxed{\mathcal{P}(\mathbf{x},t) = \frac{\mathcal{P}(\mathbf{x}_i,t_i)}{|\Psi(\mathbf{x}_i,t_i)|^2}|\Psi(\mathbf{x},t)|^2} \tag{2.19}$$

where $\mathbf{x}_i$ is the initial position of the particle which leads to $\mathbf{x}$, when evolving from t_i to t according to the dBB dynamics. As long as $\mathcal{P}(\mathbf{x}_i,t_i)/|\Psi(\mathbf{x}_i,t_i)|^2 \neq 1$, the relaxation to quantum equilibrium is clearly impossible, at least at the microscopic level. However, as argued by Valentini [15], the relaxation *is* possible at the coarse-grained level, provided the initial distribution does not display any fine-grained microstructure.

The operational definition of the coarse-graining is illustrated in figure 2.3 and is explained as follows. We divide the domain of interest $A \subset \Omega$ into small cubes of equal edge length ϵ (we call them coarse-graining cells, or CG cells for short). These CG cells do not overlap and their union is equal to A. The coarse-grained densities, which we denote by $\overline{\mathcal{P}}(\mathbf{x},t)$ and $\overline{|\Psi(\mathbf{x},t)|^2}$, are then defined as

$$\overline{\mathcal{P}}(\mathbf{x},t) = \frac{1}{\epsilon^3}\int_{\text{CG cell}\ni\mathbf{x}} d^3x\mathcal{P}(\mathbf{x},t), \tag{2.20}$$

$$\overline{|\Psi(\mathbf{x},t)|^2} = \frac{1}{\epsilon^3}\int_{\text{CG cell}\ni\mathbf{x}} d^3x|\Psi(\mathbf{x},t)|^2, \tag{2.21}$$

where the domain of integration is the CG cell containing $\mathbf{x}$. Hence, the ratio $\overline{\mathcal{P}}/\overline{|\Psi|^2}$ is not inevitably conserved along the dBB trajectories. This difference allows $\overline{\mathcal{P}}$ to possibly converge to $\overline{|\Psi|^2}$. As explained in [18], *"The coarse-graining could be understood as corresponding to a finite accuracy of physical measurements"*.

2.2.3 Time reversibility

Let us assume we have a non-equilibrium distribution $\mathcal{P}(\mathbf{x},t_i)$ which relaxes to quantum equilibrium at the coarse-grained level, under the dynamics generated by the wave function $\Psi(\mathbf{x},t)$. As the dBB theory is time-reversal invariant, in the time-reversed situation, under the dynamics generated by $\Psi^*(\mathbf{x},-t)$ we would have a distribution that moves away from quantum equilibrium. Thus it would seem that time-reversal invariance contradicts the possibility of relaxation to quantum equilibrium. This conclusion is unwarranted however: as the initial distribution $\mathcal{P}(\mathbf{x},t_i)$ relaxes to quantum equilibrium, it retains information on the original values of f (which are constant in time) and thereby acquires a fine-grained microstructure, which means that at the final time t_f, $\mathcal{P}(\mathbf{x},t_f)$ will differ significantly from $\overline{\mathcal{P}}(\mathbf{x},t_f)$. Therefore, in the time-reversed situation, the initial distribution would exhibit a fine-grained micro-structure. From this point of view the irreversible onset of quantum equilibrium [12, 6, 13] can be linked to the selection of the initial distributions for which such fine grained microstructures are absent.

In chapter 4 we will develop the present dissussion in further detail. In particular we will test the sensitivity of the convergence process in presence of microstructures in the initial distribution of positions.

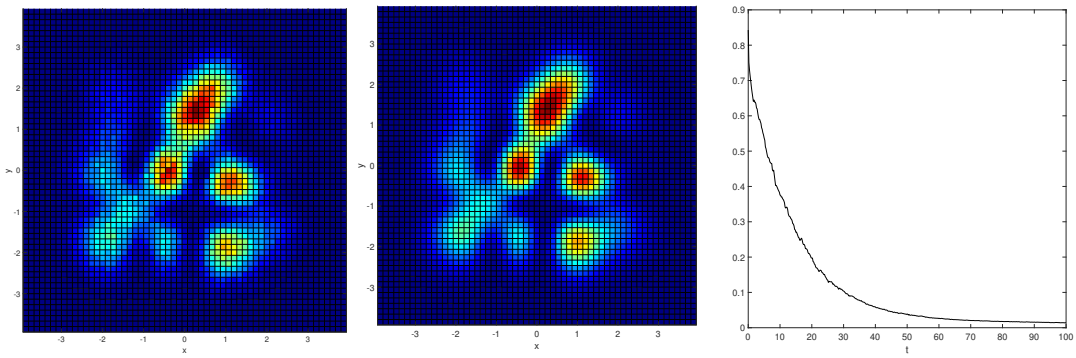

(A) The coarse-grained distribution $\overline{\mathcal{P}}$ at time $t = 100$.

(B) The quantum probability $\overline{|\Psi|^2}$ at time $t = 100$.

(C) The evolution of the associated entropy function $\overline{H}(t)$ (2.22).

FIGURE 2.4: This plot shows the convergence of $\overline{\mathcal{P}}$ to the quantum probability probability $\overline{|\Psi|^2}$ at the coarse grained level. We started with an ensemble of $N = 300\,000$ intial positions uniformly distributed on $[-2,2]$x$[-2,2]$. The coarse graining domain $[-4,4]$x$[-4,4]$ was divided by a number of 60x60 coarse grained cells. We chose in (2.26) a superposition of $M = 4^2 = 16$ modes.

2.2.4 The "H-theorem" in dBB

In order to quantify the difference between the distribution $\mathcal{P}(\mathbf{x},t)$ and the quantum equilibrium condition $|\Psi(\mathbf{x},t)|^2$ at the coarse-grained level, Valentini [14, 15, 16] has introduced the entropy-like function

$$\overline{H}(t) = \int_\Omega d^3x\, \overline{\mathcal{P}}\, \ln\left(\overline{\mathcal{P}}/\overline{|\Psi|^2}\right), \tag{2.22}$$

where $\overline{\mathcal{P}}$ and $\overline{|\Psi|^2}$ as in (2.20) and (2.21), for which numerical simulations strongly suggest that the (quantum) H-theorem holds in the sense that

$$\overline{H}(t) \leq \overline{H}(t_i), \tag{2.23}$$

It should be stressed however that this is not necessarily a monotonic decay and therefore does not prove that quantum equilibrium will always be reached. It merely indicates a tendency towards relaxation. The strongest support for the idea of relaxation to quantum equilibrium comes from numerical simulations of the evolution of non-equilibrium distributions for various quantum systems [12, 18, 19, 20, 21, 22]. The first numerical simulations were performed by Valentini and Westman [12] who showed, in the case of a 2D box, that relaxation quickly takes place for a wave function which is a superposition of the first 16 modes of energy (the superposition being equally weighted). It was also hinted that the nodes of the wave function, with their associated vorticity, play a crucial role in the relaxation process, as purveyors of chaos (or mixing) in the dynamics. This later claim was properly understood in [23]. The dependence of the relaxation timescale on the coarse-graining length ϵ and on the number of energy modes was studied in [19]. In [22], it was shown that quantum systems with a low number of modes are likely to never fully relax, in which case $\overline{H}$ reaches a non-zero residue value. However, such a scenario becomes unlikely as the number of modes increases.

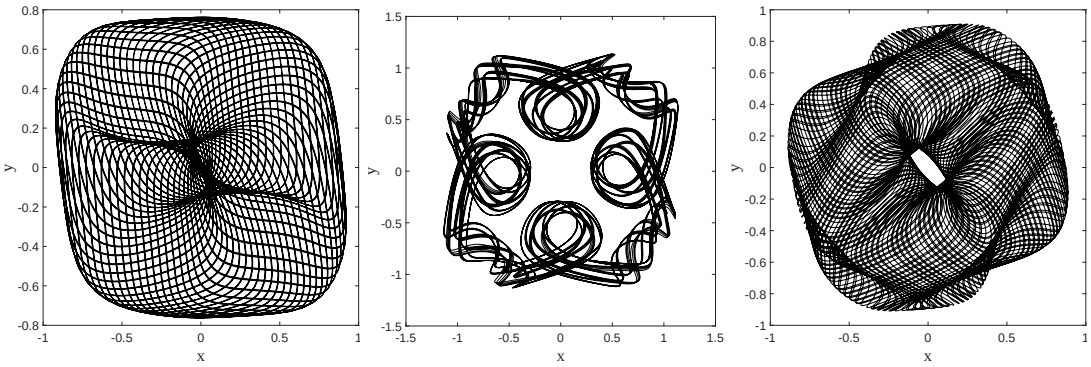

FIGURE 2.5: Plots showing three possible dBB trajectories for a single point particle in the case of the 2D harmonic oscillator (2.26) with $M = 2^2 = 4$. Each plot is associated to different initial random phases and different initial positions.

Another interesting quantity is of course the L_1 norm of the difference between $\mathcal{P}$ and the equilibrium distribution $|\Psi|^2$:

$$\mathcal{L}_1 = \int_\Omega d^3x \, |\mathcal{P} - |\Psi|^2|. \tag{2.24}$$

It was used by Petroni and Guerra [24, 25] to discuss relaxation towards equilibrium in the framework of Nelson dynamics and it is used by Efthymiopoulos et al [26] in the dBB theory. We will come back to this point in section 3.2.1.

In the framework of the quantum non-equilibrium approach, it is considered that standard quantum mechanics is only one facet of the pilot-wave theory, that of quantum equilibrium, leaving the possibility for possible new physics: that of quantum non-equilibrium. One should assume of course, that during our time we have only had (or can only have) access to systems for which quantum equilibrium has already been reached. But that does not mean that quantum non-equilibrium never existed in the early universe (which could possibly be inferred from the observation of the remnants of the early fractions of seconds of the universe, just after the big bang [27]), or that some, yet undetetected, exotic quantum systems cannot still be in quantum non-equilibrium today [28].

2.2.5 Numerical simulation in a 2D quantum harmonic oscillator (dBB)

In order to illustrate the relaxation process towards quantum equilibrium, it is necessary to define a context in which we can apply the basic ideas developped in the previous subsection. For that purpose, let us consider a 2D quantum harmonic oscillator:

$$\mathcal{H} = -\frac{p_x^2}{2m} - \frac{p_y^2}{2m} + \frac{m\omega^2}{2}\left(x^2 + y^2\right). \tag{2.25}$$

The Schrodinger equation is easily solved so that the next step is to choose a quantum state Ψ consisting of a superposition of equally weighted products of eigenstates ψ_{n_x} along X and ψ_{n_y} along Y. Increasing the number of modes M allows us to study the quantum relaxation to the Born rule $|\Psi|^2$. In fact the increase of the number of modes in the superposition of Ψ enhances the complexity of the dynamics by making the variation of the phase $\boldsymbol{\nabla} S(\mathbf{x}, t)$ non trivial.

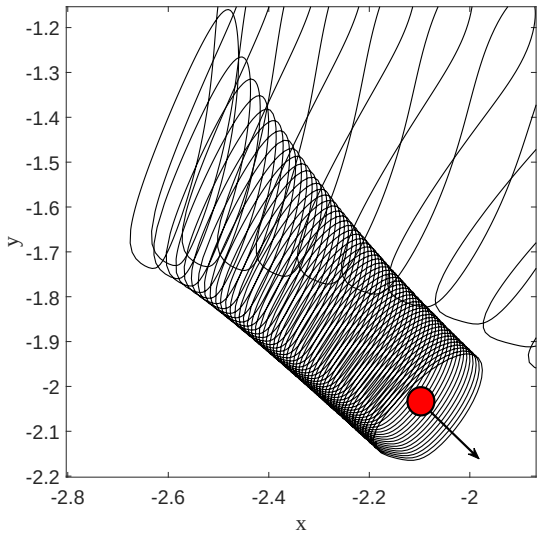

FIGURE 2.6: Plot showing the effect of a nodal point (zero of the wave-function represented by a red circle) on the dBB trajectory. The figure has been realized in the case of the 2D quantum harmonic oscillator (2.26) for $M = 2^2 = 4$.

The eigenstates are chosen among M energy (Fock) states, with randomly-chosen initial phases θ_{n_x,n_y}:

$$\boxed{\Psi(x,y,t) = \frac{1}{\sqrt{M}} \sum_{n_x=0}^{\sqrt{M}-1} \sum_{n_y=0}^{\sqrt{M}-1} e^{i\,\theta_{n_x,n_y} - i\omega\left(n_x+n_y+1\right)t}\, \psi_{n_x}(x)\, \psi_{n_y}(y)} \tag{2.26}$$

In figure (2.5) we show three possible dBB trajectories associated to the solution of the equation (2.8) for the sate Ψ above. One can obtain a huge variety of trajectories depending on the choice of M, θ_{n_x,n_y} and on the choice of the initial position. A quick remark concerns the influence of the nodal points (zeros of the distribution $|\Psi|^2$) on the trajectories. As already studied in [23, 29], the nodal points have a privileged role in the convergence toward quantum equilibrium especially in the process of mixing (it will be discussed in further details in the chapter 4.3). They can act as an attractor, i.e the trajectories can rotate around them as illustrated in figure 2.6. On the other hand, in figure (2.4) we illustrate the color plot of the distribution $\overline{\mathcal{P}}$ obtained at the equilbrium and we plot the the associated H-function (2.22) characterizing this relaxation process.

2.3 Conclusion:

In this chapter we presented the de Broglie Bohm interpretation of quantum mechanics. In a nutshell, we have introduced the minimal tools to understand the idea behind the quantum non-equilibrium theory which aims to explain the emergence of the Born rule statistics. To illustrate the process of convergence to quantum equilibrium we simulated numerically the evolution of a non-equilibrium ensemble using a two dimensional harmonic oscillator. In particular we quantified the onset of quantum equilibrium in terms of a H-function $\overline{H}(t)$ [17]. Depending on the initial distribution of particle positions, or on the complexity of the wavefunction, the quantum relaxation does not always happen. In particular, this process depends on the way the coarse graining is done and also on the possible existence of microstructures in the distribution of positions. This dependency will be studied in further detail in chapter 4 in terms of chaos and mixing.

We shall now present the stochastic extention of the dBB theory in order to conduct a comparative study of the onset of quantum equilibrium.

Bibliography

[1] Louis deBroglie. La mécanique ondulatoire et la structure atomique de la matière et du rayonnement. *J. Phys. Radium*, 8(5):225–241, 1927.

[2] David Bohm. A Suggested Interpretation of the Quantum Theory in Terms of "Hidden" Variables. I. *Phys. Rev.*, 85(2):166–179, 1952.

[3] David Bohm. A Suggested Interpretation of the Quantum Theory in Terms of "Hidden" Variables. II. *Phys. Rev.*, 85(2):180–193, 1952.

[4] Mohamed Hatifi, Ralph Willox, Samuel Colin, and Thomas Durt. Bouncing oil droplets, de broglie's quantum thermostat, and convergence to equilibrium. *Entropy*, 20(10):780, 2018.

[5] Detlef Dürr, Sheldon Goldstein, Travis Norsen, Ward Struyve, and Nino Zanghì. Can bohmian mechanics be made relativistic? *Proceedings of the Royal Society A: Mathematical, Physical and Engineering Sciences*, 470(2162):20130699, 2014.

[6] Detlef Dürr, Sheldon Goldstein, and Nino Zanghì. Bohmian mechanics and the meaning of the wave function. *arXiv preprint quant-ph/9512031*, 1995.

[7] John S Bell. *Speakable and unspeakable in quantum mechanics: Collected papers on quantum philosophy*. Cambridge university press, 2004.

[8] E. Deotto and G.-C. Ghirardi. Bohmian mechanics revisited. *Found. Phys.*, 28(1):1–30, 1998.

[9] P. R. Holland. *The quantum theory of motion: an account of the de Broglie-Bohm causal interpretation of quantum mechanics*. Cambridge University press, 1993.

[10] Franck Laloë. *Comprenons-nous vraiment la mécanique quantique?: 2e édition, révisée et augmentée*. EDP sciences, 2018.

[11] David Bohm and Jean-Pierre Vigier. Model of the causal interpretation of quantum theory in terms of a fluid with irregular fluctuations. *Phys. Rev.*, 96(1):208, 1954.

[12] Antony Valentini and Hans Westman. Dynamical origin of quantum probabilities. *Proc. R. Soc. A*, 461:253–272, 2005.

[13] Travis Norsen. On the explanation of born-rule statistics in the de broglie-bohm pilot-wave theory. *Entropy*, 20(6):422, 2018.

[14] Antony Valentini. *On the pilot-wave theory of classical, quantum and subquantum physics.* PhD thesis, SISSA, 1992.

[15] Antony Valentini. Signal locality, uncertainty and the subquantum H-theorem. I. *Phys. Lett. A*, 156:5–11, 1991.

[16] Antony Valentini. Signal locality, uncertainty and the subquantum H-theorem. II. *Phys. Lett. A*, 158:1–8, 1991.

[17] Antony Valentini. Foundations of statistical mechanics and the status of the born rule in de broglie-bohm pilot-wave theory. *arXiv preprint arXiv:1906.10761*, 2019.

[18] S. Colin and W. Struyve. Quantum non-equilibrium and relaxation to quantum equilibrium for a class of de Broglie-Bohm-type theories. *New J. Phys.*, 12:043008, 2010.

[19] M.D. Towler, N. J. Russell, and A. Valentini. Time scales for dynamical relaxation to the Born rule. *Proc. R. Soc. A*, 468:990–1013, 2011.

[20] S. Colin. Relaxation to quantum equilibrium for Dirac fermions in the de Broglie-Bohm pilot-wave theory. *Proc. R. Soc. A*, 468:1116–1135, 2012.

[21] G. Contopoulos, N. Delis, and C. Efthymiopoulos. Order in de Broglie - Bohm quantum mechanics. *J. Phys. A: Math. Theor.*, 45(16):165301, 2012.

[22] E. Abraham, S. Colin, and A. Valentini. Long-time relaxation in the pilot-wave theory. *J. Phys. A: Math. Theor.*, 47:395306, 2014.

[23] C. Efthymiopoulos, C. Kalapotharakos, and G. Contopoulos. Origin of chaos near critical points of quantum flow. *Phys. Rev. E*, 79(3):036203, 2009.

[24] Nicola Cufaro Petroni. Asymptotic behaviour of densities for Nelson processes. In *Quantum Communications and Measurement*, pages 43–52. Springer, 1995.

[25] Nicola Cufaro Petroni and Francesco Guerra. Quantum Mechanical States as Attractors for Nelson Processes. *Found. Phys.*, 25(2):297–315, 1995.

[26] C. Efthymiopoulos, G. Contopoulos, and A. C. Tzemos. Chaos in de Broglie - Bohm quantum mechanics and the dynamics of quantum relaxation. *Ann. Fond. de Broglie*, 42:133, 2017.

[27] Antony Valentini. Inflationary cosmology as a probe of primordial quantum mechanics. *Phys. Rev. D*, 82:063513, 2010.

[28] Nicolas G. Underwood and Antony Valentini. Quantum field theory of relic nonequilibrium systems. *Phys. Rev. D*, 92:063531, 2015.

[29] Athanasios C Tzemos, Christos Efthymiopoulos, and George Contopoulos. Origin of chaos near three-dimensional quantum vortices: A general bohmian theory. *Physical Review E*, 97(4):042201, 2018.

Chapter 3

A stochastic pilot wave dynamics: the Bohm-Hiley-Nelson theory

"Hakuna Matata"

Timon & Pumbaa

Summary Actually, the onset of quantum equilibrium in the framework of dBB dynamics (see e.g.[1, 2] and also [3] and references therein) and in the stochastic versions thereof ([4, 5, 6, 7, 8, 9]) is an important foundational issue in itself, which motivated numerous studies. In the case of dBB dynamics it is easy to show that in simple situations the relaxation to the Born statistical distribution does not occur at all, but recent studies [10, 11, 12, 13, 14, 15, 16] show that in sufficiently complex situations (several modes of different energies for instance) the system might exhibit mixing, which explains the onset of quantum equilibrium in such cases. In this chapter, we study in detail the quantum equilibrium in the case of Nelson-type dynamics. In particular we will see that the quantum Brownian motion imposed in such a model accelerates the relaxation to the Born's distribution $|\Psi|^2$ and in fact ensures that relaxation to it will almost always occur (here we derive a strong H theorem for the stochastic pilot wave dynamics). This chapter is adapted from [17].

3.1 A simple realization of de Broglie's quantum thermostat – Bohm-Hiley-Nelson dynamics

3.1.1 Short introduction

Let us present here the stochastic generalisations of the de Broglie-Bohm dynamics. de Broglie himself[1], in fact, considered such generalizations of the deterministic dBB dynamics (which he called the "quantum thermostat hypothesis") to be highly welcome because they might provide a physically sound picture of the hidden dynamics in the case of static quantum states. For instance, if we consider the position of an electron prepared in the ground state of a hydrogen atom, the dBB dynamics predicts that its position will remain

[1] Quoting de Broglie: *"...Finally, the particle's motion is the combination of a regular motion defined by the guidance formula, with a random motion of Brownian character... any particle, even isolated, has to be imagined as in continuous "energetic contact" with a hidden medium, which constitutes a concealed thermostat. This hypothesis was brought forward some fifteen years ago by Bohm and Vigier [1], who named this invisible thermostat the "subquantum medium"... If a hidden sub-quantum medium is assumed, knowledge of its nature would seem desirable..."* (In[18] Ch.XI: On the necessary introduction of a random element in the double solution theory. The hidden thermostat and the Brownian motion of the particle in its wave.)

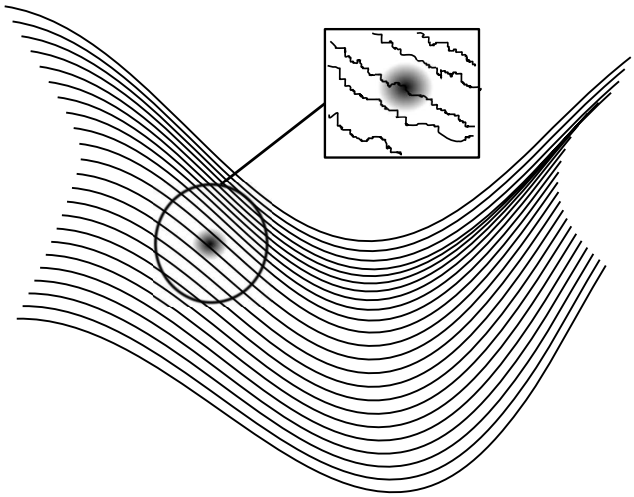

FIGURE 3.1: A particle suspended in a Madelung fluid and subject to local fluctuations.

frozen at the same place throughout time because $\boldsymbol{\nabla} S(\mathbf{x}, t) = 0$, which is counterintuitive to say the least. Adding a stochastic component to its velocity could, in principle, explain why averaging the position of the electron over time is characterized by an exponentially decreasing probability density function, in agreement with the Born rule (provided, of course, that ergodicity is present in the problem in exactly the right proportion as we will see in section 3.3.7). A first proposal in this sense was formulated by Bohm and Vigier in 1954 [1] which, later on, was made more precise by Bohm and Hiley [6], but stochastic derivations of Schrödinger's equation by Nelson[5] (and others [19, 20] in the framework of stochastic electrodynamics) can also be considered to provide models of the quantum thermostat.

3.1.2 Definition

In this chapter we shall consider a particular model of the quantum thermostat in which, as in the Bohm-Vigier model, a single spinless particle suspended in a Madelung fluid (see figure 3.1). The particle moves with the local velocity of the resulting field, given by (2.8), and is subjected to fluctuations coming from the latter. However, following Nelson, we shall model these fluctuations by means of a particular stochastic process.[2] This process is defined on a probabilistic space Ω, characterized by a probability distribution $P(\mathbf{x}, t)$ and obeys an Ito stochastic differential equation of the general form:

$$d\boldsymbol{x} = \left[\frac{1}{m} \boldsymbol{\nabla} S + \boldsymbol{\gamma} \right] \Big|_{x=x(t)} dt + \sqrt{\alpha}\, d\boldsymbol{W}(t), \tag{3.1}$$

where α is the (constant) diffusion coefficient that characterizes the strength of the random part and $d\boldsymbol{W}(t)$ is a Wiener process in three dimensions. The function $\boldsymbol{\gamma}(\mathbf{x}, t)$ in (3.1) is a systematic drift, the so-called *osmotic velocity*, which we shall fix in the following way.

[2] To be precise: our model is formally the same as Nelson's in that it relies on the same stochastic process. However, in spirit, it is closer to the Bohm-Hiley model[6] in that we do not assume to be at quantum equilibrium (an assumption which is fundamental to Nelson's theory, as was already pointed out by Bohm and Hiley[6] ; see also Ref. [4] for a detailed presentation and a comparison of both approaches).

The conservation equation of the probability distribution (which we denote by P, in order to stress the difference with the probability in the dBB dynamics which is denoted by $\mathcal{P}$) obeys a the Fokker-Planck equation:

$$\frac{\partial P}{\partial t} = -\boldsymbol{\nabla}\cdot\left(\frac{P}{m}\boldsymbol{\nabla}S + \gamma\, P\right) + \frac{\alpha}{2}\,\Delta P. \tag{3.2}$$

If we now require that the quantum equilibrium $P(q,t) = |\Psi(q,t)|^2$ is a solution of this Fokker-Planck equation, we obtain from (2.3), (2.7) and (3.2) that

$$\boldsymbol{\nabla}\cdot\left(\gamma\,|\Psi|^2 - \frac{\alpha}{2}\,\boldsymbol{\nabla}|\Psi|^2\right) = 0, \tag{3.3}$$

which is a constraint on the osmotic velocity. The simplest solution of this constraint is [21]

$$\gamma(\mathbf{x},t) = \frac{\alpha}{2}\,\frac{\boldsymbol{\nabla}|\Psi|^2}{|\Psi|^2}. \tag{3.4}$$

In the rest of the chapter we choose the osmotic drift velocity to be (3.4), with α an a priori free parameter, Nelson's choice for α ($\alpha = \hbar/m$).

In summary, our version of Nelson dynamics (due to Bohm-Hiley [6]) is fully defined by the following Ito equation,

$$\boxed{d\mathbf{x}(t) = \left[\frac{1}{m}\boldsymbol{\nabla}S + \frac{\alpha}{2}\frac{\boldsymbol{\nabla}|\Psi|^2}{|\Psi|^2}\right]\Bigg|_{x=x(t)} dt + \sqrt{\alpha}\,d\boldsymbol{W}(t)} \tag{3.5}$$

where $dW_i(t)$ represents a Wiener process with

$$< dW_i(t) >= 0 \qquad \text{and} \qquad < dW_i(t)dW_j(t') >= \frac{1}{2}\,\delta_{ij}\,\delta(\,t-t'\,), \tag{3.6}$$

while the Fokker-Planck equation for the associated probability distribution $P(\mathbf{x},t)$ obeys

$$\boxed{\frac{\partial P}{\partial t} = \frac{\alpha}{2}\,\Delta P - \boldsymbol{\nabla}\cdot\left(\frac{P}{m}\boldsymbol{\nabla}S + \frac{\alpha}{2}\frac{P}{|\Psi|^2}\boldsymbol{\nabla}|\Psi|^2\right)} \tag{3.7}$$

where $\Psi(\mathbf{x},t)$ satisfies the Schrodinger equation:

$$i\hbar\,\frac{\partial\Psi}{\partial t} = -\frac{\hbar^2}{2m}\Delta\Psi + V\Psi. \tag{3.8}$$

At quantum equilibrium, i.e. when $P(\mathbf{x},t) = |\Psi(\mathbf{x},t)|^2$, the diffusion velocity is balanced by the osmotic term and the Bohm velocity is recovered, on average.

We shall now discuss the details of the relaxation towards quantum equilibrium in this stochastic formalism.

3.2 The H-theorem for BHN dynamics

Let us start by introducing an analog of Valentini's entropy[3] (2.22) for the probability distribution $P(\mathbf{x},t)$ associated with our Nelson dynamics, as defined by (3.5–3.8),

$$H_V(t) = \int_\Omega d^3x\, P \ln\left(\frac{P}{|\Psi|^2}\right), \tag{3.9}$$

which is a special instance of a relative entropy known as the Kullback-Leibler divergence [23]. We also define a second non-negative functional,

$$L_f(t) = \int_\Omega d^3x\, f(P-|\Psi|^2), \tag{3.10}$$

where

$$f(\mathbf{x},t) = \frac{P(\mathbf{x},t)}{|\Psi(\mathbf{x},t)|^2}. \tag{3.11}$$

Note that we always impose the boundary conditions $|\Psi|^2\big|_{\partial\Omega} = P\big|_{\partial\Omega} = 0$ and $f\big|_{\partial\Omega} = 1$ so as to avoid divergence of these integrals on the boundary of Ω.

To understand why functionals (3.9) and (3.10) are non-negative and why they are zero if and only if (quantum) equilibrium is reached (that is to say when $f = 1$ everywhere in space), it is important to note that the integrands of H_V and L_f satisfy the inequalities[4]

$$(P-|\Psi|^2) \leq P \ln\frac{P}{|\Psi|^2} \leq \frac{P}{|\Psi|^2}(P-|\Psi|^2), \tag{3.12}$$

for which any of the possible equalities only hold when $P = |\Psi|^2$. Now, since both $P(\mathbf{x},t)$ and $|\Psi(\mathbf{x},t)|^2$ are probability distributions, i.e. since we have $\int_\Omega P dx = \int_\Omega |\Psi|^2 dx = 1$, it follows from (3.12) that whenever $H_V(t)$ and $L_f(t)$ are well-defined, they satisfy the inequalities:

$$0 \leq H_V(t) \leq L_f(t). \tag{3.13}$$

Moreover, for the same reason, L_f can be re-expressed as

$$\int_\Omega d^3x\, \left[f(P-|\Psi|^2) - (P-|\Psi|^2)\right], \tag{3.14}$$

the integrand in which is non-negative due to (3.12). Therefore, L_f can only be zero if its integrand is zero, i.e.: if $P = |\Psi|^2$ (if P, $|\Psi|^2$ and f are sufficiently smooth, which is something we shall always assume unless otherwise stated). Similarly[2] one also has that H_V can only be zero when $P = |\Psi|^2$ everywhere in Ω.

Let us now prove the relaxation to quantum equilibrium. Substituting $P = f\,|\Psi|^2$ in the Fokker-Planck equation (3.7), and using the continuity equation (2.3) and relation (2.7), it

[3] It should be noted that the entropy (3.9) or the functional (3.10) we shall use to quantify the relaxation to quantum equilibrium, are different from the entropies usually considered in the context of classical H-theorems (like e.g. the Boltzmann entropy). One should bear in mind however that *quantum equilibrium* is radically different from classical equilibrium [22] and has no connection whatsoever with relaxation to quantum *thermal* equilibrium, for the simple reason that the Born distribution of positions reached by an ensemble of trajectories *à la* BHN or dBB is not a thermal distribution.

[4] This is immediate from the trivial inequality: $\forall x > 0, \quad (1-1/x) \leq \ln x \leq x-1$.

is easily verified that

$$|\Psi|^2 \frac{\partial f}{\partial t} = \frac{\alpha}{2} \nabla \cdot (|\Psi|^2 \nabla f) - \frac{|\Psi|^2}{m} (\nabla f)(\nabla S). \tag{3.15}$$

Rewriting L_f as

$$L_f = \int_\Omega d^3x \, f(f-1)|\Psi|^2, \tag{3.16}$$

its behaviour in time can be calculated using (3.15), (2.3) and (2.7):

$$\frac{dL_f}{dt} = \int_\Omega d^3x \, \left[-\nabla \cdot \left(\frac{|\Psi|^2}{m} (f^2 - f) \nabla S \right) + \frac{\alpha}{2} (2f-1) \nabla \cdot (|\Psi|^2 \nabla f) \right] \tag{3.17}$$

$$= \frac{\alpha}{2} \int_\Omega d^3x \, \left[\nabla \cdot \left[(2f-1)|\Psi|^2 \nabla f \right] - 2 (\nabla f)^2 |\Psi|^2 \right] \tag{3.18}$$

which gives

$$\boxed{\frac{dL_f}{dt} = -\alpha \int_\Omega d^3x \, (\nabla f)^2 |\Psi|^2} \tag{3.19}$$

It is of course strictly negative, for all t, as long as ∇f and $|\Psi|^2$ are not identically zero. Hence, if $|\Psi|^2$ is not zero throughout Ω, L_f will decrease monotonically for as long as f is not (identically) equal to one on Ω, and therefore necessarily converges to zero, a value it can only attain when $f \equiv 1$ or, equivalently, when $P \equiv |\Psi|^2$. We have thus established a strong H-theorem showing that, in the case of BHN dynamics, any probability distribution P necessarily converges to $|\Psi|^2$, if the latter does not become identically zero. Note that this excludes the case of a free particle for which $\lim_{t \to +\infty} |\Psi(x,t)|^2 = 0$, for all x, which means that $\frac{dL_f}{dt}$ tends to zero even when f does not converge to unity (see [8] for example).

A result, similar to the above, is also easily established for H_V since L_f dominates the latter, or alternatively from the formula

$$\boxed{\frac{dH_V}{dt} = -\frac{\alpha}{2} \int_\Omega d^3x \, (\nabla f)^2 \frac{|\Psi|^2}{f}} \tag{3.20}$$

The above results show that (excluding the case of the free particle) BHN dynamics, naturally, exhibits relaxation towards quantum equilibrium, and this for general initial probability distributions (at least, as long as the initial distribution is smooth enough). In the stochastic setting it seems that there is no need for any assumptions on the microstructure of the initial distributions, nor is there any need for the coarse-grained hypothesis when deriving an H-theorem (we will pursue the present discussion in chapter 4).

Note that these results also show that we have, in fact, convergence of the distribution P to the quantum equilibrium distribution $|\Psi|^2$ in L^1 norm.

3.2.1 Convergence in L^1 norm

In this subsection we prove that the convergence in H_V implies the convergence in L_1 and we generalize the result of Petroni and Guera [8]. The functionnal L_1 is defined by

$$L_1 = \int_\Omega d^3x \, |P - |\Psi|^2|. \tag{3.21}$$

To show the convergence in L_1 let us go back to the inequalities

$$(P - |\Psi|^2) \leq P \ln \frac{P}{|\Psi|^2} \leq \frac{P}{|\Psi|^2}(P - |\Psi|^2). \tag{3.22}$$

Because of the normalization of the probabilities, the H-function (3.9) can be written as:

$$H_V = \int_\Omega d^3x \left[P \ln \left(\frac{P}{|\Psi|^2} \right) + (P - |\Psi|^2) \right] \tag{3.23}$$

now using the substitution $z = P/|\Psi|^2$ leads to

$$H_V = \int_\Omega d^3x \, |\Psi|^2 \left[z \, ln \, z - (z-1) \right]. \tag{3.24}$$

Moreover it is clear that

$$1 - \frac{1}{z} \leq ln \, z \leq z - 1 \tag{3.25}$$

with $(z \geq 0)$ for which equalities only hold when $z = 1$. After some rearrangement the above expression is rewritten as:

$$0 \leq z \, ln \, z - (z-1) \leq (z-1)^2. \tag{3.26}$$

Making the Taylor expansion around $z_0 = 1$ so that $z = 1 + x$ with $|x| \ll 1$, one finds that

$$(x+1) \, ln \, (x+1) \, - x = \frac{x^2}{2(1 + \frac{x}{3})} + \mathcal{O}(x^3) \tag{3.27}$$

We can conclude that $\forall \, z \geq 0$ (see figure 3.2)

$$z \, ln \, z \, - (z-1) \geq \frac{(z-1)^2}{2(1 + \frac{(z-1)}{3})} \tag{3.28}$$

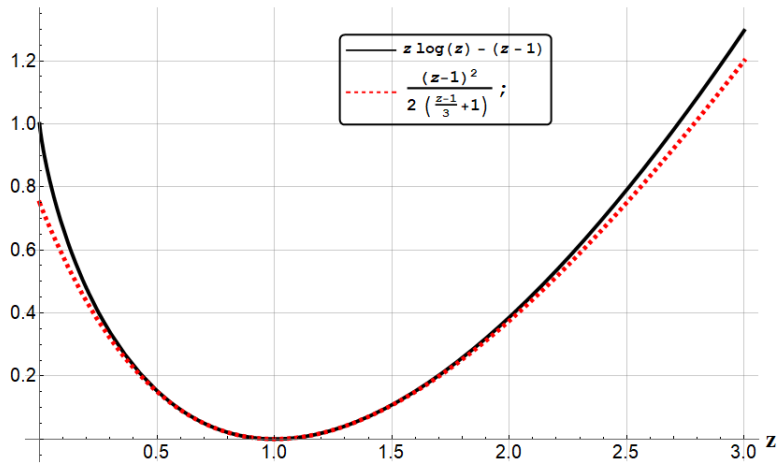

FIGURE 3.2: We illustrate here the inequality (3.28)

.

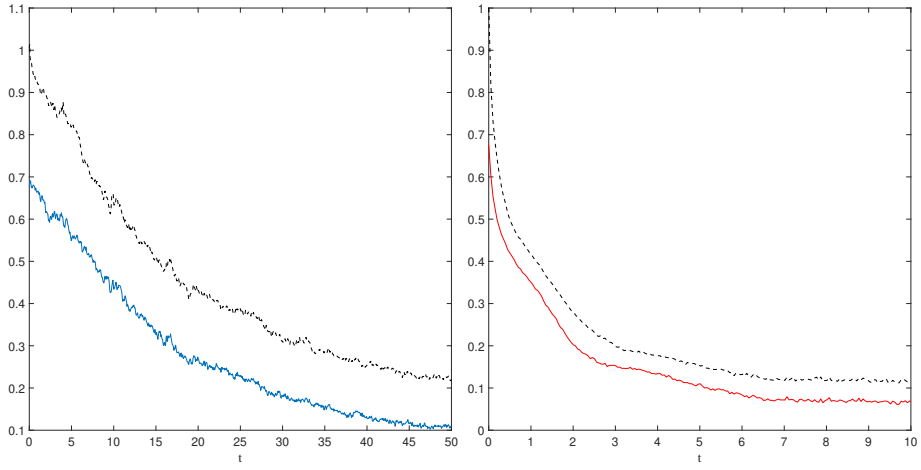

FIGURE 3.3: In this plot we ilustrate the Csiszár-Kullback-Pinsker inequality (3.33). Left: in the case of the dBB dynamics. Right: in the case of the BHN dynamics. In full line curve we plot L_1 and $\sqrt{2\,H_V}$ in dashed line. The coarse graining domain $[-4,4]$x$[-4,4]$ was divided by a number of 25x25 coarse grained cells. We chose in (2.26) a superposition of $M = 4^2 = 16$ modes.

now using (3.28) in (3.23) with $z = P/|\Psi|^2$ leads to the following inequality

$$H_V \geq \frac{1}{2}\int_\Omega d^3x\,|\Psi|^2\left[\frac{(z-1)^2}{1+\frac{(z-1)}{3}}\right] \tag{3.29}$$

then multiplying the right hand side by an integral equal to unity

$$H_V \geq \frac{1}{2}\int_\Omega d^3x\,|\Psi|^2\left[\frac{(z-1)^2}{1+\frac{(z-1)}{3}}\right]\int_\Omega d^3x\,|\Psi|^2\left[1+\frac{(z-1)}{3}\right] \tag{3.30}$$

and using the Cauchy-Bunyakovsky-Schwarz inequality

$$H_V \geq \frac{1}{2}\left[\int_\Omega d^3x\,|\Psi|\sqrt{\frac{(z-1)^2}{1+\frac{(z-1)}{3}}}\,|\Psi|\sqrt{1+\frac{(z-1)}{3}}\right]^2 \tag{3.31}$$

hence

$$H_V \geq \frac{1}{2}\left[\int_\Omega d^3x\,|P-|\Psi|^2|\right]^2 \tag{3.32}$$

thus we have

$$\boxed{\sqrt{2H_V} \geq L_1 \geq 0} \tag{3.33}$$

This inequality is known as Csiszár-Kullback-Pinsker inequality [23]. It means that the convergence in H_V also implies the convergence in L_1 through equation (3.33). In order to illustrate this result we plot in figure 3.3 the functionals L_1 and $\sqrt{2\,H_V}$ in the case of dBB and BHN dynamics using the state (2.26) with $M = 4^2 = 16$ modes.

3.2.2 Convergence in L^2 norm

We can pursue the analysis in order to show that the convergence in H_V also implies the convergence in the L^2 norm. Let us introduce the L_2 function as :

$$L_2(t) = \int_\Omega d^3x \ \left(P - |\Psi|^2\right)^2. \tag{3.34}$$

Starting from

$$H_V = \int_\Omega d^3x \, |\Psi|^2 \left[z \, ln \, z - (z-1)\right] \tag{3.35}$$

with $z = P/|\Psi|^2$ and using (3.26) and (3.28) we obtain

$$\frac{3}{2} \int_\Omega d^3x \ \left[\frac{\left(P - |\Psi|^2\right)^2}{2\,|\Psi|^2 + P}\right] \leq H_V \leq \int_\Omega d^3x \ \frac{\left(P - |\Psi|^2\right)^2}{|\Psi|^2} \tag{3.36}$$

All the distributions we used have an upper bound (no Dirac delta are used). Let $M_{|\Psi|^2}$ (resp. M_P) be the upper bound of $|\Psi|^2$ (resp. P) so that

$$\frac{1}{P + 2\,|\Psi|^2} \geq \frac{1}{M_p + 2\,M_{|\Psi|^2}} \tag{3.37}$$

and thus we have on the left of the inequality (3.36)

$$0 \leq \frac{3}{2} \frac{1}{M_p + 2\,M_{|\Psi|^2}} L_2 \leq H_V \tag{3.38}$$

Consequently, the convergence in H_V also implies the convergence in the L^2 norm. Moreover, if now $|\Psi|^2$ has a lower bound $m_{|\Psi|^2}$ with $m_{|\Psi|^2} \leq |\Psi|^2$ one finds on the right of (3.36) that

$$H_V \leq \frac{1}{m_{|\Psi|^2}} \int_\Omega d^3x \ \left(P - |\Psi|^2\right)^2 \tag{3.39}$$

We conclude that

$$\boxed{\frac{3}{2} \frac{1}{M_p + 2\,M_{|\Psi|^2}} L_2 \leq H_V \leq \frac{1}{m_{|\Psi|^2}} L_2} \tag{3.40}$$

and then that H_V can also be seen as a norm. It is now clear that the relaxation process to quantum equilibrium is an irreversible evolution minimizing the H-function. The stochastic approach is not dependent on the coarse graining, thus the present $H-$theorem remains valid for coarse grained quantities.

In what follows we shall illustrate these results by means of numerical simulations for the ground state of a 1D-harmonic oscillator in section 3.3.6, for a coherent state in section 3.4.1 and for a 2D-harmonic oscillator in section 3.4.2.

3.2.3 Discussion

A last important remark concerns the influence of possible zeros in the equilibrium distribution $\Psi(\mathbf{x}, t)$, which would give rise to singularities in the osmotic velocity terms in the Ito equation (3.5) or the Fokker-Planck equation (3.7) (or equivalently in equation (3.15)) and might make the functions H_V and L_f ill-defined.

As an exemple, in section 5.3.2 we discuss the case of the first excited state of the 1D-harmonic oscillator, for which $\Psi(\mathbf{x},t)$ has a node at $x=0$, and one could in fact imagine studying higher excited states for which one has a finite number of nodes. In that case, the osmotic velocity (3.4) will have simple poles at a finite number of positions in x. At the level of the Ito equation one would not expect a finite set of poles to cause any particular problems, not only because the probability of hitting a pole exactly in the stochastic evolution is zero but also because the osmotic term tends to move the particle away from the pole very quickly. Similarly, a finite number of simple poles in the convection-diffusion equation (3.15) for f only influences the velocity field in the convection term in a finite number of distinct places and it is to be expected that this would have the effect of actually enhancing the mixing in the system.

Moreover, it is also clear that simple nodes in $\Psi(\mathbf{x},t)$ only give rise to (a finite number of) logarithmic singularities in the integrand of H_V and that the integral (3.9) therefore still converges. The H-theorem for H_V derived above is thus still valid and an arbitrary distribution P (sufficiently smooth) will still converge to quantum equilibrium, even in the presence of nodes for $\Psi(\mathbf{x},t)$. The same cannot be said however of the function L_f as simple zeros in $\Psi(\mathbf{x},t)$ give rise to double poles in the integrand and a possible divergence of the integral (3.10). Hence, at the beginning of the evolution, for arbitary P, the function L_f might take an infinitely large value[5], but as soon as convergence sets in (which is guaranteed by the H-theorem for H_V), the divergent parts in its integrand will be smoothed out and the function L_f will take finite values that converge to zero as time goes on.[6]

3.3 Relaxation to quantum equilibrium in BHN dynamics: static case

In this section, in order to simplify the discussion, we will only consider the case of stationary states $\Psi_{st}(x)$ for the one dimensional Schrödinger equation, i.e. energy levels for which $S=-E\,t$ and which therefore have zero Bohm velocity (2.8): $\boldsymbol{\nabla} S \equiv S_x = 0$.

3.3.1 Fokker-Planck operator and a formal connection to a Schrödinger equation

There exists a wide literature [24, 25] concerning a particular method for studying the convergence of solutions of the Fokker-Planck equation to a stationary one, which is only sporadically mentioned in the literature devoted to BHN dynamics [26]. This approach makes it possible to quantify very precisely the speed of convergence to equilibrium, in terms of (negative) eigenvalues of the Fokker-Planck operator. In order to show this, let us rewrite the Fokker-Planck equation (3.7) in terms of the Fokker-Planck operator $\widehat{\mathcal{L}}$:

$$\frac{\partial P}{\partial t} = \widehat{\mathcal{L}} P = \left[-\frac{\partial \gamma}{\partial x} - \gamma(x)\frac{\partial}{\partial x} + \frac{\alpha}{2}\frac{\partial^2}{\partial x^2} \right] P, \tag{3.41}$$

where (3.4):

$$\gamma(\mathbf{x}) = \alpha \frac{\left(|\Psi_{st}|\right)_x}{|\Psi_{st}|}. \tag{3.42}$$

[5]The integrand only diverges when $|\Psi|^2 \ll P$, i.e. when it is positive.

[6]Of course, when calculating these quantities for the results of numerical simulations, there is always some amount of coarse-graining going on and genuine infinities never occur.

Note that, due to the presence of the first derivative $\frac{\partial}{\partial x}$, the $\widehat{\mathcal{L}}$ operator is not Hermitian.

Now, in order to establish the H-theorem, we must prove that in the long-time limit this equation tends to a stationary solution $P_{st} = |\Psi_{st}|^2$. The key idea here is to connect the Fokker-Planck equation to a Schrödinger-like equation with imaginary time, i.e. a diffusion equation, through the transformation

$$P(x,t) = \sqrt{P_{st}(x)}\; g(x,t), \tag{3.43}$$

under which the r.h.s. of equation (3.41) reduces to

$$\widehat{\mathcal{L}}\, P = \sqrt{P_{st}(x)}\; \widehat{\mathcal{H}}_{st}\; g(x,t), \tag{3.44}$$

where $\widehat{\mathcal{H}}_{st}$ is now a Hermitian operator:

$$\widehat{\mathcal{H}}_{st} = \frac{\alpha}{2}\frac{\partial^2}{\partial x^2} - \frac{1}{2}\left(\frac{\partial \gamma}{\partial x} + \frac{\gamma^2}{\alpha}\right). \tag{3.45}$$

The function $g(x,t)$ thus obeys a Schrödinger-like equation with an effective potential that depends on $\gamma(x)$:

$$\boxed{\frac{\partial g(x,t)}{\partial t} = \widehat{\mathcal{H}}_{st}\; g(x,t)} \tag{3.46}$$

Note that the effective potential is exactly the Bohm-quantum potential defined in (2.10) by

$$Q_\Psi = -\frac{\hbar^2}{2\,m}\frac{1}{|\Psi_{st}|}\frac{\partial^2 |\Psi_{st}|}{\partial x^2}, \tag{3.47}$$

which can be expressed in terms of the osmotic velocity (for $\alpha = \frac{\hbar}{m}$) (3.42) as:

$$\frac{Q_\Psi}{m\,\alpha} = -\frac{1}{2}\left(\frac{\partial \gamma}{\partial x} + \frac{\gamma^2}{\alpha}\right). \tag{3.48}$$

3.3.2 Superposition ansatz

We can now represent the solution of (3.46) as a superposition of discrete eigenvectors (all orthogonal, as the operator $\widehat{\mathcal{H}}_{st}$ is Hermitian) and impose the superposition ansatz [27]:

$$g(x,t) = \sum_{k=0}^{\infty} a_k(t)\, g_k(x). \tag{3.49}$$

Equation (3.46) is separable and gives rise to the eigenvalue problem:

$$\frac{1}{a_k(t)}\frac{da_k(t)}{dt} = \frac{1}{g_k(x)}\widehat{\mathcal{H}}_{st}\, g_k(x) = -\lambda_k. \tag{3.50}$$

As a result we have

$$g(x,t) = \sum_{k=0}^{\infty} a_k e^{-\lambda_k t}\, g_k(x), \tag{3.51}$$

for a set of constants a_k and where all the λ_k are real (as $\mathcal{H}$ is Hermitian), for eigenfunctions $g_k(x)$ that satisfy the orthonormality conditions:

$$\int_{-\infty}^{\infty} dx\, g_k(x) g_l(x) = \delta_{k,l}. \tag{3.52}$$

Thus, we have the expression

$$\boxed{P(x,t) = \sum_{k=0}^{\infty} a_k e^{-\lambda_k t} \sqrt{P_{st}(x)}\, g_k(x)} \tag{3.53}$$

By construction, the function $\sqrt{P_{st}(x)}$ is an eigenstate of the effective Hamiltonian with energy 0. We shall associate the label λ_0 with this energy level.

In order to have a well defined probability distribution and to avoid any divergence in time, it is clear that all eigenvalues $-\lambda_k$ have to be negative, which requires Ψ_{st} to be the ground state of the effective Hamiltonian $\mathcal{H}_{st}$. From the study of the properties of the Schrödinger equation it is clear that this will be the case if and only if $\Psi_{st}(x)$ has no zeros. In order to be self-contained however, we shall now show directly that if $\Psi_{st}(x)$ has no zeros, all λ_k are indeed positive.

3.3.3 Negativity of the eigenvalues

If one defines $p_k(x) = \sqrt{P_{st}(x)}\, g_k(x)$, it is clear from the orthonormality relations (3.52) that

$$\int_{-\infty}^{\infty} dx\, \frac{p_k(x)\, p_l(x)}{P_{st}(x)} = \delta_{k,l}, \tag{3.54}$$

where we have made explicit use of the fact that Ψ_{st} has no zeros when we divide by $P_{st}(x)$. The relations (3.52) imply that

$$\int_{-\infty}^{\infty} dx\, \frac{p_k(x)\, \widehat{\mathcal{L}}\, p_k(x)}{P_{st}(x)} = -\lambda_k, \tag{3.55}$$

while, on the other hand, equation (3.41) yields:

$$\int_{-\infty}^{\infty} dx\, \frac{p_k(x)\, \widehat{\mathcal{L}}\, p_k(x)}{P_{st}(x)} = \int_{-\infty}^{\infty} dx\, \left(\frac{p_k(x)}{P_{st}(x)}\right) \partial_x \left(-\gamma(x)\, p_k(x) + \frac{\alpha}{2}\, \partial_x p_k(x)\right). \tag{3.56}$$

If this integral converges we have that

$$\int_{-\infty}^{\infty} dx\, \left(\frac{p_k(x)}{P_{st}(x)}\right) \partial_x \left(-\gamma(x)\, p_k(x) + \frac{\alpha}{2}\, \partial_x p_k(x)\right) = -\int_{-\infty}^{\infty} dx\, \partial_x \left(\frac{p_k(x)}{P_{st}(x)}\right) \left[-\gamma(x)\, p_k(x) + \frac{\alpha}{2}\, \partial_x p_k(x)\right]. \tag{3.57}$$

This last expression can be simplified using the relation

$$\partial_x \left(\frac{p_k(x)}{P_{st}(x)}\right) = \frac{2}{\alpha\, P_{st}(x)} \left(-\gamma(x)\, p_k(x) + \frac{\alpha}{2}\, \partial_x p_k(x)\right), \tag{3.58}$$

which then yields:

$$\boxed{\int_{-\infty}^{\infty} dx\, \frac{p_k(x)\,\widehat{\mathcal{L}}\,p_l(x)}{P_{st}(x)} = -\frac{\alpha}{2}\int_{-\infty}^{\infty} dx\, P_{st}(x)\left[\partial_x\left(\frac{p_k(x)}{P_{st}(x)}\right)\right]^2 = -\lambda_k} \tag{3.59}$$

Since this integral is clearly negative, we have that λ_k is necessarily positive.

If $\Psi_{st}(x)$ does have zeros the osmotic velocity will have singularities. In the next subsection, we consider what happens in the case when $\Psi_{st}(x)$ is an excited state of the harmonic oscillator and we derive a formal solution in terms of the eigenvalues $-\lambda_k$ which are now not all negative, thus revealing the appearance of instabilities for cases where the above formalism would still be valid.

3.3.4 Bohm-Hiley-Nelson dynamics: Formal solution when Ψ_{st} is a Fock state

Let us apply the formalism outlined in sections 3.3.1 and 3.3.2 to the case of a one dimensional quantum Harmonic oscillator. We will consider static wave functions $\Psi_{st} = \sqrt{|\Psi_n(x,t)|^2}$ where the static state is a Fock state

$$\Psi_n(x,t) = \psi_n(x)e^{-i\omega\left(n+\frac{1}{2}\right)t}, \tag{3.60}$$

with

$$\psi_n(x) = \frac{1}{\sqrt{2^n n!}}\left(\frac{2a}{\pi}\right)^{\frac{1}{4}} e^{-ax^2} H_n\left(\sqrt{2a}\,x\right). \tag{3.61}$$

Here, H_n is the Hermit polynomial of order n, a is the characteristic length, and ω the pulsation which is a function of the characteristic variables of the problem: $\omega(\alpha) = 2\,a\,\alpha$. The osmotic velocity in this case reads:

$$\boxed{\gamma_n(x) = -2a\alpha\, x + \frac{2\sqrt{2\,a}\,\alpha\, n\, H_{n-1}\left(\sqrt{2a}\,x\right)}{H_n\left(\sqrt{2\,a}\,x\right)}} \tag{3.62}$$

For excited states ($n > 0$) the osmotic velocity diverges close to the nodes of the wave function (see figure 3.4). The quantum potential however takes the form:

$$Q_\Psi = -\frac{1}{2}m\,\omega^2\,x^2 + \hbar\,\omega\left(n+\frac{1}{2}\right). \tag{3.63}$$

Hence, the equation 3.49 for $g(\boldsymbol{x},t)$ is a Schrödinger Equation in an effective harmonic potential

$$\frac{\partial g}{\partial t} = \left[\frac{\alpha}{2}\frac{\partial^2}{\partial x^2} - \frac{1}{2}\frac{\omega^2}{\alpha}x^2 + \omega\left(n+\frac{1}{2}\right)\right] g. \tag{3.64}$$

By considering the following substitution we can eliminate the shift term

$$g(x,t) = e^{\omega\left(n+\frac{1}{2}\right)t}\, j(x,t), \tag{3.65}$$

and it follows that

$$\frac{\partial j}{\partial t} = \left[\frac{\alpha}{2}\frac{\partial^2}{\partial x^2} - \frac{1}{2}\frac{\omega^2}{\alpha}x^2\right] j. \tag{3.66}$$

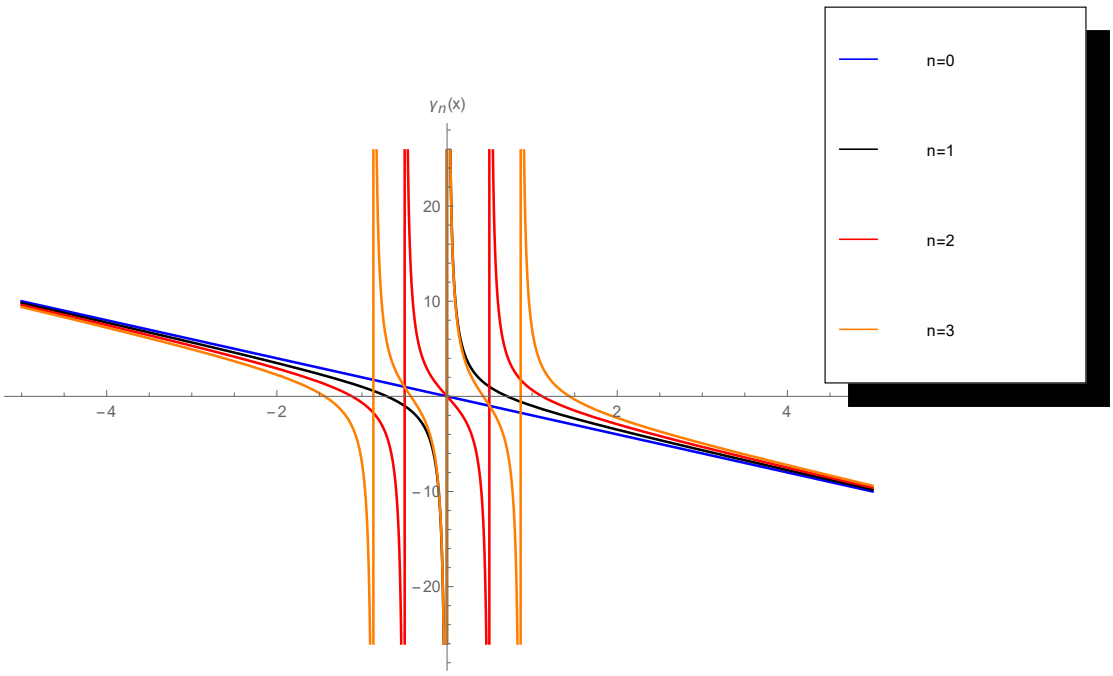

FIGURE 3.4: Plot of the osmotic velocity $\gamma_n(x)$ in the case of (3.62). Here we chose $a = 1$ and $\alpha = 1$.

By applying a slightly modified version of the procedure in 3.3.2,[7] allows us to express $P(x,t)$ over a basis of Hermite polynomials with $\lambda_k = \omega\ \left(k + \frac{1}{2}\right)$:

$$\boxed{P(x,t) = \sum_{k=0}^{\infty} a_k e^{-w(k-n)t}\, \psi_n(x)\, \psi_k(x)} \tag{3.67}$$

a_k (if well-defined) is given by:

$$a_k = \int_{-\infty}^{\infty} dx\, j(x,0)\, \psi_k(x) = \int_{-\infty}^{\infty} dx\, \frac{P(x,0)}{\psi_n(x)}\, \psi_k(x). \tag{3.68}$$

The probability is well normalized since

$$\begin{aligned} \int_{-\infty}^{\infty} dx\, P(x,t) &= \sum_{k=0}^{\infty} a_k e^{-w(k-n)t} \int_{-\infty}^{\infty} dx\, \psi_n(x)\psi_k(x) \\ &= a_n = \int_{-\infty}^{\infty} dx\, P(x,0) = 1. \end{aligned} \tag{3.69}$$

However, the superposition (3.67) will diverge in time whenever the initial distribution has a non-trivial overlap with excited states for $k < n$ (for $a_k \neq 0$) . The terms with $k > n$ decay exponentially over time at different periods which are multiple of the characteristic

[7] Instead of imposing $P(x,t) = \sqrt{P_{st}(x)}\, g(x,t)$ as we did in section 3.3, we now impose $P(x,t) = \psi_n(x)\, g(x,t)$. When $n = 0$, both procedures are equivalent but excited states ($n \neq 0$) possess zeros and are thus not always positive, which makes a difference in this case. In particular, the orthonormality relation (3.52) between eigenmodes of the Fokker-Planck operator is not fulfilled if we consider absolute values of the modes instead of their natural expression, as would have been the case in the approach of section 3.3.

time (i.e multiple of $\frac{1}{\omega}$), but those for which $k < n$ increase exponentially, which may lead to inconsistencies (like e.g. the appearance of negative probabilities). This paradoxical feature is of course due to the presence of singularities at the level of Fokker-Planck equation because of the zeros of the static distribution $\sqrt{P_{st}(x)}$, and it clearly shows the rather limited usefulness of this approach in that case.

3.3.5 Propagator and Green's function formalism

On the other hand, we can also express the solution by using the Green function formalism. The solution of (3.46) can be put in the form:

$$\begin{aligned} j(x,t) &= \sum_{k=0}^{\infty} a_k e^{-\omega\left(k+\frac{1}{2}\right)t}\,\psi_k(x) \\ &= \sum_{k=0}^{\infty}\left[\int_{-\infty}^{\infty} dx'\, j(x',0)\,\psi_k(x')\right] e^{-\omega\left(k+\frac{1}{2}\right)t}\,\psi_k(x) \\ &= \int_{-\infty}^{\infty} dx'\, j(x',0)\sum_{k=0}^{\infty}\psi_k(x)\,\psi_k(x')e^{-\omega\left(k+\frac{1}{2}\right)t} \\ &= \int_{-\infty}^{\infty} dx'\, j(x',0)\,K_{HO}(x,x',t), \end{aligned} \tag{3.70}$$

where

$$\begin{aligned} K_{HO}(x,x',t) &= \sum_{k=0}^{\infty}\psi_k(x)\,\psi_k(x')e^{-\omega\left(k+\frac{1}{2}\right)t} \\ &= \sum_{k=0}^{\infty}\frac{1}{2^k k!}\left(\frac{2a}{\pi}\right)^{\frac{1}{2}} e^{-2a\left(x^2+x'^2\right)} H_k\left(\sqrt{2a}\,x\right) H_k\left(\sqrt{2a}\,x'\right) e^{-\omega\left(k+\frac{1}{2}\right)t} \\ &= \left(\frac{a}{\pi\,\sinh(\omega\,t)}\right)^{\frac{1}{2}} e^{\frac{-a}{\sinh(\omega\,t)}\left[\left(x^2+x'^2\right)\cosh(\omega\,t)-2\,xx'\right]}. \end{aligned} \tag{3.71}$$

Introducing an imaginary time $t = i\tau$ we recover the well known propagator for the one dimensional quantum harmonic oscillator. Hence, one can easily find the Green function K_p of the Fokker-Planck equation (3.7).

Consider the expression:

$$\begin{aligned} P(x,t) &= \int_{-\infty}^{\infty} dx'\, P(x',0)\,K_P(x,x',t) \\ &= \int_{-\infty}^{\infty} dx'\,\psi_n(x')\,j(x',0)\,K_P(x,x',t), \end{aligned} \tag{3.72}$$

which should be compared to

$$\begin{aligned} P(x,t) &= \psi_n(x)e^{\omega\left(n+\frac{1}{2}\right)t}\,j(x,t) \\ &= \int_{-\infty}^{\infty} dx'\,\psi_n(x)e^{\omega\left(n+\frac{1}{2}\right)t}\;j(x',0)\,K_{HO}(x,x',t), \end{aligned} \tag{3.73}$$

which leads to the conclusion that

$$K_P(x,x',t) = \frac{\psi_n(x)}{\psi_n(x')}\,e^{\omega\left(n+\frac{1}{2}\right)t}\,K_{HO}(x,x',t). \tag{3.74}$$

This function is singular when $n \neq 0$, due to the presence of zeros in $\psi(x)$. However, when $n = 0$ it takes the form:

$$\boxed{K_P(x,x',t) = \left(\frac{a}{\pi \sinh(\omega\, t)}\right)^{\frac{1}{2}} e^{\omega\left(n+\frac{1}{2}\right)t} \times e^{\frac{-a}{\sinh(\omega\, t)}\left[(x^2+x'^2)\,\cosh(\omega\, t)+(x^2-x'^2)\,\sinh(\omega\, t)-2\,x x'\right]}} \tag{3.75}$$

3.3.6 One dimensional oscillator and the evolution of Gaussian distributions

An important property of the Green function (3.75) for this case is that if $|\Psi(x)|^2$ and $P(x,0)$ are Gaussian, then $P(x,t)$ will still be Gaussian (3.72). This property will allow us to study analytically the convergence to equilibrium. In this case, let us define the ground state as

$$|\Psi_{st}|^2 \equiv |\Psi(x)|^2 = \sqrt{\frac{2a}{\pi}} e^{-2\,a\,x^2}, \tag{3.76}$$

for which we can then write:

$$P(x,t) = \sqrt{\frac{2b(t)}{\pi}} e^{-2\,b(t)\,(x-\langle x(t)\rangle)^2}. \tag{3.77}$$

Injecting (3.77) in the Fokker-planck equation (3.41) gives a differential equation for $\langle x(t)\rangle$,

$$\frac{d\,\langle x(t)\rangle}{dt} = -2a\alpha\ \langle x(t)\rangle\,, \tag{3.78}$$

which is readily solved:

$$\boxed{\langle x(t)\rangle = \langle x_0\rangle\, e^{-2a\alpha\, t}} \tag{3.79}$$

As well as an equation for $b(t)$

$$\frac{1}{2b(t)}\,\frac{db(t)}{dt} + 2\alpha\,(b(t)-a) = 0, \tag{3.80}$$

with solution:

$$\boxed{b(t) = \frac{a}{1-\left(1-\frac{a}{b_0}\right)e^{-4a\alpha\, t}}} \tag{3.81}$$

From (3.77) and (3.81) we can then calculate the width of the non-equilibrium Gaussian as:

$$\sigma_x^2(t) \equiv \frac{1}{4b(t)} = \frac{1}{4a}\left[\left(1-e^{-4a\alpha\, t}\right) + \frac{a}{b_0}e^{-4a\alpha\, t}\right]$$

which can be re-expressed as

$$\boxed{\sigma_x^2(t) = \sigma_{eq}^2\left(1-e^{-4a\alpha\, t}\right) + \sigma_x^2(0)\, e^{-4a\alpha\, t}} \tag{3.82}$$

where σ_{eq}^2 represents the width $1/(4a)$ of the equilibrium distribution (3.76).

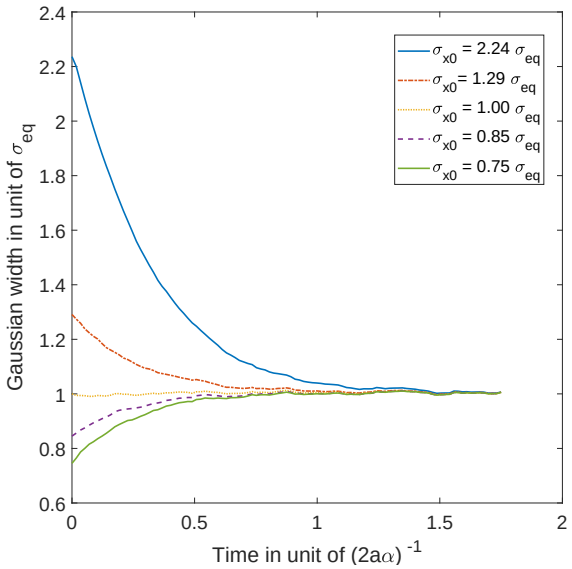

FIGURE 3.5: Simulations of 10 000 trajectories (calculated from the Ito equation (3.5) for the ground state (3.76) of the 1D harmonic oscillator), whose initial positions are normally distributed, for 5 different choices of distribution width (for $a = 0.5$ and $\alpha = 1$). We observe, in each case, convergence to the equilibrium (3.76) as predicted by the theory.

Clearly, $\langle x \rangle \overset{t\to\infty}{=} \langle x \rangle_{eq} = 0$ with a characteristic relaxation time inversely proportional to the diffusion coefficient α. Moreover,

$$\frac{d\sigma_x(t)}{dt} \propto 4a\alpha\left(\sigma_{eq}^2 - \sigma_x^2(0)\right) e^{-4a\alpha\, t}, \tag{3.83}$$

which has the same sign as that of the difference $(\sigma_{eq} - \sigma_x(0))$. Hence, $\sigma_x(t)$ converges monotonically to the equilibrium value σ_{eq}, with a characteristic time inversely proportional to the diffusion coefficient α, as confirmed by numerical simulations (see figure 3.5) of the corresponding Ito equation (3.5).

3.3.7 Ergodicity in the relaxation to quantum equilibrium for the ground state of the harmonic oscillator

We have just shown how Gaussian initial distributions converge towards quantum equilibrium, but one could also ask the same question for non-Gaussian initial distributions. Convergence is guaranteed by the H-theorem of section 3.2, but contrary to the Gaussian case, we have no clear measure for the rate of convergence, except for the entropy-like functions H_V (3.9) and L_f (3.10), or the L_1 norm (3.21), defined in section 3.2.

The evolution in time of these three quantities is shown in Figure 3.6, for the stochastic trajectories obtained from 20 000 uniformly distributed initial conditions. The relaxation towards quantum equilibrium is clearly visible in all three quantities. As expected, the convergence of H_V is extremely fast. Note that, although initially very large, L_f quickly matches L_1, up to numerical fluctuations. One important question concerning this relaxation process is of course that of possible ergodicity. In order to study the ergodic properties of the BHN dynamics in a numerical way, we choose the definition of ergodicity that is, in our approach, the easiest to test.

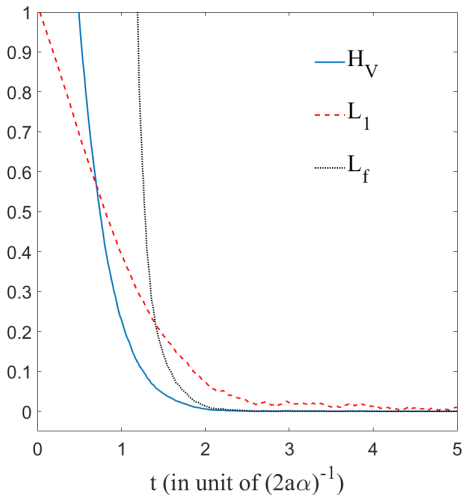

FIGURE 3.6: Time evolution of H_V (3.9), L_f (3.10) and the L_1 norm (3.21) , for a uniform initial probability distribution, calculated from the Ito equation (3.5) for the ground state of the 1D harmonic oscillator. Relaxation towards the distribution of the ground state $|\Psi_{st}|^2$ (3.76) is clearly visible. The simulation is performed for $\alpha = 1$, $a = 0.5$, $\Delta t = 0.01$, for 20 000 uniformly distributed initial conditions.

Let us first define the time average $\widehat{h}$ of a function h on Ω, by the limit (if it exists):

$$\widehat{h} = \lim_{t\to+\infty} \frac{1}{t} \int_0^t h(\mathbf{x}_{t'})\, dt', \tag{3.84}$$

where $\mathbf{x}_{t'}$ represents the position of a particle at time t', as obtained form the Ito stochastic differential equation (3.5) for an initial condition $\mathbf{x}$. We shall then say [28] that this stochastic process is ergodic if the time average of any bounded function h on Ω is always independent of $\mathbf{x}$: Since for bounded h the time average is also invariant under shifts in time, we can say that we have ergodicity if all time averages of such functions are in fact constants. The main reason for choosing this particular definition is that it is well-suited to empirical testing, since it is of course sufficient to establish constancy of the time averages for all indicator functions χ_A of arbitrary (measurable) sets $A \subset \Omega$, for the analogous property to ensue automatically for all bounded functions on Ω.[8] More precisely, we need to verify that

$$\widehat{\chi}_A = \lim_{t\to+\infty} \frac{1}{t} \int_0^t \chi_A(\mathbf{x}_{t'})\, dt', \tag{3.85}$$

is independent of both t and $\mathbf{x}$, for any measurable $A \subset \Omega$. Remember that one has of course that $\chi_A(\mathbf{x}_t) = \chi_{\phi_t^{-1}A}(\mathbf{x})$, where $\phi_t^{-1}A = \{\mathbf{x} \in \Omega \,|\, \mathbf{x}_t \in A\}$.

In the present case, i.e. that of the BHN dynamics defined by the stationary (ground) state of the 1D harmonic oscillator, it is clear that the distribution $|\Psi_{st}|^2$ obtained from the ground state eigenfunction Ψ_{st} is a stationary solution to the associated Fokker-Planck equation (3.7).

[8] Another reason for choosing this particular definition is that it can also be applied to non-stationary stochastic processes, as e.g. in the case of the coherent state of section 3.4.

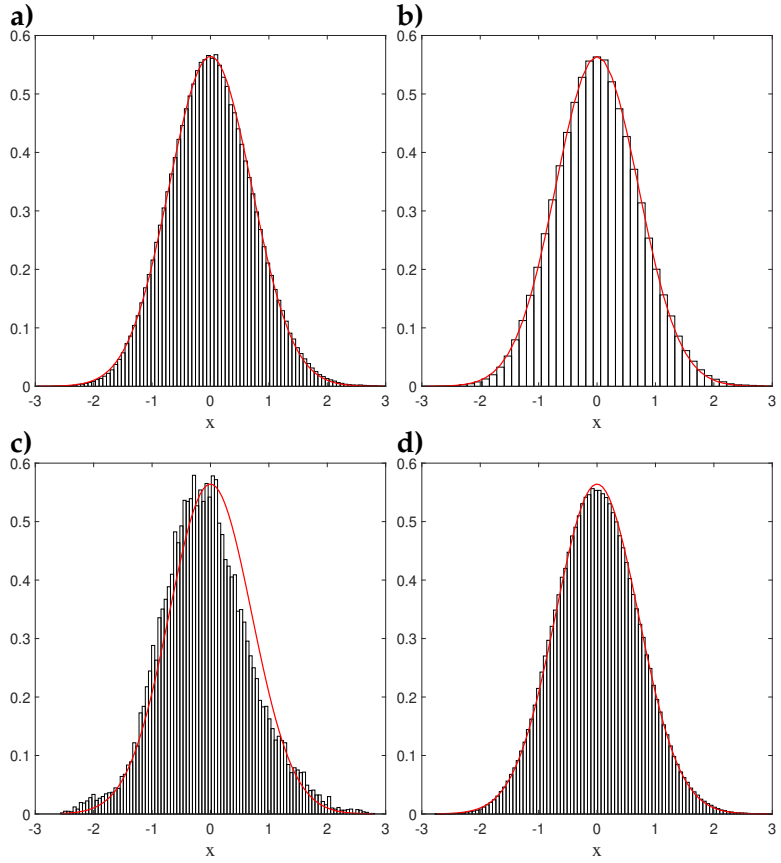

FIGURE 3.7: Histograms of the positions of a single particle, subject to BHN dynamics for the ground state of the 1D harmonic oscillator. The full (red) curve corresponds to the quantum probability $|\Psi_{st}|^2$. Here $a = 0.5$, $\alpha = 1$ and the total simulation time (t=10000) is sampled with $\Delta t = 0.01$.
a) The initial particle position is $x_0 = 2.5$ and the number of bins $N_b = 100$ (each with spatial size $\Delta x = 0.0635$). **b)** Same as *a)* but with $N_b = 50$ and $\Delta x = 0.1270$. **c)** Same as *a)* but with $t = 200$. **d)** Same as *a)* but for $x_0 = -0.85$.

This distribution provides a natural invariant measure μ on Ω: $d\mu = |\Psi_{st}|^2 dx$, for which $\int_\Omega d\mu = 1$ and

$$\mu(A) = \int_A |\Psi_{st}|^2 dx = \mu(\phi_t^{-1} A), \quad {}^\forall t > 0, {}^\forall A \in \Omega. \tag{3.86}$$

If a stationary stochastic process is ergodic, i.e. if all $\widehat{\chi}_A$ are indeed constants, the values of these constants can be easily calculated in general [29]. Suppose that for any A, $\widehat{\chi}_A = c_A$, for some constant c_A. Then one has from (3.85) that

$$\begin{aligned} c_A = \int_\Omega d\mu \, c_A &= \lim_{t\to+\infty} \frac{1}{t} \int_0^t dt' \int_\Omega d\mu \, \chi_{\phi_{t'}^{-1} A}(\mathbf{x}) \\ &= \lim_{t\to+\infty} \frac{1}{t} \int_0^t dt' \, \mu(\phi_{t'}^{-1} A) \\ &= \mu(A). \end{aligned} \tag{3.87}$$

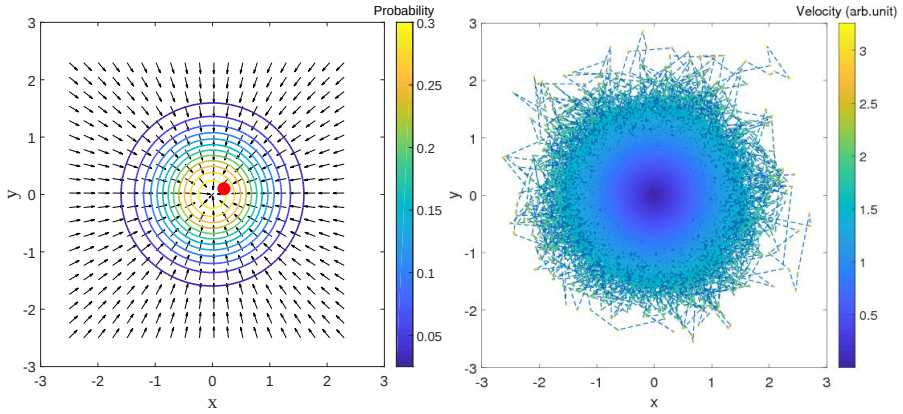

FIGURE 3.8: Left: A point-particle (the dot near the center) subject to the osmotic velocity field $-2a\alpha\,(x(t), y(t))$, due to the ground state of the 2D harmonic oscillator at time t;
Right: Color plot of the velocities along a trajectory for the evolution under BHN dynamics, for the ground state of the 2D harmonic oscillator. The simulation (for $a = 0.5$ and $\alpha = 1$) started from the initial position $(-2, 1)$ and was sampled up to $t = 1\,000$ with step $\Delta t = 0.01$.

Therefore, when one needs to decide whether or not a stationary stochastic process is ergodic, it suffices to establish that $\widehat{\chi}_A = \mu(A)$, for any $A \in \Omega$.[9]
The usual way to check this condition is to consider sampling time averages for a sufficiently refined 'binning' of Ω. Starting from a particular initial particle position $\mathbf{x}$, we calculate the trajectory $\mathbf{x}_t$ that follows from the Ito stochastic equation (3.5), for a sufficiently long time t. As was explained for the coarse-graining in section 2.2, the configuration space Ω is subdivided into a large number of non-overlapping cells or 'bins' A_k $(k = 1, \ldots, N_b)$, each with the same volume $\Delta\mathbf{x}$. The trajectory $\mathbf{x}_{t'}$ $(t' \in [0, t])$ is then sampled at regular intervals Δt, yielding $N + 1$ sample positions $\mathbf{x}_{n\Delta t}$ $(n = 0, \ldots, N)$, for $N = t/\Delta t$. We then define the sampling function $\varphi_{N,k}$

$$\varphi_{N,k} = \frac{1}{N} \sum_{n=0}^{N} \chi_{A_k}(\mathbf{x}_{n\Delta t}), \tag{3.88}$$

which is a discretization of $\frac{1}{t}\int_0^t \chi_A(\mathbf{x}_{t'})\,dt'$ in (3.85) and which gives the frequency with which the (sample of the) orbit visited the bin A_k. Hence, if in the limit $N \to +\infty$, for diminishing bin sizes $\Delta\mathbf{x}$ and sampling steps Δt, the normalized distribution obtained from $\varphi_{N,k}/\Delta\mathbf{x}$ tends to a constant distribution (and, in particular, does not depend on the initial positions $\mathbf{x}$) then the stochastic process is ergodic according to the above definition.

Moreover, since in that case $\widehat{\chi}_{A_k} = \mu(A_k)$, this normalized distribution must in fact coincide with that for the invariant measure for the stationary process. For example, in the case at hand, if the normalized distribution we obtain is indeed independent of the initial positions, then since $\mu(A_k) = |\Psi_{st}(x)|^2\big|_{x=\xi}\,\Delta x$ for some point $\xi \in A_k$, we must have that for sufficiently large N

$$\frac{\varphi_{N,k}}{\Delta x} \approx \frac{\mu(A_k)}{\Delta x} = |\Psi_{st}(x)|^2\big|_{x=\xi}, \tag{3.89}$$

i.e.: the empirical distribution obtained from this sampling time average must coincide

[9] Note that this relation in fact tells us that the time average of an indicator function is equal to its space average $\overline{\chi}_a = \int_\Omega d\mu\,\chi_A = \mu(A)$. Obviously, since the indicator functions generate all bounded functions h on Ω, this then yields the property which is usually associated with ergodicity: $\widehat{h} = \int_\Omega d\mu\,h(\mathbf{x}) = \overline{h}$.

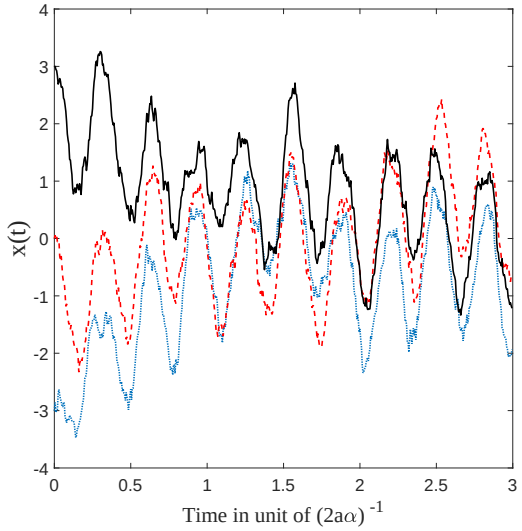

FIGURE 3.9: Numerical solutions of the Ito stochastic differential equation (3.5) corresponding to the coherent state (3.90), for three different initial conditions. We used $\bar{x}_0 = 1$, $a = 0.5$, $\alpha = 1$ and expressed the results in natural units.

with the stationary quantum probability $|\Psi_{st}|^2$. This is exactly what we obtain from our numerical simulations, as can be seen from the histograms depicted in Figure 3.7. After a certain amount of time, the histograms we obtain indeed converge to the equilibrium distribution, and this for arbitrary initial positions. The convergence clearly improves if we increase the integration time, or if we diminish the spatial size Δx of the bins (while diminishing the sampling time step in order to keep the occupancy rate of each bin high enough). Although purely numerical, we believe this offers conclusive proof for the ergodicity of the BHN dynamics associated with the ground state of the harmonic oscillator in one dimension.

The same can be said, in fact, for the 2-dimensional oscillator which will be studied in the next section. Some results of a simulation of a single trajectory under the BHN dynamics for the ground state of this system are shown in figure 3.8, in which the red dot in the plot on the left-hand side indicates the (final) position of the particle at time t. The probability distribution obtained by sampling the trajectory, clearly decreases with the distance to the origin.

3.4 Relaxation to quantum equilibrium with BHN dynamics: non-static case

3.4.1 BHN dynamics and asymptotic coherent states

Up to now, we have developed analytic and numerical tools aimed at studying the onset of equilibrium when the asymptotic equilibrium distribution is static. Actually, as the H-theorem of section 3.2 is also valid for non-stationary processes, one of course expects relaxation to take place even if the asymptotic state is not static, for instance when it is a Gaussian distribution the center of which periodically oscillates at the classical frequency ω of the oscillator without deformation (typical for coherent states).

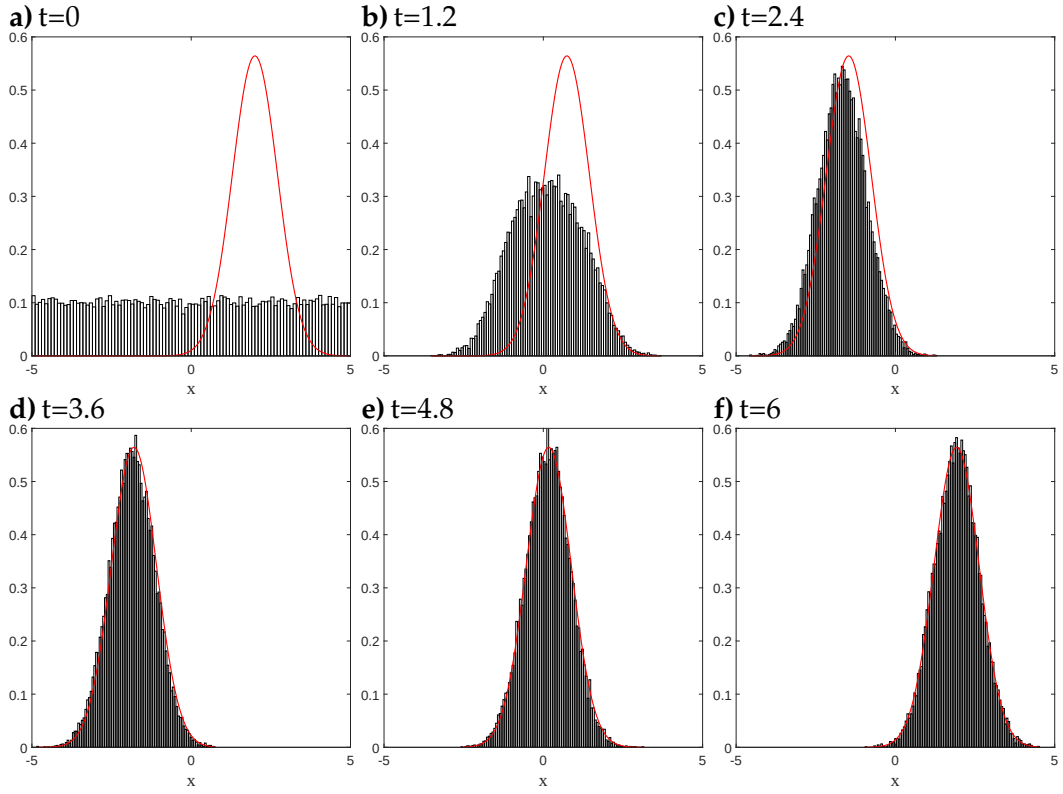

FIGURE 3.10: The time evolution of a non-equilibrium ensemble, illustrated with position histograms at six different times. The continuous curve is the squared modulus $|\Psi|^2$ for the coherent state (3.90). As can be seen from figures (d,e,f), once equilibrium is reached, the distribution clings to the coherent state and follows its oscillation faithfully. The center of the wave packet moves between -2 and 2 with a period 2π. We started from a uniform distribution of initial conditions and chose $a = 0.5$, $\alpha = 1$ and $x_0 = 2$. The sampling time step is $\Delta t = 0.01$ and the number of bins is $N_b = 50$, each with width $\Delta x = 0.0461$.

In fact, our numerical simulations not only show that equilibrium is reached even in this case, but also that this relaxation is ergodic. More precisely, we considered a wave function in the coherent state

$$\Psi(x,t) = \left(\frac{2a}{\pi}\right)^{\frac{1}{4}} e^{-a\,(x-\bar{x}_t)^2 + i\frac{\bar{p}_t\,x}{\hbar} + i\varphi(t)}, \tag{3.90}$$

where φ is a global phase containing the energy and $\bar{x}_t$ ($\bar{p}_t$) is the mean position (momentum) of a classical oscillator at time t:

$$\bar{x}_t = \bar{x}_0\, cos\,(\omega t) \quad \text{and} \quad \bar{p}_t = -m\omega\bar{x}_0\, sin\,(\omega t)\,, \tag{3.91}$$

with $\omega = 2a\alpha$ ($\alpha = \hbar/m$). For this ansatz we solved the Ito equation (3.5) numerically for a collection of initial conditions.

As can be seen on figure 3.9, the trajectories are affected by the stochastic evolution but keep oscillating at the same period because of the deterministic part of the (3.1). Notice however that the trajectories seem to be getting closer to classical trajectories that only differ from each other by a simple shift. This can be explained as follows: at equilibrium (cf. figure 3.10), the Brownian motion is balanced by the osmotic velocity and the dBB velocity is recovered "on average".

Now, the center of the Gaussian distribution moves at a classical velocity by virtue of Ehrenfest's theorem and, moreover, in the present case the dBB velocities can only depend on time and not on space as the envelope of a coherent state moves without deformation. Hence, the dBB trajectories obtained at equilibrium are, in fact, classical trajectories that only differ by a mere shift in space (the magnitude of which however may change over time).

Secondly, as can be clearly seen on figure 3.10, even for a uniform initial probability distribution, the convergence to the quantum equilibrium is remarkably fast and the converged distribution faithfully follows the oscillating motion of the non-stationary equilibrium distribution. The remarkable speed of the convergence to quantum equilibrium is corroborated by the decay of the functions H_V and L_f and of the L_1 norm shown in figure 3.11. Moreover, figure 3.12 depicts the sampling time average (as defined in section 3.3.7) of a

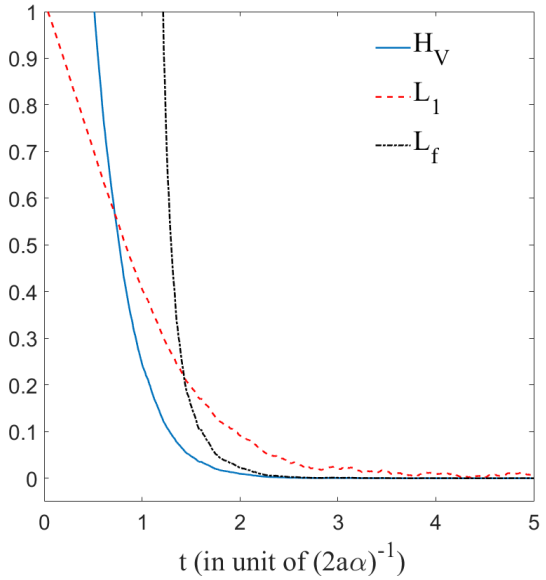

FIGURE 3.11: Time evolution of H_V (3.9), L_f (3.10) and L_1 (3.21), for a uniform initial probability distribution, showing the relaxation towards the distribution $|\Psi|^2$ of the coherent state (3.90).
The simulation is performed for $\alpha = 1$, $a = 0.5$, $\Delta t = 0.01$ and from 20 000 uniformly distributed initial conditions.

single trajectory for this non-stationary stochastic process. The convergence of the sampling distribution to a static distribution $\Phi(x)$, described by the integral of $|\Psi(x,t)|^2$ as given by (3.90), over a period of the oscillation

$$\Phi(x) = \frac{\omega}{2\pi} \int_0^{2\pi/\omega} |\Psi(x,t)|^2 dt, \tag{3.92}$$

is striking. As the asymptotic distribution $\Phi(x)$ does not depend on the choice of initial condition, we conclude that the relaxation to equilibrium for the non-stationary stochastic process associated with BHN dynamics for the coherent state (3.90) is ergodic (in the sense explained in section 3.3.7).

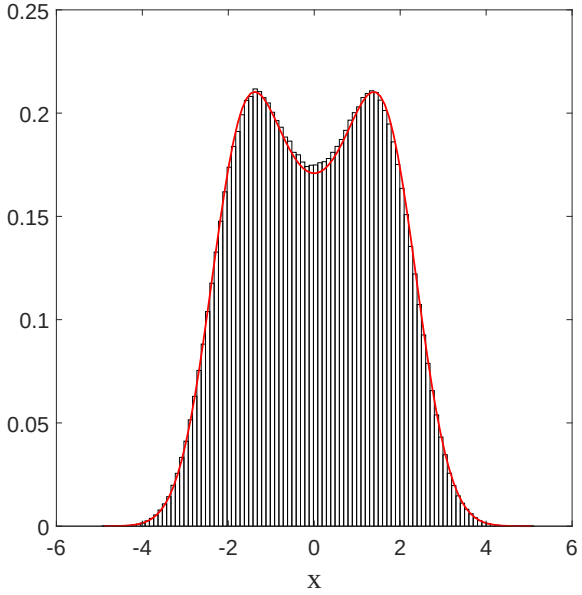

FIGURE 3.12: Histogram of the positions for a unique trajectory satisfying the Ito equation (3.5) for (3.90). The full curve corresponds to the integration of $|\Psi|^2$ over one period. The center of the wave packet moves between -2 and 2 with a period 2π. Here $a = 0.5$ and $\alpha = 1$. Total simulation time t is $t = 30\,000$ and and the samping time step is $\Delta t = 0.01$. The initial position is $x_i = 1$ and the number of bins $N_b = 100$, each with width $\Delta x = 0.1$.

3.4.2 Numerical simulation in a 2D quantum harmonic oscillator (BHN)

We then compared the relaxation process for dBB with the quantum thermostat given by BHN dynamics for $M = 4^2 = 16$ energy states. The results are shown in figure (3.13) in which the two H-functions H_V (for the dBB and for the BHN dynamics), as well as L_1 (for both the dBB and BHN dynamics) are plotted at the (same) coarse-grained level. We started from a uniform distribution of positions; we took $\alpha = 0.1$. In both cases, the position distributions $\mathcal{P}$ and P converge to $|\Psi|^2$. Moreover, we recover an exponential decay for $\bar{H}_V$, as already observed in [10], in absence of stochastic (brownian) noise *à la* Nelson. However, we observe that the convergence to equilibrium occurs faster in the presence of the quantum thermostat.

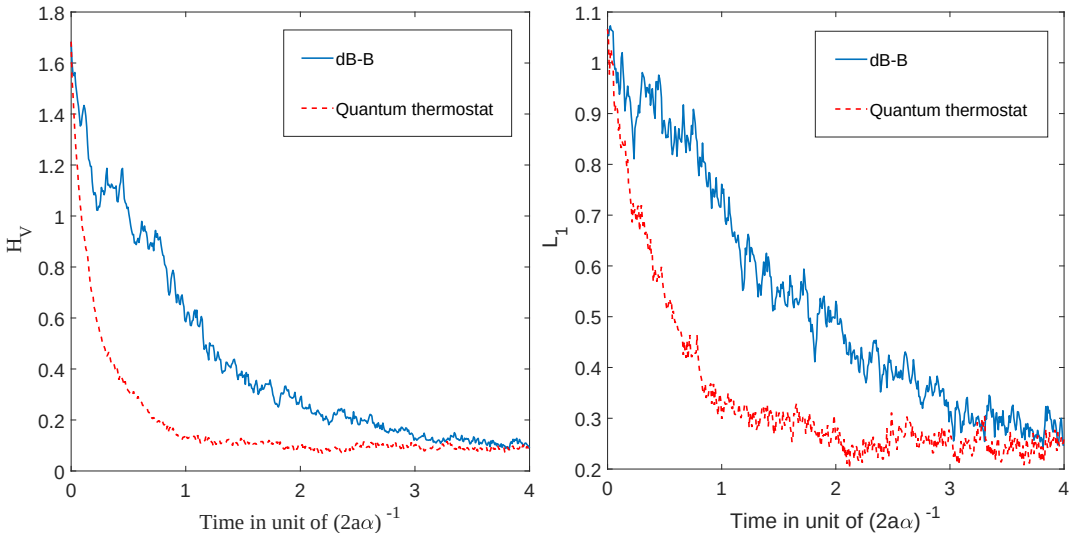

FIGURE 3.13: Plots of the evolution in time of the coarse-grained H-functions H_V (left) and L_1 (right) for the BHN and dBB dynamics. The full line corresponds to the dBB dynamics and the dashed line corresponds to the quantum thermostat. We started from 10 000 initial positions uniformly distributed in a a box of size 10x10; we chose $a = 0.5$, $\alpha = 0.1$ and $M = 4^2 = 16$ energy states.

3.5 Conclusion:

In this chapter we characterized the process of convergence towards quantum equilibrium in the framework of the Bohm-Hiley-Nelson dynamics [6]. We derived in this context a strong H-theorem that allows a qualitative and quantitative analysis of the onset of quantum equilibrium. In particular we have studied the Fokker-Planck operator in presence of zeros in the probability density $|\Psi|^2$ and have shown numerically how the convergence to equilibrium process occurs. For that purpose, we used the quantum harmonic oscillator at one and then at two dimensions, for both stationary and non stationary states. It has been shown that the BHN dynamics can be considered as ergodic. The noise plays a crucial role in the relaxation process; it accelerates the convergence to the statistical distribution $|\Psi|^2$ and ensures that this process will almost always occur. The Csiszár-Kullback-Pinsker inequality [23] which connects the functionals H_V and L_1 has been shown to be valid in this framework. Our results generalize the results by Petroni and Guerra [7, 8] concerning the relaxation towards quantum equilibrium in the framework of the BHN dynamics of a single particle in a harmonic potential. Those results only involved the L_1 norm and no H-theorem was derived at that time. In the next chapter we shall precise the differences between the stochastic dynamics and the deterministic version of the pilot wave formulation (dBB). In particular we will focus our study on the mixing (this notion will be explained) and on the process of uniformization of the initial distribution. Moreover, we will make the link between the mixing and the chaos by the use of (an estimated value) of the Lyapunov exponent.

3.A Numerical simulations

Firstly, we discuss the case of the dBB dynamics. It is assumed that we have an analytical solution of the Schrödinger equation $\Psi(t,\mathbf{x})$. We want to compute the evolution of a given initial non-equilibrium density $\mathcal{P}(t_i,\mathbf{x})$ up to a final time t_f and for intermediate time events (we denote all these events by t_k, with $t_0 = t_i$ and $t_f = t_K$). In particular, we are interested in the coarse-grained non-equilibrium density

$$\overline{\mathcal{P}}(\mathbf{x},t_k) = \frac{1}{\epsilon^3}\int_{\text{CG cell}\ni\mathbf{x}} d^3x\mathcal{P}(\mathbf{x},t_k)\,, \tag{3.93}$$

which is defined in (2.20).

Numerically, we replace that integral by a discrete sum over a finite set of points $\mathbf{x}^l$, which are uniformly distributed over the CG cells. In order to obtain the value of each $\mathcal{P}(\mathbf{x}^l,t_k)$ we use the Liouville relation

$$\frac{\mathcal{P}(\mathbf{x}^l,t_k)}{|\Psi(\mathbf{x}^l,t_k)|^2} = \frac{\mathcal{P}(\mathbf{x}^l_i,t_i)}{|\Psi(\mathbf{x}^l_i,t_i)|^2}, \tag{3.94}$$

where $\mathbf{x}^l_i$ is the position of the particle which, when evolved according to (2.8) from t_i up to t_k, gives $\mathbf{x}^l$.

In order to obtain $\mathbf{x}^l_i$ for each $\mathbf{x}^l$, we consider the time-reversed evolution with wave-function $\Psi^*(-t,\mathbf{x})$ and initial condition $\mathbf{x}^l$ at time $-t_k$. The position $\mathbf{x}^l$, if time evolved from $-t_k$ up to $-t_i$ according to (2.8), will give the position $\mathbf{x}^l_i$. As there is usually no analytical solution of (2.8), we use a Runge-Kutta (RK) algorithm [30] to obtain a numerical estimate of the position $\mathbf{x}^l_i$. In order to know if we can trust the result of the Runge-Kutta algorithm, we perform two realizations of the algorithm with different choices of a so-called tolerance parameter (the smaller the value of that tolerance parameter, the more precise the computation), say γ and $10^{-1}\gamma$. If the distance between the two positions is less than some chosen value δ, the result of the last iteration of the RK algorithm is trusted. Otherwise, we perform another iteration with $10^{-2}\gamma$ and we compare it to the previous realization of the RK algorithm. We repeat the procedure until the constraint on the distance between the two successive results of the RK algorithm is satisfied, or until we reach some minimal value of the tolerance parameter. In that case, the position $\mathbf{x}^l$ is considered as a bad position and it is discarded from the numerical integration of (2.20). This method was used in[10].

That is one possible method but we could also adopt a more brute-force method: Randomly generate a set of N initial positions according to $\mathcal{P}(t_i,\mathbf{x})$ and let them evolve according to an Euler algorithm (that is, we divide the time-interval in small time-steps of length Δt and we increment the position by $\mathbf{v}(t)\Delta t$ at each time-step). We record the positions of the N particles for each value of t_k, we count the number of particles in each CG cell for each time t_k (say n_{CG}) and we divide n_{CG} by N in order to define $\overline{\mathcal{P}}(\mathbf{x},t_k)$. The first method turns out to be more efficient in the case of the dBB dynamics but it is not applicable in the presence of stochastic terms.

In the case of Nelson dynamics we used the Euler-Maruyama method for stochastic processes to approximate the solution of the Ito equation (3.1). In the same way as Euler's method, the time T is divided into N small discrete time steps Δt. For each time t_i we generated a random variable normally distributed $\Delta W_i = \sqrt{\Delta t}\,\mathcal{N}(0,1)$. The integration scheme has the form:

$$x_{i+1} = x_i + v(x_i, i\,\Delta t)\Delta t + \sqrt{\alpha}\,\Delta W_i. \tag{3.95}$$

We invite the reader interested in the details to read [31]. The remaining question is how to choose the time step Δt so that one can trust the result of the numerical simulations. One way to do this is the following. We know that the Born distribution remains invariant under Nelson's dynamics (equivariance). We therefore start with some value for Δt and decrease it until the result of the numerical simulation confirms this theoretical prediction. We then perform the numerical simulation for the non-equilibrium distribution with the value of Δt thus obtained.

Bibliography

[1] David Bohm and Jean-Pierre Vigier. Model of the causal interpretation of quantum theory in terms of a fluid with irregular fluctuations. *Phys. Rev.*, 96(1):208, 1954.

[2] Antony Valentini. Signal locality, uncertainty and the subquantum H-theorem. I. *Phys. Lett. A*, 156:5–11, 1991.

[3] C. Efthymiopoulos, G. Contopoulos, and A. C. Tzemos. Chaos in de Broglie - Bohm quantum mechanics and the dynamics of quantum relaxation. *Ann. Fond. de Broglie*, 42:133, 2017.

[4] Partha Kyprianidis. The Principles of a Stochastic Formulation of Quantum Theory. *Found. Phys.*, 22(12):1449–1483, 1992.

[5] Edward Nelson. Dynamical Theories of Brownian Motion. *Mathematical Notes*, 131(6):2381–2396, 1967.

[6] D. Bohm and B. Hiley. Non-locality and locality in the stochastic interpretation of quantum mechanics. *Physics Reports*, 172(3):93–122, 1989.

[7] Nicola Cufaro Petroni. Asymptotic behaviour of densities for Nelson processes. In *Quantum Communications and Measurement*, pages 43–52. Springer, 1995.

[8] Nicola Cufaro Petroni and Francesco Guerra. Quantum Mechanical States as Attractors for Nelson Processes. *Found. Phys.*, 25(2):297–315, 1995.

[9] F. Guerra. Introduction to Nelson stochastic mechanics as a model for quantum mechanics. In *The Foundations of Quantum Mechanics*, pages 339–355. Kluwer Academic Publishers, 1995.

[10] Antony Valentini and Hans Westman. Dynamical origin of quantum probabilities. *Proc. R. Soc. A*, 461:253–272, 2005.

[11] S. Colin and W. Struyve. Quantum non-equilibrium and relaxation to quantum equilibrium for a class of de Broglie-Bohm-type theories. *New J. Phys.*, 12:043008, 2010.

[12] M.D. Towler, N. J. Russell, and A. Valentini. Time scales for dynamical relaxation to the Born rule. *Proc. R. Soc. A*, 468:990–1013, 2011.

[13] S. Colin. Relaxation to quantum equilibrium for Dirac fermions in the de Broglie-Bohm pilot-wave theory. *Proc. R. Soc. A*, 468:1116–1135, 2012.

[14] G. Contopoulos, N. Delis, and C. Efthymiopoulos. Order in de Broglie - Bohm quantum mechanics. *J. Phys. A: Math. Theor.*, 45(16):165301, 2012.

[15] E. Abraham, S. Colin, and A. Valentini. Long-time relaxation in the pilot-wave theory. *J. Phys. A: Math. Theor.*, 47:395306, 2014.

[16] Travis Norsen. On the explanation of born-rule statistics in the de broglie-bohm pilot-wave theory. *Entropy*, 20(6):422, 2018.

[17] Mohamed Hatifi, Ralph Willox, Samuel Colin, and Thomas Durt. Bouncing oil droplets, de broglie's quantum thermostat, and convergence to equilibrium. *Entropy*, 20(10):780, 2018.

[18] Louis de Broglie. Interpretation of quantum mechanics by the double solution theory. *Annales de la Fondation Louis de Broglie*, 12(4):1–23, 1987.

[19] Luis de La Peña and Ana Maria Cetto. *The quantum dice: an introduction to stochastic electrodynamics*. Springer Science & Business Media, 2013.

[20] Luis de la Peña, Ana María Cetto, and Andrea Valdés Hernández. *The Emerging Quantum*. Springer, 2015.

[21] Guido Bacciagaluppi. Nelsonian mechanics revisited. *Foundations of Physics Letters*, 12(1):1–16, 1999.

[22] Jean Bricmont. Bayes, Boltzmann and Bohm: Probabilities in Physics. In *Chances in Physics*, pages 3–21. Bricmont J., Ghirardi G., Dürr D., Petruccione F., Galavotti M.C., Zanghi N. (eds), Springer, 2001.

[23] A. Jüngel. *Entropy Methods for Partial Differential Equations*. Springer briefs for Mathematics, Springer, 2016.

[24] C W Gardiner. *Handbook of stochastic processes*. Springer-Verlag, New York, 1985.

[25] Hannes Risken. Fokker-planck equation. In *The Fokker-Planck Equation*, pages 63–95. Springer, 1996.

[26] Nicola Cufaro Petroni, Salvatore De Martino, and Silvio De Siena. Exact solutions of Fokker-Planck equations associated to quantum wave functions. *Physics Letters A*, 245(1-2):1–10, 1998.

[27] M. Brics, J. Kaupuzs, and R. Mahnke. How to solve fokker-planck equation treating mixed eigenvalue spectrum? *Cond. Matt. Phys.*, 16:13002, 2013.

[28] R. M. Gray. *Probability, random processes, and ergodic properties*. Springer, Dordrecht; Heidelberg, 2009.

[29] V.I. Arnold and A. Avez. *Problèmes ergodiques de la méchanique classique*. Gauthier-Villars, Paris, 1967.

[30] William H. Press, Saul A. Teukolsky, William T. Vetterling, and Brian P. Flannery. *umerical Recipes 3rd Edition: The Art of Scientific Computing*. Cambridge University Press, New York, NY, USA, 3 edition, 2007.

[31] Desmond J. Higham. An algorithmic introduction to numerical simulation of stochastic differential equations. *SIAM review*, 43(3):525–546, 2001.

Chapter 4

Role of mixing and microstructures: deterministic vs stochastic pilot wave dynamics

> "Tout étant prêt pour ma mort, j 'ai commencé à écrire ce dont justement je sais qu 'il vous serait impossible de pressentir la raison, d'apercevoir le devenir. C'est ainsi que cela se passe. C'est à votre incompréhension que je m'adresse toujours. Sans cela, vous voyez, ce ne serait pas la peine."
>
> Marguerite Duras, *L'Homme atlantique*

Summary In this chapter we compare the onset of quantum equilibrium in the (deterministic) de Broglie-Bohm (dBB) formalism with its counterpart in the (stochastic) formalism of Bohm, Hiley and Nelson. In particular, we emphasize the role played by microstructures [1, 2, 3] in position distributions in differentiating the onset of equilibrium in both situations. The present work is a continuation of the chapters 2 and 3 where ergodicity of pilot wave dynamics has been studied. The chapter is structured as follows. In section 4.1 we study the mechanism of uniformization (mixing) of two initial ensembles spatially separated, in the context of a 2D quantum harmonic oscillator. In section 4.2 we show how the presence of microstructures in the initial distribution of positions affects the process of convergence towards the statistical quantum probability. We evaluate the largest Lyapunov exponent in order to qualitatively relate the dispersion of the microstructures with the degree of chaos present in the dynamics (section 4.2.1); we also show how the presence of noise explodes the Lyapunov regime and accelerates the convergence to equilibrium (section 4.2.2). We finally introduce a new measure (inspired by Bernoulli processes) in order to measure the degree of mixing of two ensembles initially separated in space (section 4.2.3).

4.1 Uniformization and mixing

In the previous chapters we introduced the de Broglie-Bohm (dBB) dynamics and its stochastic extension *à la* Bohm-Hiley-Nelson (BHN). We also characterized the onset of quantum equilibrium for both dynamics using H theorems. For that purpose, we illustrated the evolutions of the H functions, by means of numerical simulations in the context

of a two-dimensional quantum harmonic oscillator.
In the continuity of this work, we aim to make explicit the differences that exist between the dBB and the BHN dynamics. In particular, we shall see how the relaxation process towards quantum equilibrium depends on the initial distribution of positions [1, 2, 3]. We will make a comparative study of the mechanism of uniformization for various initial distributions. To do so, we shall keep using the same two dimensional harmonic oscillator as in the chapters 2 and 3.

4.1.1 Uniformization mechanism in the de Broglie-Bohm dynamics

Let us start this study with the dBB dynamics and let us use an analogy with the thermodynamics of mixing [4]. In a nutshell, we start initially from two ensembles (say a red one and a blue one) of particle positions spatially separated. The two ensembles (say $\mathcal{R}$ for the red one and $\mathcal{B}$ for the blue one) have a different number of initial points (N_R and N_B) uniformly distributed among them (see figure 4.1).

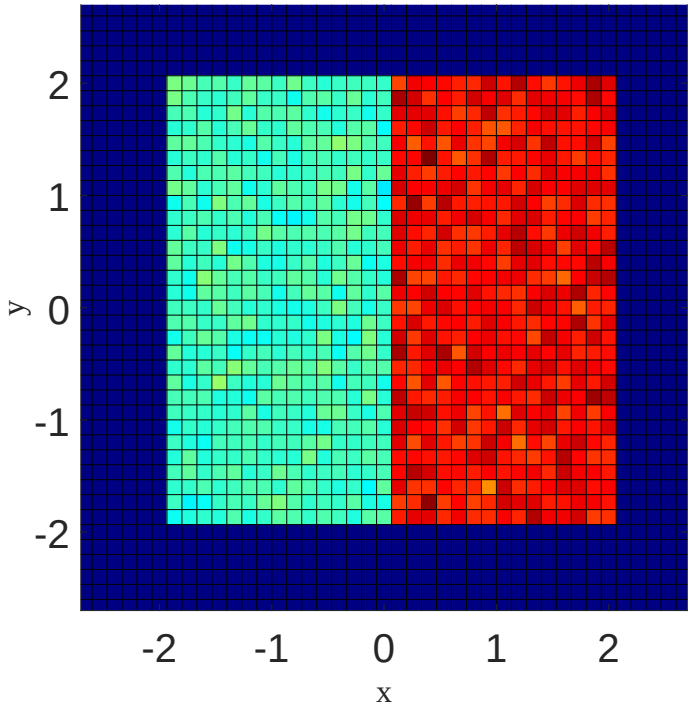

FIGURE 4.1: This figure shows the initial distribution $\overline{P}$ consisting of two sub-ensembles (in the left, the ensemble $\mathcal{B}$ with N_B points and in the right the ensemble $\mathcal{R}$ with N_R points) of particle positions spatially separated. We chose here: $N_R = 200\,000$ and $N_B = 100\,000$

It is worth emphasizing that the potential well used (2.26) has a characteristic length

$$L_{ch} = 2 \cdot \left(\frac{\hbar}{m\,\omega} \right)^{1/2} \tag{4.1}$$

which in dimensionless unit becomes equal to $L_{ch} = 2$. This is why we generated the initial ensembles of positions between $[-2, 2]$x$[-2, 2]$.

In addition, the coarse graining is done in the domain $[-4, 4]$x$[-4, 4]$ which is such that all

the trajectories are stuck in this domain as confirmed by means of numerical simulations.

Coming back to the ensembles defined above (figure 4.1). Once those ensembles of initial positions are created, we track their elements over time and we compute, for each of them, their corresponding $\overline{H}$ function (2.22). For example, in figure 4.2 we plot those $\overline{H}$ functions in the context of the 2D quantum harmonic oscillator defined in (2.26). This figure strongly suggests that the relaxation time is qualitaievely the same for the red ($\mathcal{R}$), the blue ($\mathcal{B}$) and the total ensemble ($\mathcal{R}+\mathcal{B}$). We found using an exponential fit of the entropy funtions $\overline{H}(t)$ as suggested in the reference [1], that these characteristic times are in a good approximation given by $\tau_{\mathcal{R}} \sim 15.65$, $\tau_{\mathcal{B}} \sim 15.28$ and $\tau_{\mathcal{R}+\mathcal{B}} \sim 15.39$. After these times, the $\overline{H}$ functions tend to zero and the total system reaches quantum equilibrium.

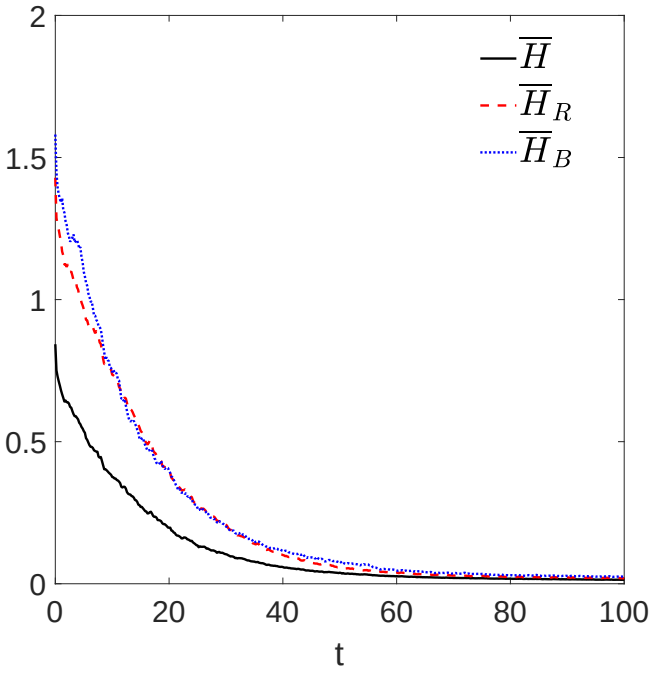

FIGURE 4.2: This figure shows the evolution of the entropy functions $\overline{H}(t)$ (2.22) for the dBB dynamics starting from the ensembles defined in figure 4.1. The blue dotted curve is associated to the ensemble $\mathcal{B}$, the dashed line to $\mathcal{R}$ and the the full line curve to the total ensemble $\mathcal{B}+\mathcal{R}$.

In order to understand how the non-equilibrium distribution becomes uniform over time, it is convenient to define the fraction number function on each CG cell, for the red and the blue mixtures, as follows:

$$n_r^{\text{cell}_{(j)}} = \frac{N_R^{\text{cell}_{(j)}}}{N_B^{\text{cell}_{(j)}} + N_R^{\text{cell}_{(j)}}}, \quad n_b^{\text{cell}_{(j)}} = \frac{N_B^{\text{cell}_{(j)}}}{N_B^{\text{cell}_{(j)}} + N_R^{\text{cell}_{(j)}}} \tag{4.2}$$

We can also define the average fraction of the two mixtures:

$$\overline{n}_r = \frac{1}{N^{cell}} \sum_{j=1}^{N^{cell}} n_r^{\text{cell}_{(j)}}, \quad \overline{n}_b = \frac{1}{N^{cell}} \sum_{j=1}^{N^{cell}} n_b^{\text{cell}_{(j)}} \tag{4.3}$$

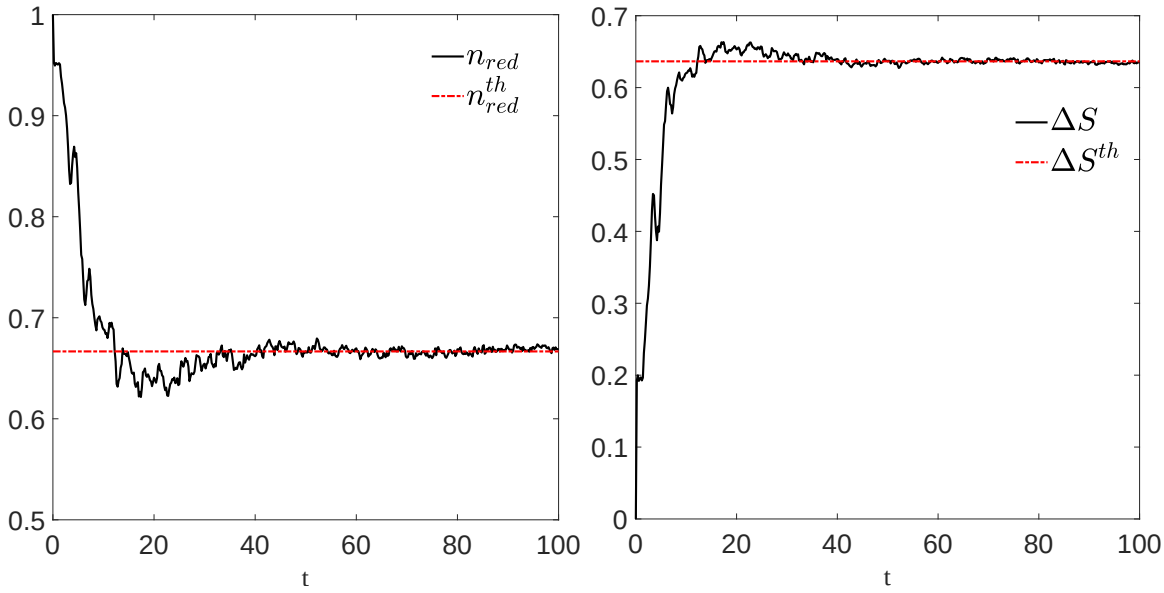

(4.5)

FIGURE 4.3: This plot shows the evolution of the average red mixture $\overline{n}_r$ on the left and the entropy of mixing ΔS. We chose here: $N_R = 200\,000$ and $N_B = 100\,000$. The function $\overline{n}_r$ is converging to $\overline{n}_r^{th} = 2/3$.

Continuing the analogy with the thermodynamics of mixing, we define an entropy of mixing as:

$$\Delta S = -\overline{n}_r \ln(\overline{n}_r) - (1 - \overline{n}_r) \ln(1 - \overline{n}_r) \tag{4.4}$$

In figure 4.3 we plot the averaged fraction number of the red mixture $\overline{n}_r$ and the associated entropy of mixing ΔS. We note that, while the red ensemble $\mathcal{R}$ is converging to the quantum equilibrium, the mixture $\overline{n}_r$ converges at the same time to the fraction $\bar{n}_r^{th} = N_R/(N_R + N_B)$. It means that on average, the same fraction of red or blue mixture (of trajectories) is present in each cell. In addition,we note that the entropy is maximal[1] after a time of the order of the characteristic time of convergence $t \sim \tau_{\mathcal{R}+\mathcal{B}}$ (with $\tau_{\mathcal{R}+\mathcal{B}} \sim 15.39$).

4.1.2 Uniformization mechanism in the Bohm-Hiley-Nelson dynamics

Let us now make this study in the framework of the stochastic dynamics (BHN). In particular, for this study we consider small fluctuations of the background field defined in (3.5) for which $\alpha \ll 1$. It is quite intuitive that if α is large, the uniformization will occur quickly because of the brownian character of the evolution. As we shall see, this acceleration of the onset of equilibrium also occurs for small values of α (small compared to unity, α being a dimensionless parameter).

Starting from the distribution corresponding to that in figure 4.1, we let each ensemble ($\mathcal{B}$ and $\mathcal{R}$) evolve according to the dynamics defined by equation (3.5).

[1] In the context of a thermodynamical system constituted by two mixing ideal gases [4], when the thermal equilibrium is reached, it means that the kinetic energy is on average equally distributed among the particles so that the entropy of mixing is maximal. Here in the quantum non-equilibrium, as a result we found that the quantity is equally distributed as the averaged fraction number of the different mixtures.

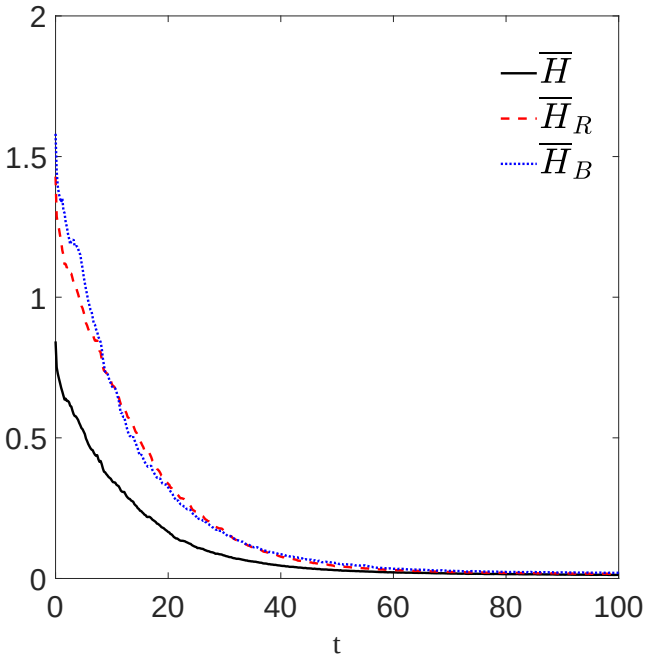

FIGURE 4.4: This figure shows the evolution of the entropy functions $\overline{H}(t)$ (2.22) in the case of the stochastic dynamics and starting from the ensembles defined in figure 4.1. The blue dotted curve is associated to the ensemble $\mathcal{B}$, the dashed line to $\mathcal{R}$ and the the full line curve to the total ensemble $\mathcal{B}+\mathcal{R}$.

In figure 4.4 we plot the H functions corresponding to each ensemble characterizing the mixtures. As in the case of the dBB dynamics, the relaxation time is globally the same for the red, the blue and the total ensemble. In figure 4.5 we compare the $\overline{H}$ functions obtained for the dBB dynamics and those obtained in the stochastic dynamics for $\alpha = 10^{-4}$. We note that, even in the case where $\alpha \ll 1$, we observed an acceleration in the convergence for the stochastic dynamics (as already seen in figure 3.13), compared to its deterministic counterpart: it is almost 10% faster according to the values of the linear fit in figure 4.5.

In figure 4.6 we compare the averaged fraction number of the red mixture (4.3) and the corresponding entropy of mixing (4.4) for both dynamics. The mixture $\overline{n}_r$ converges slightly faster to the ratio $N_R/(N_R+N_B)$ in the case of the stochastic dynamics than its deterministic counterpart. As we shall see, this effect is very sensitive to the initial distribution and gets amplified in the presence of microstructures.

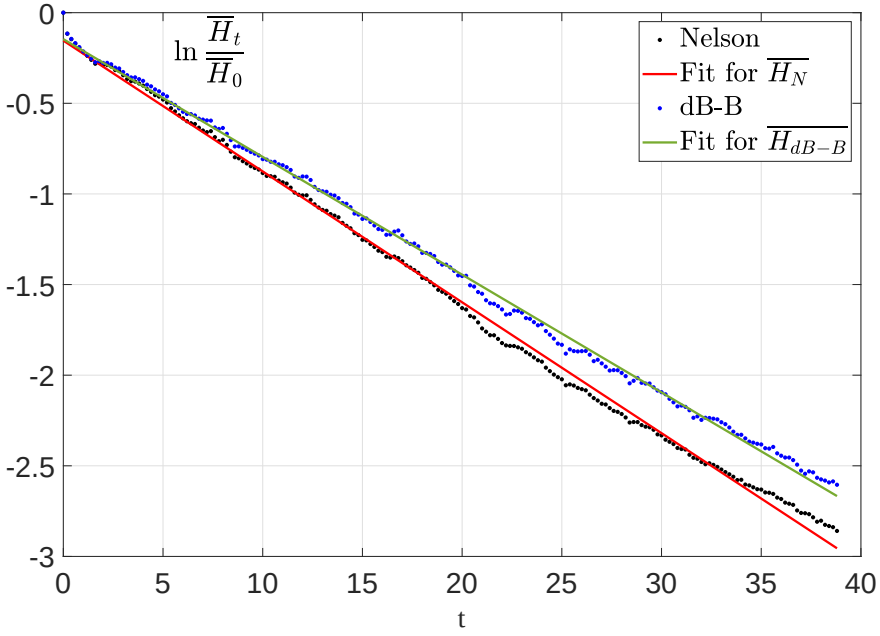

FIGURE 4.5: In this plot we compare the H-functions obtained for the de Broglie-Bohm dynamics and for the Bohm-Hiley-Nelson dynamics for $\alpha = 10^{-4}$. We plot here the logarithmic ratio $\ln\left(\overline{H}(t)/\overline{H}(t_0)\right)$. We considered for both dynamics the same initial ensemble of initial positions. We chose $N = 300\,000$ initial points uniformly distributed in the domain $[-2,2]$x$[-2,2]$. Using a linear fit we estimated the characteristic time of convergence: for the dBB dynamics we found $\tau_{\mathcal{R}+\mathcal{B}} \sim 15.39$ and for the stochastic dynamics: $\tau_{\mathcal{R}+\mathcal{B}} \sim 13.85$.

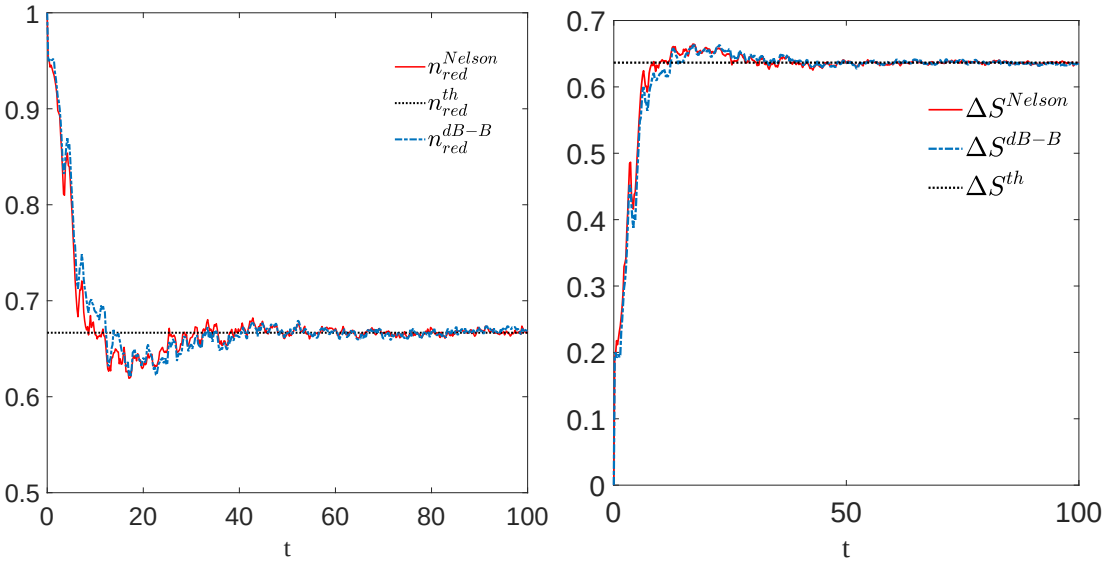

FIGURE 4.6: This plot shows the evolution of the average red mixture $\overline{n}_r$ on the left and the entropy of mixing ΔS for the stochastic evolution (3.5). As before: $N_R = 200\,000$ and $N_B = 100\,000$. The function $\overline{n}_r$ is converging to $\overline{n}_r^{th} = 2/3$.

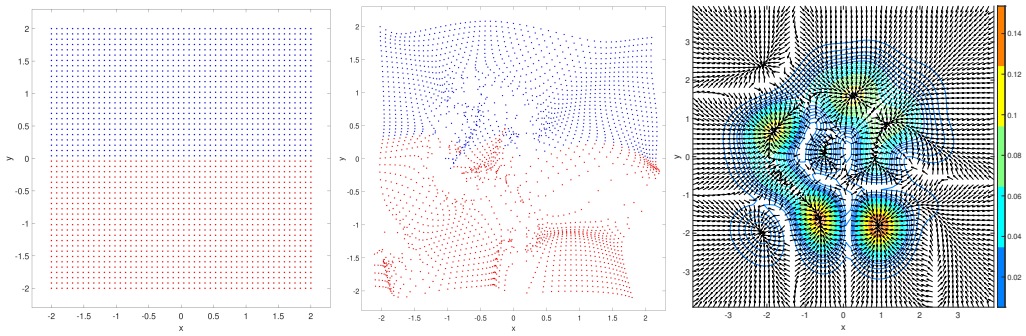

FIGURE 4.7: We plot in a) the initial distribution of points. B) The distribution at time $t = 0.2$. C) The function $|\Psi|^2$ at $t = 0$ with its gradients. We chose here 50x50 "clusters" of 20 points each, separated by a distance $|\mathbf{d_0}| \sim 10^{-8}$ among them in each cluster. We choose $N_R = N_B =$ 50x25x20 .

4.2 Mixing in presence of Microstructures

4.2.1 Microstructure in the de Broglie-Bohm dynamics

In the previous section, the initial positions were randomly distributed in each ensemble. Here we study what happens in the relaxation process when the two ensembles exhibit organized microstructures. In figure 4.7a we illustrate a new initial distribution for the red and the blue mixtures, in which the lower half of the domain $[-2,2]\times[-2,2]$ consists only of red points and the upper half only of blue ones. However, each such 'point' is in reality a cluster of points, with a microstructure made of 20 points arranged in a two dimensional grid initially separated by a distance $|\mathbf{d_0}| \sim 10^{-8}$. In figure 4.7b the clusters move along the dB-B trajectories to areas where the density $|\Psi|^2$ is different from zero (figure 4.7c). If we zoom in on an elementary volume of space, it will be seen that the clusters are always present until a certain time after which they start to disappear.

Intuitively, it is clear that if the dynamics is not sufficiently chaotic (for example with a small number of modes M in the superposition in (2.26)) it will imply that the "cluster" will survive over time. Moreover, the increase of the number of modes in the superposition of the pilot wave enhances the complexity of the dynamics by making the variation of the phase nontrivial which in turn increases the chaos [5, 6, 7, 8, 9].

In figure 4.8a we plot the average distance $|\overline{\mathbf{d}}(t)|$ between the points of the microstructures inside each "cluster". In the time interval $[0, \tau_{\mathcal{R}+\mathcal{B}}]$ (where $\tau_{\mathcal{R}+\mathcal{B}}$ was defined in figure 4.5) the logarithm of the distance is linear and we can estimate the time at which the clusters start to disappear (see figure 4.8b). This time is inversely proportional to the largest Lyapunov exponent Λ which characterize the degree of chaos present in the dynamics. The largest Lyapunov exponent Λ is indeed related to the averaged "interclusters" distance $|\overline{\mathbf{d}}(t)|$ by:

$$\frac{\dot{d}(t)}{d(t)} \sim \Lambda, \quad \text{so that} |\overline{\mathbf{d}}(t)| \sim |\overline{\mathbf{d_0}}|\, e^{\Lambda t}. \tag{4.6}$$

If we estimate the Lyapunov time $\tau_\Lambda = 1/\Lambda$ (where Λ is the Lyapunov exponent) with a linear fit as in figure 4.8, we find a value of approximately $\tau_\Lambda \sim 1.4$. This estimate of the largest Lyapunov exponent is in accordance with the value $\Lambda = 0.6721$ computed in figure 4.9 using a standard algorithm [10, 11].

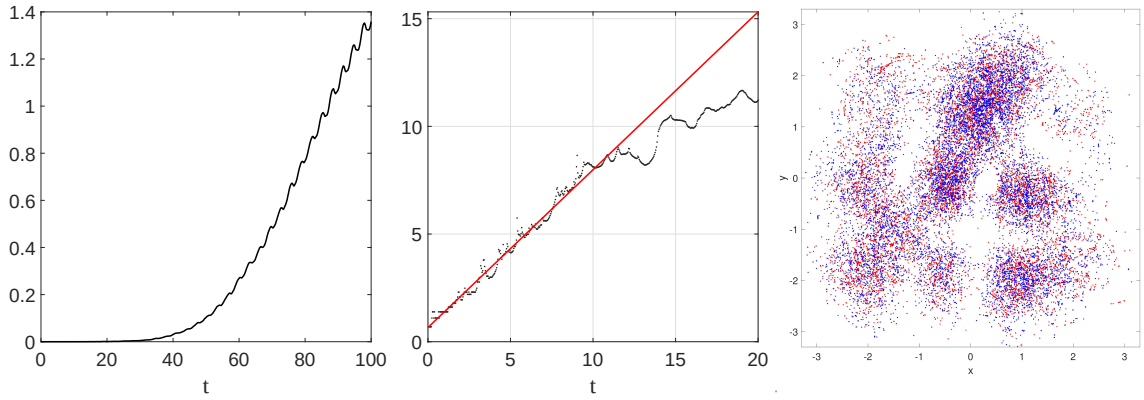

FIGURE 4.8: This plot shows the evolution of the distances between the microstructures inside each "cluster". In a) the averaged distance $|\overline{\mathbf{d}}(t)|$ between the points of the microstructures. B) We plot here $\ln\left(|\overline{\mathbf{d}}(t)|/|\overline{\mathbf{d_0}}|\right)$ and we estimate the Lyapunov exponent as the slope of the full-line curve. C) The distribution at time $t = 100$. We chose here 50x50 "clusters" of 20 points. $N_R = N_B =$ 50x25x20.

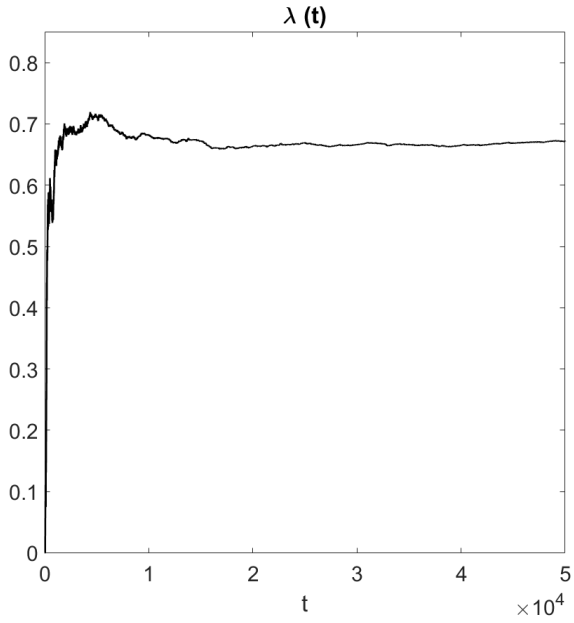

FIGURE 4.9: Estimate of the largest Lyapunov exponent for the dBB dynamics using the algorithm in Appendix 4.A. This estimate was made after averaging 150 orbits uniformly distributed $(x_0, y_0) \in [-2,2]$x$[-2,2]$. We used $d_0 = 10^{-8}$, $t = 5.10^4$ and with a time step $\Delta t = 10^{-3}$.

It is worth noting that if we now go back to figure 4.5, where we imposed an initial homogeneous distribution of 300 000 points, which corresponds to a distance between two points of the order of $|\overline{\mathbf{d_0}}| \sim 5 \cdot 10^{-5}$. We can then predict, according to (4.6), that after a time of about 10 times τ_Λ (i.e $10 \times \tau_\Lambda \approx 15$), the distance between two initially neighboring points will be of the order of $5{\cdot}10^{-5} \cdot e^{10} \sim 1.1$, which is of the order of the size of the domain where the particle is confined. Therefore, it this also is in full agreement with our estimate of the time required for establishing quantum equilibrium (for the dBB dynamics:$\tau_{\mathcal{R}+\mathcal{B}} \sim 15.39$).

A second remark concerns this 'Lyapunov regime' during which the global dynamics in the system is correctly predicted by the value of the Lyapunov exponent. This regime is limited in time: an exponential amplification of discrepancies in initial conditions is, de facto, limited in our case due to the confinement imposed by the harmonic potential. Therefore the exponential growth saturates after a while, which can be observed at the level of the picture in the middle of the figure 4.8.

Actually, as we have checked directly after visualizing a dynamical movie of the trajectories of the ensemble, the Lyapunov time is of the order of the time of passage in the vicinity of a zero of the wave function, which confirms previous studies [7, 5] which demonstrated that the chaotic properties of the dynamics have to be attributed to the mixing occurring in the vicinity of the zeros of the wave function (where the gradient of the phase may take huge values, which strongly increases the dBB guidance velocities).

4.2.2 Microstructure in the Bohm-Hiley-Nelson dynamics

We have found in a previous section that the stochastic evolution, even with a small diffusion coefficient ($\alpha = 10^{-4}$), induces a speed-up in the mechanism of uniformization. In this section we identify the origin of this difference by looking at the evolution occurring at the microscopic level. Similarly to the procedure made in section 4.2.1 but within the framework of the stochastic dynamics, we focus here on the effect of the microstructures on the relaxation process.

To do so, let us consider the figure 4.10 in which we plot the averaged distance $|\overline{\mathbf{d}}(t)|$ between the points in each microstructure under a stochastic BHN evolution. The distance $|\overline{\mathbf{d}}(t)|$ grows quickly compared to the dBB dynamics. The mechanism of uniformization is thus more efficient in the case of the stochastic dynamics as pointed out in the previous section: even with a small diffusion coefficient ($\alpha = 10^{-4}$) the brownian character of the evolution implies a quick disappearance of the microstructures. Visually, from figure 4.10, we can estimate the convergence time $\tau_{\mathcal{R}+\mathcal{B}}$ which is necessary for the clusters to grow to a size comparable to the size of the domain where the particle is confined. This time is of the order of 14, i.e. $14 \sim 13.85$, which corresponds to the convergence time that we obtained through a linear fit at the level of figure 4.5 where we found that for the BHN dynamics $\tau_{\mathcal{R}+\mathcal{B}} \sim 13.85$.

Let us now estimate the chaos of the BHN dynamics making use of the procedure developed in the case of the dBB dynamics (section 4.2.1), which appeared to be very successful in that case. The main result is encapsulated in figure 4.11 in which we plot the largest Lyapunov exponent computed following [10, 11]. The numeric value for the Lyapunov exponent converges to $\Lambda \sim 5.26$. The Lyapunov time τ_Λ is then given by $\tau_\Lambda \sim 1/\Lambda \sim 0.19$ which is almost ten times smaller than the chaotic time of the dBB dynamics.

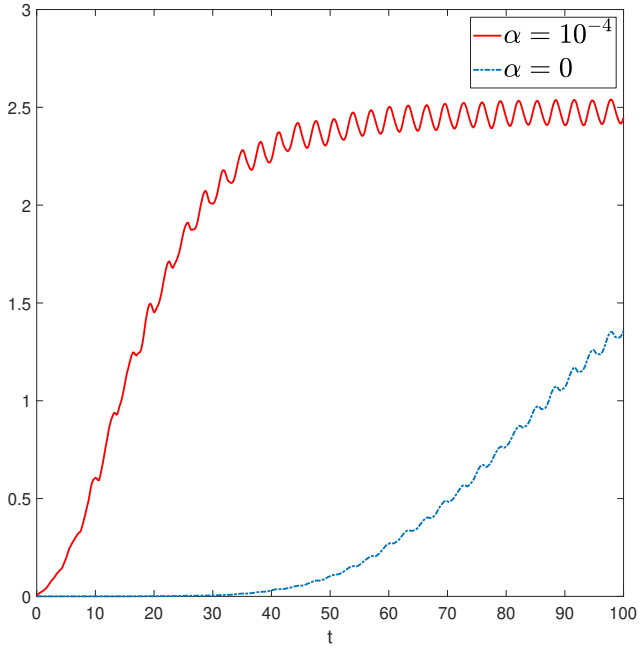

FIGURE 4.10: This plot shows the evolution of the interdistance $|\overline{\mathbf{d}}(t)|$ of the microstructures inside each "cluster". The red full line curve corresponds to the stochastic dynamics and the blue dotted curve corresponds to the dBB dynamics.

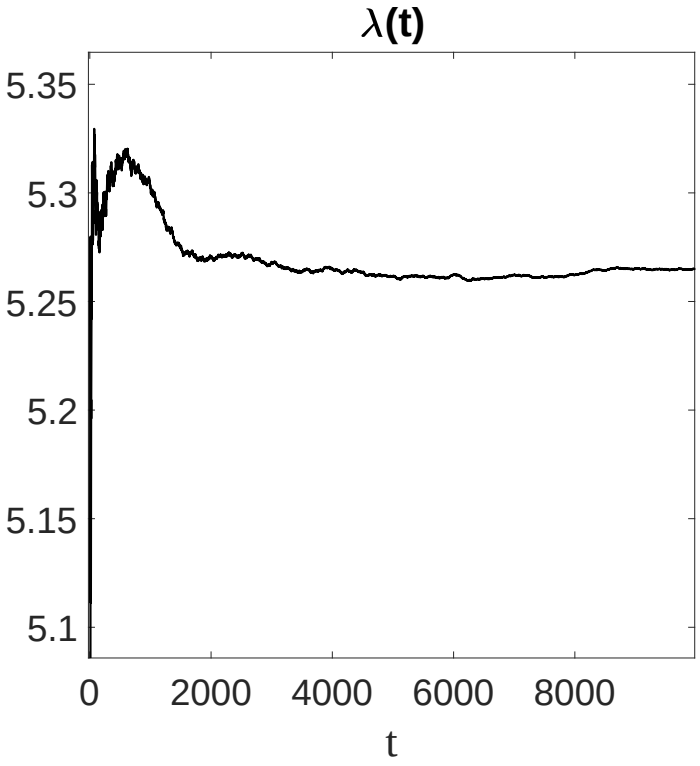

FIGURE 4.11: Estimate of the largest Lyapunov exponent for the stochastic dynamics using the algorithm in Appendix 4.A. This estimate was made after averaging 150 orbits uniformly distributed. We used $d_0 = 10^{-8}$, $t = 10^4$ and with a time step $\Delta t = 10^{-3}$.

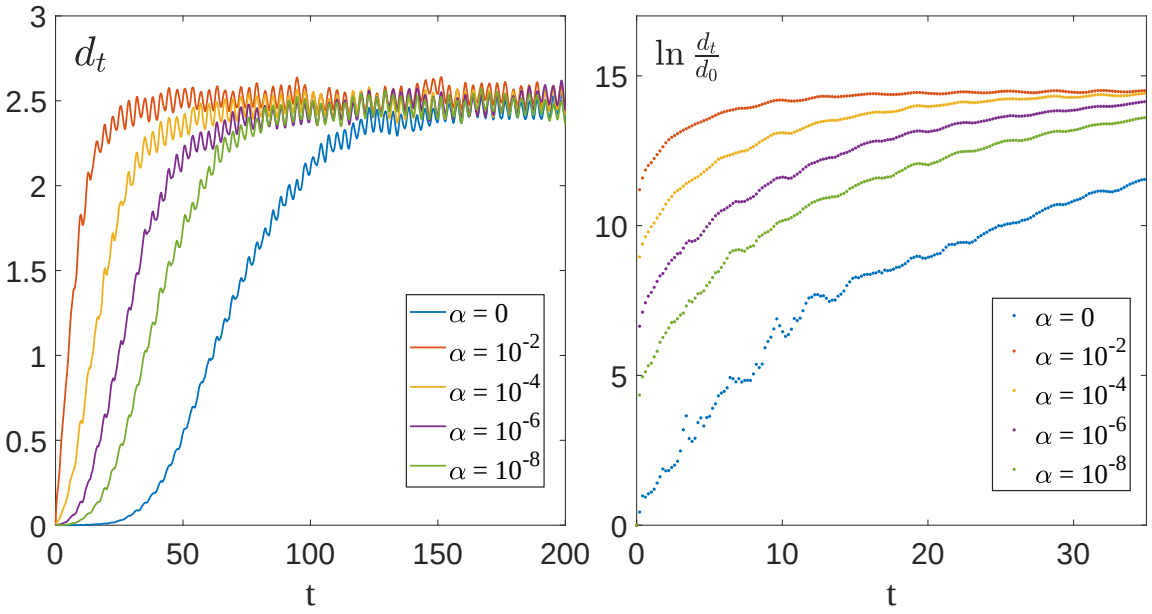

FIGURE 4.12: This plot shows the evolution of the interdistance $|\overline{\mathbf{d}}(t)|$ of the microstructures inside each "cluster" of two points. Here the initial distance d_0 between the two points is $d_0 = 10^{-6}$.

We could then try to deduce the convergence time to equilibrium in the same way as for the dBB dynamics. According to an analysis similar to that of section 4.2.1, we would find that the distance reached when, the initially homogeneous ensemble of 300 000 points, approaches equilibrium ought to be equal to $5{\cdot}10^{-5} \cdot e^{100} \sim 1.1 \cdot e^{90}$ which is obviously wrong. Alternatively, we should find that after a time equal to 10 times $\tau_\Lambda \sim 1.9$ (τ_Λ is now of the order of 0.19), the distance between two, initially, neighboring points will be of the order of $5{\cdot}10^{-5} \cdot e^{10} \sim 1.1$, which contradicts the data encapsulated in figure 4.10.

This shows that the Lyapunov exponent is ill-suited for characterizing the dynamics in presence of the BHN noise. A direct estimate based on figure 4.10 delivers the correct answer. Actually if we try to fit the red full line curve of figure 4.10 with an exponential curve (as we done for the de Broglie-Bohm case 4.8) or with a curve that is quadratic in time curve (purely brownian motion) we again fail. The dynamics in the BHN case is thus clearly different. Although the precise details of this dynamics remain to be investigated, it is apparent that the spread of neighboring trajectories is much faster, at least initially, than one would expect if the underlying mechanism would be purely chaotic as it is in the dBB case. One tentative explanation might be that the combination of brownian motion and chaos which appears during the passage close to a zero of the wave function will cause the divergence of the osmotic velocity (3.4). Our observation is confirmed by the plots of figure 4.12 which clearly show that an exponential in time growth (*à la* Lyapunov) only occurs in the absence of noise ($\alpha = 0$).

In figures 4.20 (in appendix 4.B) we illustrate and we compare the evolution of the microstructures through the dBB and the stochastic dynamics at different times. These figures strongly suggest that the mechanism of uniformization is indeed more efficient in the case of the stochastic dynamics as pointed out along this chapter. Even with a small diffusion coefficient ($\alpha = 10^{-4}$) the brownian character of the evolution implies a quick

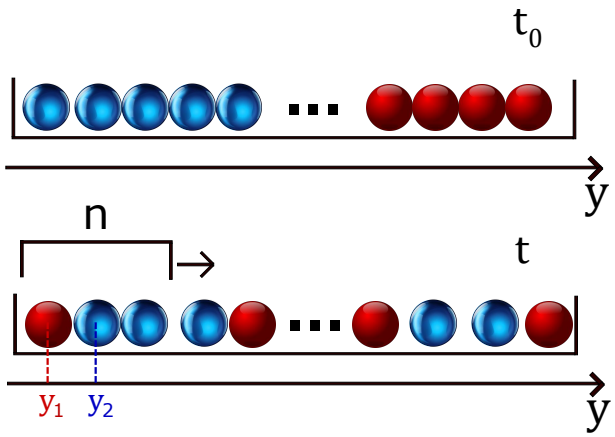

FIGURE 4.13: At $t = t_0$ two ensembles of initial points are placed on both sides of a box. The ensembles evolve in time according to the dB-B (or stochastic) dynamics. During the evolution we look at the sequence of blue/red points in the sub-intervals n

disappearance of the microstructures. Moreover, in these figures we can notice the presence of the nodes of the wave function. With their associated vorticity, they have a crucial role in the process of uniformization and they act like purveyors of chaos [7] (or mixing) in the dynamics.

4.2.3 Convergence to the Bernoulli statistics

In section 4.1, we looked at the statistics at the coarse-grained level. Here we pay particular attention to the statistics at the level of the microstructures, with the aim of introducing a measure of mixing which does not depend on any coarse graining. To do so, we recorded all the trajectories ($N = N_B + N_R$) corresponding to each ensemble $\mathcal{R}$ and $\mathcal{B}$. We considered initial ensembles with and without microstructures. We then projected all the trajectories along one axis (for example the $y-$axis) and computed the probability of having a particular sequence of blue (n_B) and red (n_R) points in a sub-interval of $n = n_R + n_B$ points (see figure-4.13).

We illustrate in figure-4.14-a and in figure-4.14-b the occurrence probability of having $\{n_B = 1, n_R = 1\}$ in a sub-interval $n = 2$ without and with clusters of 20 microstructures (using $|\overline{\mathbf{d_0}}| = 10^{-8}$ for the moment), as defined and used in the previous sections. As expected, this plot shows the fundamental difference between the deterministic and the stochastic dynamics in the presence of the microstructures. In fact, the dBB evolution, contrary to the stochastic dynamics, is strongly affected by the presence of the microstructures because of equation 2.17. Now when the spacing inside the microstructures $|\overline{\mathbf{d_0}}|$ increases, the mixing occurs more quickly as can be seen in figure 4.15 were $P_{1,1}$ is plotted (where we chose pairs of points with a spacing $|\overline{\mathbf{d_0}}| = 10^{-6}$). This figure has to be compared with figure 4.12 in which the initial spacing $|\overline{\mathbf{d_0}}|$ is the same. It indicates that the probability $P_{1,1}$ saturates at the same time that the one required to saturate the distance due to the confinement imposed by the potential well (roughly at $t = 50$ for the BHN dynamics and at $t = 100$ for the dBB dynamics).

As a result, it turns out that the probabilities P_{n_B,n_R} converges to the Bernoulli statistics

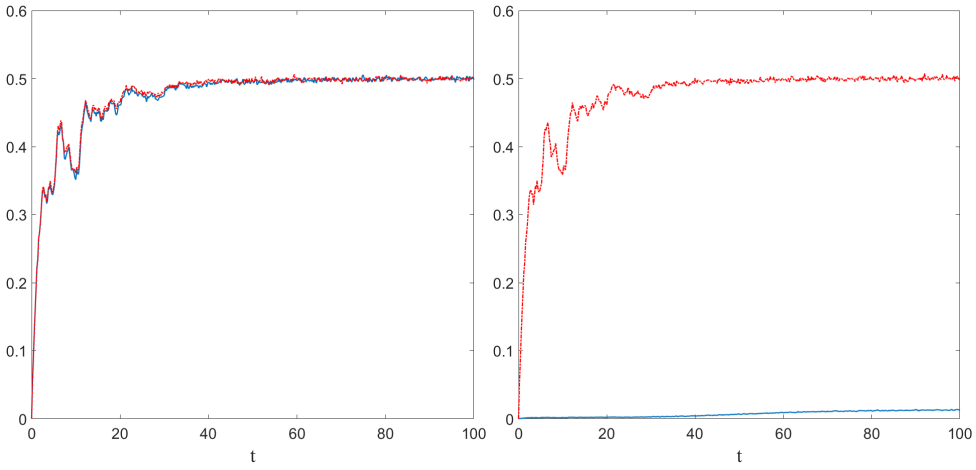

FIGURE 4.14: Plot of the occurrence probability P_{n_B,n_R} of having a sequence of a blue point followed by a red point $\{n_B = 1,n_R = 1\}$: a) without microstructures and b) with clusters of 20 microstructures and with a spacing $|\overline{\mathbf{d_0}}| = 10^{-8}$. The dB-B dynamics is associated to the full line curve (blue) and the stochastic dynamics to the dashed line (red). We chose here $\alpha = 10^{-4}$.

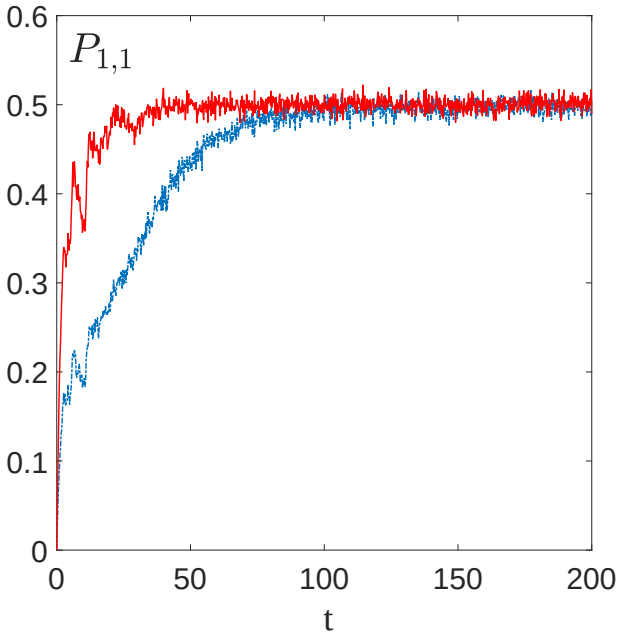

FIGURE 4.15: Plot of the occurrence probability P_{n_B,n_R} of having a sequence of $\{n_B = 1,n_R = 1\}$ with microstructures (in this case we chose pairs with a spacing $|\overline{\mathbf{d_0}}| = 10^{-6}$). The dB-B dynamics is associated to the full line curve (blue) and the stochastic dynamics to the dashed line (red). We chose here $\alpha = 10^{-4}$.

as confirmed by means of numerical simulations. In the Bernoulli statistics, the probability of having n_R red and n_B blue points in an interval of $n_R + n_B$ points is given by

$$P_{n_B,n_R} = \frac{(n_B + n_R)!}{n_B!\, n_R!}\, P_R^{n_R}\, P_B^{n_B} \tag{4.7}$$

or in terms of a parameter λ defined by ($N_B = \lambda\, N_R$):

$$P_{n_B,n_R} = \frac{(n_B + n_R)!}{n_B!\, n_R!} \left(\frac{1}{1+\lambda}\right)^{n_R} \left(\frac{\lambda}{1+\lambda}\right)^{n_B} \tag{4.8}$$

At equilibrium, the mixing ensures that the blue and the red points are dispersed in such a way that the most probable sequence of points in a sub-interval $n = n_R + n_B$ respects the ratio $n_B/n_R = \lambda$, on average.

To take the analysis one step further, we plot in figure 4.17 the histograms of P_{n_B,n_R} for different combinations $\{n_B,n_R\}$ at $t = 100$ for the dBB and the BHN dynamics. Typically, in the present configuration, at $t = 100$ the quantum equilibrium is reached in absence of microstructures (according to the figures 4.2 and 4.4), this is why we chose this time. We illustrate, first, those histograms in the figures 4.17-a and 4.17-b which are realized using an uniform initial distribution of positions that does not have microstructures. We note that the probabilities P_{n_B,n_R} indeed converges to the Bernoulli statistics for different combinations of $\{n_B,n_R\}$ for both dynamics. We thus compared quantitatively the absolute difference between the probability of figure-4.17 with the Bernoulli statistics and we found

$$\sum_{n_R=0}^{5}\sum_{n_B=0}^{5} |P_{n_B,n_R} - P^{dBB}_{n_B,n_R}| = 0.07 \quad \text{and} \quad \sum_{n_R=0}^{5}\sum_{n_B=0}^{5} |P_{n_B,n_R} - P^{BHN}_{n_B,n_R}| = 0.06, \tag{4.9}$$

which strongly confirms the validity of the convergence to the Bernoulli statistics in absence of microstructures. In the figures 4.17-c and 4.17-d we add the microstructures in the initial distribution of positions by using 50x50 "clusters" of 20 points spatially separated by $|\overline{\mathbf{d_0}}| = 10^{-8}$. As a result we found that the BHN dynamics is not affected by the presence of microstructures while the dBB is strongly affected. Making the same quantitative comparison we found

$$\sum_{n_R=0}^{5}\sum_{n_B=0}^{5} |P_{n_B,n_R} - P^{dBB}_{n_B,n_R}| = 7.40 \quad \text{and} \quad \sum_{n_R=0}^{5}\sum_{n_B=0}^{5} |P_{n_B,n_R} - P^{BHN}_{n_B,n_R}| = 0.04, \tag{4.10}$$

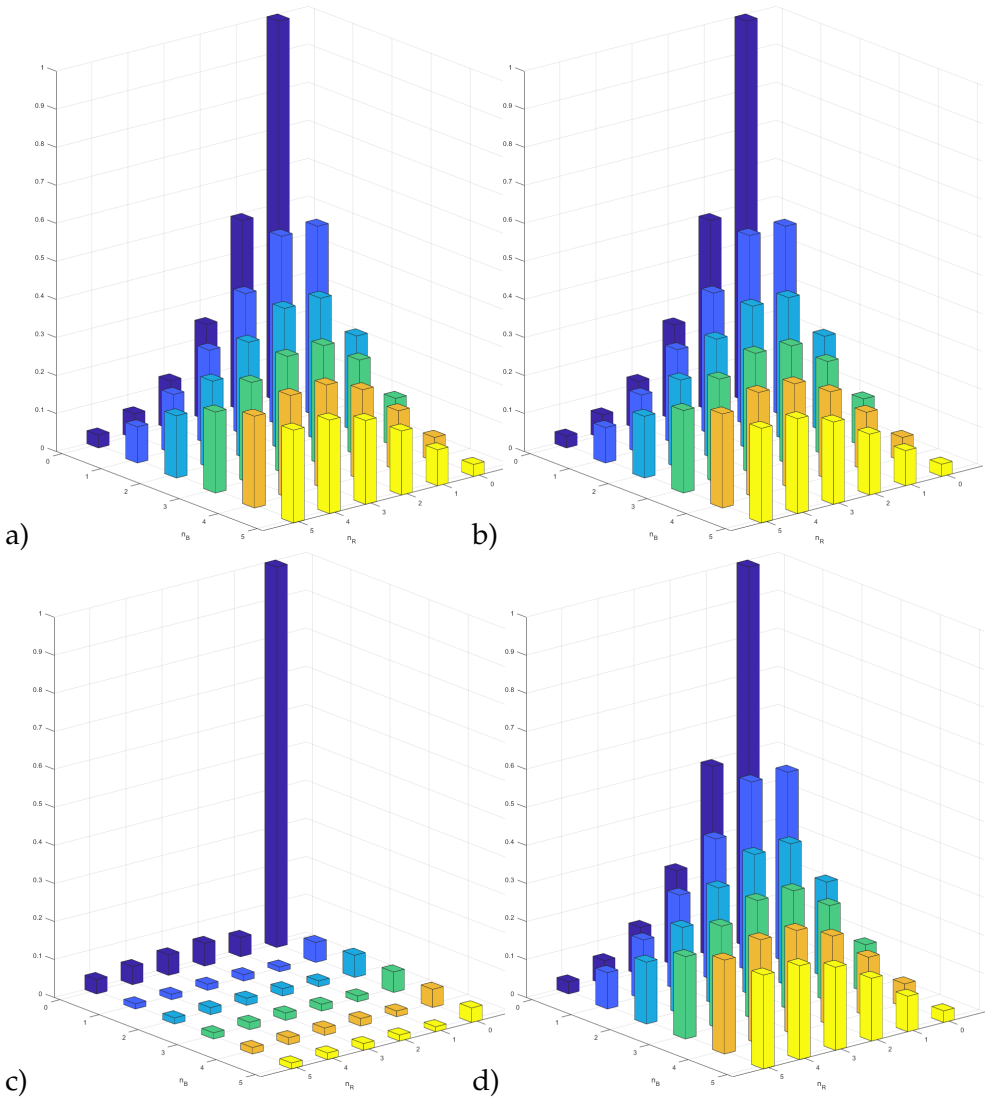

FIGURE 4.17: Probablity diagrams P_{n_B,n_R} at $t = 100$ and $|\overline{\mathbf{d_0}}| = 10^{-8}$ for : a) dBB (without microstructures), b) BHN (without microstructures), c) dBB (with microstructures), d) BHN (with microstructures).

4.3 Conclusions

Our study confirms results that were previously obtained regarding the onset of quantum equilibrium in the case of dBB dynamics [2, 7]. In particular, it confirms the role of the zeros of the wave function regarding the chaotic nature of the dynamics, which itself can be quantified making use of the Lyapunov exponent (section 4.2.1). In the case of the dBB dynamics we showed that the convergence to equilibrium crucially depends on the initial distribution [1, 2], a property which can be put in relation with the Lyapunov exponent [6, 5] (section 4.2.1), and is confirmed by the introduction of a new measure based on Bernoulli statistics (section 4.2.3).

In the presence of noise however (BHN dynamics) our results show that the Lyapunov analysis is largely irrelevant: it does not allow us to quantify the emergence of the quantum equilibrium (section 4.2.2). In this case (stochastic dynamics) our results rather show that the convergence to equilibrium becomes insensitive to the initial distribution after some time.

4.A Largest Lyapunov exponent

The Lyapunov exponent is a parameter quantifying the degree of sensitivity to the initial conditions. It is given theoretically by the formula

$$\Lambda = \lim_{t\to\infty}\left(\lim_{d_0\to 0}\frac{1}{t}\ln\left(\frac{d(t)}{d(0)}\right)\right) \tag{4.11}$$

where $d(t)$ is the distance between two trajectories intially at very small distance d_0. However, the largest Lyapunov exponent can be estimated numerically by using the algorithm present in [12]. This procedure can be summarized with the following procedure. We choose at $t = t_0$ two initial points $x_1(t_0)$ and $x_2(t_0)$ separated by a distance d_0 chosen to be small enough ($d_0 \sim 10^{-8}$ is sufficient). These two points evolve during a unique iteration Δt (see figure 4.18). We compute the new distance d_1 and we estimate the value of $\ln(d_1/d_0)$.

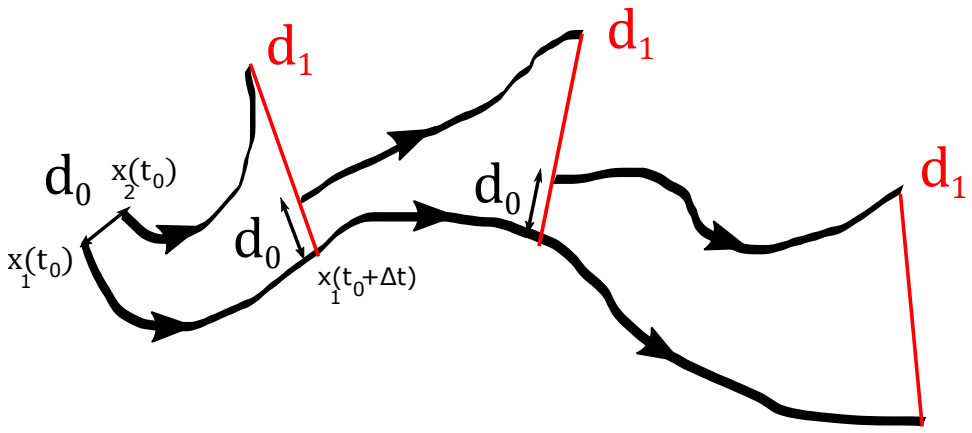

FIGURE 4.18: Illustration of the algorithm [12] used to estimate numerically the largest Lyapunov exponent

In the next step, we rescale one of the trajectories ($\boldsymbol{x_2}$ in figure 4.18) by readjusting the separation. The rescaling is done in a way that the new distance is d_0 and the direction is still in the same orientation as d_1. We then repeat the procedure and we estimate for each iteration the value of $\ln(d_1/d_0)$. The largest Lyapunov exponent is given in a good approximation for a long simulation time T by

$$\Lambda(\boldsymbol{x}_{1,0}, \boldsymbol{x}_{2,0}) \sim \frac{1}{T}\sum_{i=1}^{N}\ln\left(\frac{d_1(i)}{d_0}\right) \tag{4.12}$$

We found for $d_0 = 10^{-8}$, $T = 5.10^5$ and for $\Delta t = 10^{-3}$ a Lyapunov exponent $\Lambda \sim 0.6721$. Notice that this procedure has been successfully tested by us in the case of the Lorenz and the Rossler attractors.

4.B Appendix: Time evolution of the microstructures: dBB vs BHN dynamics

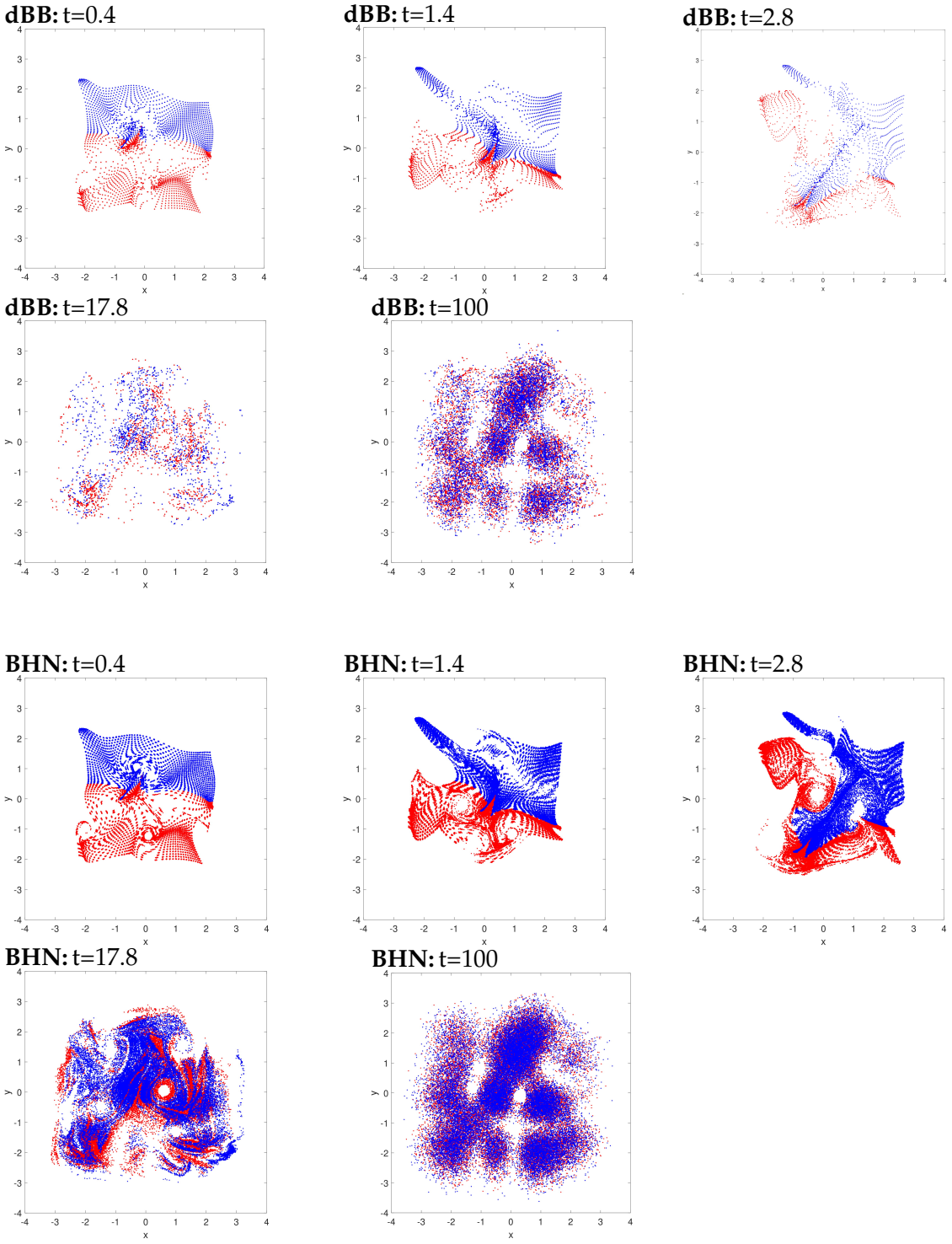

FIGURE 4.20: This plot shows the evolution of the microstructures at different time for the dBB dynamics on the top and for the BHN dynamics on the bottom. The initial ensemble of positions was the one in figure 4.7. We chose here 50x50 "clusters" of 20 points. $N_R = N_B =$ 50x25x20.

Bibliography

[1] Antony Valentini and Hans Westman. Dynamical origin of quantum probabilities. *Proc. R. Soc. A*, 461:253–272, 2005.

[2] Travis Norsen. On the explanation of born-rule statistics in the de broglie-bohm pilot-wave theory. *Entropy*, 20(6):422, 2018.

[3] Antony Valentini. Foundations of statistical mechanics and the status of the born rule in de broglie-bohm pilot-wave theory. *arXiv preprint arXiv:1906.10761*, 2019.

[4] E Fermi. *Thermodynamics*. Dover Publications, 1956.

[5] C. Efthymiopoulos, G. Contopoulos, and A. C. Tzemos. Chaos in de Broglie - Bohm quantum mechanics and the dynamics of quantum relaxation. *Ann. Fond. de Broglie*, 42:133, 2017.

[6] G. Contopoulos, N. Delis, and C. Efthymiopoulos. Order in de Broglie - Bohm quantum mechanics. *J. Phys. A: Math. Theor.*, 45(16):165301, 2012.

[7] C. Efthymiopoulos, C. Kalapotharakos, and G. Contopoulos. Origin of chaos near critical points of quantum flow. *Phys. Rev. E*, 79(3):036203, 2009.

[8] E. Abraham, S. Colin, and A. Valentini. Long-time relaxation in the pilot-wave theory. *J. Phys. A: Math. Theor.*, 47:395306, 2014.

[9] Alexandre Cesa, John Martin, and Ward Struyve. Chaotic bohmian trajectories for stationary states. *Journal of Physics A: Mathematical and Theoretical*, 49(39):395301, 2016.

[10] Giancarlo Benettin, Luigi Galgani, and Jean-Marie Strelcyn. Kolmogorov entropy and numerical experiments. *Physical Review A*, 14(6):2338, 1976.

[11] Giancarlo Benettin, Luigi Galgani, Antonio Giorgilli, and Jean-Marie Strelcyn. Lyapunov characteristic exponents for smooth dynamical systems and for hamiltonian systems; a method for computing all of them. part 1: Theory. *Meccanica*, 15(1):9–20, 1980.

[12] AJ Lichtemberg and MA Lieberman. Regular and chaotic dynamics, 1992.

Chapter 5

Droplets: wave particle duality at the macroscopic scale ?

> "J'adore l'eau. Dans 20-30 ans, y'en aura plus."
>
> JCVD

Summary In this chapter, we discuss the possible analogy between the experiments with macroscopic bouncing oil droplets and the quantum wave-particle duality. To do so we shall use the formalism developed in chapter 2, chapter 3 and chapter 4. 'Walkers' are realized as oil droplets generated at the surface of a vibrating oil bath. As shown by Couder and Fort [1, 2, 3], the vibration of the bath prevents the coalescence of the droplets at the surface, allowing them to remain stable for very long times. Moreover, the trajectories of the walkers are guided by an external wave [4, 5] that they themselves generate at the surface of the oil bath. From this point of view, walkers are reminiscent of wave-particle duality [2, 6] and they seem to offer deep analogies with de Broglie-Bohm particles [7]. Up to now, different aspects of walker dynamics have been studied in a purely classical framework, typically in a hydrodynamical approach [3, 5]. Here in this chapter we study walker phenomenology in a quantum approach in which we propose experimental tests aimed at validating the relevance of BHN's and dBB's formalism in order to mimic the dynamics of droplets. This chapter is adapted from [8].

5.1 Wave particle duality at the macroscopic scale ?

5.1.1 Introduction

Walkers consist of oil droplets bouncing at the surface of a vibrating bath of oil (figure 5.1.1), excited at the edge of the Faraday resonance regime; the walkers are prevented from coalescing into the bath because the vibration creates an air film at the interface between the surface of the bath and the droplet. As was noted in [9], *...Walkers exhibit rich and intriguing properties.... For instance, when the walker passes through one slit of a two-slit device, it undergoes the influence of its "pilot-wave" passing through the other slit, in such a way that, after averaging over many trajectories, the interference pattern typical of a double-slit experiment is restored despite the fact that each walker passes through only one slit. The average trajectories of the drops exhibit several other quantum features such as orbit quantization [10], quantum tunneling, single-slit diffraction, the Zeeman effect and so on. Another surprising feature is a pseudo-gravitational interaction that has also been observed between two droplets [1]. ...*

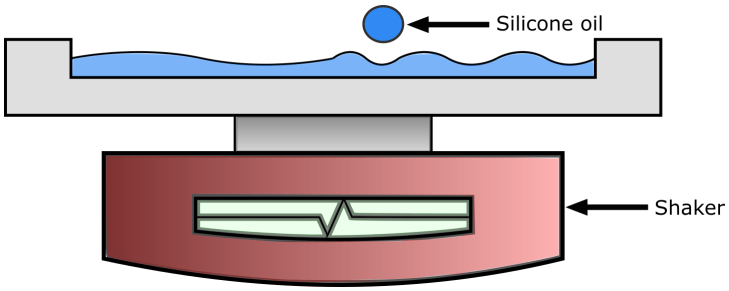

FIGURE 5.1: Illustration of the experimental setup.

These observations suggest that a 'fluidic', hydrodynamical formulation of wave mechanics is possible, in which the droplet would play the role of de Broglie's soliton, while the properties of the environmental bath are assigned to the pilot wave of de Broglie....

In view of these observations, de Broglie's original ideas have regained a certain prominence recently, since these walkers/bouncers were realized in the laboratory with artificial macroscopic systems. These unexpected developments not only show that de Broglie's ideas encompass a large class of systems, but they might in the future also allow us to build a bridge between quantum and classical mechanics, where ingredients such as nonlinearity, solitary waves and wave monism play a prominent role (see [9] for a review, and [11, 12] for an alternative approach). Certain models address their deformations due to their bouncing off the surface of the bath, in function of the density and viscosity of the oil and other parameters [5]. Other studies describe the dynamics of the surface waves that the walkers generate during the bouncing process, and how those waves in turn guide their trajectories. In these models, this complex behavior is characterized by a memory time which relates the dynamics of the walker bouncing at time t, to its successive bouncing positions in the past [13, 14]. The presence of such a memory effect establishes a first difference with quantum mechanics. Normally, in quantum mechanics, it is assumed that all results of any possible future measurements to be performed on a quantum system, are encapsulated in its present quantum state [15]: its wave function at the present time t. Droplets also transcend the most common interpretations of quantum theory which prohibit any description of the system in terms of instantaneous, classical-like, trajectories. Droplets and their trajectories are visible with the naked eye at any time and standard interpretations of quantum mechanics do not apply.

This is why we believe that it is necessary and worthwhile to adapt realist (causal) formalisms such as de Broglie-Bohm (dBB) dynamics[16, 17] or a stochastic version à la Nelson[18], to explore the analogy with quantum systems. This is the main motivation of the present chapter.

5.1.2 A quantum approach ?

To begin with, it is important to keep in mind that there is a fundamental difference between walker trajectories and quantum trajectories. The quantum description is intrinsically probabilistic and non-classical, while there exist regimes in which the trajectory of the walkers is indeed deterministic and classical (for example, when they bounce exactly in phase with the bath, they can be shown to follow straight lines at constant velocity [19, 20, 21, 22]). However, there also exist regimes in which a Brownian motion is superimposed on their flow lines (e.g. above the Faraday threshold), and other regimes where

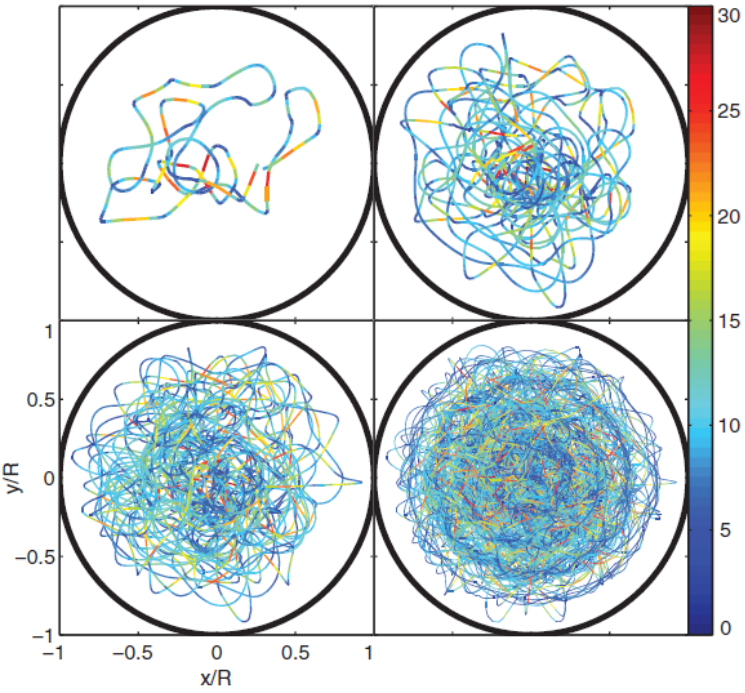

FIGURE 5.2: Figure adapted from [4], trajectory of a single droplet in a circular corral showing a wavelike statistics. The colorplot shows the norm of the velocity

the trajectories appear to be chaotic[5]. In fact, in several regimes droplets appear to exhibit ergodic behavior . In practice, ergodicity has been established on the basis of the following observations: if we prepare a walker at the surface of the liquid bath (a corral for instance), it will progressively explore each part of the surface, following an apparently random motion [4]. If one then visualizes the statistics of the sojourn time (see figure 5.2) of the walker in each of these regions, a striking pattern emerges, bearing more than a simple resemblance to an interference pattern[4, 7]. It is this, again remarkable, manifestation of wave-particle duality that first attracted our attention and which lies at the origin of this chapter. Here, it is worth noting that thus far there is no experimental evidence that droplets indeed follow de Broglie-Bohm and/or Nelson trajectories. Our approach therefore differs radically from previous studies on droplets, in the sense that we impose a quantum dynamic by brute force whereas, until now, the attempt to illustrate how chaos may underlie quantum stochasticity has been a pillar of the research on walkers/droplets. In particular, there exists (as far as we know) no way to derive an effective Schrödinger equation from hydrodynamical models of droplets.

By choosing exactly the opposite approach, i.e. by imposing quantum-like dynamics on the droplets, we pursue two goals. The first one is to formulate precise quantitative predictions regarding this relaxation process, which can possibly be validated by future experiments. A second objective is to show, for the first time, that certain dBB trajectories present a deep structural resemblance with certain trajectories that have been reported in the literature about droplets trapped in a harmonic potential. This constitutes a preliminary attempt, ultimately aimed at establishing a dynamics that would combine stochastic and/or dBB dynamics with a feedback of the trajectory on the wave, a problem which has never been addressed in the framework of dBB or BHN dynamics, but which is a fundamental feature of droplet phenomenology.

This is why droplets are appealing, because if their dynamics does present analogies with dBB dynamics, their study will allow us to observe relaxation to (quantum) equilibrium 'in real time' in the lab., with our naked eyes, which is not possible with quantum systems for which we have no direct access to individual trajectories. If one wants to investigate the onset of equilibrium in dBB dynamics, one obviously has to consider non-static asymptotic distributions since in static cases the dBB dynamics freezes the trajectories (as the phase of the wave function is then position independent). Even in the case of a coherent state (see section 3.4.1) the distribution of dBB positions would never reach equilibrium because it moves as a whole (as the shape of a coherent state remains the same throughout time). In a sense coherent states behave as solitary waves.

5.1.3 The quantum corral

It has been shown that the walkers can exhibit complex trajectories and periodic orbits can emerge. For example in [23] they simulated droplets trajectories in a circular geometry and they observed those periodic orbits emerging from their models (in figure 5.3a we adapted one of those orbits). It should be stressed that their model has been confronted to experimental observations. A result of a simulation in the case of the dBB dynamics can be seen in figure 5.3b where the numerical trajectory was obtained for a single particle starting from the initial position $(0, -0.1)$. We considered a superposition of $M = 3$ energy eigenstates (equally weighted with randomly-chosen initial phases θ_m) associated to the quantum corral which is described by the following wavefunction:

$$\Psi(r, \varphi, t) = \sum_{m=-1}^{1} C_m \, e^{i\,\theta_m - i\omega_{1,m}\,t} \, J_m\left(Z_{1,m}\,\frac{r}{R}\right) e^{-im\varphi}, \tag{5.1}$$

where $2R$ is the size of the box, C_m a complex coefficient, Z_{nm} is the n^{th} zero of J_m and $\omega_{nm} = \frac{\hbar}{2m}\left(\frac{Z_{nm}}{R}\right)^2$. Quantitatively those trajectories are very similar as can be seen in

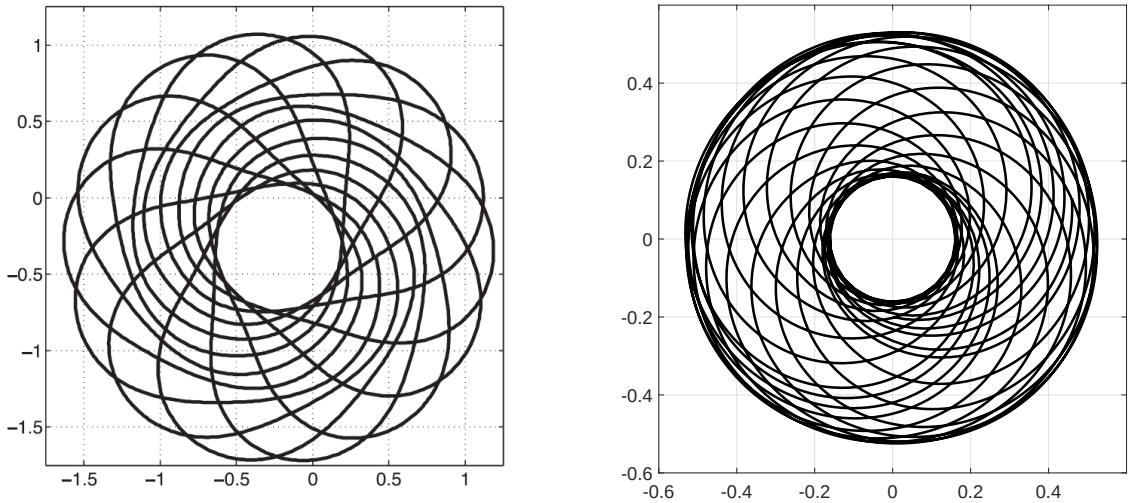

(A) Figure adapted from [23]. (B) de Broglie-Bohm trajectory.

FIGURE 5.3: Here we compare simulations of a trajectory for: (A) a droplet and (B) a dBB trajectory associated to (5.1).

figure 5.3. We shall now qualitatively describe this analogy in the case of the 2-D harmonic oscillator.

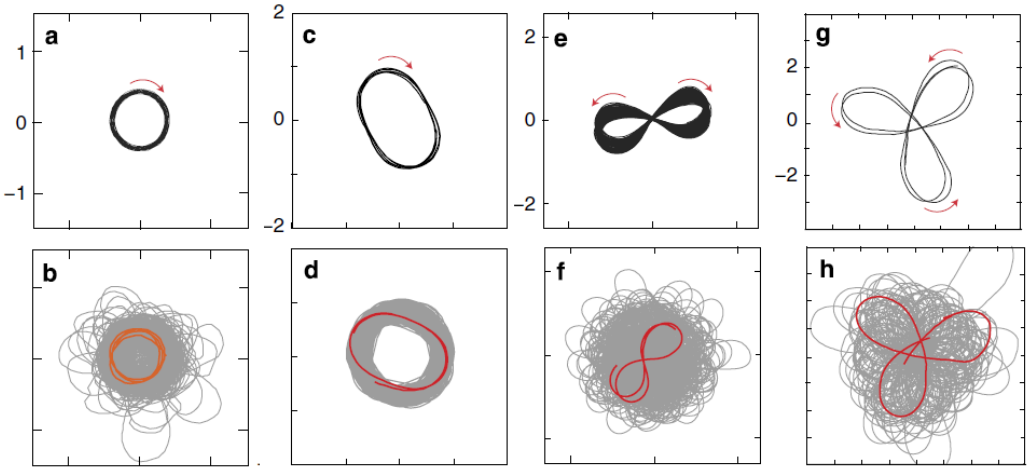

FIGURE 5.4: Figure adapted from [14], stable droplets trajectories observed for different quantized number (n, m). In figure: (a-b) circular orbit obtained for $(n = 1, m = \pm 1)$; (c-d) oval orbit obtained for $(n = 2, m = \pm 2)$; (e-f) the lemniscates for $(n = 2, m = 0)$ and (g-h) the trefoil for $(n = 4, m = \pm 2)$.

5.2 Dynamical model for droplets and double quantization of the 2-D harmonic oscillator

In this section we shall focus on the description of droplets dynamics as in [14, 10], for a magnetized droplet moving in an isotropic 2-D harmonic potential. We shall show that dBB dynamics allows us to reproduce some of the main features of the experimental observations (see figure 5.4). In [14, 10], it is reported that stable structures appear in the droplets dynamics whenever a double quantization condition is satisfied. The Hamiltonian of the isotropic 2-D harmonic oscillator [24] being invariant under rotations, we may indeed impose a double quantization constraint, requiring that the energy states of the 2D quantum harmonic oscillator are also eigenstates of the angular momentum. In polar coordinates, these states (which are parameterized by two quantum numbers, the energy number n and the magnetic number m) are expressed as follows[25]:

$$\psi_{n,m}(r,\theta,t) = \sqrt{\frac{a}{\pi}\frac{k!}{(k+|m|)!}}\, e^{-\frac{ar^2}{2}} \left(\sqrt{a}\, r\right)^{|m|} \mathcal{L}_k^{|m|}\left[a\, r^2\right] e^{-i\omega(n+1)t+im\theta} \tag{5.2}$$

where $\mathcal{L}_k^{|m|}$ are the generalized Laguerre polynomials and $k = \frac{n-|m|}{2}$. Note that these solutions are linear combinations of the product of solutions (3.61) in x and y. A first experimental result reported in [14] is the following: trajectories are chaotic and nearly unpredictable unless the spring constant of the harmonic potential takes quantized values which are strongly reminiscent of energy quantization (under the condition that, during the experiment, the size of the orbits is fixed once and for all). For quantized energies, in our case, it is given at $2D$ by $E_n = (n+1)\,\hbar\omega$, for some 'effective' value of $\hbar$ to be determined from actual experiments. Stable orbits appear to which one can attribute yet another quantum number, this time for the angular momentum, which is strongly reminiscent of the magnetic number (the eigenvalue of the orbital momentum, perpendicular to the surface of the vessel, is given by the product of $\hbar$ and m). In [14] (see figure 5.4) it is shown, for instance, that for the first excitation (n=1, $m = \pm 1$) droplet orbits are circular or oval, turning clockwise or anti-clockwise depending on the sign of m.

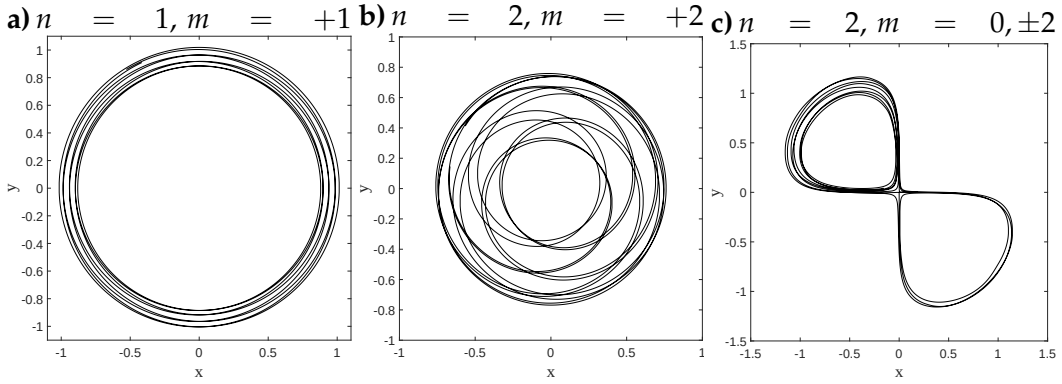

FIGURE 5.5: dB-B trajectories obtained for a single point particle in a superposition of eigenstates (5.3). Each plot is associated to a different combination (n, m), as indicated. In the graphs **(a,b)** we imposed $a = 1$, and $\omega = 1$, $\frac{\xi_0}{\xi_2} = 0.05$ and $\omega = 0.5$, $\frac{\xi_0}{\xi_3} = 0.05$ respectively ; for **(c)** we imposed $a = 3, \omega = 0.5$, $\frac{\xi_0}{\xi_3} = 0.0708$, $\frac{\xi_0}{\xi_2} = 0.0456$ and $\frac{\xi_0}{\xi_1} = 0.0773$.

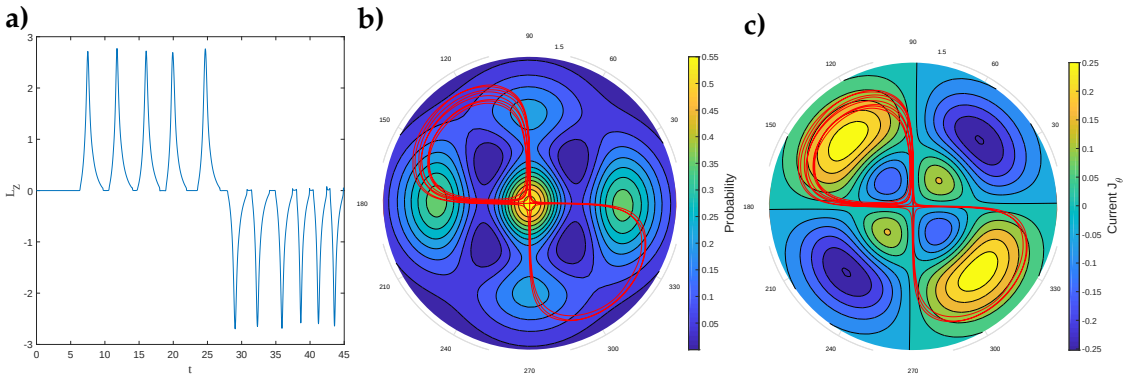

FIGURE 5.6: Plots of three quantities associated to the lemniscate in figure 5.5*c*. a) shows the L_z-component of the angular momentum and the polar plots b) and c) show the probability density $|\psi|^2$ (b) and the θ-component of the probability current (2.4) along the trajectory (c).

At the second energy level (n=2, $m = -2, 0, +2$), ovals appear again for $m = \pm 2$ and lemniscates for an average value angular momentum $< m >= 0$. At the fourth energy level (n=4, $m = -4, -2, 0, 2, 4$) trefoils appear (for $m = \pm 2$).

We simulated dBB trajectories, always considering a superposition of one of the aforementioned doubly quantized eigenstates $\psi_{n,m}$ with the ground state:

$$\Psi(r, \theta, t) = \xi_0 \, e^{-i\varphi_0} \, \psi_{0,0}(r, \theta, t) + \sum_{j=0}^{n} \xi_{j+1} \, e^{-i\varphi_{j+1}} \, \psi_{n,-n+2j}(r, \theta, t) \tag{5.3}$$

where φ_j and ξ_j are real numbers with $0 < \xi_0 \ll \xi_{j\neq 0}$. Computing the guidance relation (2.8) for a single eigenstate (5.2), one ends up with a value for ∇S for which the trajectories are circles of radius R around the origin, with tangential velocities proportional to m/R. In particular, the dynamics is frozen when $m = 0$.

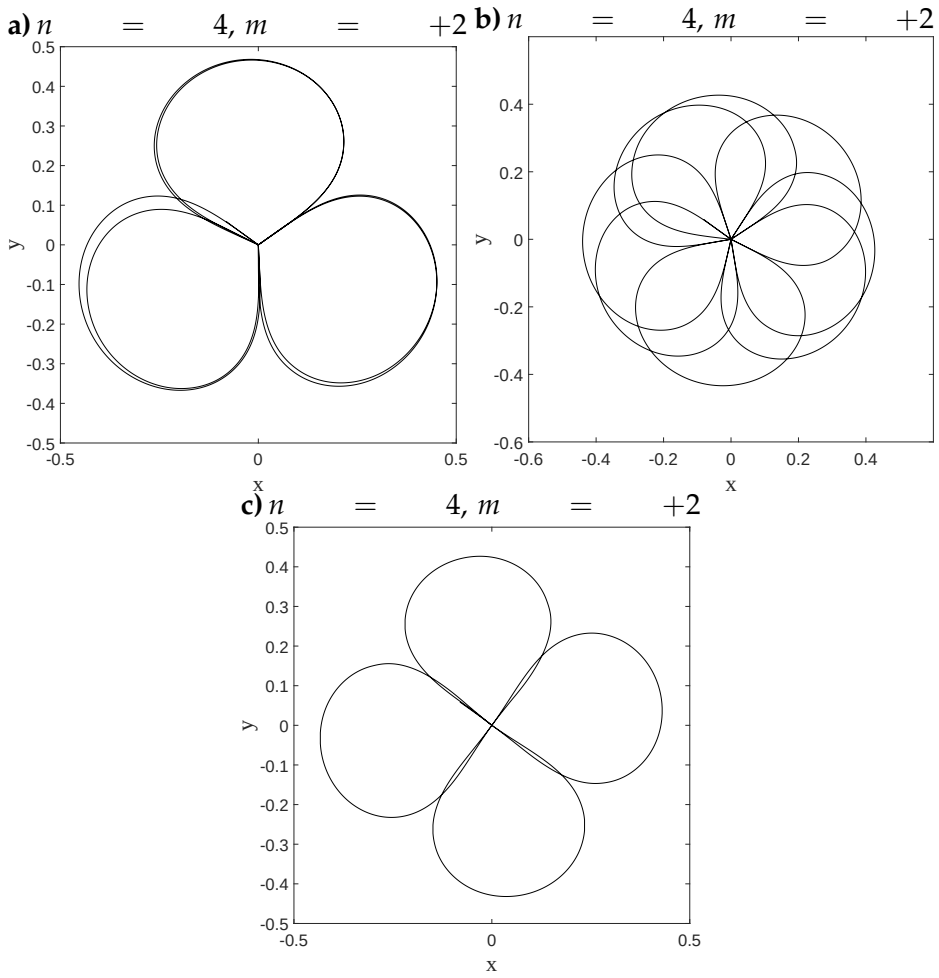

FIGURE 5.7: dB-B trajectories obtained for a single point particle in a superposition of eigenstates (5.3). Plots (a, b) correspond to $\omega = 0,7$ and $\omega = 1$ respectively. Case c is obtained after multiplying the amplitude of the $(n, m) = (4, 2)$ state by a complex phase ($e^{(0.3i)}$). We took $a = 1$ in all cases.

Mixing the wave function with the ground state, however, generates a periodic (in time) component in the dBB velocity field, which turns circular orbits into ovals when ξ_0 is small enough, and eventually generates more complex structures like rosaces.
We also tuned the energy difference between the ground state and the excited states such that two timescales characterize the dynamics. These are the "centrifugal" period, necessary for drawing a full circle around the origin, which varies as m/R^2, and the "Bohr" period which varies like $T/(n+1)$, where T is the classical period of the oscillator. Tuning these parameters we were able to simulate dBB trajectories very similar to those reported in [14]. For instance, we found circles and ovals (see figures 5.5 a, b) for $(n, m) = (1, 1)$ and $(n, m) = (2, 2)$. Note that the lemniscate cannot be obtained with a superposition of the ground state and the $(n, m) = (2, 0)$ state for which dBB velocities are necessarily purely radial, contrary to the suggestion made in[14], but rather should be generated with a superposition of the ground state with $(n, m) = (2, +2), (2, -2)$ and $(2, 0)$ in which the weights of the $m = +2$ and -2 components are slightly different (see figure 5.5 c). Figure 5.6 shows further detail of the evolution along this trajectory.

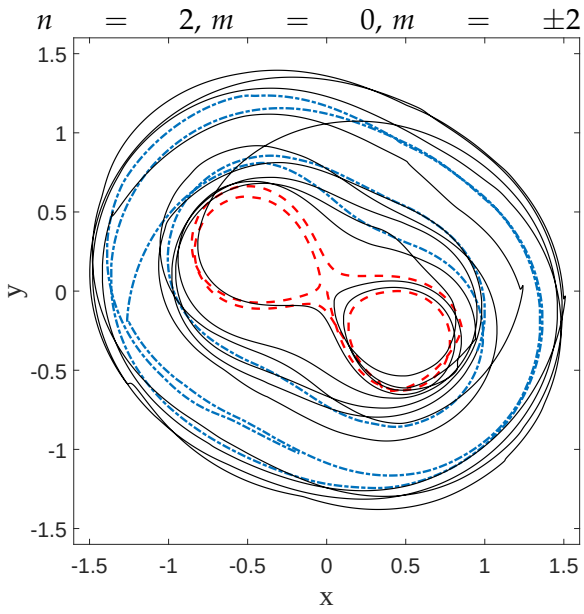

FIGURE 5.8: dB-B trajectories obtained for a single point particle in a superposition of eigenstates (5.3) showing intermittent transitions between two types of trajectories. The relevant parameter values are $\omega = 0.2$, $a = 1$ and $\frac{\xi_0}{\xi_3} = 0.0342$, $\frac{\xi_0}{\xi_2} = 0.2547$ and $\frac{\xi_0}{\xi_1} = 0.0505$.

Tuning the energy, we were also able to generate a trefoil and a "rosace" (see figure 5.7). It is worth noting however that chaos is omnipresent in the dBB dynamics for this system, in the sense that the trajectories exhibit an extreme sensitivity to the initial conditions, which explains why these dBB orbits mimicking stable droplets orbits are in general unstable. For instance, figure 5.8 shows intermittent transitions between an oval trajectory and a lemniscate (as has also been reported in [14]), for a superposition of the ground state with the $(n, m) = (2, +2), (2, -2)$ and $(2, 0)$ states. Preliminary results furthermore show that the trajectories are also unstable under BHN dynamics, i.e. in the presence of "noise", whenever this noise (parameterized by α in (3.5)) exceeds a critical value. Therefore, although our approach might not explain all details of the double quantization reported in [14], it does reproduce many of its essential features and we believe it would be very interesting to be able to deepen this analogy. For instance, having access to the empirical values of the weights of the ground state, or of the effective values of $\hbar$ and of the mass in the case of droplets would allow us to test our model in real detail.

Another experiment, reported in [26], during which both the position of the droplet and the excitation of the bath are monitored, and where a superposition between two distinct modes of the bath is reported, could also provide more insight and might offer some means to test the validity of our model: using exactly the same observation device, but this time in the case where the droplet undergoes a 2-D isotropic potential, would allow one to check whether the modes of the bath are similar to the (n, m) quantum modes which we associate with the quantized droplets trajectories.

5.3 BHN dynamics: a phenomenological dynamical model for walkers?

5.3.1 Predictions in the 2D harmonic oscillator

It is therefore interesting to compare predictions that we, on our side, can make in the framework of BHN dynamics, with actual experimental observations of droplets dynamics[1]. To our mind, one important comparison to make concerns the convergence to equilibrium.

For example, if the initial distribution of positions projected along a reference axis, say X, fits a mixture of the ground state and the nth Fock state ($n = 1, 2 \cdots$) for the 2D harmonic oscillator (conveniently weighted in order to respect the ineluctable constraint of positivity), our Nelson-like model predicts that the typical time of convergence to equilibrium will scale like the inverse of the eigenvalue of the nth Fock state, i.e. as $1/n$, which constitutes a very precise quantitative prediction. This follows from the representation (3.53), when $\sqrt{P_{st}(x)}$ is the Gaussian ground state of the 1D harmonic oscillator and where the eigenfunctions g_k are the Fock states given in (3.60) (this, of course, because of the separability of the Schrödinger equation and of our Nelson dynamics along X and Y in the case of an isotropic 2D oscillator).

A possible way to measure this characteristic time would be to record the projections along X of trajectories that correspond to an equally spaced grid of initial positions, weighted such as to fit a mixture of the ground state with the nth Fock state ($n = 1, 2 \cdots$), and to compare the histogram constructed in this way at different times with theoretical predictions derived from (3.53).

Another precise quantitative (theoretical) prediction, which is even simpler to verify, is that if we prepare a droplet many times at exactly the same initial position, the position obtained after averaging over all trajectories will (1) decrease exponentially in time and (2) be characterized by a decay time which scales like $1/a\alpha$, by virtue of the discussion in section 3.3.6 and in particular equation (3.79).

It has been suggested that droplet trajectories might be characterized by a quantum-like Zitterbewegung, which can be seen in relativistic quantum dynamics as an intrinsic brownian motion at the Compton scale [28, 29] and various proposals have been formulated in order to express the amplitude and frequency of this Zitterbewegung [5, 30] in terms of the parameters characterizing droplet dynamics. Exploring these analogies in depth lies beyond the scope of this thesis, but the aforementioned attempts, obviously, pave the way for relating brownian motion to droplet trajectories.

5.3.2 Presence of zeros in the interference pattern

One of our first motivations, when we decided to incorporate a Brownian component in the dBB theory in order to simulate the dynamics of droplets, was the pioneering paper [4] reporting on observations of a walker trapped in a spherical 2D cavity (corral), for which the histogram of positions occupied over time by a single droplet trajectory faithfully reproduces the Bessel function J_0[2] (see figure 5.2).

[1] See [27] for a pioneering work very similar to ours in the case of the double slit experiment.

[2] Which is also related to the Green function of the Helmholtz equation, with a typical length equal to the Faraday wave length of the vibrating bath over which droplets propagate [21].

These observations reveal, in a telling way, the presence of a pilot-wave that guides the dynamics of the particles, and also raise the question of ergodicity.

If we try the approach we used for the 2D harmonic oscillator in the case of the corral (effectively replacing the Gaussian ground state of the 2D harmonic oscillator by the zero order Bessel function), we are immediately confronted with problems caused by the presence of zeros in the Bessel function. Certain formal methods aimed at solving the Fokker-Planck equation (such as those introduced in section 3.3.6) are only relevant when the pilot wave possesses no zeros. In particular, the eigenvalues $-\lambda_k$ of the Fokker-Planck operator (3.50) are not always negative when zeros are present, which of course would menace the stability of the relaxation process. However, as we already indicated in section 3.2, although the effect of zeros of the pilot wave in our Nelson dynamics is by no means trivial, there are several observations that indicate that this problem is not really crucial.

First of all, as mentioned in section 3.2, the Wiener process makes it in principle possible to "jump" over the zeros of the equilibrium distribution. This has actually been confirmed in numerical simulations for the case of the 1D harmonic oscillator, where we imposed that the equilibrium distribution P_{st} is the square modulus of the first excited (Fock) state (3.60), with amplitude:

$$P_{st} = |\Psi_{st}|^2 = |\Psi_1(x,t)|^2 = \left(\frac{2a}{\pi}\right)^{\frac{1}{2}} \left(a\,x^2\right) e^{-2ax^2}. \tag{5.4}$$

Indeed, as can be clearly seen from Figure 5.9, the particle will, from time to time, jump over the zero in the middle (with the same probability from left to right as in the opposite direction), in such a way that finally the trajectory covers the full real axis, while the histogram of positions faithfully reproduces the quantum prediction $P_{st} = |\Psi_{st}|^2 = |\Psi_1(x,t)|^2$. This indicates that even in the presence of a zero in the equilibrium distribution, the relaxation process is still ergodic. The relaxation of a uniform initial distribution to this quantum equilibrium is shown in Figure 5.10, for the quantities H_V, L_f and L_1.

A second indication that the problem posed by the presence of zeros is not so serious, stems in fact from the experimental observations. Indeed, if we study the observations reported in [4] for the case of a corral, it is clear that the minima of the histogram expressing the distribution of positions of the droplet are in fact not zeros. This, undoubtedly, due to the presence of a non-negligible residual background. Actually, without this background, the droplet would never pass between regions separated by zeros: due to the rotational symmetry of the corral, the zeros form circles centered at the origin and the position histogram obtained from a trajectory would remain confined to a torus comprising the initial position. This, however, is clearly not the case. Which then suggests the following strategy: to simulate BHN dynamics with a static distribution $P_{st} = |\Psi_{st}|^2$ given by the Bessel function J_0 but supplemented with a constant positive background ϵ,

$$d\mathbf{x}(t) = \frac{\alpha}{2} \frac{\boldsymbol{\nabla} J_0(r)^2}{J_0(r)^2 + \epsilon}\, dt + \sqrt{\alpha} d\boldsymbol{W}(t). \tag{5.5}$$

In this case, the singularities of the Fokker-Planck equation automatically disappear and, despite the fact that we have no analytic expression for the solutions as in the case of the ground state of the harmonic oscillator, we are able to numerically simulate BHN dynamics without difficulty. The results of these simulations are shown in Figure 5.11.

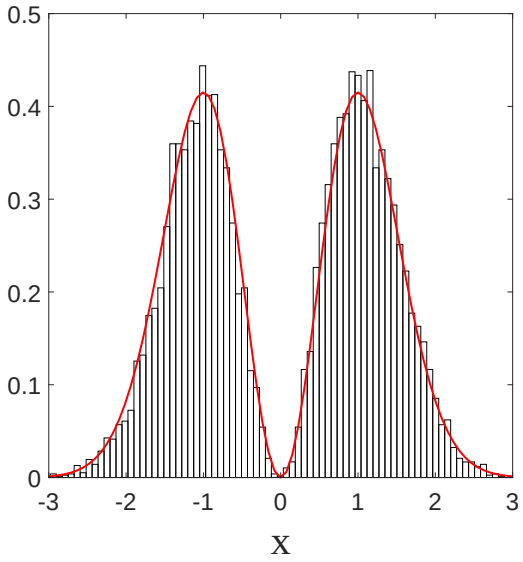

FIGURE 5.9: Histogram of the positions in x of a single particle, in the case of the first fock state (5.4). The full curve (red) corresponds to the quantum probability $|\Psi_1|^2$. Here $a = 0.5$ and $\alpha = 1$. The total simulation time t is $t = 1000$ and the sampling time step is $\Delta t = 0.01$. The initial position is $x_i = 1$ and the number of bins $N_b = 75$, each with width $\Delta x = 0.08$.

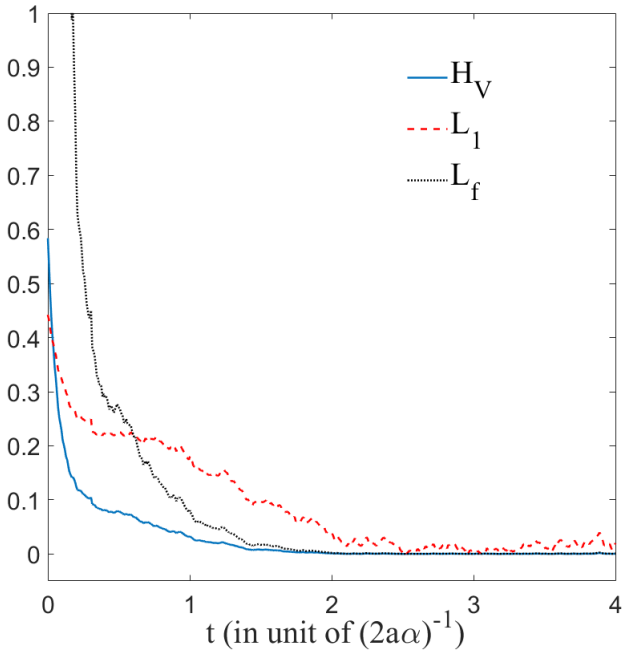

FIGURE 5.10: Evolution in time of H_V (3.9), L_f (3.10) and of the L_1 (3.21) norm, for a uniform initial probability distribution, showing the relaxation towards the distribution of the first excited state $|\Psi_1|^2$ (5.4). The simulation is performed for $\alpha = 1$, $a = 0.5$, $\Delta t = 0.01$ and from 20 000 uniformly distributed initial conditions.

The osmotic velocity in the BHN dynamics clearly tends to bring back the particle to regions where $|\Psi|^2$ has extrema and the resemblance with the plot on the left is striking.

The fact that this result again does not depend on the choice of initial condition strongly suggests that the relaxation process to quantum equilibrium is also ergodic in this case.

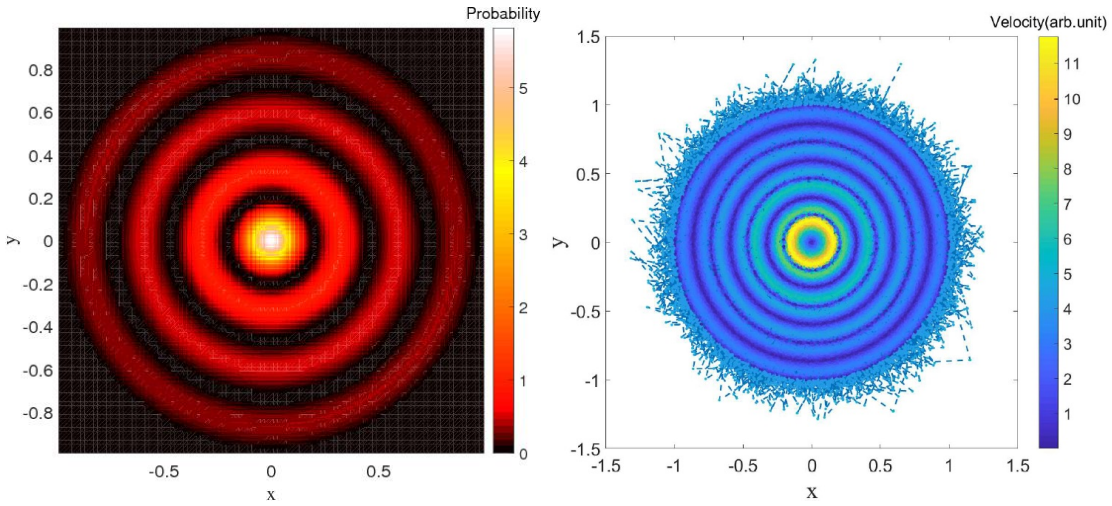

FIGURE 5.11: Left: The quantum probability associated to the Bessel function of the first kind J_0. Right: Color plot of the velocities reached along the trajectory for an evolution corresponding to (5.5). The initial position was $(1,1)$, the simulation time $t = 5\,000$ and the sampling time step $\Delta t = 0.005$. We chose $\alpha = 0.1$, $\epsilon = 0.2$ and the size of the domain is $L = 2$. On the boundary we impose a harmonic field force of the form: $-2a\alpha\,\mathbf{r}$.

5.3.3 Effective dynamics

One could even conceive dynamical models "in-between" BHN, dBB and classical dynamics, characterized by two monitoring parameters (e.g. one parameter (ϵ) quantifying the degree of classicality [31, 32] and another one (ϵ') quantifying the degree of noise [33] as :

$$dx = (1-\epsilon)\left(\left[\frac{1}{m}\boldsymbol{\nabla}S + \epsilon'\,\frac{\alpha}{2}\,\frac{\boldsymbol{\nabla}|\Psi|^2}{|\Psi|^2}\right]\Big|_{x=x(t)} dt + \sqrt{\alpha\epsilon'}\,d\boldsymbol{W}(t)\right) + \epsilon\, V_{classical}\,dt, \qquad (5.6)$$

This idea is illustrated in figure (5.12) where we show trajectories obtained in the case of the double slit experiment, ranging from a quantum behavior (with noisy dB-B trajectories à la Nelson, see [27] for a similar work) to a purely classical, noiseless behavior (with straight line [19, 20, 21, 22])) passing through an in-between region where superpositions are still present. In order to compute classical trajectories, we associated for each position a normally distributed random velocity. We established the histograms of the distribution of positions on the arrival after a time 0.3 (in dimensionless units). The average value as well as the standard deviation of the distribution of classical velocities have been chosen in such a way that the spread of the resulting classical probability has approximately the same order of magnitude as the quantum (Nelson) one. We chose $x_s = 1$, $\sigma = 0.15$, $\Delta t = 0.001$ and $\nu = 0.5$. Figures (5.12) respectively correspond to the choices $\epsilon' = 1$ and $(\epsilon = 1, \epsilon = 1/2, \epsilon = 0)$. This model could maybe explain qualitatively why interference effects are observed [1] in certain double slit experiments performed with droplets and absent in others [34, 35] (see [36] for a review).

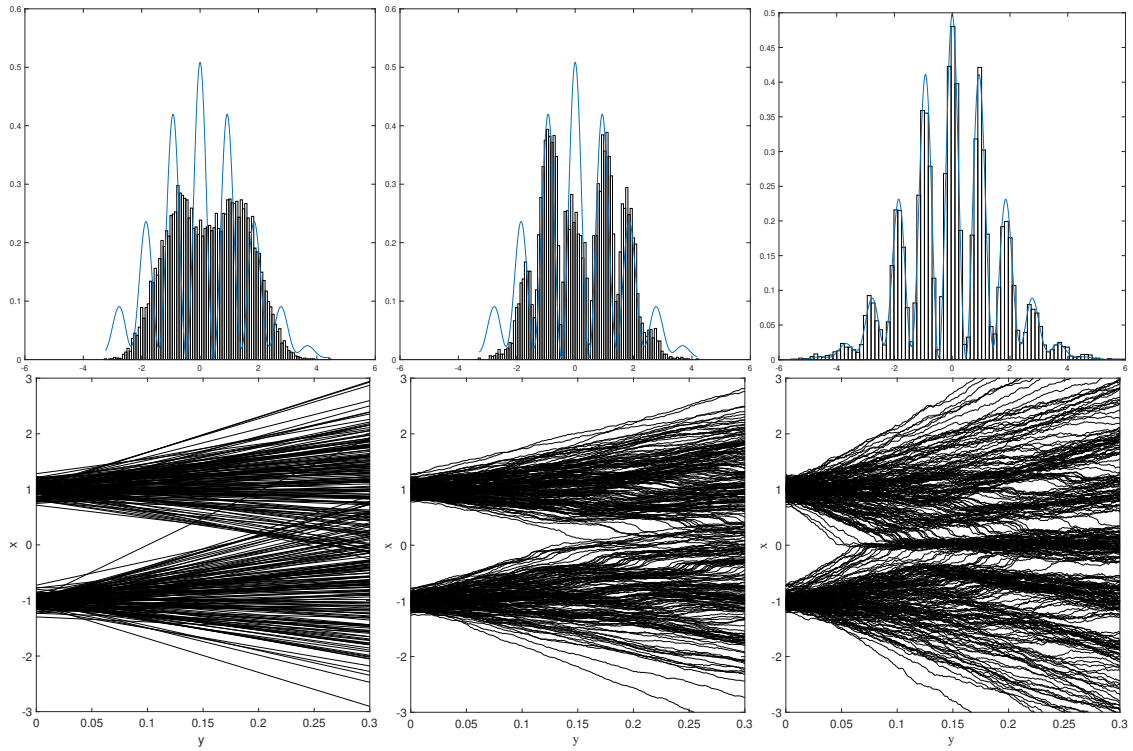

FIGURE 5.12: Numerical simulations of the double-slit experiment: classical trajectories (right), and distribution of arrivals on a screen (left). The curve (blue) corresponds to the quantum probability $|\Psi|^2$.

5.3.4 Discussion

Finally, it is worth recalling some of the problems that arose when, first de Broglie, and then Bohm and Nelson developed their theories aimed at deriving quantum dynamics (statistics) as an emergent property, i.e., resulting from an underlying "hidden" dynamics. The most severe problem is undoubtedly non-locality, which was recognized by Bohm[16, 17] to be an irreducible feature of dBB dynamics (see also[37, 38] for similar conclusions concerning Nelson-type dynamics). Today, under the influence of the work of John Bell [39] and his followers, it is widely recognized that quantum theory is irreducibly non-local, which makes it particularly difficult to mimic with classical models. Another problem concerns the fact that the pilot wave is a complex function. This poses still unresolved problems in the case of BHN dynamics because Nelson's diffusion process does not make it possible to fix the phase of the wave function unequivocally[40, 41].

In our approach, which is mainly of quantum inspiration, complex wave functions and imaginary phases appear spontaneously, but if we wish to scrutinize the link with the empirically observed modes at the surface of oil baths [14, 10, 30, 26], it will be important to interpret the exact meaning of this complex phase.

5.4 Conclusion

In this chapter we studied stochastic, Nelson-like dynamics (BHN), as well as dBB dynamics, with the aim of simulating the dynamics of droplets. The stochastic approach has the merit that it explicitly takes into account the influence of noise on the dynamics [42, 43]. In contrast to certain experiments where noise is considered to be a parameter that should be minimized, here, noise is considered to be a relevant parameter for the dynamics (see also [27]). For instance, as we have shown, it plays an essential role in the relaxation towards equilibrium and in the ergodicity of the dynamics. In the dBB approach, on the other hand, the main ingredient is the chaotic nature of the dynamics [44]. Both models thus shed a different light on the dynamics and could possibly fit diverse set of regimes in droplets dynamics. Ultimately, experiment ought to indicate whether it is relevant, regarding droplets phenomenology, to formalize the dynamical influence of noise à la Bohm-Hiley-Nelson as we did in the present section. We actually formulated several proposals in this sense in section 5.3.1. As we also emphasized throughout the present chapter, our models should be seen as a first step in the direction of a dynamical model, still to write, combining Nelson's stochastic dynamics (and/or dBB dynamics) and memory effects. To conclude, in our view, the programs that aim at simulating droplet dynamics with quantum tools or at describing the emergence of quantum dynamics based on droplet dynamics, are still largely incomplete and raise challenging fundamental questions. This Pandora box is now open and it will not be closed soon, which is however not something to be feared as it offers new and stimulating perspectives for future research in the field.

Bibliography

[1] Y. Couder and E. Fort. Single-particle diffraction and interference at a macroscopic scale. *Phys. Rev. Lett.*, 97:15410, 2006.

[2] Y. Couder, A. Boudaoud, S. Protière, and E. Fort. Walking droplets, a form of wave-particle duality at macroscopic scale? *Europhysics News*, 41(1):14–18, 2010.

[3] Y. Couder, S. Protière, E. Fort, and A. Boudaoud. Dynamical phenomena: walking and orbiting droplets. *Nature*, 437:208, 2005.

[4] Daniel M Harris, Julien Moukhtar, Emmanuel Fort, Yves Couder, and John W.M. Bush. Wavelike statistics from pilot-wave dynamics in a circular corral. *Phys. Rev. E.*, 88:011001, 2013.

[5] John W M Bush. Pilot-wave hydrodynamics. *Annu. Rev. Fluid Mech.*, 47:269–292, 2015.

[6] Y. Couder and E. Fort. Probabilities and trajectories in a classical wave-particle duality. *J. Phys.: Conf. Ser.*, 361:012001, 2012.

[7] John W. M. Bush. The new wave of pilot-wave theory. *Physics Today*, 68(8):47, 2015.

[8] Mohamed Hatifi, Ralph Willox, Samuel Colin, and Thomas Durt. Bouncing oil droplets, de broglie's quantum thermostat, and convergence to equilibrium. *Entropy*, 20(10):780, 2018.

[9] S. Colin, T. Durt, and R. Willox. L. de Broglie's double solution program: 90 years later. *Annales de la Fondation Louis de Broglie*, 42:19, 2017.

[10] Matthieu Labousse, Anand U Oza, S. Perrard, and J. W.M. Bush. Pilot-wave dynamics in a harmonic potential: Quantization and stability of circular orbits. *Physical Review E*, 93(3):033122, 2016.

[11] Christian Borghesi. Dualité onde-corpuscule formée par une masselotte oscillante dans un milieu élastique: étude théorique et similitudes quantiques. *arXiv preprint arXiv:1609.09260*, 2016.

[12] Christian Borghesi. Equivalent quantum equations with effective gravity in a system inspired by bouncing droplets experiments. *arXiv preprint arXiv:1706.05640*, 2017.

[13] Antonin Eddi, Eric Sultan, Julien Moukhtar, Emmanuel Fort, Maurice Rossi, and Yves Couder. Information stored in Faraday waves: the origin of a path memory. *Journal of Fluid Mechanics*, 674:433–463, 2011.

[14] Stéphane Perrard, Matthieu Labousse, Marc Miskin, Emmanuel Fort, and Yves Couder. Self-organization into quantized eigenstates of a classical wave-driven particle. *Nature communications*, 5:3219, 2014.

[15] Thomas Durt. Do dice remember? *International journal of theoretical physics*, 38(1):457–473, 1999.

[16] David Bohm. A Suggested Interpretation of the Quantum Theory in Terms of "Hidden" Variables. I. *Phys. Rev.*, 85(2):166–179, 1952.

[17] David Bohm. A Suggested Interpretation of the Quantum Theory in Terms of "Hidden" Variables. II. *Phys. Rev.*, 85(2):180–193, 1952.

[18] Edward Nelson. Dynamical Theories of Brownian Motion. *Mathematical Notes*, 131(6):2381–2396, 1967.

[19] Matthieu Labousse. *Etude d'une dynamique à mémoire de chemin: une expérimentation théorique*. PhD thesis, Université Pierre et Marie Curie UPMC Paris VI, 2014.

[20] Emmanuel Fort, Antonin Eddi, Arezki Boudaoud, Julien Moukhtar, and Yves Couder. Path-memory induced quantization of classical orbits. *Proceedings of the National Academy of Sciences*, 107(41):17515–17520, 2010.

[21] Rémy Dubertrand, Maxime Hubert, Peter Schlagheck, Nicolas Vandewalle, Thierry Bastin, and John Martin. Scattering theory of walking droplets in the presence of obstacles. *New Journal of Physics*, 18(11):113037, 2016.

[22] Loic Tadrist, Jeong-Bo Shim, Tristan Gilet, and Peter Schlagheck. Faraday instability and subthreshold faraday waves: surface waves emitted by walkers. 2017.

[23] Anand U Oza, Øistein Wind-Willassen, Daniel M Harris, Rodolfo R Rosales, and John WM Bush. Pilot-wave hydrodynamics in a rotating frame: Exotic orbits. *Physics of Fluids*, 26(8):082101, 2014.

[24] YF Chen, YP Lan, and KF Huang. Observation of quantum-classical correspondence from high-order transverse patterns. *Physical Review A*, 68(4):043803, 2003.

[25] Diu B. Cohen-Tannoudji, C. and F. Laloe. *Quantum Mechanics*. Wiley, 1977.

[26] Cristea-Platon T. Sáenz, P.J. and J. Bush. Statistical projection effects in a hydrodynamic pilot-wave system. *Nature*, 14:3, 2017.

[27] Gerhard Grössing. Sub-quantum thermodynamics as a basis of emergent quantum mechanics. *Entropy*, 12(9):1975–2044, 2010.

[28] D. Hestenes. The zitterbewegung interpretation of quantum mechanics. *Founds. of Phys.*, 20:10, 1990.

[29] S. Colin and H. M. Wiseman. The zig-zag road to reality. *J. Phys. A: Math. Theor.*, 44(34):345304, 2011.

[30] T. Gilet. Quantumlike statistics of deterministic wave-particle interactions in a circular cavity. *Phys. Rev. E*, 93:042202, 2016.

[31] Hideo Nitta and Tomoshige Kudo. Time of arrival of electrons in the double-slit experiment. *Physical Review A*, 77(1):14102, 2008.

[32] Partha Ghose. A continuous transition between quantum and classical mechanics. I. *Found. Phys.*, 32(6):871–892, 2002.

[33] Mark Davidson. A generalization of the Fényes-Nelson stochastic model of quantum mechanics. *Letters in Mathematical Physics*, 3(4):271–277, 1979.

[34] Anders Andersen, Jacob Madsen, Christian Reichelt, Sonja Rosenlund Ahl, Benny Lautrup, Clive Ellegaard, Mogens T Levinsen, and Tomas Bohr. Double-slit experiment with single wave-driven particles and its relation to quantum mechanics. *Phys. Rev. E*, 92:013006, 2015.

[35] Tomas Bohr, Anders Andersen, and Benny Lautrup. Bouncing droplets, pilot-waves, and quantum mechanics. In *Recent Advances in Fluid Dynamics with Environmental Applications*, pages 335–349. Springer, 2016.

[36] Giuseppe Pucci, Daniel M Harris, Luiz M Faria, and John W M Bush. Walking droplets interacting with single and double slits. *Journal of Fluid Mechanics*, 835:1136–1156, 2018.

[37] D. Bohm and B. Hiley. Non-locality and locality in the stochastic interpretation of quantum mechanics. *Physics Reports*, 172(3):93–122, 1989.

[38] E. Nelson. Review of stochastic mechanics. *J. of Phys.: Conf. Ser.*, 361:012011, 2012.

[39] J.S. Bell. On the EPR paradox. *Physics*, 1:165, 1964.

[40] Guido Bacciagaluppi. A Conceptual Introduction to Nelson's Mechanics. In *Endophysics, time, quantum and the subjective*, pages 367–388. R. Buccheri, M. Saniga, A. Elitzur (eds), World Scientific, 2005.

[41] T. Wallstrom. Inequivalence between the Schrödinger equation and the Madelung hydrodynamic equations. *Phys. Rev. A*, 49:1613, 1994.

[42] T. Durt. L. de Broglie's double solution and gravitation. *Annales de la Fondation Louis de Broglie*, 42:73, 2017.

[43] M. Hatifi, C. Lopez-Fortin, and T. Durt. De Broglie's double solution: limitations of the self-gravity approach. *Annales de la Fondation Louis de Broglie*, 43:63, 2018.

[44] C. Efthymiopoulos, G. Contopoulos, and A. C. Tzemos. Chaos in de Broglie - Bohm quantum mechanics and the dynamics of quantum relaxation. *Ann. Fond. de Broglie*, 42:133, 2017.

Part II

Part II: Non-linearity in Quantum mechanics

Chapter 6

Semi-classical gravity: the Schrodinger-Newton equation

"Faut mettre des chiffres maintenant."

Thomas DURT

Summary In this chapter we introduce the Schrodinger-Newton equation [1, 2, 3, 4, 5, 6, 7, 8], an integro-differential non-linear equation derived from a semi-classical approximation of gravity. The model has been initially proposed as a possible non-linear generalization of the quantum dynamics which might, among other things, solve the measurement problem (that will be briefly discussed in section 6.1.2). In particular, we will see that the idea of a non-linear underlying theory can be related to the double solution program proposed by Louis de Broglie [9, 10]. We shall apply this program (section 6.2) in the framework of the Schrodinger-Newton equation for the purpose of deriving a generalized guidance equation for this non-linear dynamic. In chapter 7 we will also propose two experiments aiming at testing the Schrodinger Newton equation. This chapter is adapted from [11].

6.1 Non-Linearity and Quantum Mechanics

6.1.1 Introduction and motivation

In classical mechanics, it is usual to consider point particles when we describe the motion of macroscopic systems. On the other hand, the standard quantum theory says that even a macroscopic system like a cat can be in a superposition of distant localized states. Since the theory is linear at all scales, there is a priori no reason that the superposition principle doesn't hold for macroscopic systems. However, this is not in accordance with what we experiment in our daily life, i.e. all the macroscopic objects are well localized in space. This problem finds origin in the linearity of the Schrodinger equation. In addition, the Schrodinger equation can be seen as a heat-like equation with an imaginary diffusion coefficient. Hence, a particle is described by a wave function which tends to spread over time so that it is difficult to explain why particles remain sharply localized in space as we are used to observe in the macroscopic scale. The linearity is actually at the foundation of the measurement problem.

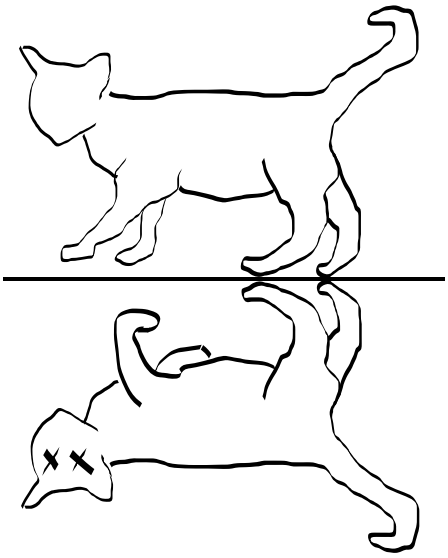

FIGURE 6.1: The paradox due to the linearity of the Schrodinger equation is illustrated here with the famous macroscopic superposition of the Schrodinger cat, i.e. the cat is both alive and dead.

6.1.2 The measurement problem

As already discussed in part I, the double-slit experiment suggests that quantum particles behave like waves. However, when a quantum measurement is performed, the particle is found to be in a unique position. According to the standard interpretation, it means that the probability is instantaneously collapsing into a dirac delta function centered in the position of the measured particle. Consequently, because of the non-linear character of the collapse, after the measurement, the probability is no longer a superposition of solution of the linear Schrodinger equation. In figure (6.2), we illustrate the measurement problem in the simple case of a qubit made by a superposition of the two possible outcomes $|a_1\rangle$ or $|a_2\rangle$ (it can be for example, the spin of an electron or the energy levels of a two-level atom). Before the measurement, because of the linearity of the Schrodinger equation, any linear combination of the form:

$$|\Psi\rangle \propto \alpha\ |a_1\rangle + \beta\ |a_2\rangle \tag{6.1}$$

is also a solution. However, after the measurement of the state it is only possible to obtain experimentally either the eigenvalue:

$$a_1 \text{ with a probability } \frac{|\alpha|^2}{(|\alpha|^2+|\beta|^2)} \text{ or the eigenvalue } a_2 \text{ with a probability } \frac{|\beta|^2}{(|\alpha|^2+|\beta|^2)}.$$

Hence, the superposition principle which is at the core of the linearity is no longer valid. It leads to a paradoxical interpretation of the measurement in which the Schrodinger wave seems to be affected by the measurement itself. A large majority of physicists simply accepted the probabilistic interpretation as enough satisfactory even if it does not solve that problem.

To conclude, the non-linear character of the collapse suggests to consider the existence of a possible nonlinear underlying theory.

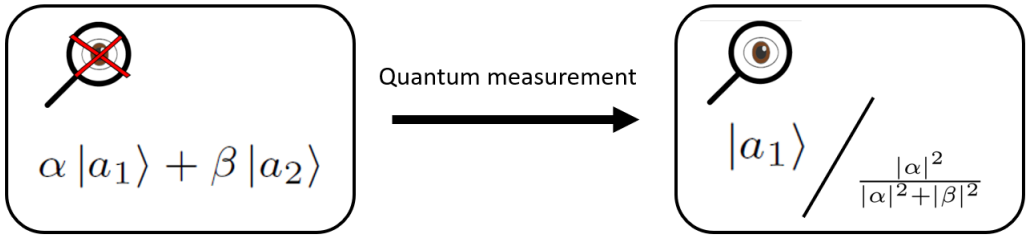

FIGURE 6.2: Measurement

Following this line of thought several physicist[1] in the past wondered if it was possible to modify nonlinearly the unitary Schrodinger evolution (and if it yes how to do it properly).

6.1.3 A first attempt of non-linear quantum theory: the self-gravity approach

The irreducibly linear nature of Schrödinger equation is still an open question today. As far as we know, no fundamental non-linearity has been detected yet at the quantum level and the superposition principle is usually accepted to be a universal principle with the status of a law of Nature. There even exist no-go theorems [16, 15] aimed at proving that linearity is the price to pay to preserve Einsteinian causality (subsection 7.4), which is another pillar of modern physics. At the other side, non-linear generalizations of the (otherwise linear) Schrödinger equation pave the way to realistic solutions of the measurement problem in full accordance with de Broglie's double solution program [17, 18, 19]. The basic idea underlying this approach is that non-linearity would be at the source of the so-called collapse process (this question will be discussed in chapter 7), ultimately explaining the corpuscular properties exhibited by quantum systems. Following this line of thought, self-gravity (in its commonly accepted formulation [7, 20, 1, 8, 2, 3, 4, 5, 6]) is particularly promising because it enables to predict that the micro-macro (quantum-classical) transition occurs for objects having a mass above say 10^9 a.m.u. [1]. For lighter objects (atoms, molecules, small aggregates) self-gravity is however predicted to be so weak that no measurable violation of the superposition principle is possible, in agreement with all experimental data collected so far. For sufficiently massive objects (having a mass above 10^9 a.m.u.), the non-linearity activated by self-gravity is in principle sufficiently strong for localizing the wave function of the quantum object in a region small compared to its physical size, in which case the object behaves as a localized particle, which is one of the goals of de Broglie's double solution program [21, 19]. Of course, in this approach, the double solution program is, contrary to de Broglie's original formulation, not realized for ALL objects: it would work only if the object is massive enough. Another problem in orthodox self-gravity., regarding the realization of de Broglie's program, is that there is no double solution: either the wave function is self-collapsed and then it is no longer a solution of the linear Schrödinger equation, or it fulfills the linear equation which means that self-gravity is so weak that it can consistently be neglected.

[1] Since 1927, there were few attempts to consider non-linear modifications of the Schrodinger, for example [12, 13, 14, 15]

de Broglie actually faced a similar dilemna in 1927 which brought him to formulate the guidance condition [18] according to which corpuscles/solitons follow the de Broglie-Bohm guidance equation, but there is no indication that this principle is valid in the framework of orthodox self-gravity[2].

6.1.4 The Schrodinger-Newton equation

It is common in the literature to represent quantum effects due to self-gravitation through the Schrödinger-Newton equation [1, 2]

$$i\hbar\frac{\partial\Psi(t,\mathbf{x})}{\partial t} = -\frac{\hbar^2}{2m}\Delta\Psi(t,\mathbf{x}) + V_{ext}(\mathbf{x},t)\Psi(\mathbf{x},t) + \int d^3x'|\Psi(t,\mathbf{x}')|^2 V(|\mathbf{x}-\mathbf{x}'|)\Psi(t,\mathbf{x}), \quad (6.2)$$

where $V(d) = -Gm^2/d$ and $V_{ext}(\mathbf{x},t)$ an external potential. This equation can be shown to result from the mean field coupling proposed by Møller [3] and Rosenfeld [5] in the non-relativistic limit [1, 8]. In a nutshell, Moller and Rosenfeld considered a semi classical approach in which the (quantum) matter (encoded by the stress energy tensor $\widehat{\mathcal{T}}_{\mu\nu}$) is evolving in a (classical) space time (encoded by the Einstein's tensor $\mathcal{G}_{\mu\nu}$). They proposed to start from a slightly modified Einstein equation:

$$\mathcal{G}_{\mu\nu} = 8\pi G\ \langle\Psi|\,\widehat{\mathcal{T}}_{\mu\nu}\,|\Psi\rangle\,, \quad (6.3)$$

in which the quantum operator $\widehat{\mathcal{T}}_{\mu\nu}$ is taken as an expectation value with respect to a given quantum state $|\Psi\rangle$. In the newtonian limit, the gravitational potential is shown to obey a Poisson equation:

$$\nabla^2\Phi = 4\pi Gm\ \langle\Psi|\,\widehat{\rho}\,|\Psi\rangle \quad (6.4)$$

where $\widehat{\rho}$ is the mass distribution. After some calculations it yields to the expression (6.2). This is valid in principle when the object is an elementary particle. If the object possesses an internal structure, it is necessary to integrate the self-gravitational potential over the internal degrees of freedom of the object [7]. In the case of a rigid homogeneous nanosphere one finds that, at short distance, instead of the Newton potential V, the effective self-interaction can be expressed [7, 22] in terms of $d = |\mathbf{x}_{\rm CM} - \mathbf{x}'_{\rm CM}|$, with $\mathbf{x}_{\rm CM}$ the center of mass of the nanosphere as follows:

$$V^{\rm eff}(d) = \frac{Gm^2}{R}\left(-\frac{6}{5} + \frac{1}{2}\left(\frac{d}{R}\right)^2 - \frac{3}{16}\left(\frac{d}{R}\right)^3 + \frac{1}{160}\left(\frac{d}{R}\right)^5\right) \quad (d \le 2R), \quad (6.5)$$

where R is the radius of the nanosphere. This expression is valid when d is smaller than twice the radius of the sphere. For larger distances, that is to say whenever d is larger than twice the size of the object, the integration of the internal contributions can be realized easily, making use of Gauss's theorem. Then, we recover the usual Coulomb-like shape, also valid in the case of a non-composite object (6.2):

$$V^{\rm eff}(d) = -\frac{Gm^2}{d} \quad (d \ge 2R). \quad (6.6)$$

[2] D. Fargue has shown in the past [17] that in the case of free propagation, there exist certain non-linear equations admitting solitonic solutions moving along straight lines, respecting thereby the guidance condition derived from a plane wave type solution of the free linear Schrödinger equation, but in our view this property is merely a consequence of the Galilei invariance of the non-linear equation considered by D. Fargue in his study [19]. As far as we know no confirmation of the validity of the guidance equation has been obtained outside from this particular situation (free evolution plus Galilei invariance)

The resulting integro-differential evolution law of the center of mass wavefunction (CMWF) now reads

$$i\hbar\frac{\partial\Psi(t,\mathbf{x}_{\mathrm{CM}})}{\partial t} = -\frac{\hbar^2}{2m}\Delta\Psi(t,\mathbf{x}_{\mathrm{CM}})+V_{ext}(\mathbf{x}_{\mathrm{CM}},t)\Psi(\mathbf{x}_{\mathrm{CM}},t) + \int d^3,\mathbf{x'}_{\mathrm{CM}}|\Psi(t,\mathbf{x'}_{\mathrm{CM}})|^2 V^{\mathrm{eff}}(|\mathbf{x}_{\mathrm{CM}}-\mathbf{x'}_{\mathrm{CM}}|)\Psi(t,\mathbf{x}_{\mathrm{CM}}), \tag{6.7}$$

where $V^{\mathrm{eff}}(|\mathbf{x}_{\mathrm{CM}}-\mathbf{x'}_{\mathrm{CM}}|)$ is fully defined through equations (6.5,6.6). In the limit where the wave function of the center of mass is peaked over a region small in comparison to R, the effective potential can be considered as quadratic:

$$V^{\mathrm{eff}}(d) \sim \frac{G\,m^2}{R}\left(-\frac{6}{5}+\frac{1}{2}\left(\frac{d}{R}\right)^2\right) \tag{6.8}$$

so that equation (6.7) is rewritten as a Schrodinger equation in a harmonic like potential :

$$i\hbar\frac{\partial\Psi(t,\mathbf{x}_{\mathrm{CM}})}{\partial t} = -\frac{\hbar^2}{2m}\Delta\Psi(t,\mathbf{x}_{\mathrm{CM}})+V_{ext}(\mathbf{x}_{\mathrm{CM}},t)\Psi(\mathbf{x}_{\mathrm{CM}},t) + \frac{m\omega_{SN}^2}{2}\left(\mathbf{x}_{\mathrm{CM}}-<\mathbf{x}_{\mathrm{CM}}>\right)^2\Psi(t,\mathbf{x}_{\mathrm{CM}}), \tag{6.9}$$

where now

$$\omega_{SN} = \sqrt{\frac{G\,m}{R^3}} \tag{6.10}$$

is related to the the spring constant of the harmonic like oscillator (6.9). For instance, for a nanosphere of radius $R = 100$ nm and with a mass $m = 10^{10}$ atomic mass unit, $\omega_{SN} \sim 1.10^{-3}$ Hz. This is a very general result, not only valid for spherical objects, as has been shown in ref.[6]: whenever the extent of the CMWF is small enough, the effective self-gravitational potential is quadratic (see also Refs.[23, 24]).

6.2 De Broglie double solution program

Briefly summarized, Louis de Broglie suggested [25] a wave monistic alternative solution of the measurement problem, i.e. in this line of thought we can fully describe physical phenomenons by considering only waves. Especially, according to him, a quantum system could be described by two waves. The particle gets represented by a solitary wave (a soliton) which is solution of a self-focusing non-linear Schrodinger equation which compensate the natural spread of the wavefunction and by the pilot-wave, solution of the linear Schrodinger equation which guides the solitary wave through de guidance equation (2.8). Louis de Broglie called this solution: the double-solution program (we schematically present this idea in figure 6.3).

Originally, Louis de Broglie [26, 25, 27] conceived this model by considering that the total wave function should be written as the sum of the pilot wave and of a solitary wave. He tried to derive the guidance equation from this hypothesis but he never managed to derive it. In the derivation of the guidance equation (2.8) by David Bohm, it is has if the soliton is reduced to a mathematical point without any spatial structure.

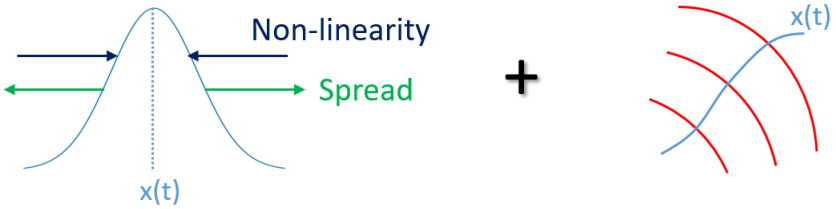

FIGURE 6.3: We illustrate here the double solution program of Louis de Broglie. In blue the peaked solitary wave which represents the particle and which has $x(t)$ as a center. The trajectory of $x(t)$ obeys by a guidance equation coming from the linear pilot wave (in red).

In order to explore possible realization of de Broglie's double solution program in the absence of the guidance condition, an other approach has been developed in the past another approach in order to derive a generalized guidance equation from the double solution program. In summary, instead of considering the sum of the two waves, it was proposed to study the product of these two (this is the so-called factorizability ansatz [28, 19]). One of the reasons for exploring this possibility is the recognition that the superposition principle is no longer valid whenever non-linearities are present. The other reason is the aforementioned difficulty (impossibility?) to derive the guidance condition from the non-linear dynamics. It has been shown in the past that a generalized guidance condition [19] results from the factorizability ansatz, in which, in first approximation, the velocity of the localized soliton is the sum of the de Broglie-Bohm velocity and of an internal velocity. It has also been shown by then that the approximation is good provided the soliton is peaked enough. In order to verify the validity of this result, we considered here a particular regime of self-gravity, the so-called quadratic regime [1, 6, 7], valid when the size of the object is large compared to the soliton. In this regime, the evolution is endowed with a remarkable property: it is gaussian; in other words, gaussian states remain gaussian throughout the evolution [20].

6.2.1 Factorization ansatz, double solution and self-gravity

In this section we shall impose the factorization ansatz [28] according to which the total wave function $\Psi(t,x)$ can be written as the product of a pilot wave $\Psi^L(t,x)$ and of a peaked soliton $\Psi^{NL}(t,x)$:

$$\Psi(t,x) = \Psi^L(t,x) \cdot \Psi^{NL}(t,x), \tag{6.11}$$

where $\Psi(t,x)$ is solution of the Schrödinger equation:

$$i\hbar \frac{\partial \Psi(t,x)}{\partial t} = \left[-\frac{\hbar^2}{2m}\frac{\partial^2}{\partial x^2} + \frac{k^{ext.}x^2}{2} + \frac{k^{SN}}{2}\,(x - <x>)^2 \right] \Psi(t,x), \tag{6.12}$$

with $k^{SN} = m\,\omega_{SN}^2$ and $\Psi^L(t,x)$ is solution of the following linear Schrödinger equation:

$$i\hbar \frac{\partial \Psi^L(t,x)}{\partial t} = \left[-\frac{\hbar^2}{2m}\frac{\partial^2}{\partial x^2} + \frac{k^{ext.}x^2}{2} \right] \Psi^L(t,x). \tag{6.13}$$

Originally, the ansatz (6.11) has been introduced [28] in order to describe the phenomenology of walkers[3]. In the case of droplets, our basic motivation for imposing the factorization ansatz is that walkers prepared at different positions and represented by Ψ^{NL} always see the same bath (environment) represented by Ψ^{L}.

In order to test such an ansatz, let us for simplicity impose that $\Psi(t,x)$, $\Psi^L(t,x)$ (and thus $\Psi^{NL}(t,x)$) are gaussian:

$$\Psi(t,x) = e^{-Ax^2/2+Bx+C}, \quad \Psi^L(t,x) = e^{-A^Lx^2/2+B^Lx+C^L} \text{ and } \quad \Psi^{NL}(t,x) = e^{-A^{NL}x^2/2+B^{NL}x+C^{NL}},$$

where the factors $A, A^L, A^{NL}, B, B^L, B^{NL}, C, C^L, C^{NL}$ are time-dependent and complex functions of time. The real part of C, C^L and C^{NL} is constrained by the normalization of the wave function (which remains constant throughout time), and their imaginary part can be seen as a global, purely time-dependent, phase, irrelevant from the physical point of view. Having this in mind, one sees that the full wave function $\Psi(t,x)$, the pilot wave $\Psi^L(t,x)$ and the soliton $\Psi^{NL}(t,x)$ can be consistently parameterized by 4 real parameters; the full wave function for instance is entirely defined (up to an irrelevant global phase) by the 4 real parameters a_1, a_2, b_1, b_2:

$$a_1 = \mathcal{R}e\, A, \quad a_2 = \mathcal{I}m\, A, \quad b_1 = \mathcal{R}e\, B, \quad b_2 = \mathcal{I}m\, B.$$

A similar parameterization holds for the pilot wave and the soliton. If now we impose the constraints (6.11,6.12,6.13), the dynamics reads (making use of the fact that $<x> = \frac{b_1}{a_1}$):

$$\begin{aligned}
\dot{a_1} &= 2\frac{\hbar}{m}a_1 \cdot a_2 & \dot{a_1^L} &= 2\frac{\hbar}{m}a_1^L \cdot a_2^L \\
\dot{a_2} &= -\frac{\hbar}{m}(a_1^2 - a_2^2) + \frac{k^{ext.} + k^{SN}}{\hbar} & \dot{a_2^L} &= -\frac{\hbar}{m}((a_1^L)^2 - (a_2^L)^2) + \frac{k^{ext.}}{\hbar} \\
\dot{b_1} &= \frac{\hbar}{m}(a_1 b_2 + a_2 b_1) & \dot{b_1^L} &= \frac{\hbar}{m}(a_1^L b_2^L + a_2^L b_1^L) \\
\dot{b_2} &= -\frac{\hbar}{m}(a_1 b_1 - a_2 b_2) + \frac{k^{SN} b_1}{a_1 \hbar} & \dot{b_2^L} &= -\frac{\hbar}{m}(a_1^L b_1^L - a_2^L b_2^L),
\end{aligned}$$

and we also have the trivial and useful relations :

$$\begin{aligned}
a_1^{NL} = a_1 - a_1^L, \quad a_2^{NL} = a_2 - a_2^L, \\
b_1^{NL} = b_1 - b_1^L, \quad b_2^{NL} = b_2 - b_2^L
\end{aligned}$$

6.2.2 Generalized guidance equation.

In ref [19] the author showed in the framework of the factorization ansatz (6.11) the following property (from now on denoted the generalized guidance condition):

$$\frac{d<\mathbf{x}>_t^{NL}}{dt} = \mathbf{v}_{drift} = \underbrace{\frac{1}{m}\nabla S_L(\mathbf{x},t)\Big|_{\mathbf{x}=<\mathbf{x}>_t^{NL}}}_{\mathbf{v}_{dB-B}} + \underbrace{\frac{<\Psi^{NL}|\frac{\hbar}{im}\nabla|\Psi^{NL}>}{<\Psi^{NL}|\Psi^{NL}>}}_{\mathbf{v}_{int.}} \tag{6.14}$$

[3] See chapter 5 for what concerns droplets phenomenology.

where S_L represents the phase of the pilot wave Ψ^L and $<\mathbf{x}>_t^{NL}$ the center of the peaked soliton. The above generalized guidance equation contains the well-known Madelung-de Broglie-Bohm [29, 30, 31] contribution ($\mathbf{v}_{dB-B}$ is interpreted as the guidance velocity (2.8)), plus a new contribution, an "internal" velocity reflecting the contributions of the internal structure of the soliton :

$$\mathbf{v}_{int.} = \frac{<\Psi_{NL}|\frac{\hbar}{im}\bigtriangledown|\Psi_{NL}>}{<\Psi_{NL}|\Psi_{NL}>} \tag{6.15}$$

In order to test the range of validity of the generalized guidance equation through a concrete example, we numerically solved the dynamical systems (6.14). By doing so, we were able to obtain plots of the parameters $<x>$, $<p>$, σ_x^2 and σ_p^2 in function of time. These four parameters respectively represent the average values of the position, the velocity and their variances; in the case of a gaussian wave packet $\Psi(t,x) = e^{-Ax^2/2+Bx+C}$ they are in one to one correspondence with the four complex parameters a_1, a_2, b_1, b_2:

$$<x> = \frac{b_1}{a_1}, \quad <p> = \frac{b_2 a_1 - a_2 b_1}{a_1}, \quad \sigma_x^2 = \frac{1}{2\,a_1}, \quad \sigma_p^2 = \frac{\hbar^2|A|^2}{2\,a_1} \tag{6.16}$$

Similar relations hold in the case of the gaussian wave packets Ψ^L and Ψ^{NL}. In order to check that the generalized guidance condition is indeed well satisfied, we had to evaluate, in function of time the following quantities:

i) v_{drift} the time derivative of the position of the barycenter of the solitonic wave packet

$$<\mathbf{x}>_t^{NL} = \frac{\int dx' |\Psi^{NL}(t,x')|^2 x'}{\int dx' |\Psi^{NL}(t,x')|^2} = \frac{b_1^{NL}}{a_1^{NL}} \tag{6.17}$$

ii) the de Broglie-Bohm velocity

$$v_{dBB} = \frac{1}{m}\bigtriangledown S_L(\mathbf{x},t)\Big|_{\mathbf{x}=<\mathbf{x}>_t^{NL}} = \frac{1}{m}\left(b_2^L - a_2^L <\mathbf{x}>_t^{NL}\right) \tag{6.18}$$

iii) the internal velocity

$$v_{int} = \frac{<p>_t^{NL}}{m} = \frac{1}{m}\frac{(b_2^{NL}a_1^{NL} - a_2^{NL}b_1^{NL})}{a_1^{NL}} \tag{6.19}$$

As can be seen in figure 6.4, v_{drift} and $v_{dBB} + v_{int.}$ are not distinguishable and thus establishing the validity of the generalized guidance condition in this case. Actually, we may also retrieve the generalized guidance condition by an analytic argument, remarking that, combining (ii) and (iii) above we obtain

$$v_{dBB} + v_{int} = \frac{1}{m}\left(b_2^L + b_2^{NL} - \frac{b_1^{NL}}{a_1^{NL}}\left(a_2^L + a_2^{NL}\right)\right) = \frac{1}{m}\left(b_2 - a_2 <\mathbf{x}>_t^{NL}\right). \tag{6.20}$$

This expression has to be compared with the average velocity of the "full" wave packet Ψ which is nothing else than $\frac{1}{m}\cdot(b_2 - \frac{b_1}{a_1}\cdot a_2) \approx \frac{1}{m}\cdot(b_2 - <\mathbf{x}>_t^{NL}\cdot a_2^{NL})$ because in the regime considered by us $<\mathbf{x}>_t = \frac{b_1}{a_1} \approx <\mathbf{x}>_t^{NL}$, due to the fact that the weight (size) of the pilot wave is quite smaller (larger) than the weight (size) of the soliton ($a_1^L <<< a_1^{NL}$). Then the velocity of the full packet also coincides with the drift velocity (6.14) of the soliton.

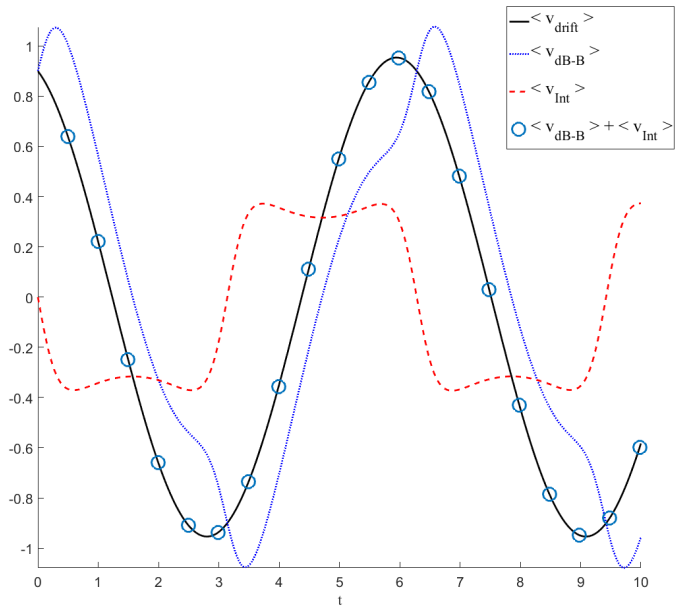

FIGURE 6.4: Plot of $v_{dBB}, v_{int.}, v_{dBB} + v_{int.}$ and $v_{drift} = \frac{d}{dt}(x_0^{NL})$ in function of time; space and time were rescaled and are of the order of unity.

This being said, it is worth noting that the drift velocity looks classical, as is obvious from a phase space representation of the average trajectory $(x_0^{NL}, \frac{dx_0^{NL}}{dt})$ which looks perfectly circular provided we rescale one of the variables appropriately as can be seen from figure 6.5.

This property was already noted before in ref [6], whom authors remarked that when the dynamics obeys equations (6.14), the first moments of the distribution of positions and velocities are not affected at all by the non-linear coupling. One can prove this result rigorously on the basis of the dynamics (6.14), but this property is not a coincidence; as was noted in [23, 19], one can explain the emergence of classical trajectories in terms of a generalized Ehrenfest theorem as we shall discuss in the next section. The second moments σ_x^2 and σ_p^2 are nevertheless modified by the evolution. In our case, self-gravity results into a breathing of the wave packet [32, 20], which is very explicitly shown in figure 6.6.

Actually there exists a stable radius for the gaussian packets for which self-gravity and spreading behavior exactly compensate each other. In full analogy with coherent oscillator states the size of these generalized coherent states is of the order of

$$\sqrt{\frac{\hbar}{\sqrt{k^{SN}m}}} \tag{6.21}$$

as confirmed by numerical simulations (this is so at least when we impose that the ratio $k^{SN}/k^{ext.}$ is equal to 10^3, in which case the small fluctuations of the shape of the generalized coherent states induced by the external harmonic potential are negligible). This can be seen from figure 6.6 which shows that when $\sigma_x^2 \approx \frac{\hbar}{\sqrt{k^{SN}m}}$ the shape of the wave packet remains stable, and that if it is slightly disturbed, the size of the wave packet oscillates (breathes) around this equilibrium value.

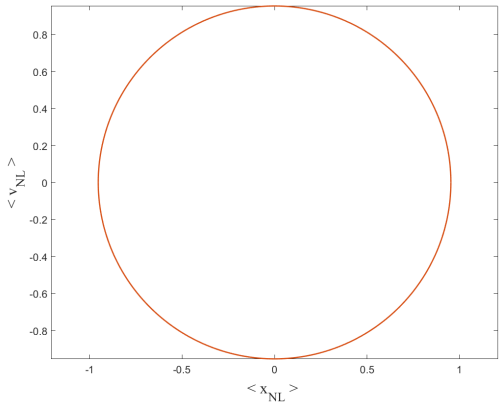

FIGURE 6.5: Plot of $(<\mathbf{x}>_t^{NL}, \frac{d<\mathbf{x}>_t^{NL}}{dt})$ in appropriate units, illustrating the validity of a generalized Ehrenfest's theorem.

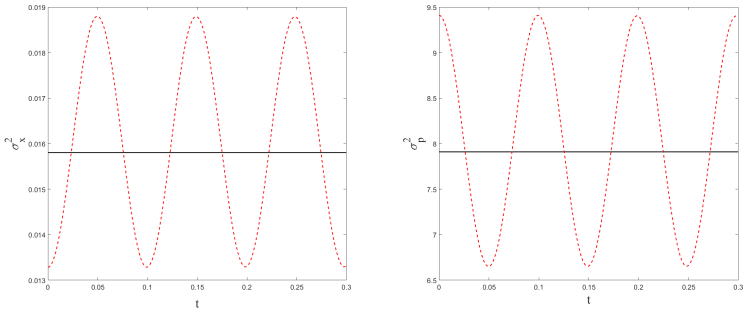

FIGURE 6.6: Time evolution of the second moments σ_x^2 and σ_p^2 with self-gravity for a "coherent" state (black) such that $\sigma_x^2 \approx \frac{\hbar}{\sqrt{k^{SN}m}}$ and for an arbitrary state (red).

A similar study was already performed in the past [6, 23], motivated by the ambition to experimentally observe manifestations of self-gravity through their influence on the dynamical properties of a mesoscopic object trapped in a harmonic potential. In those studies however, the self-gravitational interaction always appeared to be very small and was treated as a perturbation. Actually, self-gravity is so weak that up to now it was impossible to experimentally observe its potential manifestations. In the approach proposed here however, we do not impose that the norm of the wave function is equal to unity, as is the case in orthodox self-gravity. The reason therefore is that we consider that the wave function is attached to a solitonic self-collapsed solution of the non-linear dynamics which behaves as a corpuscle [19], and ought not to be confused with the pilot wave, solution of the linear Schrödinger equation for which normalization to unity ($\int dx|\Psi(t,x)|^2 = 1$) is traditionally required, in agreement with Born's probabilistic interpretation. This constraint is generally overlooked in the framework of usual (linear) quantum mechanics because the normalization of a solution of a linear equation does not affect the properties of the solution, such a solution being always defined up to an arbitrary multiplicative factor.

On the contrary this is no longer so as far as we consider non-linear equations.
In our approach, we consider that the normalization factor of the solitonic wave representing the corpuscle is huge compared to unity, and it is rather the external potential that is treated as a perturbation. This is why we explore the solutions of the non-linear dynamics in a regime which has been unexplored before, regime in which the effective coupling constant characterizing self-gravity is quite larger than the spring constant attached to the external (trapping) potential. In the practice, we considered a situation for which the ratio between the non-linear and linear spring constants $\frac{k^{SN}}{k^{ext.}}$ is equal to 10^3.

6.2.3 Generalised Ehrenfest theorem.

Equations (6.2) and (6.7) are invariant under Galilean transformations, which expresses that self-gravity does not result into self-acceleration, in accordance with Noether's theorem. This implies that even if a harmonic oscillator is self-gravitating, the average position of its center of mass rigorously obeys Newton equation and indeed we find that

$$\frac{d^2 < x >}{dt^2} = -\omega_{ext.}^2 < x > -\frac{\omega_{SN}^2}{2} \int dx \int dx' |\Psi(t,x)|^2 |\Psi(t,x')|^2 \cdot 2(x - x'), \qquad (6.22)$$

where

$$\int dx \int dx' |\Psi(t,\mathbf{x})|^2 |\Psi(t,\mathbf{x}')|^2 \cdot 2(x - x') = 0. \qquad (6.23)$$

Thus $< x >$ will oscillate at the classical frequency $\omega_{ext.}/2\pi$. This constraint imposes severe limitations to our original program which was to realize de Broglie's double solution program, and thus to derive de Broglie-Bohm dynamics as a consequence of the factorization ansatz. We found that de Broglie-Bohm trajectories coincide with classical trajectories which is not at all the result that we were looking for [19]. In other words, we aimed at deriving de Broglie-Bohm dynamics and instead we found classical dynamics, a rather disappointing result. It is worth noting at this level that orthodox self-gravity exhibits the same features: in the classical limit (for macroscopic objects counting at least of the order of 10^{23} nucleons), in situations where self-gravitational collapse results in an extremely peaked localization of the center of mass wavefunction (CMWF) of the object we may neglect quantum fluctuations around the barycenter of the CMWF so that in virtue of the generalized Ehrenfest's theorem dynamics is FAPP classical. From this point of view, in both approaches (ours and "orthodox" self-gravity), we predict that localized objects obey classical dynamics in good approximation which is however satisfactory if we wish to deal with the classical limit. However the classical limit is only one side of the measurement problem. The other side of the measurement problem is related to the probabilistic nature of the quantum predictions which was already discussed in part I.

6.3 Conclusion:

In this chapter, we presented the Schrodinger Newton equation and proposed to apply in this framework a prototype of the double solution program of Louis de Broglie. We considered a particular case in which self-gravity is treated in the quadratic regime for which gaussian states are preserved through the dynamics. We have thus numerically integrated the non-linear dynamics associated to the evolution of a self-gravitating gaussian wave packet trapped in an external harmonic potential. By doing so we have confirmed that we can in principle derive a generalized guidance equation for such non-linear dynamics. In particular, we have shown that the trajectories of the soliton are classical. Contrary to our primary hope which was to retrieve de Broglie-Bohm dynamics we noted that the internal velocity may not be neglected and even more, that it conspires, in agreement with the generalized Ehrenfest theorem presented in section 6.2.3, to restore classical dynamics.

This finally brings us to invoke, as a last resort aimed at realizing de Broglie's program, the presence of a suitable combination of non-linear and stochastic component on the dynamics, aimed at neutralizing the internal velocity while preserving equivariance. Moreover, as has been noted by Gisin [33], the combination of non-linearity and stochasticity is also an essential tool of collapse models (as we shall see in the next chapter) which are introduced in such way that causality is preserved (it is expressed through the no signaling condition [34, 21, 35]). This combination is also present in Nelson's model (see chapter 3 with the osmotic velocity) and even in all "shut up and compute" simulations of the Monte-Carlo type where an effective collapse is implemented. Our analysis suggests that, probably, all approaches inspired by the double solution program of de Broglie [36, 18, 9] will have to include stochasticity as an essential ingredient in order to tackle the hard task of mimicking quantum mechanics with realistic models. Bohm and Vigier [37] as well as de Broglie [27] arrived to a similar conclusion; de Broglie attributed the origin of the stochastic quantum "zero-point field fluctuations" to a quantum thermostat or subquantum field, the study of which constitutes still today one of the main open questions in the framework of realistic hidden variables theories.

The Schrodinger-Newton equation is however interesting, even if it does not lead to de Broglie guidance equation, it explains why macroscopic objects are localized in space and why they follow classical dynamics. From this point of view, the Schrodinger-Newton equation deserves to be tested experimentally.

In the next chapter we shall see how to test the non-linear Schrodinger equation by considering two experiments.

Bibliography

[1] L. Diósi. Gravitation and quantum-mechanical localization of macro-objects. *Physics Letters A*, 105(4):199 – 202, 1984.

[2] KRW Jones. Newtonian quantum gravity. *Australian Journal of Physics*, 48(6):1055–1082, 1995.

[3] C Moller. The energy-momentum complex in general relativity and related problems. In *Colloq. Int. CNRS*, volume 91, pages 15–29, 1959.

[4] Roger Penrose. On gravity's role in quantum state reduction. *General relativity and gravitation*, 28(5):581–600, 1996.

[5] L. Rosenfeld. On quantization of fields. *Nuclear Physics*, 40:353 – 356, 1963.

[6] Huan Yang, Haixing Miao, Da-Shin Lee, Bassam Helou, and Yanbei Chen. Macroscopic quantum mechanics in a classical spacetime. *Physical review letters*, 110(17):170401, 2013.

[7] S. Colin, T. Durt, and R. Willox. Can quantum systems succumb to their own (gravitational) attraction? *Class. Quantum Grav.*, 31:245003, 2014.

[8] Domenico Giulini and André Großardt. The schrödinger–newton equation as a non-relativistic limit of self-gravitating klein–gordon and dirac fields. *Classical and Quantum Gravity*, 29(21):215010, 2012.

[9] Louis De Broglie. *Non-linear wave mechanics: A causal interpretation*. Elsevier Publishing Company, 1960.

[10] Louis Victor Pierre Raymond de Broglie. Une tentative d'interprétation causale et non linéaire de la mécanique ondulatoire: la théorie de la double solution. 1956.

[11] M. Hatifi, C. Lopez-Fortin, and T. Durt. De Broglie's double solution: limitations of the self-gravity approach. *Annales de la Fondation Louis de Broglie*, 43:63, 2018.

[12] Iwo Bialynicki-Birula and Jerzy Mycielski. Nonlinear wave mechanics. *Annals of Physics*, 100(1-2):62–93, 1976.

[13] Shimony A. Proposed neutron interferometer test of some nonlinear variants of wave mechanics. *Phys. Rev. A 20, 39*, 1979.

[14] Steven Weinberg. Testing quantum mechanics. *Annals of Physics*, 194(2):336–386, 1989.

[15] Joseph Polchinski. Weinberg's nonlinear quantum mechanics and the einstein-podolsky-rosen paradox. *Physical Review Letters*, 66(4):397, 1991.

[16] Nicolas Gisin. Weinberg's non-linear quantum mechanics and supraluminal communications. *Physics Letters A*, 143(1-2):1–2, 1990.

[17] D Fargue. Permanence of the corpuscular appearance and non linearity of the wave equation. In *The wave-particle dualism*, pages 149–172. Springer, 1984.

[18] D Fargue. Louis de broglie's "double solution" a promising but unfinished theory. *Ann. Fond. de Broglie*, 42(1):9, 2017.

[19] T. Durt. L. de Broglie's double solution and gravitation. *Annales de la Fondation Louis de Broglie*, 42:73, 2017.

[20] Samuel Colin, Thomas Durt, and Ralph Willox. Crucial tests of macrorealist and semiclassical gravity models with freely falling mesoscopic nanospheres. *Physical Review A*, 93(6):062102, 2016.

[21] S. Colin, T. Durt, and R. Willox. L. de Broglie's double solution program: 90 years later. *Annales de la Fondation Louis de Broglie*, 42:19, 2017.

[22] Roger Penrose. On the gravitization of quantum mechanics 1: Quantum state reduction. *Foundations of Physics*, 44(5):557–575, 2014.

[23] André Großardt, James Bateman, Hendrik Ulbricht, and Angelo Bassi. Optomechanical test of the schrödinger-newton equation. *Physical Review D*, 93(9):096003, 2016.

[24] André Großardt. Approximations for the free evolution of self-gravitating quantum particles. *Physical Review A*, 94(2):022101, 2016.

[25] Louis De Broglie. *Non-linear wave mechanics: A causal interpretation*. Elsevier Publishing Company, 1960.

[26] Louis De Broglie. An introduction to the study of wave mechanics. 1930.

[27] Louis de Broglie. Interpretation of quantum mechanics by the double solution theory. *Annales de la Fondation Louis de Broglie*, 12(4):1–23, 1987.

[28] Thomas Durt. Generalized guidance equation for peaked quantum solitons and effective gravity. *EPL (Europhysics Letters)*, 114(1):10004, 2016.

[29] David Bohm. A Suggested Interpretation of the Quantum Theory in Terms of "Hidden" Variables. I. *Phys. Rev.*, 85(2):166–179, 1952.

[30] David Bohm. A Suggested Interpretation of the Quantum Theory in Terms of "Hidden" Variables. II. *Phys. Rev.*, 85(2):180–193, 1952.

[31] P. R. Holland. *The quantum theory of motion: an account of the de Broglie-Bohm causal interpretation of quantum mechanics*. Cambridge University press, 1993.

[32] Enrique Ruíz Arriola and Juan Soler. A variational approach to the schrödinger–poisson system: asymptotic behaviour, breathers, and stability. *Journal of Statistical Physics*, 103(5-6):1069–1105, 2001.

[33] Nicolas Gisin. Stochastic quantum dynamics and relativity. *Helv. Phys. Acta*, 62(4):363–371, 1989.

[34] J.S. Bell. On the EPR paradox. *Physics*, 1:165, 1964.

[35] T Durt. About the possibility of supraluminal transmission of information in the bohm-bub theory. *Helvetica Physica Acta*, 72(5-6):356–376, 1999.

[36] G. Bacciagaluppi and A. Valentini. *Quantum Theory at the Crossroads: Reconsidering the 1927 Solvay Conference*. Cambridge University Press, Cambridge, 2010.

[37] David Bohm and Jean-Pierre Vigier. Model of the causal interpretation of quantum theory in terms of a fluid with irregular fluctuations. *Phys. Rev.*, 96(1):208, 1954.

Chapter 7

Experiment proposals to test non-linear quantum mechanics *à la* Schrodinger-Newton

> "If we are going to stick to this damned quantum-jumping, then I regret I ever had anything to do with quantum theory."
>
> E. Schrodinger

Summary We propose in this chapter two experimental tests aimed at putting into evidence the existence of a non-linear self-interaction à la Schrodinger-Newton. The first test involves a Humpty-Dumpty Stern-Gerlach experiment [1]. The second one implements the idea that decoherence can be used as a tool for controlling and tailoring the evolution of a quantum system. Moreover it incorporates the concept of mobility [2] (that we shall define in what follows), which is central in the derivation of Gisin's famous no-go theorem about non-linearity [3]. To put it simply, this theorem relates the presence of a non-linearity to the violation of quantum signaling.

7.1 Measuring self-gravity in a Stern-Gerlach Humpty-Dumpty experiment.

7.1.1 "Coherence of quantum gravity" at the nanoscale: recent proposals.

Two very similar experiments [4, 5] have been proposed recently aimed at revealing quantum gravity effects. The figure 7.1 has been adapted from [4] to illustrate the main idea behind these proposals. Roughly speaking, these experiments involved two spin $1/2$ mesoscopic systems (e.g. a NV center in a diamond nanocrystal) simultaneously released from two traps placed side by side and falling through magnetic fields. The magnetic fields are configured in such a way that the wave packet of each spin $1/2$ system gets split into two (say Left $|L,\uparrow\rangle_i$ and Right $|R,\downarrow\rangle_i$ where $i = 1,2$) parallel beams at the beginning of the free fall and recombined at the end. This is a so-called Humpty-Dumpty Stern-Gerlach experiment [1].

The basic idea of these proposals is the following: depending on its path, a branch of a bi-localized mesoscopic particle will feel a different gravitational interaction.

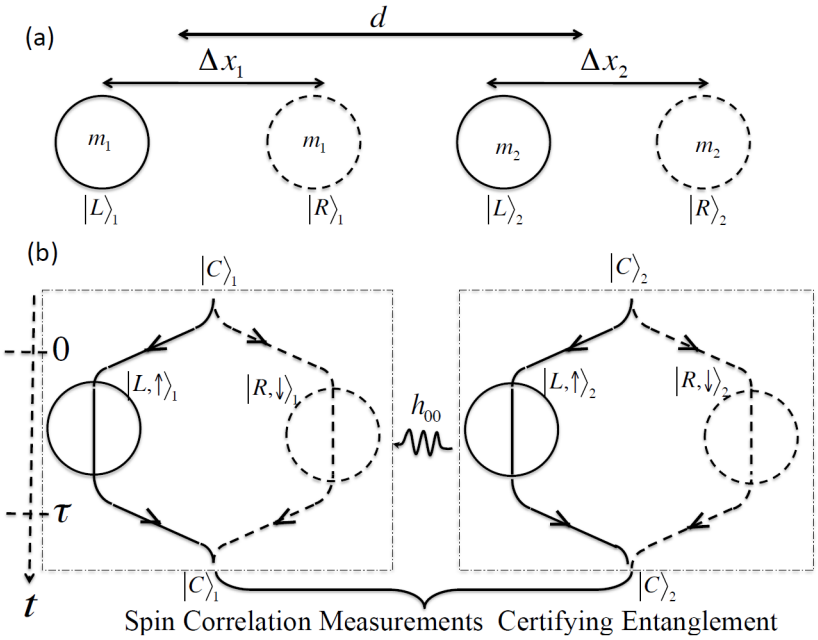

FIGURE 7.1: Figure adapted from [4]. This figure illustrates an experiment which uses the principle of Stern Gerlach interferometry with the aim of testing quantum gravity effects.

Typically, the total gravitational energy of each packet (corresponding to $|j\rangle_1$ or $|j\rangle_2$ where $j = L$ or R) is the sum of the Newton interaction between this packet and the other bi-localized states ($|L\rangle_2$ and $|R\rangle_2$ or $|L\rangle_1$ and $|R\rangle_1$). Hence, during the free fall, each of the four packets accumulates a phase shift which is proportional to the sum of the gravitational interactions with the two components of the other mesoscopic particle. After getting recombined the spins appear to be entangled by gravity.

Performing a spin tomography could, in principle, reveal this entanglement which would be the first manifestation of gravity in this regime and thus revealing what is called by the authors the quantum coherence of the gravitational interaction. It is worth noting that in both proposals, no explicit model of interaction has been written. It is clear however that the authors assume that the experimental conditions are such that we are in a nearly classical regime, where the energy of interaction between two distant masses 1 and 2 obeys Newton's expression:

$$V_{1,2} = -\frac{G\, m_1\, m_2}{d_{1,2}} \tag{7.1}$$

Actually, a direct analogy with electro-magnetism and Coulomb interaction suggests two possible phenomenological potentials of interaction to be tested in their experimental proposal.

- The first one, of classical nature [6]

$$V_{1,2}^{\text{class.}} = -G\, m_1\, m_2 \int d^3x \int d^3x' \frac{\rho_1(\mathbf{x}')\rho_2(\mathbf{x})}{|\mathbf{x}-\mathbf{x}'|} \tag{7.2}$$

where, when 1 and 2 are not entangled, ρ_i can be factorized so that $\rho_i(\mathbf{x}) = \Psi_i^*(\mathbf{x})\,\Psi_i(\mathbf{x})$ with $i = 1, 2$.

Otherwise, if they are described by a first-quantized wave function $\Psi_{1,2}(\mathbf{x}_1, \mathbf{x}_2)$ defined in 6D configuration space (with possibly spin contributions that we omit here to write explicitly for simplicity), the local 3D densities are the marginals of the 6D distribution:

$$\rho_1(\mathbf{x}') = \int d^3x_2 |\Psi_{1,2}(\mathbf{x}_1, \mathbf{x}_2)|^2 \quad \text{and} \quad \rho_2(\mathbf{x}') = \int d^3x_1 |\Psi_{1,2}(\mathbf{x}_1, \mathbf{x}_2)|^2 \tag{7.3}$$

- The second one, inspired by Coulomb interaction in the first-quantized Hydrogen/Helium atom, reads:

$$V_{1,2}^{quant.} = -G\, m_1\, m_2 \int d^3x_1 d^3x_2 \frac{|\Psi_{1,2}(\mathbf{x}_1, \mathbf{x}_2)|^2}{|\mathbf{x}_1 - \mathbf{x}_2|} \tag{7.4}$$

It is not our goal to study these models in depth but the idea is that the phase shifts are proportional to $\int dt V$. In fact, when we prepare at time $t = 0$ the spinors 1 and 2 in a factorizable state of the form

$$|\Psi(t=0)\rangle_{1,2} = \frac{1}{2}\,(|L\rangle_1 + |R\rangle_1)\,(|L\rangle_2 + |R\rangle_2) \tag{7.5}$$

the state at time t will be equal to

$$\begin{aligned} |\Psi(t=\tau)\rangle_{1,2} = \frac{1}{2}\,(|L\rangle_1\,|L\rangle_2\,e^{i\,\varphi_{LL}} + |R\rangle_1\,|L\rangle_2\,e^{i\,\varphi_{RL}} + |L\rangle_1\,|R\rangle_2\,e^{i\,\varphi_{LR}} \\ + |R\rangle_A\,|R\rangle_B\,e^{i\,\varphi_{RR}}) \end{aligned} \tag{7.6}$$

where we defined the phase φ_{ij} as

$$\varphi_{ij} = \int dt \frac{V_{ij}}{\hbar} \tag{7.7}$$

with i (resp. j) is L or R. Hence, if the potential of interaction is (7.1) we get

$$\varphi_{ij} = -\frac{G\, m_1\, m_2}{\hbar} \int_0^\tau dt \frac{1}{d_{ij}(t)} \tag{7.8}$$

where $d_{ij}(t)$ is the distance between the center of each packet corresponding to the states $|i\rangle_1$ and $|j\rangle_2$. In [4, 5], the authors estimated the phase shifts using (7.8).

If now we use the potential $V_{1,2}^{class.}$ defined in (7.2 with 7.3), we get the same results excepted that the phase shifts are twice smaller. It is easy to show that entanglement is generated only if the factorizability of $|\Psi(t)\rangle_{1,2}$ is broken which provides the following constraint

$$\int_0^\tau dt(V_{LL} + V_{RL}) \neq \int_0^\tau dt(V_{LR} + V_{RR}) \mod 2\pi \tag{7.9}$$

We shall no longer explore these proposals much in detail here, but we propose another experiment in which only one Humpty-Dumpty Stern-Gerlach experiment is performed instead of two, aimed at revealing the existence of self-gravity *à la* Schrodinger-Newton.

7.1.2 The single spin Humpty-Dumpty Stern Gerlach experiment as a test for the Schrodinger-Newton equation

The main difference between our proposal and the two aforementioned proposals [4, 5] is that in our case the spin 1/2 mesoscopic particle interacts with itself due to self-gravity. Consequently, the self-gravitational dephasing between the two wave packets ($|L\rangle$ and $|R\rangle$) will lead in our case to a rotation of the spin, which can as well be revealed by spin tomography after completion of the Humpty-Dumpty experiment.

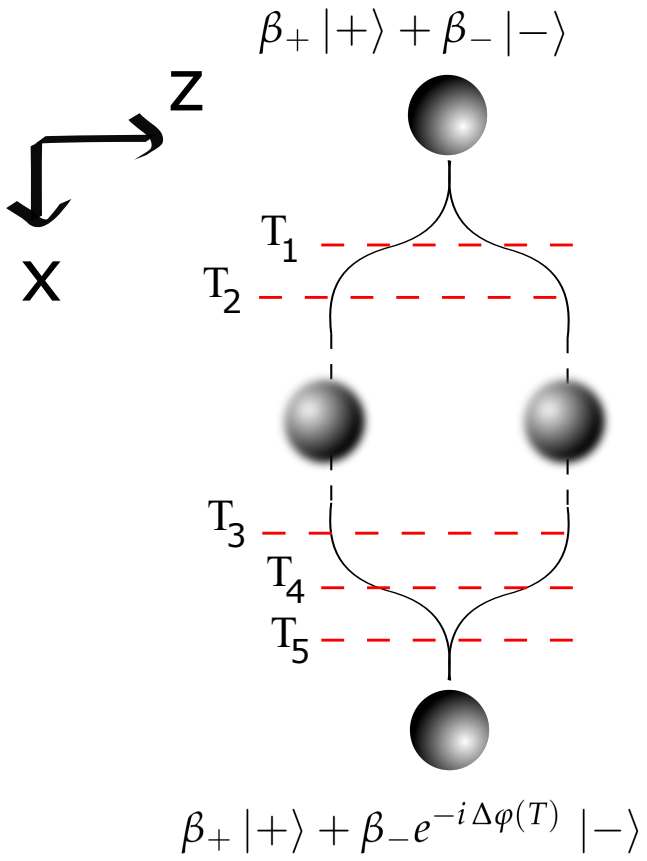

FIGURE 7.2: Illustration of the Humpty-Dumpty experiment [1] discussed in section 7.1.2. We rotated by 90° the figure 7.1, i.e. here the z-axis corresponds to the x-axis of figure 7.1. We consider here a unique mesoscopic sphere (NV center in a diamond nanocrystal) of radius $R = 1 \cdot 10^{-6}$ m and with a mass $m = 5.5 \cdot 10^{-15}$ Kg for which the Stern-Gerlach setup is applied. The time-step T_i are defined in appendix 7.A.2

We consider in what follows a description in the comoving frame (freely falling) so that the problem reduces to a one-dimensional Stern Gerlach Humpty-Dumpty experiment for which we choose z as the axis of quantification (see figure 7.2). We denote by $|+\rangle$ the state previously denoted $|R\rangle$ and by $|-\rangle$ the state previously denoted $|L\rangle$.

7.1.2.1 A wave packet description

Let us compute analytically the phase shift using gaussian wave packets. To do so we shall use a one-dimensional approximation of the Schrodinger-Newton equation (6.7). To begin with, let us start by writing down the general expression of the quantum state

$$\Psi(z,t) = \sum_{i=\{+,-\}} \beta_i \, \psi_i(z,t) \; |i\rangle \tag{7.10}$$

The β_i are complex number such as $|\beta_+|^2 + |\beta_-|^2 = 1$ and ψ_i is the spatial and normalized complex wavefunction corresponding to the state $|i\rangle$. In this study we consider the following Hamiltonian:

$$\mathcal{H} = -\frac{\hbar^2}{2\,m}\frac{\partial^2}{\partial z^2} + \frac{g\mu_B}{2}\left(B_0 - B_0' z\right) \otimes \sigma_z + \widehat{V}_G(z,t) \tag{7.11}$$

where B_0 is the magnetic field and B_0' is its gradient, μ_B is the Bohr magneton and $g \sim 2$ is the electronic g-factor. From (7.10) one can associate the following probability density:

$$|\Psi(z,t)|^2 = \sum_{i=\{+,-\}} |\beta_i|^2 \, |\psi_i(z,t)|^2. \tag{7.12}$$

Thus, the one-dimensional Schrodinger-Newton potential [7] can be approximated (6.7) as

$$\widehat{V}_{G,\pm}(z,t) = \underbrace{\left[\frac{m}{2}\,\omega_{SN}^2\,(z - \langle z\rangle_\pm)^2 - \frac{6}{5}\frac{G\,m^2}{R}\right]|\beta_\pm|^2}_{\text{Self-interaction } \pm \to \pm} + \underbrace{f_\mp(z,t)\,|\beta_\mp|^2}_{\text{Self-interaction } \mp \to \pm} \tag{7.13}$$

If the distance between the two packets $|\langle z\rangle_+ - \langle z\rangle_-| \leq 2R$ then $f_\mp(z,t)$ is expressed[1] as

$$f_\mp(t) = \left[\frac{m}{2}\,\omega_{SN}^2\,(z - \langle z\rangle_\mp)^2 - \frac{6}{5}\frac{G\,m^2}{R}\right] \tag{7.14}$$

so that the self-gravitational interaction is the same for both paths, i.e. $\widehat{V}_{G,+}(z,t) = \widehat{V}_{G,-}(z,t)$.

Now if $|\langle z\rangle_+ - \langle z\rangle_-| \geq 2R$ then $f_\mp$ takes the form of a Newton-like potential

$$f_\mp(t) = -G\,m^2\,\frac{1}{|\langle z\rangle_+ - \langle z\rangle_-|} \tag{7.15}$$

Each branch of the superposition is then solution of the following non-linear Schrodinger equation:

$$\boxed{i\hbar\,\frac{\partial\psi_\pm(z,t)}{\partial t} = \left[-\frac{\hbar^2}{2\,m}\frac{\partial^2}{\partial z^2} + \widehat{V}_{G,\pm}(z,t)\right]\psi_\pm(z,t)} \tag{7.16}$$

[1] Actually, the Schrodinger-Newton self-interaction can be neglected compared to the standard Stern-Gerlach potential [8, 9] in the time intervals $[0, T_2]$ and $[T_3, T_5]$ (see figure 7.5). However, it plays a role in the interval $[T_2, T_3]$ through the Newton-like potential (7.15).

7.1.2.2 Estimate of the phase

Generally, a Schrodinger equation of the form

$$i\hbar\,\frac{\partial\psi_\pm(z,t)}{\partial t} = \left[-\frac{\hbar^2}{2\,m}\,\frac{\partial^2}{\partial z^2} + V_{0,\pm}(t) + V_{1,\pm}(t)\,z + V_{2,\pm}(t)\,z^2\right]\,\psi_\pm(z,t) \tag{7.17}$$

can be solved using a gaussian wave function

$$\psi_\pm(z,t) = \exp\left[-A_\pm(t)\frac{z^2}{2} + B_\pm(t)z + C_\pm(t)\right] \tag{7.18}$$

where $A_\pm(t)$, $B_\pm(t)$ and $C_\pm(t)$ are complex functions of time. Thus one can show that

$$\begin{cases} i\,\frac{dA_\pm(t)}{dt} &= \frac{\hbar}{m}\,A_\pm(t)^2 - 2\,\frac{V_{2,\pm}(t)}{\hbar} \\ i\,\frac{dB_\pm(t)}{dt} &= \frac{\hbar}{m}\,A_\pm(t)\,B_\pm(t) + \frac{V_{1,\pm}(t)}{\hbar} \\ i\,\frac{dC_\pm(t)}{dt} &= \frac{\hbar}{2\,m}\,\left[A_\pm(t) - B_\pm(t)^2\right] + \frac{V_{0,\pm}(t)}{\hbar}\,. \end{cases} \tag{7.19}$$

With $V_{k,\pm}$, $k = 0,1,2$, is defined by (7.11) and (7.13). Now writing $X(t) = x_1(t) + i\,x_2(t)$ where by X we mean A, B or C, it can be also shown that $c_{2,\pm}$ is solution of

$$\frac{dc_{\pm,2}(t)}{dt} = \frac{\hbar}{2\,m}\,\left[b_{1,\pm}^2 - b_{2,\pm}^2 - a_{1,i}\right] - \frac{V_{0,\pm}(t)}{\hbar} \tag{7.20}$$

Noting that

$$\langle z\rangle_\pm = \frac{b_{1,\pm}}{a_{1,\pm}} \quad\text{and}\quad \langle p\rangle_\pm = \hbar\,\left(b_{2,\pm} - a_{2,\pm}\,\langle z\rangle_\pm\right). \tag{7.21}$$

We can rewrite (7.20) to finally get

$$\boxed{\frac{dc_{\pm,2}(t)}{dt} = \frac{\hbar}{2\,m}\,\left[\langle z\rangle_\pm^2\,\left(a_{1,\pm}^2 - a_{2,\pm}^2\right) - 2\,\frac{\langle p\rangle_\pm\,\langle z\rangle_\pm}{\hbar}\,a_{2,\pm} - \frac{\langle p\rangle_\pm^2}{\hbar^2} - a_{\pm,1}\right] - \frac{V_{0,\pm}(t)}{\hbar}} \tag{7.22}$$

with

$$V_{0,\pm} = V_{B_0} + \left(\frac{m}{2}\,\omega_{SN}^2\,\langle z\rangle_\pm^2 - \frac{6}{5}\,\frac{G\,m^2}{R}\right)\,|\beta_\pm|^2 + \begin{cases} \left(\frac{m}{2}\,\omega_{SN}^2\,\langle z\rangle_\mp^2 - \frac{6}{5}\,\frac{G\,m^2}{R}\right)\,|\beta_\mp|^2 & \text{if} \quad |\langle z\rangle_+ - \langle z\rangle_-| \le 2R \\ -G\,m^2\,\frac{1}{|\langle z\rangle_+ - \langle z\rangle_-|}\,|\beta_\mp|^2 & \text{otherwise.} \end{cases}$$

Knowing $\langle z\rangle_\pm$, $\langle p\rangle_\pm$ and $A_\pm(t)$ allows us to solve this equation and to deduce the phase difference between the two quantum paths $|+\rangle$ and $|-\rangle$.

The expressions for $\langle z\rangle_\pm$ and $\langle p\rangle_\pm$ can be found in appendix 7.A.2. The functions $A_\pm(t)$

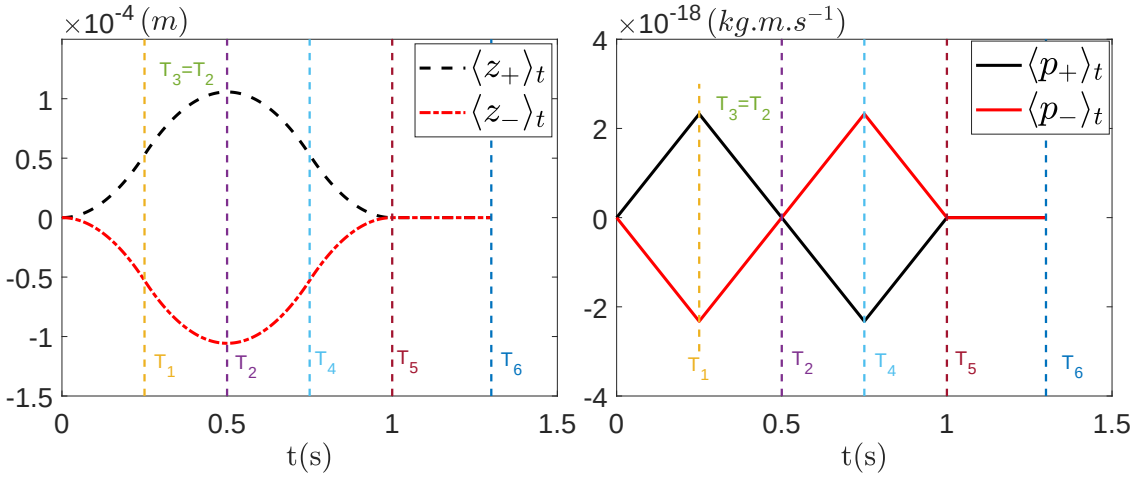

FIGURE 7.3: We illustrate here, the time evolution of $\langle z\rangle_\pm$ and $\langle p\rangle_\pm$. We rotated by 90° the figure 7.1, i.e.the z-axis here corresponds to the x-axis of figure 7.1

are solved in appendix 7.A.1 and are shown to obey

$$\boxed{A_\pm(t) = \nu\,\frac{m\,\omega_{SN}}{\hbar}\,\frac{1+c_0\,e^{-2i\nu\,t}}{1-c_0\,e^{-2i\nu\,t}}} \quad \text{with} \quad \boxed{\nu = \begin{cases} 1 & \text{if} \quad |\langle z\rangle_+ - \langle z\rangle_-| \leq 2R \\ |\beta_\pm| & \text{otherwise.} \end{cases}}$$

and with $c_0 = \frac{\hbar}{m\,\omega_{SN}}\left(\frac{A_0 - \nu\,m\omega_{SN}/\hbar}{A_0 + \nu\,m\omega_{SN}/\hbar}\right)$.

Note that the expression of $A_\pm(t)$ traduces the fact that (when $|\langle z\rangle_+ - \langle z\rangle_-| > 2R$) each part of the bi-localized mass oscillates at frequencies which are weighted by the square root of the quantum weight (i.e.by $|\beta_\pm|$) of the superposition. Actually, if we have a strict equality $|\beta_+| = |\beta_-| = 1/\sqrt{2}$ we find by symmetry that the phase shift is zero, i.e. we have $c_+ - c_- = 0$.

7.1.2.3 Numerical simulations

Let us illustrate, by means of numerical simulations, the experimental proposal discussed above (7.1.2). To do so we used the data reproduced from [4]. We consider a mesoscopic mass $m = 5.5 \cdot 10^{-15}$ kgs with radius $R = 1 \cdot 10^{-6}$ m, with an initial spread in position $\sigma_{x,0} = 10^{-9}$ m. We also considered $|\beta_+| = 1/\sqrt{2} - 0.1$ and we used a field gradient $B_0' = 10^6$ T.m^{-1}. For example, in figure 7.3 we plot the trajectories $\langle z\rangle_\pm$ and the momentum $\langle p\rangle_\pm$ of each wave packet whose expressions are found in appendix 7.A.2.

When the two wave packets ψ_L and ψ_R are recombined (using a magnetic field oriented in the opposite direction), the state becomes:

$$\Psi(z,t) = \left[\beta_+\,|+\rangle + \beta_- e^{-i\,\Delta\varphi(T)}\,|-\rangle\right]\,\psi(z,t), \quad \text{where} \quad \Delta\varphi(T) = (c_+ - c_-) \tag{7.23}$$

Where T is the total time of the experiment. In figure 7.4 (left) we plot the phase shift $\Delta\varphi(T)$ in the case where the packets are directly recombined (it corresponds in appendix 7.A.2 to the case $T_3 = T_2$). The phase shift is almost zero ($\sim -7 \cdot 10^{-3}$) in this particular case.

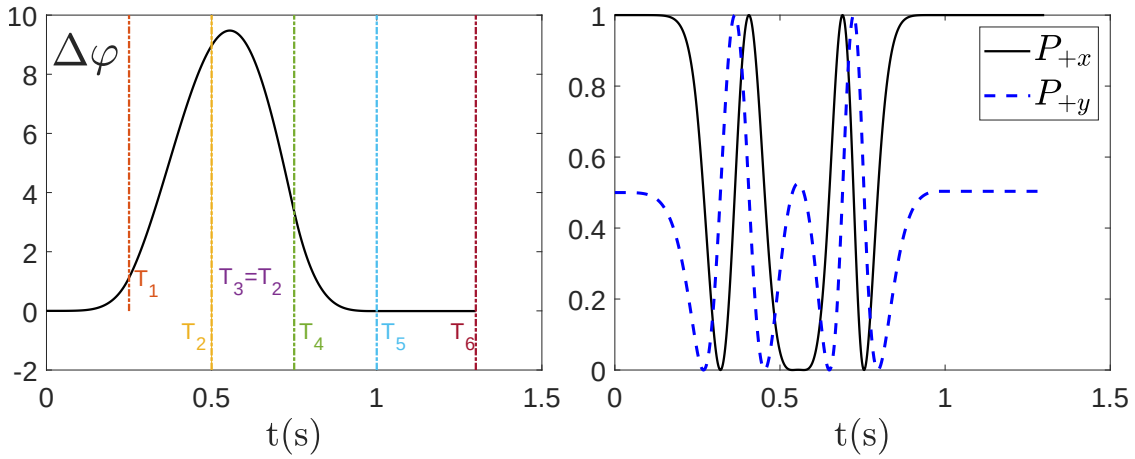

FIGURE 7.4: Left: we plot the phase shift in the case $T_3 = T_2$ (no free fall). Right: we plot the corresponding probability to find the state in $|x\rangle_+$ (resp. $|y\rangle_+$). Those plots are associated to the evolution 7.3. We chose $|\beta_+| = \frac{1}{\sqrt{2}} - 0.1$

The present model predicts Rabi oscillations (precession) (figure 7.4 : right) in the plane perpendicular to the direction of quantization z. In the plane (x, y) we get the following probabilities:

$$P_{\pm x} = \frac{1}{2}\left(1 \pm \cos(\Delta\varphi)\right) \quad \text{and} \quad P_{\pm y} = \frac{1}{2}\left(1 \mp \sin(\Delta)\right) \tag{7.24}$$

where the following basis have been used

$$|+/-\rangle_x = \frac{1}{\sqrt{2}}\left(|+\rangle \pm |-\rangle\right) \quad \text{and} \quad |+/-\rangle_y = \frac{1}{\sqrt{2}}\left(|+\rangle \pm i\,|-\rangle\right) \tag{7.25}$$

Actually, the phase shift is made by several and non-trivial contributions as can be seen in (7.23). If we naively only take account of the contribution $\frac{6}{5}\frac{Gm^2}{\hbar R}\left(T_3 - T_2\right)\left(|\beta_+|^2 - |\beta_-|^2\right)$ we expect to find a phase shift of the order of -60 for $T_3 - T_2 = 10$ s. However, compensations occur (that we cannot explain yet) so that the final phase shift taking account of the total contribution is of the order of $\Delta\varphi \sim -0.25$ as can be seen in figure 7.6. Measuring this phase shift would, in principle, enable us to reveal the existence of self-gravity *à la* Schrodinger-Newton.

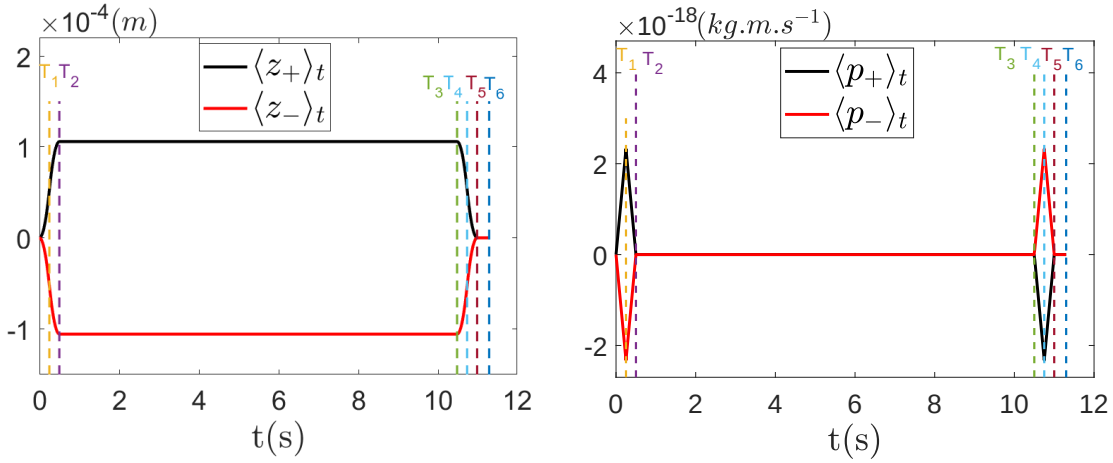

FIGURE 7.5: We illustrate here, the time evolution of $\langle z \rangle_{\pm}$ and $\langle p \rangle_{\pm}$.

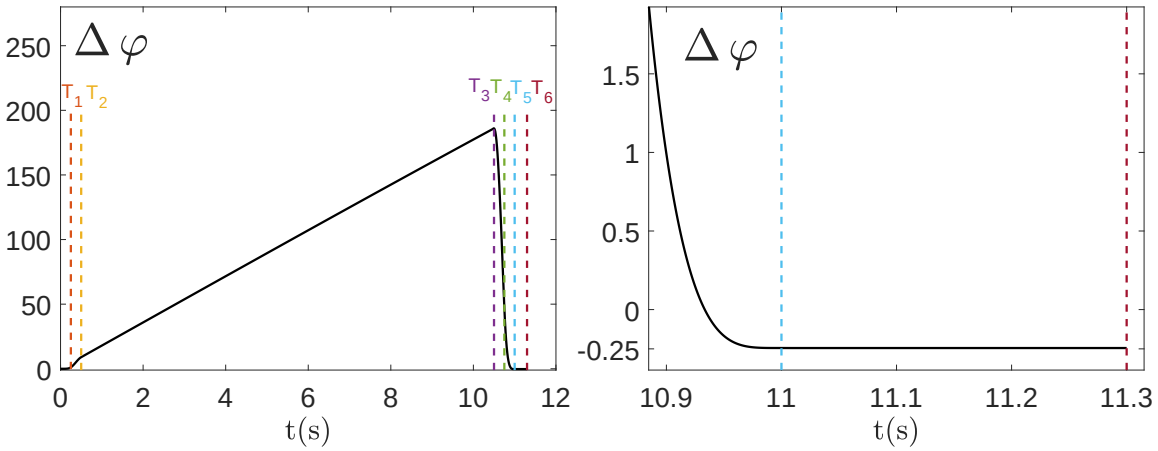

FIGURE 7.6: Left: we plot the phase shift in the case of a free fall of $T_3 - T_2 = 10$ s. Right: Zoom of the figure in the left. Note that the accumulated phase nearly vanishes during the recombination. Those plots are associated to the evolution 7.5. We chose $|\beta_+| = \frac{1}{\sqrt{2}} - 0.1$

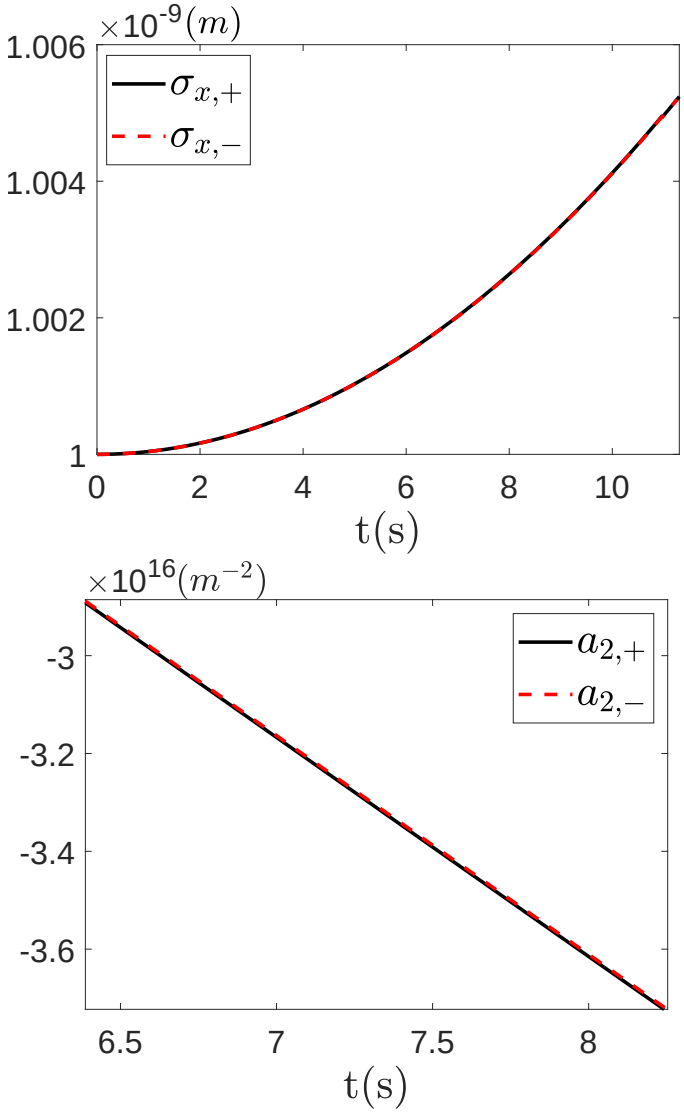

FIGURE 7.7: Left: we plot the spread in position of the wave packets $|+\rangle$ and $|-\rangle$, $\sigma_{x,\pm} = \frac{1}{\sqrt{2\,a_{1,\pm}}}$. Right: we plot $a_{2,\pm}$.

7.2 No-go theorems: nonlinearity vs. nonlocality and no-signaling

In realistic experiments, quantum decoherence is omnipresent and must be taken into account in the description. This idea brought us to study the inter-relation that exists between decoherence and non-linear modifications of the Schrodinger dynamics (especially in the case of the Schrodinger-Newton equation). By doing so, we emphasized the role played by the non-linearity to differentiate different realizations of the same master equation. Making use of GRW [10] model we simulate decoherence in presence of self-gravity.

7.2.1 Gisin's no-go theorem, realism and nonlocality.

Several authors [11], [3], [2] have shown that any non-linear modification of the Schrodinger equation will necessarily imply non-locality in configuration space. In particular, according to Gisin [3], those non-linear modifications would allow to distinguish different realizations of the same density matrix (see the no-signaling theorem in appendix 7.B). This idea is linked to what is called in the literature by mobility property [2] which was made explicit by Mielnik [12]. This property connects the presence of a nonlinearity in the dynamics to the possibility to differentiate non-orthogonal states, which ultimately makes it possible to differentiate two realizations of a same density matrix and thus two unravelings of a same master equation.

As written in [13] *" ... by performing a local measurement on a system A that is entangled with a distant system B, one is able, by collapsing the full wave function, to obtain realizations of the reduced density matrix of the system B which differ according to the choice of the measurement basis made in the region A. Therefore, in principle, nonlinearity can be a tool for sending classical information faster than light, contradicting the no-signaling property valid in the framework of linear quantum mechanics [3]."*

However there exist a class of collapse models (for example the QMUPL and the GRW model which are presented in appendix 7.C and 7.D) which are built with a suitable combination of non-linearity and stochasticity that forbid faster than light communications. This situation "of peaceful coexistence" between special relativity and quantum mechanics is made possible by the fact that the collapse is not a deterministic process but a stochastic one. This constitutes the so-called no-signaling condition (see appendix 7.B): due to the intrinsic quantum randomness of the collapse, it is actually impossible to send a classical signal faster than light. Therefore, as was shown by Gisin, in many collapse models (we can mention for example [10, 14, 15, 16, 17, 18]), when a collapse occurs the Born rule is preserved [19].

Now about the non-locality, as also written in [13]:

"... The question of nonlocality, as well as the question of relativistic invariance are problematic in all *realistic interpretations of the quantum theory. For instance, in an apparently Lorentz covariant collapse model (cf. appendix A of [13]) – the so-called flash ontology proposed by Tumulka [18] – it is assumed that spontaneous localizations are distributed according to a Lorentz-covariant distribution, when computed in different inertial frames. However, as noted in [20], one is always required in this model to select a privileged frame to begin with. Once such a frame is selected, Tumulka's model makes it possible to compute the influence of quantum jumps (flashes) on the wave function assigned to the system (here N non-interacting particles obeying Dirac's equation), but this aspect of the model is manifestly not Lorentz covariant, although the resulting distribution of quantum jumps (flashes or events in space-time)* is *Lorentz covariant.*

This is a general feature of dB-B and collapse models (and more generally of all collapse models, as explained in [21]): a privileged frame must be chosen in which nonlocality is necessarily present. It is however generally admitted that Gisin's no-go theorem does hold in the case of purely deterministic generalizations of the linear Schrödinger equation, such as the aforementioned Schrödinger-Newton equation (6.2) *[22, 23] or the NLS equation, for the simple reason that in the case of deterministic evolution equations, stochasticity is in principle absent..."*

This being said, there do exist several different ways to interpret Gisin's result as is explained in [13]. In particular, as mentioned in [13], a possible route for circumventing Gisin's theorem consists of identifying particles with solitonic solutions of a nonlinear modification of Schrödinger's equation. If, in accordance with the de Broglie double solution program, their trajectories would obey dB-B dynamics, then, making use of the aforementioned results concerning the Born rule and no-signaling (see e.g. the proof are given in appendix 7.B and in [13]), the no-signaling condition would be respected once the process of relaxation is achieved.

This problem has been discussed in the previous section, and it has been shown however that Ehrenfest's theorem causes serious problems regarding the derivation of the guidance equation, in the case of deterministic non-linear evolutions *à la* Schrodinger-Newton (see chapter 6). This brings us to another strategy which as explained in the same paper [13], consists of **Not circumventing Gisin's theorem**, that is to say in accepting the idea of the existence of a privileged reference frame in which supraluminal telegraphy is possible. Accepting the implications of Gisin's theorem, for instance in the framework of semi-classical gravity models *à la* Newton-Schrodinger, leads then to the question of when and where nonlocal, supraluminal communication is possible.

Actually, several experiments were performed by Gisin's group in the past [24] (see also [25] for proposals of similar tests to be realized in satellites) aimed at revealing hypothetical finite speed influences (spooky actions at a distance) that might occur during the collapse process. These experiments can be seen as quantum counterparts of similar experiments realized in the 19th century by Fizeau, Hoek, Michelson-Morley and others in order the reveal the existence of an hypothetical electro-magnetic aether.

As far as we know, however, no systematic study of nonlinearity induced signaling has been performed up to now. For instance, it is not clear yet to which extent the various nonlinear extensions of the Schrödinger equation mentioned in [13] have been ruled out by Gisin's experiments. Moreover, the self-gravitational coupling being very weak, one can expect the violation of the no-signaling property to be weak [23] as well, but to the best of our knowledge, a quantitative estimate of this violation has never been obtained. A way for doing so consists in realizing different unravellings of the same master equation expressing the decoherence that results from various couplings to the environment, in the presence of self-gravity, in order to explicitly estimate to which extent the non-linearity will differentiate the resulting density matrices. This idea is developed below.

7.3 A corollary of Gisin's no-go theorem: how to detect non-linearity making use of decoherence.

As written in [26]:

... Several experimental tests of the limits of the superposition principle have been proposed in the past, to be realized in the mesoscopic domain, which could reveal (or negate) the existence of the various extensions of the Schrödinger equation that have been proposed so far (spontaneous localization mechanism [27, 28], self-gravity [7, 29], etc.). Recent progress in quantum technology (in particular in quantum optomechanics [30]) nourishes the hope that it will soon be possible to scrutinize the superposition principle at the level of mesoscopic objects (e.g. nanospheres) of masses larger than 10^6 a.m.u. [31, 32, 33, 34]. Typically, the experiments proposed so far consist in measuring the decay of interferences exhibited by these objects and in checking whether this decay can be explained solely in terms of environmental (non-exotic) decoherence sources. The realization of these experiments would make it possible, among others, to test the validity of exotic decoherence models for spontaneous localization such as the Ghirardi-Rimini-Weber (GRW) [10], Pearle [14] and Continuous Spontaneous Localisation (CSL) [35] models (for an extensive review of these models we invite the reader to consult reference [15])...

As has been shown [26] in the past, non-interferometric versions of such experiments are not only sensitive to decoherence, but could also possibly reveal the influence of self-gravitational effects at the classical-quantum transition. In the same paper it has been shown that, due to the non-linearity of the Schrödinger-Newton equation, the usual treatment in terms of master equations is not relevant because different realizations of the same density matrix do not necessarily lead to the same density matrix in the future [3], as explained before. New techniques have been developed, however, for dealing with these problems in the case of a freely falling nanoparticle [7, 26].

The present experimental proposal is a variation on the theme explored in [26], which is the interplay between decoherence and self-gravity. As a corollary of Gisin's theorem, we shall show here that different realizations of a same decoherence process can be differentiated in presence of self-gravity. Here we shall use the GRW model [10] as a model of decoherence. Readers who are not familiar with the present formalism are advised to read appendix 7.C and 7.D for a more detailed explanation. In these appendixes we present, among other things, the technical tools used in this chapter and we also discuss the stability of the GRW process.

7.4 Unraveling of the master equation

Let us first summarize the global idea that characterizes the GRW model (for more detail see appendix 7.D). In short, the GRW model is a model of spontaneous localization which can be used as a decoherence model. This process is characterized by a parameter that we shall call Λ which is the product of two other parameters that we shall call α and Γ. The first parameter, α is the inverse of the square of the localization length induced by a quantum jump and the second one, Γ is the inverse of the average time between two quantum jumps. The trick that we imagined for achieving this experimental proposal, is to choose several GRW realizations of decoherence characterized by a same decoherence parameter Λ (with $\Lambda = \alpha \cdot \Gamma$) but for different values of ϵ (with $\epsilon = \left(\frac{\hbar\,\alpha}{m\,\Gamma}\right)^{1/2}$), i.e. the product between α and Γ is the same while their ratio is different.

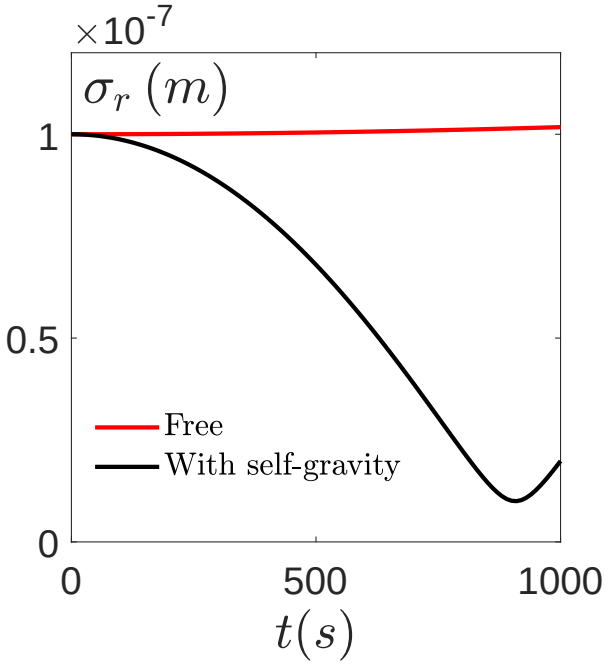

FIGURE 7.8: In this figure we plot the total spread in position of the center of mass wave function of a gold nanosphere of radius $R = 100$ nm and density $\rho = 20\,000$ kg.m^{-3}. This spread is ploted in the case of a free evolution and in the case of the Schrodinger-Newton equation following the algorithm proposed in [26]. Here we chose an initial spread $\sigma_{r,0} = 10^{-7}$ m and we used the value of Λ defined in (7.28).

Roughly speaking, to realize such quantum jumps, we may bombard the freely falling nanosphere with photons of wavelength of the order of $1/\sqrt{\alpha}$ at a rate Γ. We considered in what follows, four different GRW processes characterized by the same value of $\Lambda = \alpha \cdot \Gamma$ but for different values of $\epsilon = \left(\frac{\hbar\alpha}{m\Gamma}\right)^{1/2}$.

These unravellings are all characterized by an asymptotic value of the size $\sigma_i = \sqrt{Q_i}$ of the individual wave packets as explained in appendix 7.D. When ϵ is a small parameter, the size of the wave packet collapses to this (unique) asymptotic value after a few collisions. Otherwise, it oscillates between a maximal and a minimal value that can be estimated numerically and/or analytically in certain cases as we show in appendix.

In figure 7.9 we compare the time evolution of the individual quantum spreads in position in absence of self gravity, in the case of the GRW model and in the case of the QMUPL. In absence of self-gravity and in the limit $\epsilon \ll 1$, these processes are indistinguishable because they depends only on Λ (resp λ for the QMUPL model). In presence of self-gravity however the non-linearity may get activated provided the size of individual wave packets is of the order of the size of

$$R_L = \frac{\hbar^2}{Gm^3} \tag{7.26}$$

where R_L is known as the Lieb radius.

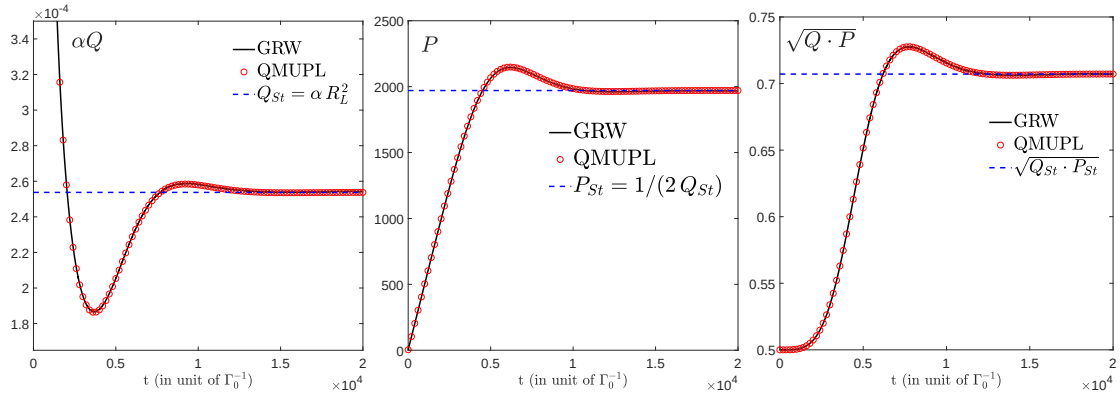

(A) (B) (C)

FIGURE 7.9: In this figure we plot the individual spread in position of the center of mass wave function of a nanosphere of radius $R = 100$ nm and density $\rho = 4\,000$ kg.m^{-3} using the GRW model 7.D and the QMUPL 7.C. In A we plot the individual spread in position $\sigma_{x,i} = \sqrt{\mathcal{Q}_i}$, in B we plot the individual spread in momentum $\sigma_{p,i} = \sqrt{\mathcal{P}_i}$ and in C we plot their product. The product $\mathcal{Q}_i\,\mathcal{P}_i$ converges to twice the value allowed by the Heisenberg saturation. Here $\epsilon = 3.59 \cdot 10^{-4}$, $\alpha = 2.05 \cdot 10^{11}$ m^{-2} and $\Gamma = 10\,\mathrm{s}^{-1}$.

It can be shown (see appendix 7.F equation (7.118) and also see [26]) that the condition to have the Lieb radius R_L as the asymptotic value of $\mathcal{Q}$ (the spread in position) constraint the value $\alpha\Gamma$ to

$$\Lambda = \alpha\,\Gamma = \frac{G^4\,m^{11}}{\hbar^7} \tag{7.27}$$

Indeed, we have for example in the case of the QMUPL model

$$\boxed{\mathcal{Q}^*_{qmupl} = \left(\frac{\hbar\,\alpha}{m} \cdot \frac{\alpha\,\hbar^7}{G^4\,m^{11}}\right)^{1/2} = \alpha\,R_L^2} \tag{7.28}$$

where here $\mathcal{Q}^*_{qmupl}$ is the dimensionless individual spread in position which is also the extent of the wave packet. For example in figure 7.9 appendix 7.D we plot the evolution of $\mathcal{Q}$ in the case of the GRW and the QMUPL model under the constraint (7.28). It can be seen that this spread converges to the Lieb radius as an asymptotic value.

In figure 7.8, we plot the total spread in position of the center of mass wave function of a gold nanosphere numerically solved from the Schrodinger equation with and without self gravity. In this regime, when Λ takes the value in (7.28), the effect of the self-gravity activated [26]. In addition, contrary to the spread (which can be related to the extent of the wave packet) obtained in the free evolution, the spread in the case with self-gravity does not increases indefinitely but oscillates. In figure 7.10 we plot the total spread in position in the case of the GRW model with and without self gravity for 10^4 realizations of the process. As shown in appendix equation (7.87), the theoretical value of the spread is predicted by the formula [10, 36]

$$\sigma_r(t) = \sigma_{r,0}\sqrt{1 + \frac{9\,\hbar^2\,t^2}{4\,m^2\,\sigma_{r,0}^4} + \frac{\Lambda\hbar^2\,t^3}{2\,m^2\sigma_0^2}}. \tag{7.29}$$

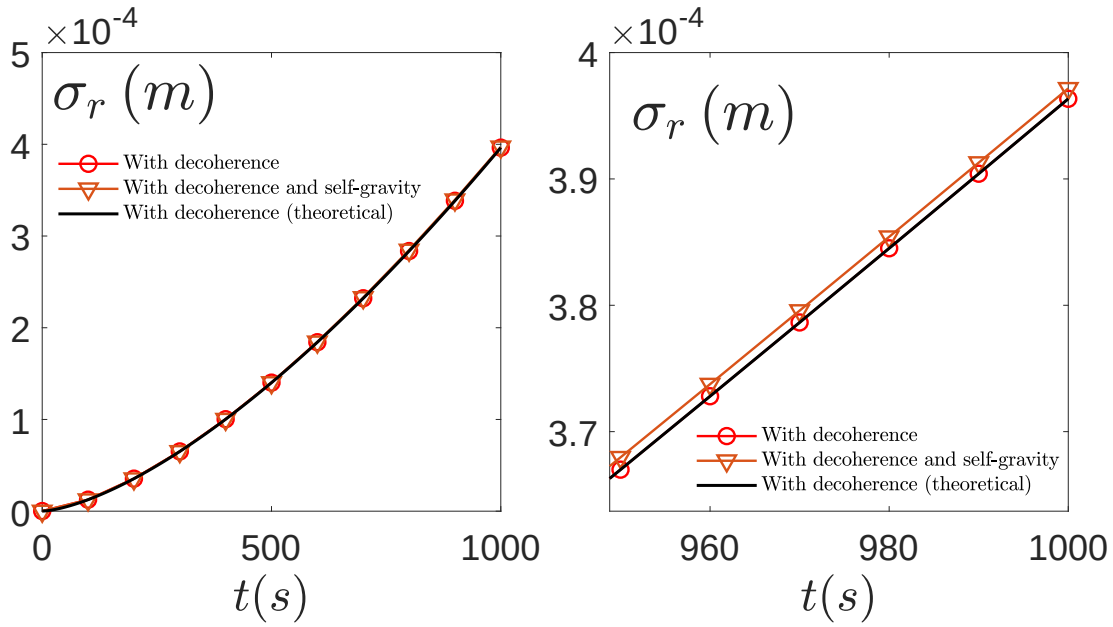

FIGURE 7.10: In this figure we plot (Left) the total spread in position of the center of mass wave function of a gold nanosphere of radius $R = 100$ nm and density $\rho = 20\,000$ kg.m^{-3}. In the Right we plot a zoom of the figure in the left. This spread was computed from the GRW model for 10^4 realizations and is plotted in the case with and without sefl-gravity *à la* Schrodinger-Newton. Here we chose an initial spread $\sigma_{r,0} = 10^{-7}$ m and we used the value of Λ defined in (7.28).

The figure 7.10 confirms the validity of our numerical simulations since it is in agreement with the theoretical function (7.29). The final results are encapsulated in figure 7.11 where it is shown that, indeed, different unravellings of a same master equation (in absence of self-gravity) get differentiated in the case of self-gravity.

7.5 Conclusion:

Here we proposed two experimental tests aimed at putting into evidence the existence of a non-linear self-interaction à la Schrodinger-Newton. The first test involved a Humpty-Dumpty Stern-Gerlach experiment. Such an experiment has actually not yet been realized, due to limitations imposed by decoherence, but hopefully it could be realized in a near future, being given the serious progresses realizing in the previous decades in trapping and cooling mesoscopic quantum systems in processes characterized by a very low degree of decoherence (very low temperatures and nearly perfect vacuum). The second one implements the idea that decoherence can be used as a tool for controlling and tailoring the evolution of a quantum system. Moreover it incorporates the concept of mobility which is central in the derivation of Gisin's famous no-go theorem about non-linearity. This theorem relates the presence of a non-linearity to the violation of quantum signaling.

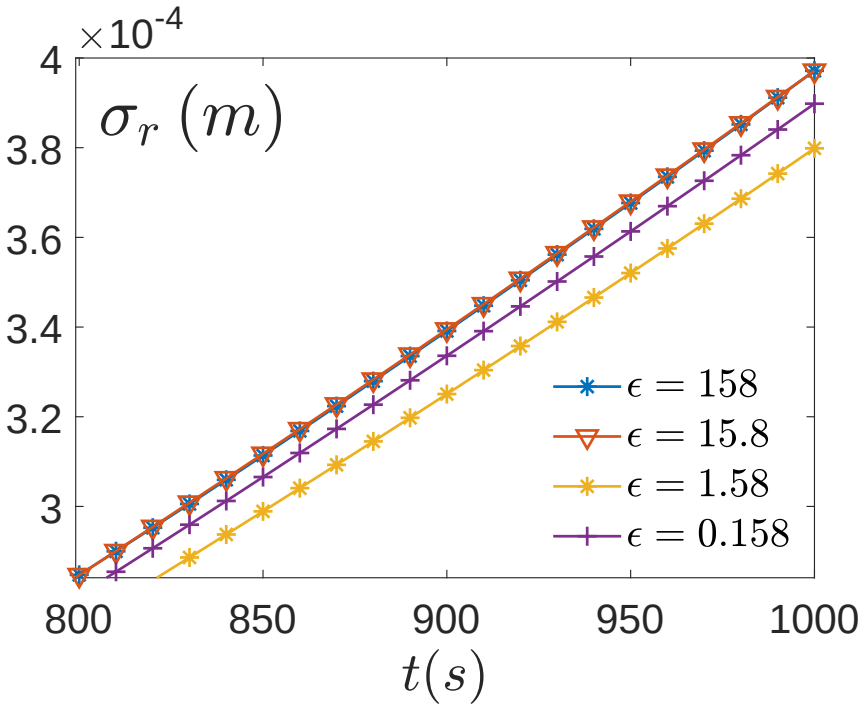

FIGURE 7.11: Here we illustrate four unravelings of the same density matrix associated to the GRW model for 10^4 realizations of the process. In other words we plot the spread in position of the center of mass wavefunction for the same value Λ but for different ϵ. Here we chose a gold nanosphere of radius $R = 100$ nm with a density $\rho = 20\,000$ kg.m^{-3} and we chose an initial spread $\sigma_{r,0} = 10^{-7}$ m.

7.A Humpty-Dumpty Stern-Gerlach experiment

7.A.1 Equation of $A_\pm(t)$

Here the following equation for $A_\pm(t)$ is solved

$$i\,\frac{dA_\pm(t)}{dt} = \frac{\hbar}{m}\,A_\pm(t)^2 - 2\,\frac{V_{2,\pm}(t)}{\hbar} \tag{7.30}$$

where

$$V_{2,\pm}(t) = \begin{cases} \frac{m\,\omega_{SN}^2}{2} & \text{if} \quad |\langle z\rangle_+ - \langle z\rangle_-| \leq 2R \\ \frac{m\,\omega_{SN}^2}{2} & |\beta_\pm|^2 \quad \text{otherwise.} \end{cases} \tag{7.31}$$

It is useful to use a set of dimensionless variables such that

$$X(t) = A_\pm(t)\,L^2 \quad \text{and} \quad s = \omega_{SN}\,t \tag{7.32}$$

with

$$L^2 = \frac{\hbar}{m\,\omega_{SN}} \tag{7.33}$$

Thus we get

$$i\,\frac{dX}{ds} = X^2 - \nu^2 \quad \text{where} \quad \nu^2 = \begin{cases} 1 & \text{if} \quad |\langle z\rangle_+ - \langle z\rangle_-| \leq 2R \\ |\beta_\pm|^2 & \text{otherwise.} \end{cases} \tag{7.34}$$

then

$$\frac{dX}{(X-\nu)\,(X+\nu)} = -i\,ds \tag{7.35}$$

which can be put in the form

$$\frac{dX}{2\,\nu}\left(\frac{1}{X-\nu} - \frac{1}{X+\nu}\right) = -i\,ds \tag{7.36}$$

after integration we get

$$\ln\left(\frac{X-\nu}{X+\nu}\,\frac{X_0-\nu}{X_0+\nu}\right) = -2i\nu\,s \tag{7.37}$$

with $X_0 = X(t=0)$ and $c_0 = \frac{X_0-\nu}{X_0+\nu}$. Finally it reads

$$\boxed{X(s) = \nu\,\frac{1+c_0\,e^{-2i\nu\,s}}{1-c_0\,e^{-2i\nu\,s}}} \quad \text{or} \quad \boxed{A_\pm(t) = \nu\,\frac{m\,\omega_{SN}}{\hbar}\,\frac{1+c_0\,e^{-2i\nu\,t}}{1-c_0\,e^{-2i\nu\,t}}}$$

with

$$\nu = \begin{cases} 1 & \text{if} \quad |\langle z\rangle_+ - \langle z\rangle_-| \leq 2R \\ |\beta_\pm| & \text{otherwise.} \end{cases} \tag{7.38}$$

7.A.2 Time evolution (see figure 7.5)

- $T_0 \longrightarrow T_1$

$$\langle p_\pm \rangle = \pm \frac{g\mu_B}{2} B_0' \, t \quad \text{and} \quad \langle z_\pm \rangle = \pm \frac{g\mu_B}{4\,m} B_0' \, t^2 \tag{7.39}$$

- $T_1 \longrightarrow T_2$

$$\langle p_\pm \rangle = \mp \frac{g\mu_B}{2} B_0' \, (t - 2\,T_1) \quad \text{and} \quad \langle z_\pm \rangle = \mp \frac{g\mu_B}{4\,m} B_0' \, \left(t^2 - 4\,T_1\,t + 2\,T_1^2\right) \tag{7.40}$$

- $T_2 \longrightarrow T_3$

$$\langle p_\pm \rangle = 0 \quad \text{and} \quad \langle z_\pm \rangle = \pm \frac{g\mu_B}{2\,m} B_0' \, T_1^2 \tag{7.41}$$

- $T_3 \longrightarrow T_4$

$$\langle p_\pm \rangle = \mp \frac{g\mu_B}{2} B_0' \, (t - T_3) \quad \text{and} \quad \langle z_\pm \rangle = \mp \frac{g\mu_B}{4\,m} B_0' \, \left[(t - T_3)^2 - 2\,T_1^2\right) \tag{7.42}$$

- $T_4 \longrightarrow T_5$

$$\langle p_\pm \rangle = \pm \frac{g\mu_B}{2} B_0' \, (t - T_5) \quad \text{and} \quad \langle z_\pm \rangle = \pm \frac{g\mu_B}{4\,m} B_0' \, (t - T_5]^2 \tag{7.43}$$

Note that in order to achieve the recombination we must require that

$$T_2 - T_1 = T_4 - T_3 = T_5 - T_4 = T_1 \tag{7.44}$$

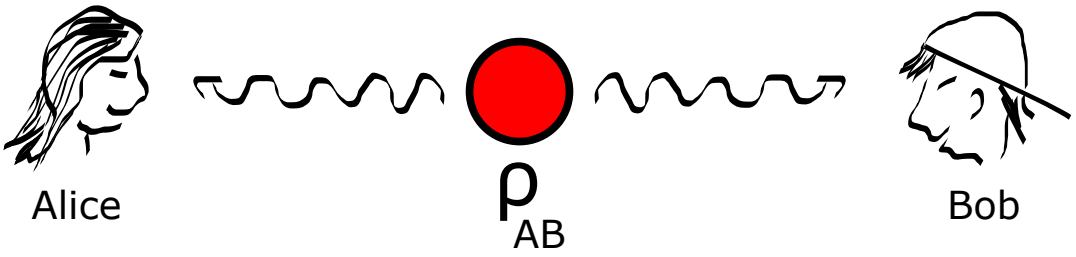

FIGURE 7.12: Alice and Bob sharing an entangled state.

7.B Collapse and causality: no-signaling theorem

The thought experiment below helps to understand the link that exists between the collapse of the wave function and the causality through the no-signaling theorem. Let us consider a quantum system made by a pair of entangled state (for example photons). Now suppose that Alice and Bob share this entangled state and are spatially separated. In other words, a part of the state goes to the left (Alice) and the other part to the right (Bob). Now imagine that Alice has the possibility to measure, from this state, two quantities say $\widehat{O}_1^A$ or $\widehat{O}_2^A$. Using the spectral decomposition we can write $\widehat{O}_j^A = \sum_n o_{n,j}^A \widehat{P}_{n,j}^A$ with $j = 1, 2$.

If Alice decides to perform a measurement, the state of Bob reduces to the statistical mixture defined in the following way:

$$\rho_B^j = \sum_n p_n^j \frac{\left(\widehat{P}_{n,j}^A \otimes \mathcal{I}^B\right) \rho_{AB} \left(\widehat{P}_{n,j}^A \otimes \mathcal{I}^B\right)}{Tr\left[\left(\widehat{P}_{n,j}^A \otimes \mathcal{I}^B\right) \rho_{AB}\right]} \tag{7.45}$$

- In the numerator the total state ρ_{AB} is projected into the corresponding eigenvalue obtained by Alice, this is the collapsed state:

$$\left(\widehat{P}_{n,j}^A \otimes \mathcal{I}^B\right) \rho_{AB} \left(\widehat{P}_{n,j}^A \otimes \mathcal{I}^B\right) \tag{7.46}$$

- The denominator is the normalization of the projected state

$$Tr\left[\left(\widehat{P}_{n,j}^A \otimes \mathcal{I}^B\right) \rho_{AB}\right] \tag{7.47}$$

- p_n^j is the Born rule corresponding to the superposition of the mixture. Actually, this probability is also the probability that Alice has found the eigenvalue $o_{n,j}^A$.

$$p_n^j = Tr\left[\left(\widehat{P}_{n,j}^A \otimes \mathcal{I}^B\right) \rho_{AB}\right] \tag{7.48}$$

So the expression above (7.45) can be simplified

$$\rho_B^j = \sum_n \left(\widehat{P}_{n,j}^A \otimes \mathcal{I}^B\right) \rho_{AB} \left(\widehat{P}_{n,j}^A \otimes \mathcal{I}^B\right) \tag{7.49}$$

The collapse is by definition non-linear because it suppresses the superposition, but as we see (7.49) is linear in the density matrix.

Finally, (7.49) is simply the partial trace of the global state with respect to Alice state:

$$\rho_B^j = Tr_A[\,\rho_{AB}\,] \tag{7.50}$$

So the important thing to notice is that the effect of the measurement of Alice implies a linear operation $Tr_A[\,...\,]$ on the global state ρ_{AB}. Bob perceives Alice measurement as a linear quantum operation performed on the state. This simplification is made possible on the one hand because of the linearity of the mathematical quantum operation and on the second because p_n^j is the Born rule which is also the normalization in the denominator. This process preserves Bob's reduced density matrix (7.49) which prevents superluminal signaling. If Bob makes the measurement before or after Alice, nothing changes in the statistics of his outcomes which are given by the reduced density matrix.

7.C The QMUPL model

We saw in chapter 6 that the linearity of the quantum theory is at the foundation of the measurement problem. A way to solve the measurement problem and to avoid a possible violation of the causality through 7.B, is to reconsider the way we deal with the quantum evolution by modifying the Schrodinger equation. This modification can be done, for example, with a suitable combination of nonlinear and stochastic terms in such a way that the Gisin no-go theorem is still respected. This procedure is at the foundations of the collapse models which are quickly discussed in this appendix.

7.C.1 Definitions

Let us start by considering a toy model, i.e.the Quantum Mechanics with Universal Position Localization (QMUPL) model. It has been initially proposed [37] by Gisin and Percival in 1992 to explain the collapse of the wave function and have been studied in detail in [38]. This model has the peculiarity of being mathematically simple but allowing the description of a large number of physical phenomenons. We consider a state $|\Psi\rangle$ defined in a Hilbert space and subject to continuous and stochastic collapses in position. The general evolution can be put in the Ito form:

$$d\,|\Psi\rangle = \underbrace{-\frac{i}{\hbar}\widehat{H}\,|\Psi\rangle\,dt}_{\text{Schrodinger evolution}} + \underbrace{\widehat{\mathcal{D}}\,|\Psi\rangle\,dt}_{\text{Deterministic drift}} + \underbrace{\sum_n \widehat{\mathcal{S}}_n\,|\Psi\rangle\,dW_n}_{\text{Stochastic terms}} \tag{7.51}$$

Where $\widehat{\mathcal{D}}$ and $\widehat{\mathcal{S}}_n$ are quantum operators acting on the state $|\Psi\rangle$ and dW_n a complex Wigner process with the following properties:

$$dW_n(t)\,dt = 0, \qquad dW_n(t)\,dW_m(t) = 0, \qquad \text{and} \qquad dW_m(t)\,\overline{dW_n}(t') = \delta_{mn}\,dt. \tag{7.52}$$

For the next it is necessary to remind the formula of the Ito product:

$$d\,(\mathcal{X}_t\mathcal{Y}_t) = \mathcal{Y}_t\,d\mathcal{X}_t + \mathcal{X}_t\,d\mathcal{Y}_t + d\mathcal{X}_t\,d\mathcal{Y}_t. \tag{7.53}$$

Using this formula and the normalization condition $d\langle\Psi|\Psi\rangle = 0$ leads to the following constraints for the operators $\widehat{\mathcal{D}}$ and $\widehat{\mathcal{S}}_n$:

$$\langle\Psi|\,\widehat{\mathcal{D}} + \widehat{\mathcal{D}}^\dagger + \sum_n \widehat{\mathcal{S}}_n^\dagger \widehat{\mathcal{S}}_n\,|\Psi\rangle = 0 \tag{7.54}$$

$$\langle\Psi|\,\widehat{\mathcal{S}}_n\,|\Psi\rangle = 0 \tag{7.55}$$

In particular, the QMUPL model is constructed to collapse the quantum state in position so that $\widehat{\mathcal{D}}$ and $\widehat{\mathcal{S}}_n$ are chosen as follows:

$$\widehat{\mathcal{S}}_n = \sqrt{\lambda_n}(\widehat{x}_n - \langle\widehat{x}_n\rangle), \qquad \widehat{\mathcal{D}} = -\sum_n \frac{\lambda_n}{2}\,(\widehat{x}_n - \langle\widehat{x}_n\rangle)^2, \tag{7.56}$$

where λ_i is a phenomenological parameter describing the "strength" of the collapse felt by the particle i when collapsing into the position $\langle\widehat{x}_i\rangle$. In summary the QMPUL model is defined by the following Ito differential equation:

$$d\,|\Psi\rangle = \left[-\frac{i}{\hbar}\widehat{H}\,dt - \sum_n \frac{\lambda_n}{2}\,(\widehat{x}_n - \langle\widehat{x}_n\rangle)^2\,dt + \sqrt{\lambda_n}\sum_n (\widehat{x}_n - \langle\widehat{x}_n\rangle)\,dW_n\right]|\Psi\rangle\,. \tag{7.57}$$

Note that the term $(\widehat{x}_n - \langle\widehat{x}_n\rangle)^2$ is reminiscent of the evolution in the framework of the Schrodinger Newton (6.9) in the quadratic regime but with an imaginary spring constant. Moreover, it is shown in [38] (whre the QMUPL model is used as a spontaneous localization model) that the parameter λ grows proportionally to the mass:

$$\lambda = \frac{m}{m_0}\lambda_0 \tag{7.58}$$

where m_0 is chosen to be the mass of a nucleon $m_0 = 1{,}67.10^{-27}$ kg and λ_0 is purely phenomenological. However, we will briefly see in the next subsection that it can also be related to the quantum decoherence parameter within the framework of open quantum systems.

7.C.2 The master equation of the QMUPL model

For simplicity, let us start in the case of a single particle:

$$d\,|\Psi\rangle = \left[-\frac{i}{\hbar}\widehat{H}\,dt - \frac{\lambda}{2}\,(\widehat{x} - \langle\widehat{x}\rangle)^2\,dt + \sqrt{\lambda}\,(\widehat{x} - \langle\widehat{x}\rangle)\,dW\right]|\Psi\rangle\,. \tag{7.59}$$

From that Ito form we can define the stochastic density matrix such as $d\rho_t = d\,(|\Psi\rangle\langle\Psi|)$ which using 7.53 can be shown to evolve according to:

$$d\rho_t = \underbrace{-\frac{i}{\hbar}\left[\widehat{H}, \rho_t\right]\,dt}_{\text{Schrodinger evolution}} \underbrace{-\frac{\lambda}{2}\left\{\widehat{x}^2\,\rho_t + \rho_t\,\widehat{x}^2 - 2\,\widehat{x}\,\rho_t\,\widehat{x}\right\}\,dt}_{\text{Jump operator in position}} \tag{7.60}$$

$$\underbrace{+\sqrt{\lambda}\,\left[(\widehat{x} - \langle\widehat{x}\rangle)\rho_t\,dW + \rho_t(\widehat{x} - \langle\widehat{x}\rangle)\,\overline{dW}\right]}_{\text{Stochastic terms}} \tag{7.61}$$

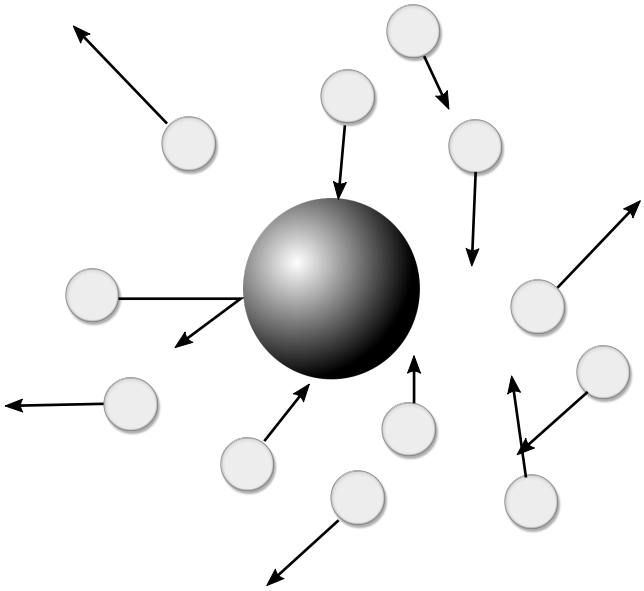

FIGURE 7.13: Here we illustrate the decoherence induced by the scattering of environmental particles.

Now taking the average over many realizations $\mathbb{E}[d\rho_t]$ gives the evolution for the quantum density matrix ρ which is defined as $\rho = \mathbb{E}[\rho_t]$. Where here $\mathbb{E}[\cdot]$ denotes the mathematical average over many realizations of the stochastic process. As a result, the master equation for the density matrix takes the following Lindblad form:

$$\frac{d\rho}{dt} = -\frac{i}{\hbar}\left[\widehat{H},\rho\right] - \frac{1}{2}\left(\widehat{L}^{\dagger}\widehat{L}\rho + \rho\widehat{L}^{\dagger}\widehat{L} - 2\,\widehat{L}\,\rho L^{\dagger}\right) \tag{7.62}$$

with $\widehat{L} = \sqrt{\lambda}\,\widehat{x}$. The Lindblad form has the particularity to preserve on the one hand the linearity of ρ while on the other it preserves the hermicity of ρ and its normalization (the sum of the eigenvalues is still equals to unity, i.e.Tr$[\rho] = 1$).

The master equation 7.62 can be put in the following compact form:

$$\frac{d\rho}{dt} = -\frac{i}{\hbar}\left[\widehat{H},\rho\right] - \frac{\lambda}{2}\left[\widehat{x},[\widehat{x},\rho]\right] \tag{7.63}$$

which in the position representation $\langle y|\,\rho\,|x\rangle$ is rewritten as:

$$\frac{\partial\rho(\mathbf{x},\mathbf{y},t)}{dt} = -\frac{i\hbar}{2\,m}\left(\frac{\partial^2}{\partial\mathbf{y}^2} - \frac{\partial^2}{\partial\mathbf{x}^2}\right)\rho(\mathbf{x},\mathbf{y},t) - \frac{\lambda}{2}\,(\mathbf{x}-\mathbf{y})^2\,\rho(\mathbf{x},\mathbf{y},t) \tag{7.64}$$

This equation corresponds to a limit case of the GRW model that we shall define in section 7.D.

7.C.3 Link with the quantum decoherence

The master equation 7.64 and the parameter λ can be interpreted in terms of quantum decoherence. In the common interpretation, it is agreed that a superposition of microscopic state can be created experimentally.

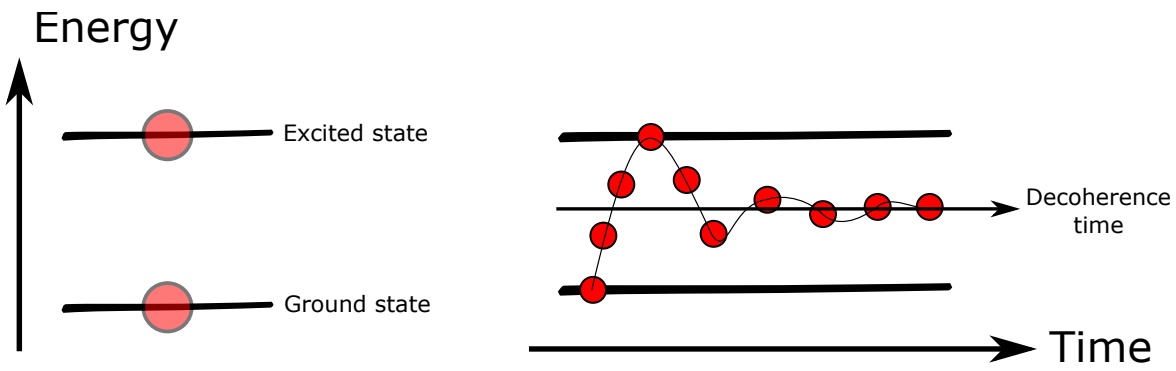

FIGURE 7.14: Rabi oscillations versus decoherence.

For example, if one applies a coherent electromagnetic field with a proper frequency on a quantum two levels atom (see figure 7.14) , the later will experience Rabi oscillation between its ground and its excited state. The superposition principle has been tested for electrons, neutrons and small atoms in [39, 40]. In a realistic experiment, the atom is never isolated completely, he can for example undergo collisions with other atoms or can be interacting with a thermal bath (see figure 7.13). In that case, the superposition disappears after a certain time known as decoherence time. As explained in [36] (p.131), in the case of localizations due to environmental scattering, the change of the reduced density matrix (in the position representation) is shown to evolve according to the equation :

$$\frac{\partial \rho(\mathbf{x},\mathbf{y},t)}{dt} = -\frac{i\hbar}{2\,m}\left(\frac{\partial^2}{\partial \mathbf{y}^2} - \frac{\partial^2}{\partial \mathbf{x}^2}\right)\rho(\mathbf{x},\mathbf{y},t) - \Lambda_{sc}\,(\mathbf{x}-\mathbf{y})^2\,\rho(\mathbf{x},\mathbf{y},t) \tag{7.65}$$

where Λ_{sc} is the scattering constant containing the details of the interaction and which is computed in the long wavelength limit ([36] p.130). The above master equation is exactly the one derived in the QMUPL model 7.64 if one identifies the Lindblad coefficient $\lambda/2$ with the scattering constant Λ_{sc}. Hence, the coefficient λ can be interpreted as a scattering constant which encapsulates the informations of the interaction with the environment.

For example in figure (7.15) we illustrate this effect on the density matrix $\rho(\mathbf{x},\mathbf{y},t)$ at two different times using an initial wavefunction made by a superposition of two gaussians :

$$\Psi(x,0) = N\left[e^{-\frac{(x-\mathrm{x0})^2}{4\sigma_x^2}} + e^{-\frac{(x+\mathrm{x0})^2}{4\sigma_x^2}}\right] \tag{7.66}$$

The anti-diagonal terms of the density matrix $\rho(\mathbf{x},\mathbf{y},t)$ tend to zero with a characteristic timescale of spatial interference:

$$\tau_D = \frac{2}{\lambda\,(x-y)^2}. \tag{7.67}$$

Using this analogy we will in chapter 8 study the inter-relation between decoherence and the doppler cooling.

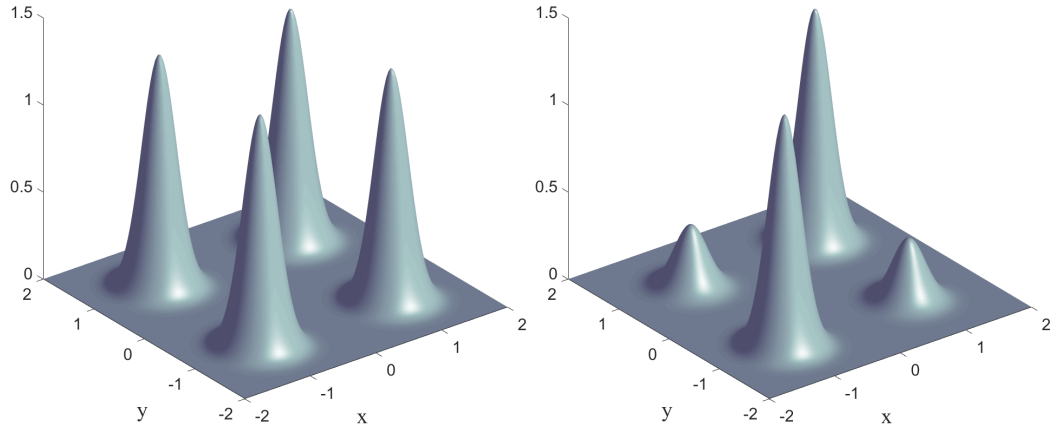

FIGURE 7.15: Here we illustrate the effect of decoherence in the anti-diagonal terms of the density matrix $\rho(\mathbf{x}, \mathbf{y}, t)$.

7.D Decoherence in the GRW model

The collapse model we present in this section will be also used in the next chapter as a model of decoherence in the Doppler cooling. Here, we shall focus on the stability of the GRW process. In addition we will compare the predictions made by this model with the QMUPL model introduced in section 7.C. In particular, we will see that it is roughly the same formalism as the one developed for the QMUPL model excepted that the collapse in the GRW model is not a continuous process.

7.D.0.1 Quantum decoherence *à la* GRW

In the GRW model the collapse in positions of the wavefunction occurs spontaneously in time following a Poisson time-distribution. The model is described and characterized by two parameters; i.e.a characteristic length $1/\sqrt{\alpha}$ which provides informations about the spatial interval in which the collapse can occur and a characteristic frequency Γ which is the frequency of the Poisson distribution of the quantum jumps. Note that in the GRW model (as well as in the QMUPL model), the frequency increases proportionally to the number of particles; this is why, according to these models, a macroscopic object is well localized in space, in the sens that its center of mass has always a well localized position. As the QMUPL model, the GRW model provides useful tools for simulating the quantum decoherence process.

In a nutshell, the density matrix ρ in the GRW model is solution of the following master equation:

$$\frac{d\rho}{dt} = -\frac{i}{\hbar}\,[H,\rho] - \Gamma\,(\,\rho - T[\rho]\,) \tag{7.68}$$

where Γ is the frequency of localizations and $T[\rho]$ is a superoperator acting on ρ in the following way:

$$T[\rho] = \int d^3x\, \widehat{J}_x\, |\Psi\rangle\, \langle\Psi|\, \widehat{J}_x \quad \text{with} \quad \widehat{J}_x = \left(\frac{\alpha}{\pi}\right)^{3/4} \exp\left(-\frac{\alpha}{2}\,(\widehat{x}-a)^2\right) \tag{7.69}$$

$\widehat{J}_x$ is the so-called jump factor which in the GRW model takes the form of a normalised Gaussian function and α provides informations about the spatial interval in which the localization occurs. The master equation (7.68) can be rewritten in the position representation (by taking the operation $\langle x| \dots |y\rangle$) as:

$$\frac{\partial \rho(\mathbf{x},\mathbf{y},t)}{dt} = -\frac{i\hbar}{2\,m}\left(\frac{\partial^2}{\partial \mathbf{y}^2} - \frac{\partial^2}{\partial \mathbf{x}^2}\right)\rho(\mathbf{x},\mathbf{y},t) - \Gamma\left(1 - e^{-\frac{\alpha}{4}(\mathbf{x}-\mathbf{y})^2}\right)\rho(\mathbf{x},\mathbf{y},t) \tag{7.70}$$

The probability of collapsing the wave function in a time interval dt is then given by $\Gamma\,dt$, otherwise there is a probability $1-\Gamma\,dt$ that the evolution follows the Schrodinger equation. The second term in the right will cause an exponential decay of the non-diagonal terms. To see it, let us consider this second term only:

$$\frac{\partial \rho(\mathbf{x},\mathbf{y},t)}{dt} = -\Gamma\left(1 - e^{-\frac{\alpha}{4}(\mathbf{x}-\mathbf{y})^2}\right)\rho(\mathbf{x},\mathbf{y},t) \tag{7.71}$$

It is important to note that if the region of localization is quite larger than the size of individual wavefunctions $|\mathbf{x}-\mathbf{y}| \ll \frac{1}{\sqrt{\alpha}}$ (the so-called long wavelength limit (LWL)) then [10] we get from (7.71)

$$\frac{\partial \rho(\mathbf{x},\mathbf{y},t)}{dt} = -\frac{\alpha\,\Gamma}{4}\,(\mathbf{x}-\mathbf{y})^2\,\rho(\mathbf{x},\mathbf{y},t) \tag{7.72}$$

This is almost the same master equation previously found in (7.64) (up to a factor 2) and found in (7.65) (up to a factor 4). We can then deduce (in this regime) the link between decoherence and collapse models *à la* GRW (resp. QMUPL) through the correspondence :

$$\lambda = \frac{\alpha\,\Gamma}{2} \quad \text{and} \quad \lambda = 2\,\Lambda_{sc} \tag{7.73}$$

where λ is the collapse parameter of the QMUPL model, the parameters $\alpha\,\Gamma$ comes from the GRW model and Λ_{sc} is the scattering constant containing the details of the interaction with the environment.

Actually in the GRW model, a large number of properties only depend on the product of Γ and α:

$$\Lambda = \alpha \cdot \Gamma \tag{7.74}$$

In the other limit (short wavelength limit (SWL)) defined by $|\mathbf{x}-\mathbf{y}| \gg \frac{1}{\sqrt{\alpha}}$, the master equation for the density matrix reduces to the von Neumann equation [10]

$$\frac{\partial \rho(\mathbf{x},\mathbf{y},t)}{dt} = -\frac{i\hbar}{2\,m}\left(\frac{\partial^2}{\partial \mathbf{y}^2} - \frac{\partial^2}{\partial \mathbf{x}^2}\right)\rho(\mathbf{x},\mathbf{y},t) - \Gamma\,\rho(\mathbf{x},\mathbf{y},t) \tag{7.75}$$

The advantage of the GRW Monte Carlo-type unravelling of the decoherence process is that it contains both regimes (both master equations (7.72) and (7.75)) as limiting cases, which makes it an excellent model for mimicking decoherence [41] in the case where, throughout the evolution, the system would pass through different regimes (SWL and LWL).

7.D.0.2 Useful formulas for the GRW model

By definition (7.69), the GRW model is built to preserve gaussian states. Let us first consider a gaussian state at 1D of the form

$$\psi(x,t) = \frac{1}{\mathcal{N}} \exp^{-A(t)\,x^2/2 + B(t)\,x}, \quad \text{where} \quad \frac{1}{\mathcal{N}} = \left(\frac{\text{Re } A_i}{\pi}\right)^{\frac{1}{4}} \exp\left(-\frac{\text{Re}^2\ B_i}{2\,\text{Re } A_i}\right). \tag{7.76}$$

and where $A(t)$ and $B(t)$ are complex functions of time. From these functions it can be shown that the average position $\langle q_i \rangle$ and momentum $\langle p_i \rangle$ evolve according to

$$\langle q_i \rangle = \frac{\text{Re } B_i}{\text{Re } A_i}, \quad \langle p_i \rangle = m \langle v_i \rangle = \hbar \frac{\text{Im } B_i \text{ Re } A_i - \text{Im } A_i \text{ Re } B_i}{\text{Re } A_i} \tag{7.77}$$

and the corresponding variance in position $\mathcal{Q}$ and in momentum $\mathcal{P}$ evolve according to

$$\mathcal{Q}_i = \langle q_i^2 \rangle - \langle q_i \rangle^2 = \frac{1}{2\ \text{Re } A_i}, \quad \mathcal{P}_i = m^2 \left(\langle v_i^2 \rangle - \langle v_i \rangle^2\right) = \frac{\hbar^2}{2\ \text{Re } A_i} |A_i|^2 \tag{7.78}$$

It is also useful to introduce the qp-correlation $\mathcal{R}$ as

$$\mathcal{R}_i = \sqrt{\mathcal{Q}_i \mathcal{P}_i - \hbar^2/4} = \frac{\hbar}{2} \frac{\text{Im } A_i}{\text{Re } A_i}. \tag{7.79}$$

As has been shown in [10], at each jump the quantities $\langle q \rangle$,$\langle p \rangle$, $\mathcal{Q}$ and $\mathcal{P}$ change as follows

$$\langle q_f \rangle = \langle q_i \rangle + \frac{2\alpha \mathcal{Q}_i}{\sqrt{\alpha(1 + 2\alpha \mathcal{Q}_i)}} \xi \tag{7.80}$$

$$\langle p_f \rangle = \langle p_i \rangle + \frac{2\alpha \mathcal{R}_i}{\sqrt{\alpha(1 + 2\alpha \mathcal{Q}_i)}} \xi \tag{7.81}$$

$$\mathcal{Q}_f = \frac{\mathcal{Q}_i}{\sqrt{\alpha(1 + 2\alpha \mathcal{Q}_i)}} \tag{7.82}$$

$$\mathcal{P}_f = \frac{\mathcal{P}_i + \hbar^2\, \alpha\, (1 + \alpha\ \mathcal{Q}_i)}{\sqrt{\alpha(1 + 2\alpha \mathcal{Q}_i)}} \tag{7.83}$$

where ξ is a random number normally distributed. At each localization, the center of the wave packet jumps randomly according to (7.69) while at the same time, its extent shrinks. As a matter of fact the function A before (A_i) and after the jump (A_f) are linked by the relation $A_f = A_i + \alpha$ thus the extent of the wave function $\mathcal{Q}_f < \mathcal{Q}_i$.

Between two collisions the evolution is ruled by the free Schrödinger equation.

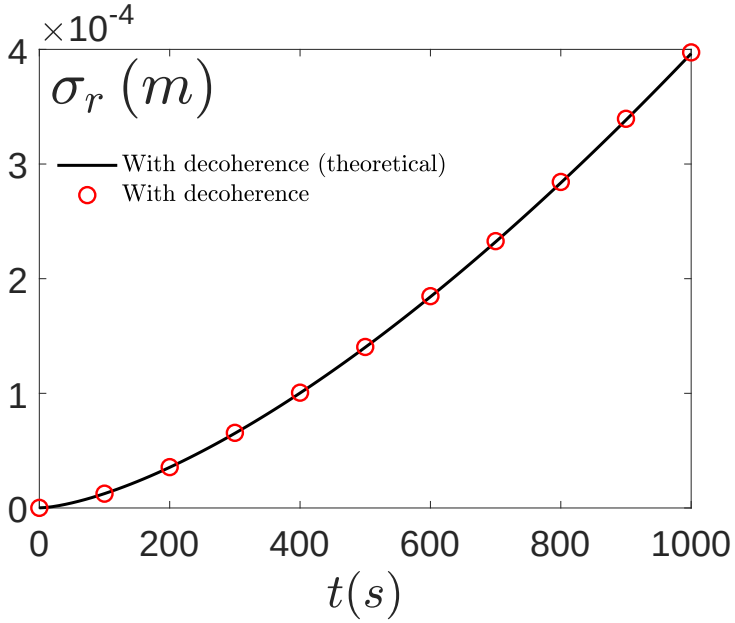

FIGURE 7.16: Here we illustrate the spread in position of the center of mass wavefunction of a gold nanosphere of radius $R = 100$ nm and with a density $\rho = 20\,000$ kg.m^{-3}. It can be seen that the evolution of spread is in accordance wit the theoretical function (7.87). Here we chose $\sigma_{r,0} = 10^{-7}$ m.

Thus, it can be shown[2] that during the Schrodinger evolution that:

$$\mathcal{Q}(t) = \mathcal{Q}(0) + 2\mathcal{R}(0)t/m + \mathcal{P}(0)t^2/m^2 \tag{7.84}$$

$$\mathcal{P}(t) = \mathcal{P}(0) \tag{7.85}$$

$$\mathcal{R}(t) = \sqrt{\mathcal{Q}(0)\cdot\mathcal{P}(0) + (\mathcal{P}(0)t/m)^2 - \hbar^2/4} \tag{7.86}$$

Of course, experimentally, we have no access to the individual trajectories followed by the wavefunction 7.9, but averaging over numerous realizations of the stochastic localization mechanism by a quantum Monte-Carlo procedure makes it possible to predict the average evolution of the object, that is of the associated density matrix. As shown in the original GRW paper, globally, the spread of the density matrix diffuses even faster than in the absence of jumps, because of the dispersion of the positions at which jumps occur, according to the formula [10, 36] at 3D we get:

$$\sigma_r(t) = \sigma_{r,0}\sqrt{1 + \frac{9\,\hbar^2\,t^2}{4\,m^2\,\sigma_{r,0}^4} + \frac{\Lambda\hbar^2\,t^3}{2\,m^2\sigma_0^2}}. \tag{7.87}$$

Imposing $\Lambda = 0$ in (7.87) we recover the usual expression for the spread of a freely expanding gaussian wave packet.

[2] We refer the reader to the paper [10] in which the formulas are explicitly derived.

7.E Stability in GRW

7.E.1 Map 1

In the original paper of GRW [10], the authors briefly studied the stability of the solutions $\mathcal{Q}$ and $\mathcal{P}$ resulting from an evolution under a GRW process. This work was done in a particular limit (that we will make explicit in what follows) so that we propose here to develop and to generalize this work. They supposed [10] for simplicity that the localization process of the ensemble occurs at successive time interval $\tau = 1/\Gamma$. It should be stressed however that it is an approximation of the real underlying process, but we shall suppose that such an approximation is valid; we will use this approximation to characterize the stability of the GRW model.

They represented [10] each cycle (starting from a localization process) by the following schematic map:

$$\begin{cases} \mathcal{Q} = \mathcal{Q}_i \xrightarrow{\text{GRW Localization}} \mathcal{Q}_f = \mathcal{Q}(0) \xrightarrow{\text{Schrodinger Evolution}} \mathcal{Q}(\tau) = \mathcal{Q}' \\ \\ \mathcal{P} = \mathcal{P}_i \xrightarrow{\text{GRW Localization}} \mathcal{P}_f = \mathcal{P}(0) \xrightarrow{\text{Schrodinger Evolution}} \mathcal{P}(\tau) = \mathcal{P}' \end{cases} \tag{7.88}$$

From the above it can be shown that:

$$\mathcal{Q}' = \frac{\mathcal{Q}}{1+2\,\alpha\,\mathcal{Q}} + 2\frac{\left(\mathcal{Q}\mathcal{P} - \hbar^2/4\right)^{1/2}}{1+2\alpha\,\mathcal{Q}}\,\frac{1}{m\,\Gamma} + \frac{\mathcal{P} + \hbar^2\alpha\,(1+\alpha\,\mathcal{Q})}{1+2\alpha\,\mathcal{Q}}\,\frac{1}{m^2\,\Gamma^2} \tag{7.89}$$

$$\mathcal{P}' = \frac{\mathcal{P} + \hbar^2\alpha\,(1+\alpha\,\mathcal{Q})}{1+2\alpha\,\mathcal{Q}}. \tag{7.90}$$

It is however important to notice that this cycle is not the only possible one. In section 7.E.2 we will consider another possible cycle made by an evolution which starts from a Schrodinger evolution and is followed by a GRW localization. The map will lead to other stable solutions (Q, P) which will be used to generalize the results obtained by GRW in their paper [10].

Let us first come back to the cycle (7.88), its equilibrium is defined by the double conditions $\mathcal{Q} = \mathcal{Q}'$ and $\mathcal{P} = \mathcal{P}'$. As suggested by the authors in [10], for what follows it is useful to introduce the parameter $\epsilon = \left(\frac{\alpha\hbar}{m\,\Gamma}\right)^{1/2}$ and thus the dimensionless set of variables (x, y) defined through

$$x = \alpha\,\mathcal{Q} \quad \text{and} \quad y = \frac{\alpha}{m^2\,\Gamma^2}\,\mathcal{P}. \tag{7.91}$$

The set of equations (7.89-7.90) are then rewritten as

$$x' = \mathcal{F}\,[x, y] = \frac{x}{1+2\,x} + 2\,\frac{\left(x\,y - \epsilon^4/4\right)^{1/2}}{1+2\,x} + \frac{y + \epsilon^4\,(1+x)}{1+2\,x} \tag{7.92}$$

$$y' = \mathcal{G}\,[x, y] = \frac{y + \epsilon^4\,(1+x)}{1+2\,x}. \tag{7.93}$$

In their paper, the authors treated the case of a very small value ϵ (which is chosen to be of the order of 10^{-12}) and they claimed to have found a unique stable solution for the pair $(\mathcal{Q}, \mathcal{P})$. Notice that this value of ϵ is a consequence of a phenomenological and fixed choice of the parameter α and Γ (adobted by GRW [10] in their model of spontaneous localization). Those parameters are chosen in a way that macroscopic superpositions are prohibited while it preserves the microscopic dynamics. In chapter 8, we will relax this assumption and we will see that depending on the considered physical experiment, if one wants to use the GRW model as a decoherence model one should adapt the choice of the parameters α and Γ. In particular, we shall see in the case of the Doppler cooling that α and Γ can be related respectively to the photon wavelength of the laser and to the spontaneous decay rate of the cooled atom.

7.E.1.1 Solutions at equilibrium

Here what we mean by equilibrium is when the natural spread of the Schrodinger evolution compensates the GRW localization; i.e.when $x' = x$ and $y' = y$. Coming back to the set of equations (7.92-7.93), it turns out that at equilibrium

$$y = \epsilon^4 \frac{1+x}{2\,x} \tag{7.94}$$

$$P_\epsilon(x) = -4x^3 + 2\epsilon^2 x\sqrt{1+2x} + \epsilon^4(1+x)(1+2x) = 0. \tag{7.95}$$

Those equations admit two analytical and physically relevant solutions which are functions of ϵ :

$$x_1^*(\epsilon) = \frac{1}{4}\left(\epsilon^4 + \sqrt{\epsilon^4\,(\epsilon^4+4)}\right) \tag{7.96}$$

$$x_2^*(\epsilon) = \frac{1}{8}\left(\epsilon^4 + \sqrt{\epsilon^4+16}\,\epsilon^2 + \sqrt{2}\sqrt{\epsilon^8 + 12\epsilon^4 + \sqrt{\epsilon^4+16}\,\epsilon^6 + 4\sqrt{\epsilon^4+16}\,\epsilon^2}\right) \tag{7.97}$$

and where the imaginary and the negative solutions of 7.95 have all been discarded because $\mathcal{Q}$ is real and positive. The same can be done for y using equation 7.94:

$$y_1^*(\epsilon) = \frac{1}{2}\sqrt{\epsilon^4\,(\epsilon^4+4)} \tag{7.98}$$

$$y_2^*(\epsilon) = \frac{\epsilon^2\left(\sqrt{\epsilon^4+16} - \epsilon^2\right)\sqrt{\epsilon^8 + 12\epsilon^4 + \sqrt{\epsilon^4+16}\epsilon^6 + 4\sqrt{\epsilon^4+16}\epsilon^2}}{16\sqrt{2}} \tag{7.99}$$

As an example, we plot in figure 7.17a (resp. figure 7.17b) the solutions x_1^* and x_2^* (resp. y_1^* and y_2^*) in function of ϵ. The difference $\Delta_x(\epsilon) = |x_2^*(\epsilon) - x_1^*(\epsilon)|$ (resp. $\Delta_y(\epsilon) = |y_2^*(\epsilon) - y_1^*(\epsilon)|$) is also plotted in figure 7.17c (resp. in figure 7.17d).

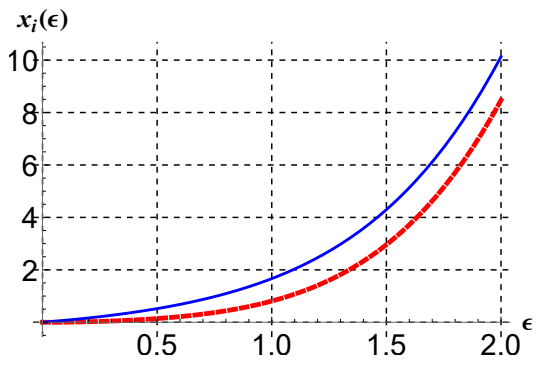

(A) The red curve corresponds to x_1^* and the blue curve to x_2^*.

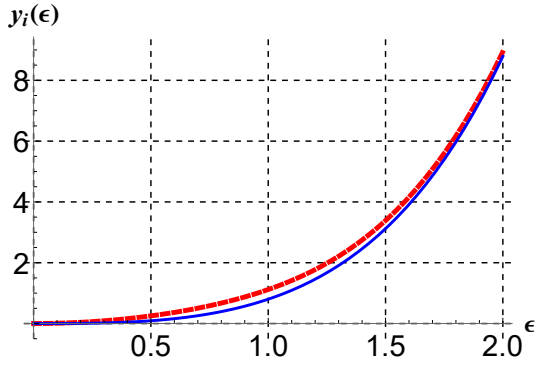

(B) The red curve corresponds to y_1^* and the blue curve to y_2^*.

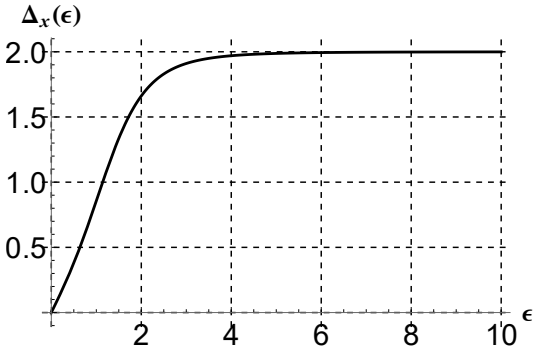

(C)

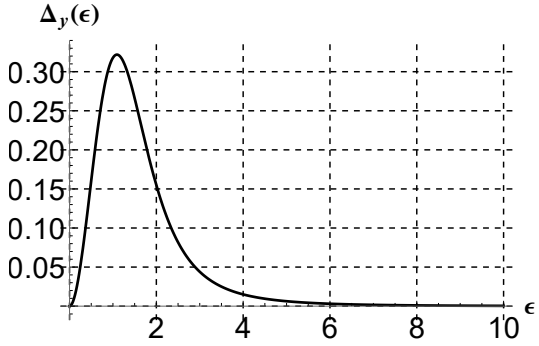

(D)

FIGURE 7.18: Here we plot the the solutions x_i^* in figure A (resp. y_i^* in figure B) at equilibrium in function of ϵ. We also plot their distance $\Delta_x(\epsilon) = |x_2^*(\epsilon) - x_1^*(\epsilon)|$ in figure C (resp. $\Delta_y(\epsilon) = |y_2^*(\epsilon) - y_1^*(\epsilon)|$ in figure D).

When ϵ tends to zero (this is the limit case considered by GRW [10]) the two solutions can be developed in series of ϵ as:

$$x_1^* = \frac{\epsilon^2}{2} + \mathcal{O}(\epsilon^4) \qquad x_2^* = \frac{\epsilon}{\sqrt{2}} + \frac{\epsilon^2}{2} + \frac{3\,\epsilon^3}{8\,\sqrt{2}} + \mathcal{O}(\epsilon^4) \tag{7.100}$$

$$y_1^* = \epsilon^2 + \mathcal{O}(\epsilon^4) \qquad y_2^* = \frac{\epsilon^3}{\sqrt{2}} + \mathcal{O}(\epsilon^4) \tag{7.101}$$

or in terms of $(\mathcal{Q}, \mathcal{P})$ as:

$$\mathcal{Q}_1^* = \frac{1}{2}\,\frac{\hbar}{m\,\Gamma} + \mathcal{O}(\epsilon^2) \qquad \mathcal{Q}_2^* = \frac{1}{\sqrt{2}}\left(\frac{\hbar}{m\alpha\,\Gamma}\right)^{1/2}\left[1 + \frac{1}{\sqrt{2}}\,\epsilon + \mathcal{O}(\epsilon^2)\right] \tag{7.102}$$

$$\mathcal{P}_1^* = m\Gamma\,\hbar + \mathcal{O}(\epsilon^2) \qquad \mathcal{P}_2^* = \frac{\hbar^2}{\sqrt{2}}\left(\frac{\alpha m\,\Gamma}{\hbar}\right)^{1/2}\left[1 + \mathcal{O}(\epsilon^2)\right] \tag{7.103}$$

Notice that in the limit $\epsilon \ll 1$, the product $\mathcal{Q}_i^*\,\mathcal{P}_i^*$ of any of the pair gives the same result; which is twice the value allowed by the Heisenberg saturation. We shall now discuss the stability of the above solutions.

7.E.1.2 Stability of the solutions

It should be stressed that the stability depends only on the value of ϵ. In the limit $\epsilon \ll 1$, the unique stable solution is the pair (x_2^*, y_2^*). To see this, let us first apply successively the map (7.92,7.93) on a pair of points $(\widetilde{x}_i^*, \widetilde{y}_i^*)$ chosen to be close to (x_i^*, y_i^*). For example we can choose in the limit $\epsilon \to 0$: $\widetilde{x}_1^* = \frac{\epsilon^2}{2}$ and $\widetilde{x}_2^* = \frac{\epsilon}{\sqrt{2}}$ which are the first non-zero term of the series expansion of x_1^* and x_2^*.

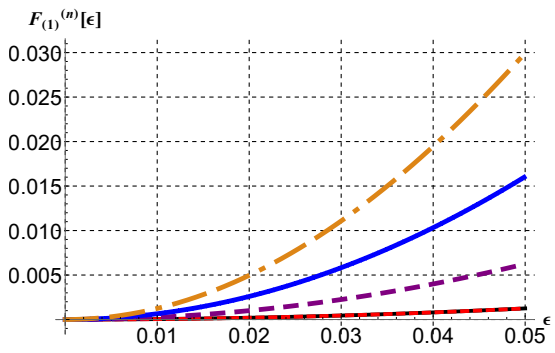

(A) In the case of (x_1^*, y_1^*).

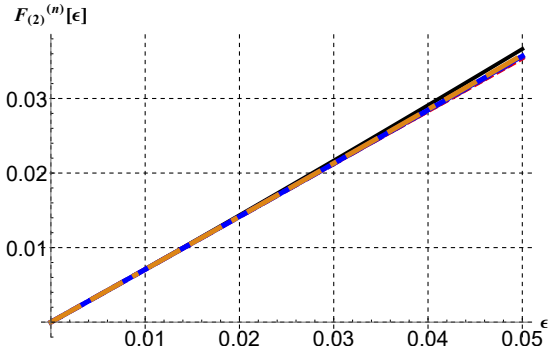

(B) In the case of (x_2^*, y_2^*).

FIGURE 7.19: Plot of successive applications of the map defined in (7.92,7.93) when $\epsilon \ll 1$. The black curve corresponds to the solutions $x_i^*(\epsilon)$ defined in (7.97) and the red curve is $\widetilde{x}_i^*(\epsilon)$. The purple, the blue and the golden curves are obtained after $n = 1$, $n = 2$ and $n = 3$ applications of the cycle on $\widetilde{x}_1^* = \frac{\epsilon^2}{2}$ (Left) and on $\widetilde{x}_2^* = \frac{\epsilon}{\sqrt{2}}$ (Right).

One can easily see that:

$$\widetilde{x}_1^* = \frac{\epsilon^2}{2}, \qquad \mathcal{F}\left[\widetilde{x}_1^*, \widetilde{y}_1^*\right] = \frac{5\,\epsilon^2}{2} + \mathcal{O}(\epsilon^3), \qquad \mathcal{F}\left[\mathcal{F}\left[\widetilde{x}_1^*, \widetilde{y}_1^*\right], \mathcal{G}\left[\widetilde{x}_1^*, \widetilde{y}_1^*\right]\right] = \frac{13\,\epsilon^2}{2} + \mathcal{O}(\epsilon^3)$$

$$\widetilde{x}_2^* = \frac{\epsilon}{\sqrt{2}}, \qquad \mathcal{F}\left[\widetilde{x}_2^*, \widetilde{y}_2^*\right] = \frac{\epsilon}{\sqrt{2}} + \mathcal{O}(\epsilon^2), \qquad \mathcal{F}\left[\mathcal{F}\left[\widetilde{x}_2^*, \widetilde{y}_2^*\right], \mathcal{G}\left[\widetilde{x}_2^*, \widetilde{y}_2^*\right]\right] = \frac{\epsilon}{\sqrt{2}} + \mathcal{O}(\epsilon^2)$$

In the case of $\widetilde{x}_1^*$, each iteration increases its distance to x_1^* (which acts like a repellor) while for $\widetilde{x}_2^*$ the distance to x_2^* decreases (x_2^* acts like an attractor). In figure 7.19 we plot three successive applications of the cycle (7.92,7.93) on $(\widetilde{x}_i^*, \widetilde{y}_i^*)$ in the limit $\epsilon \ll 1$. Those figures also confirm that (x_2^*, y_2^*) acts like the unique attractor of the process. It should be noted that this result is in agreement with the conclusion obtained in the paper [10].

In the other limit, when $\epsilon \gg 1$ it should be noticed that the difference between the two solutions x_1^*, x_2^* tends to a finite value $\Delta_x \to 2$ (see figure 7.17c and figure 7.17d) while in momentum it tends to $\Delta_y \to 0$. In this limit (x_1^*, y_1^*) and (x_2^*, y_2^*) are both attractors of the process as can be seen in figures 7.20 which shows the convergence to the value x_i^* (defined in (7.19b)) when three successive applications of the map (7.92,7.93) are done starting from a common initial point $\widetilde{x}_i^* = \epsilon$.

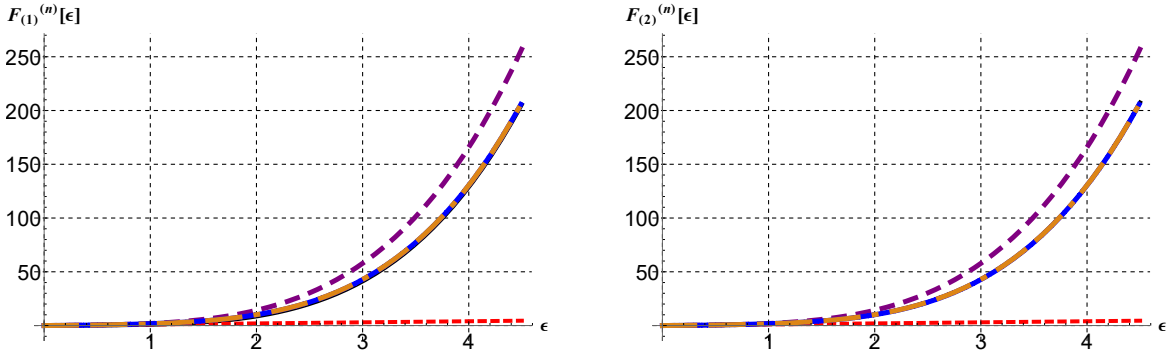

(A) In the case of (x_1^*, y_1^*).

(B) In the case of (x_2^*, y_2^*).

FIGURE 7.20: Plot of successive applications of the map defined in (7.92,7.93) on $\widetilde{x}_i^* = \epsilon$. The black curve corresponds to the solutions $x_i^*(\epsilon)$ defined in (7.97) and the red curve is $\widetilde{x}_i^*(\epsilon)$. The purple, the blue and the golden curves are obtained after $n = 1$, $n = 2$ and $n = 3$ applications of the cycle starting from a common initial point $\widetilde{x}_i^* = \epsilon$.

7.E.1.3 Jacobian matrix for the mapping 1

We shall now quantitatively describe the stability. To do so let us consider the Jacobian matrix which in the following will be expressed at equilibrium (i.e.when $x' = x$ and when $y' = y$). We associate to the process (7.92-7.93) the following Jacobian matrix:

$$\mathcal{J}(x,\epsilon) = \begin{pmatrix} \frac{\partial \mathcal{F}}{\partial x} & \frac{\partial \mathcal{F}}{\partial y} \\ \frac{\partial \mathcal{G}}{\partial x} & \frac{\partial \mathcal{G}}{\partial y} \end{pmatrix}\Bigg|_{y=\epsilon^4 \frac{1+x}{2x}} = \begin{pmatrix} \frac{-(2x+1)\epsilon^4 - x\sqrt{(2x+1)\epsilon^4} + \sqrt{(2x+1)\epsilon^4} + x}{x(2x+1)^2} & \frac{\frac{2x\sqrt{(2x+1)\epsilon^4}}{\epsilon^4} + 2x + 1}{(2x+1)^2} \\ -\frac{\epsilon^4}{2x^2+x} & \frac{1}{2x+1} \end{pmatrix}.$$

Its eigenvalues can be deduced from its characteristic polynomial. As a reminder this polynomial at $2D$ takes the form :

$$P(\lambda) = \lambda^2 - \mathrm{Tr}\left[\mathcal{J}\right]\lambda + \mathrm{Det}\left[\mathcal{J}\right] \tag{7.104}$$

and its roots are in fact the eigenvalues of $\mathcal{J}$. Thus we find

$$\lambda_\pm = \frac{\mathrm{Tr}\left[\mathcal{J}\right] \pm \sqrt{\mathrm{Tr}\left[\mathcal{J}\right]^2 - \mathrm{Det}\left[\mathcal{J}\right]}}{2} \tag{7.105}$$

Those roots depend on the trace and on the determinant of $\mathcal{J}$ but also on the discriminant Δ of its characteristic polynomial. We illustrate in figure 7.21 those quantities in function of ϵ and at $x = x_i^*$. When $\Delta \leq 0$ the eigenvalues are complex conjugate. This is true for $\lambda_\pm(x_2^*)$ for any value ϵ as can be seen in figure 7.21. In addition the modulus $|\lambda_\pm(x_2^*)|$ is always smaller than one as can be seen in figure 7.22. Those informations provide criterions to prove the stability of (x_2^*, y_2^*). In the case of (x_1^*, y_1^*) it is globally unstable until a critical value $\epsilon_c \sim 0.65$ from which it starts to be stable.

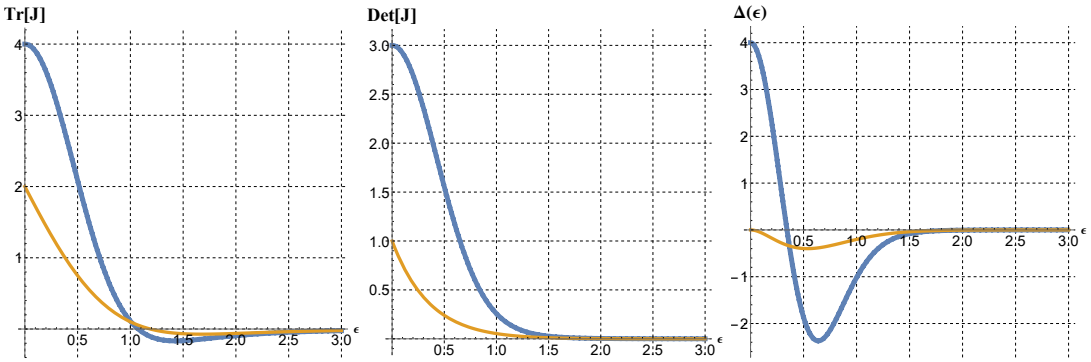

FIGURE 7.21: We illustrate here three functions associated to the Jacobian matrix (7.104) taken in $x = x_i^*$ (in blue for x_1^* and in golden for x_2^*. From the left to the write we plot: the trace, the determinant and the discriminant of the characteristic polynomial (7.104).

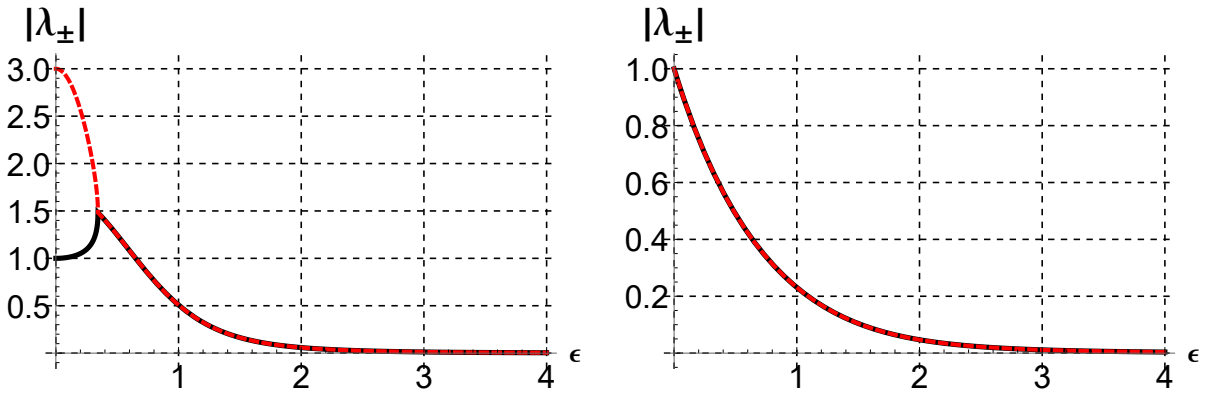

(A) In the case of (x_1^*, y_1^*).

(B) In the case of (x_2^*, y_2^*).

FIGURE 7.22: We plot here the norm of the eigenvalues (7.105) in function of ϵ, at $x = x_i^*$. The red dashed curve corresponds to $|\lambda_+|$ and the full black line corresponds to $|\lambda_-|$.

7.E.2 Map 2

To take the analysis one step further, let us briefly discuss the other possible cycle and its possible stable solutions $(\mathcal{Q}^*,\mathcal{P}^*)$. There is infact no justification to only consider the cycle defined in 7.88. Instead of starting the cycle with a localization, let us now consider the following map:

$$\begin{cases} \mathcal{Q} = \mathcal{Q}(0) \xrightarrow{\text{Schrodinger Evolution}} \mathcal{Q}(\tau) = \mathcal{Q}_i \xrightarrow{\text{GRW Localization}} \mathcal{Q}_f = \mathcal{Q}' \\ \mathcal{P} = \mathcal{P}(0) \xrightarrow{\text{Schrodinger Evolution}} \mathcal{P}(\tau) = \mathcal{P}_i \xrightarrow{\text{GRW Localization}} \mathcal{P}_f = \mathcal{P}' \end{cases} \tag{7.106}$$

From the cycle above it can be shown using the following dimensionless set of parameters u and v (in order to differentiate them from x and y):

$$u = \alpha\, \mathcal{Q} \quad \text{and} \quad v = \frac{\alpha}{m^2\, \Gamma^2}\, \mathcal{P}. \tag{7.107}$$

that

$$u' = \mathcal{M}[u,v] = \frac{u + 2\left(u\,v - \epsilon^4/4\right)^{1/2} + v}{1 + 2\left[u + 2\left(u\,v - \epsilon^4/4\right)^{1/2} + v\right]} \tag{7.108}$$

$$v' = \mathcal{N}[u,v] = \frac{v + \epsilon^4\,(1+v)}{1+2\,v}. \tag{7.109}$$

One can notice that u' is always less than one. Moreover, it is worth noting that there is no direct analytical solutions for $u' = u$ and $v' = v$. However, thanks to the work carried in the previous subsection, the following study will be easily derived. Let us call $\widehat{\mathcal{S}}$ the operation that evolves the quantum state under the free Schrodinger equation and $\widehat{\mathcal{G}}$ the operation that localizes the state. Thus we can write:

$$\widehat{\mathcal{S}}\,\widehat{\mathcal{G}}\,x_i^* = x_i^* \quad \longrightarrow \quad \widehat{\mathcal{G}}\widehat{\mathcal{S}}\,\underbrace{\widehat{\mathcal{G}}\,x_i^*}_{u_i^*} = \underbrace{\widehat{\mathcal{G}}\,x_i^*}_{u_i^*}$$

If now we call $u_i^* = \mathcal{G}\,x_i^*$ it follows that u_i^* is the equilibrium state of the map defined above; i.e.we have $\widehat{\mathcal{G}}\widehat{\mathcal{S}}\,u_i^* = u_i^*$.

7.E.2.1 Check with simulations of the GRW process

Here we simulate the GRW process and we plot the evolution of $\alpha\ \mathcal{Q}$ in function of time. We also illustrate with an histogram the fluctuations of its values taken during its evolution. In figure 7.23 the simulation was done for $\epsilon = 0.06$. The analytical expression found in (7.97) predicts a value at equilibrium $x_2^*(0.06) \sim 0.044$ and using the solution of (7.108) we predict $u_2^*(0.06) \sim 0.041$. In this regime (where ϵ is small compared to unity), those values are close and are both in accordance with the position of the peak of the histogram of $\alpha\ \mathcal{Q}$. The width of the distribution reflects the limitations of the initial approximation; i.e.about the periodicity τ of the cycle. In reality, the cycle occurs in a statistical way (following a Poisson distribution) every $\tau + \delta\tau$ which induces fluctuations on $\alpha\ \mathcal{Q}$.

Note also that only the assumption $\epsilon \ll 1$ has been made so far (in the literature about the GRW model) but no assumption was made for $\epsilon \gtrsim 1$. In figure 7.24 we considered $\epsilon = 0.6141$. In this regime we note the appearance of a multitude of peaks on the histogram of $\alpha\ \mathcal{Q}$. As a result it shows the complexity of the underlying process and the limitations of the approximation used so far to describe its stability.

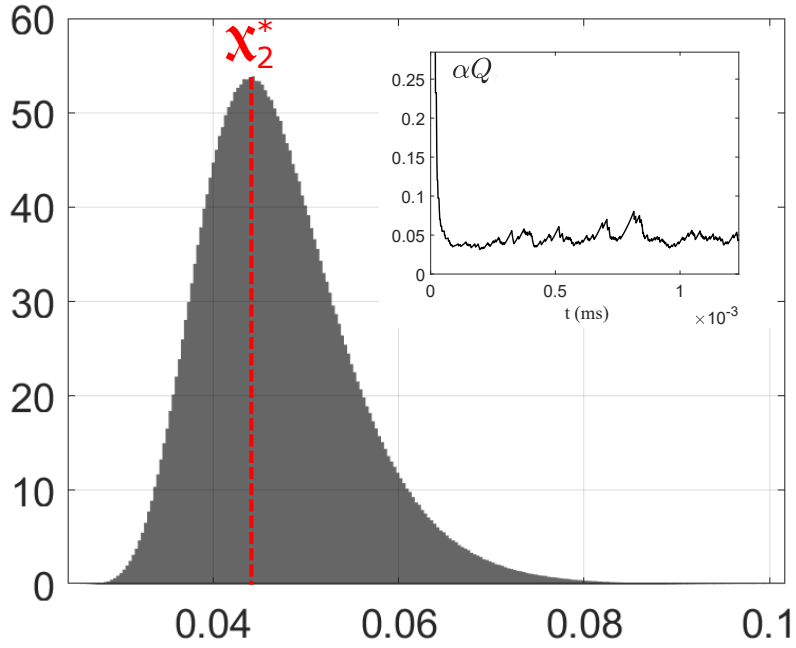

FIGURE 7.23: We illustrate here the time evolution of $\mathcal{Q}$ and an histogram of its values at equilibrium. We chose $\Gamma = 143.10^6$, $\alpha = 3.3410^{14}$ and $m = 40$ a.m.u. so that $\epsilon = 0.06$.

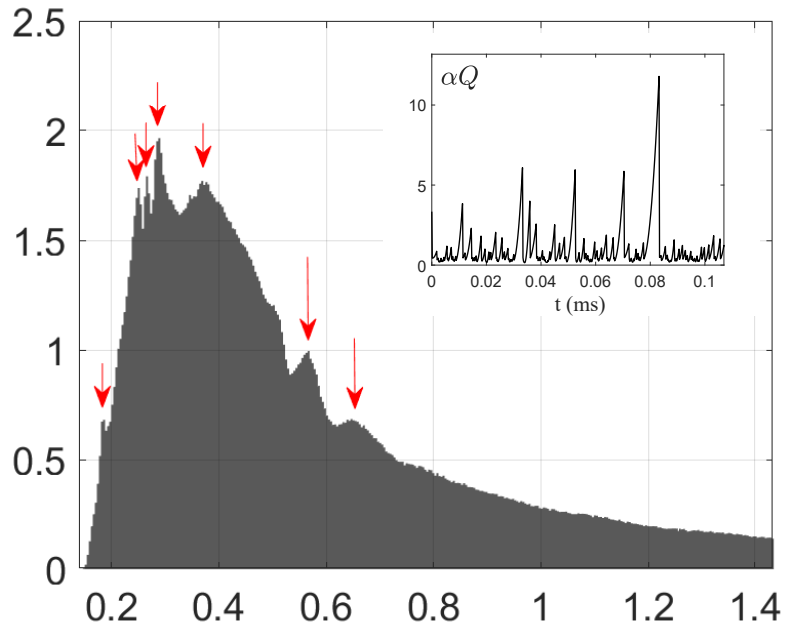

FIGURE 7.24: We illustrate here the time evolution of $\mathcal{Q}$ and an histogram of its values at equilibrium. We chose $\Gamma = 14.10^5$, $\alpha = 3.3410^{14}$ and $m = 40$ a.m.u. so that $\epsilon = 0.61$. This figure shows the appearance of a multitude of peaks in the regime where $\epsilon \sim 1$.

7.F GRW versus QMUPL: stability

In the limit $\epsilon \to 0$ where $\epsilon = \sqrt{\frac{\hbar\,\alpha}{m\,\Gamma}}$, the master equation of the GRW model can be "unraveled" with the QMUPL model (see section 7.C) and as we shall show, the asymptotic values of $\mathcal{Q}$ then coincide. For example from the QMUPL (7.59) it can be shown for a free gaussian state of the form

$$\psi(x,t) = \frac{1}{\mathcal{N}}\,\exp^{-A(t)\,x^2/2+B(t)\,x} \tag{7.110}$$

that

$$i\,\frac{dA(t)}{dt} = \frac{\hbar}{m}\,A^2 + i\,\lambda \tag{7.111}$$

thus using a dimensionless set of variables ($A = \widetilde{A}\,\alpha$ and $t = \widetilde{t}/\Gamma$) The above equation is rewritten as

$$i\,\frac{d\widetilde{A}(\widetilde{t})}{d\widetilde{t}} = \epsilon^2\,\widetilde{A}^2 + \frac{i}{2} \tag{7.112}$$

where we used the fact that $\lambda = \alpha\,\Gamma/2$ (see (7.73)) and $\epsilon = \sqrt{\frac{\hbar\,\alpha}{m\,\Gamma}}$

At equilibrium we get

$$\epsilon^2\,\widetilde{A}_{st}^2 + \frac{i}{2} = 0 \tag{7.113}$$

from which we can deduce for the real ($a_{1,st}$) and the imaginary part ($a_{2,st}$) of $\widetilde{A}_{st}$:

$$a_{1,st}^2 - a_{2,st}^2 = 0 \tag{7.114}$$

$$2\,a_{1,st}\,a_{2,st} = -\frac{1}{2\,\epsilon^2} \tag{7.115}$$

now injecting (7.115) in (7.114) leads to a fourth-degree polynomial in $X = a_{1,st}$:

$$X^4 - \frac{1}{16\,\epsilon^4} = 0 \tag{7.116}$$

whose unique solution (real and positive) is found to be

$$a_{1,st} = \frac{1}{2\,\epsilon} \tag{7.117}$$

thus

$$\mathcal{Q}^*_{qmupl} = \frac{1}{2\,a_{1,st}} = \epsilon \tag{7.118}$$

This solution is exactly the stable solution found for the GRW model in (7.100) in the limit $\epsilon \ll 1$. This is confirmed by numerical simulations as can be seen in figure 7.9. This confirms that the GRW model and the QMUPL give the same asymptotic value in the limit of small ϵ.

Bibliography

[1] Marlan O Scully, Berthold-Georg Englert, and Julian Schwinger. Spin coherence and humpty-dumpty. iii. the effects of observation. *Physical Review A*, 40(4):1775, 1989.

[2] Marek Czachor. Mobility and non-separability. *Foundations of Physics Letters*, 4(4):351–361, 1991.

[3] Nicolas Gisin. Weinberg's non-linear quantum mechanics and supraluminal communications. *Physics Letters A*, 143(1-2):1–2, 1990.

[4] Sougato Bose, Anupam Mazumdar, Gavin W Morley, Hendrik Ulbricht, Marko Toroš, Mauro Paternostro, Andrew A Geraci, Peter F Barker, MS Kim, and Gerard Milburn. Spin entanglement witness for quantum gravity. *Physical review letters*, 119(24):240401, 2017.

[5] Chiara Marletto and Vlatko Vedral. Gravitationally induced entanglement between two massive particles is sufficient evidence of quantum effects in gravity. *Physical review letters*, 119(24):240402, 2017.

[6] C Anastopoulos and Bei-Lok Hu. Comment on" a spin entanglement witness for quantum gravity" and on" gravitationally induced entanglement between two massive particles is sufficient evidence of quantum effects in gravity". Technical report, 2018.

[7] S. Colin, T. Durt, and R. Willox. Can quantum systems succumb to their own (gravitational) attraction? *Class. Quantum Grav.*, 31:245003, 2014.

[8] Bailey C Hsu, Manuel Berrondo, and Jean-François S Van Huele. Stern-gerlach dynamics with quantum propagators. *Physical Review A*, 83(1):012109, 2011.

[9] Daniel E Platt. A modern analysis of the stern–gerlach experiment. *American Journal of Physics*, 60(4):306–308, 1992.

[10] Gian Carlo Ghirardi, Alberto Rimini, and Tullio Weber. Unified dynamics for microscopic and macroscopic systems. *Physical Review D*, 34(2):470, 1986.

[11] Joseph Polchinski. Weinberg's nonlinear quantum mechanics and the einstein-podolsky-rosen paradox. *Physical Review Letters*, 66(4):397, 1991.

[12] Bogdan Mielnik. Phenomenon of mobility in non-linear theories. *Communications in Mathematical Physics*, 101(3):323–339, 1985.

[13] S. Colin, T. Durt, and R. Willox. L. de Broglie's double solution program: 90 years later. *Annales de la Fondation Louis de Broglie*, 42:19, 2017.

[14] Philip Pearle. Combining stochastic dynamical state-vector reduction with spontaneous localization. *Physical Review A*, 39(5):2277, 1989.

[15] Angelo Bassi, Kinjalk Lochan, Seema Satin, Tejinder P Singh, and Hendrik Ulbricht. Models of wave-function collapse, underlying theories, and experimental tests. *Reviews of Modern Physics*, 85(2):471, 2013.

[16] Lajos Diósi. Models for universal reduction of macroscopic quantum fluctuations. *Physical Review A*, 40(3):1165, 1989.

[17] Stephen L Adler. *Quantum theory as an emergent phenomenon: The statistical mechanics of matrix models as the precursor of quantum field theory*. Cambridge University Press, 2004.

[18] Roderich Tumulka. A relativistic version of the ghirardi–rimini–weber model. *Journal of Statistical Physics*, 125(4):821–840, 2006.

[19] Nicolas Gisin. Stochastic quantum dynamics and relativity. *Helv. Phys. Acta*, 62(4):363–371, 1989.

[20] Michael Esfeld and Nicolas Gisin. The grw flash theory: a relativistic quantum ontology of matter in space-time? *Philosophy of Science*, 81(2):248–264, 2014.

[21] Bogdan Mielnik. The paradox of two bottles in quantum mechanics. *Foundations of Physics*, 20(6):745–755, 1990.

[22] Stefan Nimmrichter and Klaus Hornberger. Stochastic extensions of the regularized schrödinger-newton equation. *Physical Review D*, 91(2):024016, 2015.

[23] Mohammad Bahrami, André Großardt, Sandro Donadi, and Angelo Bassi. The schrödinger–newton equation and its foundations. *New Journal of Physics*, 16(11):115007, 2014.

[24] Daniel Salart, Augustin Baas, Cyril Branciard, Nicolas Gisin, and Hugo Zbinden. Testing the speed of 'spooky action at a distance'. *Nature*, 454(7206):861, 2008.

[25] David Rideout, Thomas Jennewein, Giovanni Amelino-Camelia, Tommaso F Demarie, Brendon L Higgins, Achim Kempf, Adrian Kent, Raymond Laflamme, Xian Ma, Robert B Mann, et al. Fundamental quantum optics experiments conceivable with satellites—reaching relativistic distances and velocities. *Classical and Quantum Gravity*, 29(22):224011, 2012.

[26] Samuel Colin, Thomas Durt, and Ralph Willox. Crucial tests of macrorealist and semiclassical gravity models with freely falling mesoscopic nanospheres. *Physical Review A*, 93(6):062102, 2016.

[27] Stefan Nimmrichter, Klaus Hornberger, Philipp Haslinger, and Markus Arndt. Testing spontaneous localization theories with matter-wave interferometry. *Physical Review A*, 83(4):043621, 2011.

[28] Stefan Gerlich, Sandra Eibenberger, Mathias Tomandl, Stefan Nimmrichter, Klaus Hornberger, Paul J Fagan, Jens Tüxen, Marcel Mayor, and Markus Arndt. Quantum interference of large organic molecules. *Nature communications*, 2:263, 2011.

[29] James R van Meter. Schrödinger–newton 'collapse'of the wavefunction. *Classical and Quantum Gravity*, 28(21):215013, 2011.

[30] Markus Aspelmeyer, Pierre Meystre, and Keith Schwab. Quantum optomechanics. *Physics Today*, 65(7):29–35, 2012.

[31] Markus Arndt, Angelo Bassi, Domenico Giulini, Antoine Heidmann, and Jean-Michel Raimond. Fundamental frontiers of quantum science and technology. *Procedia Computer Science*, 7:77–80, 2011.

[32] Oriol Romero-Isart, Anika C Pflanzer, Mathieu L Juan, Romain Quidant, Nikolai Kiesel, Markus Aspelmeyer, and J Ignacio Cirac. Optically levitating dielectrics in the quantum regime: Theory and protocols. *Physical Review A*, 83(1):013803, 2011.

[33] Oriol Romero-Isart, Anika C Pflanzer, Florian Blaser, Rainer Kaltenbaek, Nikolai Kiesel, Markus Aspelmeyer, and J Ignacio Cirac. Large quantum superpositions and interference of massive nanometer-sized objects. *Physical review letters*, 107(2):020405, 2011.

[34] Rainer Kaltenbaek, Gerald Hechenblaikner, Nikolai Kiesel, Oriol Romero-Isart, Keith C Schwab, Ulrich Johann, and Markus Aspelmeyer. Macroscopic quantum resonators (maqro). *Experimental Astronomy*, 34(2):123–164, 2012.

[35] Gian Carlo Ghirardi, Philip Pearle, and Alberto Rimini. Markov processes in hilbert space and continuous spontaneous localization of systems of identical particles. *Physical Review A*, 42(1):78, 1990.

[36] M. Schlosshauer. *Decoherence and the Quantum-to-Classical Transition*. Springer, Heidelberg Berlin, 2007.

[37] Nicolas Gisin and Ian C Percival. The quantum-state diffusion model applied to open systems. *Journal of Physics A: Mathematical and General*, 25(21):5677, 1992.

[38] A. Bassi, K. Lochan, S. Satin, T. P. Singh, and H. Ulbricht. Models of wave-function collapse, underlying theories, and experimental tests. *Rev. Mod. Phys.*, 85:471–527, 2013.

[39] S. Nimmrichter, K. Hornberger, P. Haslinger, and M. Arndt. Testing spontaneous localization theories with matter-wave interferometry. *Phys. Rev. A*, 83:043621, 2011.

[40] S.J. Gerlich, S. Eibenberger, M. Tomandl, S. Nimmrichter, K. Hornberger, J. Tüxen, M. Mayor, and M. Arndt. Quantum interference of large organic molecules . *Nature Communications*, 2:263, 2012.

[41] B. Vacchini. On the precise connection between the GRW master-equation and master-equations for the description of decoherence. *J. Phys. A*, 40:2463–2473, 2007.

Chapter 8

Interplay between decoherence and cooling

父さんが残した　熱い想い
母さんがくれた　あのまなざし

君をのせて

Summary In conventional treatments of Doppler cooling the atom is often treated as a classical material point. Here we represent the state of the atom by a gaussian quantum wave function, which doubles the numbers of degrees of freedom. In addition to describe the atom with its classical position and velocity, we add to the description two quantum degrees of freedom: the individual spreads in position and in momentum which are constrained by Heisenberg uncertainty. Resorting to the Ghirardi-Rimini-Weber model of decoherence, we study the interplay between decoherence and Doppler cooling

8.1 Introduction

In the previous section we proposed two experimental tests aimed at putting into evidence the existence of a self-gravitational interaction *à la* Schrodinger-Newton. In the past, a test was proposed in the same context [1] in which a nanosphere was trapped and prepared in a gaussian state with an extent of the order of the Lieb radius (7.26). Thereafter the bead was released from the trap and evolved freely during several minutes before being measured in the position basis. As was shown in [1] the square root deviation of the distribution of positions was narrower when self-gravity is present, and after several minutes of free-flight the narrowing was of the order of several tenths of nanometers, a measurable effect. However, it should be emphasized that this experimental proposal is difficult to realize for several reasons:

I- It requires the use of a satellite. As a matter of fact, a free flight of several minutes is only possible in an inertial (gravitation-free) environment.

II- As has been shown in [1] decoherence has to remain weak, otherwise decoherence effects will mask those of self-gravity, which requires to work in extreme vacuum, at very low temperature. Moreover, decoherence increases more quickly than self-gravity with the size of the nanosphere so that it is only at the mesoscopic transition that the experiment can be realized.

III- The initial spread of the gaussian state (of the order of 100 nanometer for a bead of radius 100 nanometer) is quite larger than the spread that can be achieved in optical traps (from $10^{-12} - 10^{-10}$ m).

The problems **I** and **II** can be overcome in principle, but at the time it was not clear how to overcome the problem **III**. In [1] the authors investigated the possibility to tailor the size of the wave function of the (center of mass of the) bead making use of decoherence. This idea was considered in detail in the previous chapter in which we have seen that the width of each gaussian state (corresponding to individual realizations of the stochastic GRW localization process) quickly converges to an asymptotic value (for example see the wiggly curves in figure 8.1).

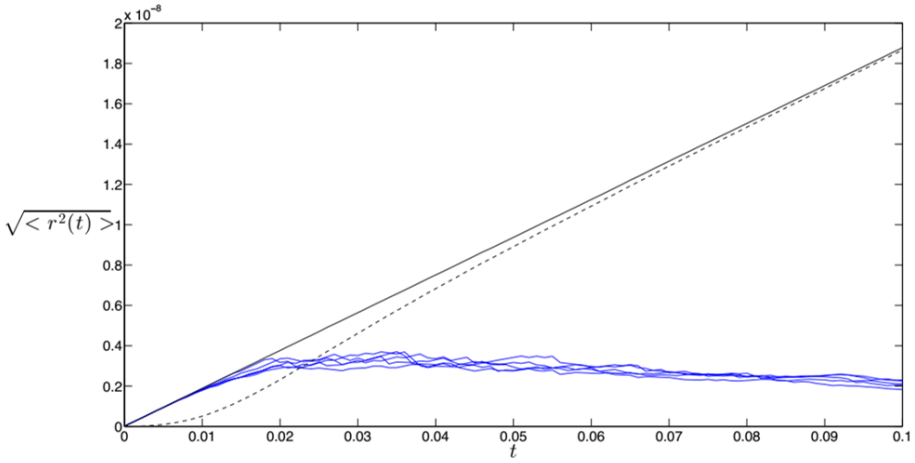

FIGURE 8.1: Here we illustrate the effect of a bombardment of a Gold nanosphere by photons on its averaged position spread (of its center of mass wave function (CMWF) expressed in m). The wiggly curves on the bottom represent five individual quantum realizations corresponding to $(\sigma_r)_Q \equiv \sqrt{\mathcal{Q}_x + \mathcal{Q}_y + \mathcal{Q}_z}$ where $\mathcal{Q}_i$ is defined in (8.3). The dotted curve corresponds to the classical average spread of the central positions of individual wave functions (averaged over 10 000 realizations): $(\sigma_r)^2_{cl} \equiv \sum_{i=x,y,z} \left(\langle q_i^2 \rangle - \langle q_i \rangle^2\right)$. The full curve corresponds to the total position spread (i.e.., the square root of the sum of the squares of the spread of individual wave functions and of the dotted curve): $(\sigma_r)^2_{total} \equiv (\sigma_r)^2_C + (\sigma_r)^2_Q$. The theoretical value computed from equation (7.87) is nearly identical to the simulated curve.

It is important to keep in mind that the decoherence process *à la* GRW is characterized by a moderate heating of the quantum system (the latter being due to the Brownian motion of the velocity caused by the quantum jumps). In absence of a specific cooling mechanism, the effective cooling of the quantum degrees of freedom must get counterbalanced by a heating of the classical ones, in virtue of energy conservation. Based on this property, the authors of [1] proposed a novel way of 'tailoring' the quantum state of the nanospheres by means of intentional decoherence, in order to escape the severe constraints imposed by the optical traps needed in a real experiment. Their conclusion was: *Obviously, this model is oversimplified, and it is beyond the scope of the present paper to develop it in more detail. It does suggest however that an in-depth theoretical and experimental investigation of a situation in which the nanosphere is submitted to a bombardment by light of well-chosen frequency and intensity such that the photonic wind slows down the nanosphere (as in cold atom cooling) and at the same time tailors the individual wave functions according to our needs, might be called for. Combining both*

features (cooling and localization) constitutes an answer of principle to the challenges raised by the preparation process required in our experimental proposal.

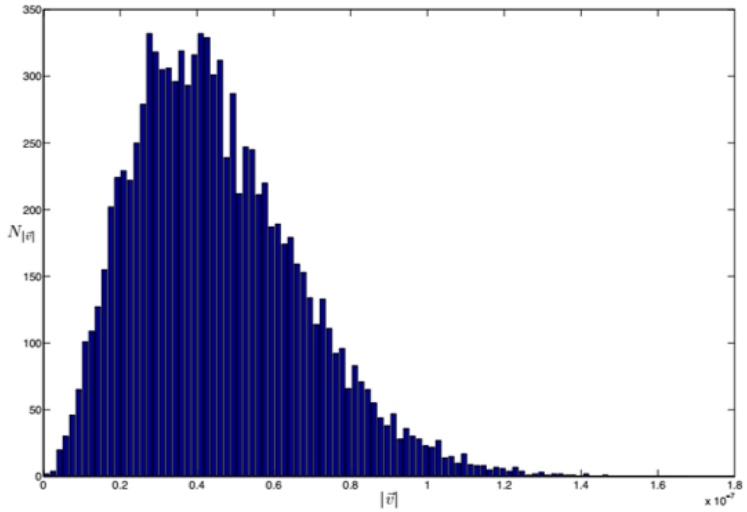

FIGURE 8.2: Histogram of the distribution of the classical velocities (m/s) during the decoherence process shown in figure 8.1 after 0.01 s.

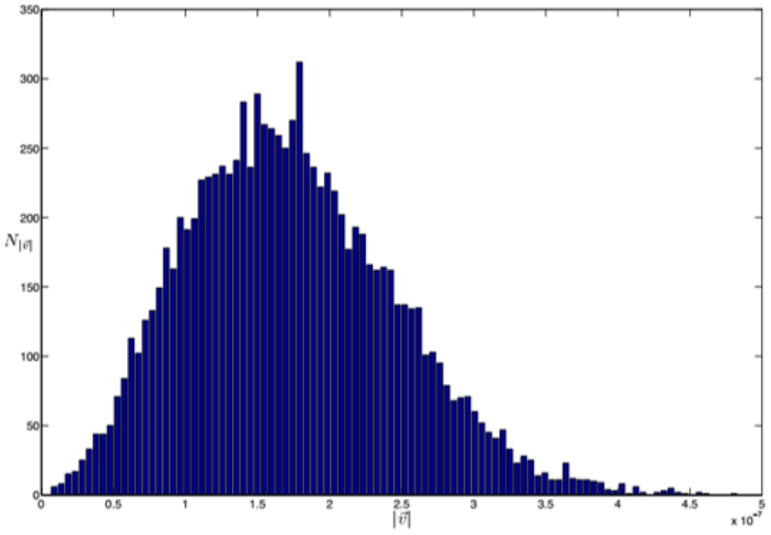

FIGURE 8.3: Histogram of the distribution of the classical velocities (m/s) during the decoherence process shown in figure 8.1 after 0.2 s.

In the present chapter we shall develop this idea and study the interplay of cooling and decoherence. It is worth noting that this topic seemingly did not deserve much attention in the past, among others, probably because the development of laser cooling at one side and decoherence at the other side were to some extents simultaneous (for example the GRW paper [2] was published in 1986, while the famous paper [3] "optical molasses" by Lett *et al.* which is one of the most influential pioneer papers in the field of Doppler cooling was published in 1989).

8.1.1 Motivation

There are several techniques of laser cooling [4, 3, 5, 6, 7, 8, 9, 10, 11]. The first one that has been used and that will be considered in this chapter is the Doppler cooling methods [12, 13]. It is based on the interaction of light and matter. During this interaction, a two-level atom alternates between its ground and its excited state. Using this property as well as that of the Doppler effect it was shown [12] that one could cool atoms with lasers very efficiently. This discovery is at the heart of a quantum technological revolution that led to various applications from purely fundamentals to applied physics. In the standard description of the doppler cooling, the internal degrees of freedom (energy levels, spin ...) are treated quantum mechanically. While the external degrees of freedom (positions, velocities ...) are most often treated classically.

In the semi-classical approach, the atom is described like a classical and point like particle. It is worth noting that due to the presence of spontaneous emission, the atom must be treated as an open quantum system, interacting with its environment. From this point of view it is legitimate to investigate the role played by quantum external degrees of freedom, among others for what concerns decoherence.
This constitutes the main objective of the present chapter, which is to study the interplay between decoherence and cooling, at the level of atomic external degrees of freedom.

8.1.2 Our approach

In order to better understand the role played by the quantum degrees of freedom, we shall systematically consider that at each time the total system is a mixture of gaussian pure states so that each atomic state i is represented by a wave function (in position representation[1]):

$$\psi_i(q,t) = \frac{1}{\mathcal{N}} \exp^{-A_i(t)\,q^2/2 + B_i(t)\,q}, \quad \text{where} \quad \frac{1}{\mathcal{N}} = \left(\frac{\text{Re } A_i}{\pi}\right)^{\frac{1}{4}} \exp\left(-\frac{\text{Re}^2\ B_i}{2\,\text{Re } A_i}\right). \tag{8.1}$$

Therefore, a gaussian state is characterized by four real parameters, Re A_i, Im A_i, Re B_i and Im B_i. Those parameters are linked to the following "classical" quantities $\langle q \rangle$ and $\langle p \rangle$

$$\langle q_i \rangle = \frac{\text{Re } B_i}{\text{Re } A_i}, \quad \langle p_i \rangle = m \langle v_i \rangle = \hbar \frac{\text{Im } B_i \text{ Re } A_i - \text{Im } A_i \text{ Re } B_i}{\text{Re } A_i} \tag{8.2}$$

But also to two "quantum" quantities $\mathcal{Q}_i$ and $\mathcal{P}_i$ which are the corresponding variances in position and momentum

$$\mathcal{Q}_i = \langle q_i^2 \rangle - \langle q_i \rangle^2 = \frac{1}{2\text{ Re } A_i}, \quad \mathcal{P}_i = m^2 \left(\langle v_i^2 \rangle - \langle v_i \rangle^2\right) = \frac{\hbar^2}{2\text{ Re } A_i} |A_i|^2 \tag{8.3}$$

In particular, $\mathcal{Q}_i$ and $\mathcal{P}_i$ are constrained by Heisenberg uncertainties

$$\mathcal{Q}_i \cdot \mathcal{P}_i \geq \frac{\hbar^2}{4} \tag{8.4}$$

As explained in the introduction, the conventional approach to Doppler cooling consists of neglecting the role played by $\mathcal{Q}_i$ and $\mathcal{P}_i$, based on the implicit assumption that $\mathcal{P}_i$ is small

[1] Passing to 3 spatial dimensions would not significantly affect our analysis at this level so that, we shall assume here that the propagation is axial (say along the X direction) in order to simplify the treatment.

(i.e. the wave packet is nearly monochromatic) while it is neither necessary nor useful to know the position of the atom with accuracy better than say $\sqrt{\frac{\hbar^2}{4\mathcal{P}_i}}$.

Describing the atom by a (mixture of) gaussian states will allow to double the numbers of degrees of freedom. As a matter of fact, in addition to the classical position and velocity, which are associated to the first moments of the corresponding observables ($\langle q_i \rangle$ and $\langle p_i \rangle$), we add the quantum degrees of freedom associated to their second moments ($\mathcal{Q}_i$ and $\mathcal{P}_i$). Our main goal consists of simulating decoherence, resorting to GRW's process [2] which is an unraveling of the master equation associated to decoherence (7.64) valid in both the long and short wavelength regimes. It is a gaussian process so that at each time the quantum state associated to an individual "trajectory" (or realization of the GRW stochastic process) is a gaussian state, which explains our choice to represent the density matrix as a mixture of gaussian states.

It is worth noting that we do not use GRW stochastic process as it was originally intended (see chapter 7 for more detail). The two characteristic parameters of the decoherence, which are the number of jumps by unit of time Γ and the typical localization size associated to a jump $1/\sqrt{\alpha}$, are not fixed according to GRW hidden variable theory but are, in the present approach, dictated by the physical conditions of the experiment.

8.1.3 A generalized thermal (Maxwell-Boltzmann) distribution

It is worth noting that the classical average position $\langle q \rangle$ as well as the quantum variance in position $\mathcal{Q}$ are not constrained, which means that generalized thermal states are characterized by well-defined statistical distributions in momentum space only. In order to simulate a cooling process during which atoms originate from the same source located at $q = 0$, we shall impose as initial condition that $\langle q \rangle(t = 0) = 0$ and $\mathrm{Im}\, A(t = 0) = 0$. With these supplementary constraints, the initial (generalized) thermal distribution is unambiguously defined by two parameters, T_{cl} and T_Q.

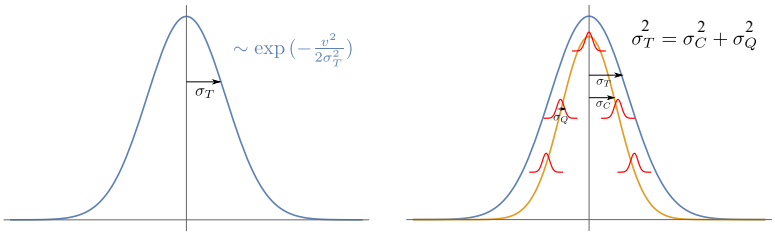

FIGURE 8.4: Gaussian distribution of velocities (left) resulting from a time-of-flight measurement. It is shown in the text to correspond to a preparation at time $t = 0$ of a (generalized thermal) mixture of gaussian wave packets of the type $\sqrt{\frac{1}{2\pi\sqrt{\mathcal{Q}}}}\exp\left(-q^2/4\sqrt{\mathcal{Q}} + ik_{cl}\cdot x\right)$ such that $\forall k_{cl}, \sqrt{\mathcal{P}}/m = \sqrt{k_B T_Q/m}$, while the "classical" velocity $\hbar k_{cl}/m$ is gaussian distributed with a standard deviation $\sigma_C = \sqrt{k_B T_C/m}$. Note that each gaussian wave packet saturates Heisenberg uncertainties at time $t = 0$ so that $\sqrt{\mathcal{P}}/m = \frac{1}{m}(\hbar/2\sqrt{\mathcal{Q}})$.

As we shall see, if we measure the distribution of momenta (velocities) of the system through a time-of-flight experiment, everything happens as if the generalized thermal distribution was a classical (Maxwell-Boltzmann) distribution of temperature $T = T_{cl} + T_Q$ (figures 8.4, left, and 8.5, left).

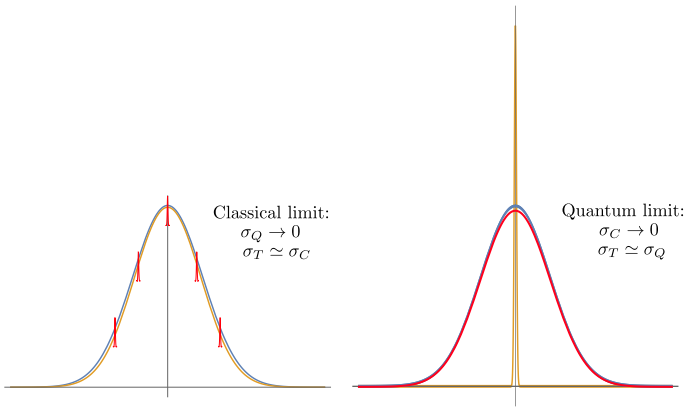

FIGURE 8.5: Two extreme situations corresponding to the right of figure 8.4, considered in the quantum (right) and classical (left) limit. Quantum degrees of freedom are plotted in red and classical ones in gold. The blue curve is the observed velocity distribution after a time of flight experiment, in the limit of large times-of-flight (T.O.F.). It is the same in both cases.

In other words it is gaussian distributed symmetrically around zero, with a variance equal to the sum of the classical and of the quantum variances (figure 8.4, right).
The corresponding distributions are schematically plotted at the level of figures 8.4 and 8.5. In particular, if we perform a time-of-flight experiment at the end of which we measure the distribution of positions, nothing distinguishes a purely classical distribution ($T = T_{cl}$, $T_Q = 0$, figure 8.5, left) from a purely quantum one ($T = T_Q$, $T_{cl} = 0$, figure 8.5, right). The distribution of positions is gaussian in both cases, characterized by the same average value and the same standard deviation ($\sqrt{k_B T/m} \cdot T.O.F.$, where $T.O.F.$ is the time-of-flight (this result is valid in the limit where $T.O.F.$ is large enough). The initial velocities are deduced[2] from the final positions at the end of the T.O.F. experiment by dividing the observed position by the T.O.F. (in accordance with the experimental scheme proposed by Feynman and Hibbs [14] in the quantum case for which $T_{cl} = 0$).

8.1.4 Estimate of the relevant parameters

To begin with, let us first recall the process of Doppler cooling of one atom. In particular, we consider an individual cycle, during which an atom absorbs a photon emitted by the lasers, reemits a spontaneous photon, absorbs again a photon and so on. We shall consider situations during which the process of cooling is realized in the low intensity regime, so that we are in the weak coupling regime [3] and it makes sense to describe this process [15, 16] in terms of absorption and emission rates *à la* Einstein. To do so, let us introduce the probabilities per unit of time:

[2] Using the properties of the propagator of the free Schrödinger equation, Feynman and Hibbs established [14] that $\lim_{t\to\infty} |\Psi(x,t)|^2 dx|_{x=pt/m} = |\tilde{\Psi}(p/\hbar, t=0)|^2 dp$ where $\tilde{\Psi}(k, t=0)$ is the Fourier transform of the initial wave function: $\tilde{\Psi}(k, t=0) = (1/\sqrt{2\pi}) \int_{-\infty}^{+\infty} exp(-ikx)\Psi(x, t=0)$.

- $\Gamma_\pm$ to absorb a photon denoted here $\Gamma_\pm$ in order to stress that we consider a situation with two lasers, emitting along $+X$ and $-X$ respectively: $\Gamma_\pm = \Gamma_+ + \Gamma_-$.

- Γ_0 to emit spontaneously a photon. Γ_0 is the so-called spontaneous emission rate.

Here we consider the low intensity regime in which stimulated emission can be neglected. Thus, the probability to find an atom in its excited (or in its ground) state can be shown to obey

$$\frac{1/\Gamma_0}{1/\Gamma_0 + 1/\Gamma_\pm}, \quad \text{or} \quad \frac{1/\Gamma_\pm}{1/\Gamma_0 + 1/\Gamma_\pm} \tag{8.5}$$

Γ_0 can be computed making use of Fermi's golden rule, or estimated empirically by measuring the linewidth of the transition addressed during the cooling process. In order to estimate $\Gamma_\pm$, it appears to be useful to express the temporal evolution of the system in terms of the density matrix associated to the internal degrees of freedom of the atom as we shall do now.

8.1.5 Description in terms of the density matrix

Before implementing decoherence in the Doppler cooling, let us first present quickly the theoretical tools that will be necessary for the following. The interaction of a two-level atom with an external and classical electric field (here the field generated by the lasers) is described by a total Hamiltonian H_T made by the sum of the free Hamiltonian

$$H_0 = \begin{pmatrix} \omega_0 & 0 \\ 0 & 0 \end{pmatrix} \tag{8.6}$$

with the Hamiltonian of interaction H_{int}, which after the dipolar approximation reads:

$$H_{int} = -\overrightarrow{d} \cdot \overrightarrow{E} \quad \text{where} \quad \overrightarrow{E} = E_0 \cos(\omega_L t). \tag{8.7}$$

In the rotating wave approximation, we get

$$H_T = H_0 + H_{int} = \hbar \begin{pmatrix} \omega_0 & \Omega_L \cos(\omega_L t) \\ \Omega_L^* \cos(\omega_L t) & 0 \end{pmatrix} \tag{8.8}$$

where $\Omega_L = -\frac{E_0}{\hbar} \langle g | \overrightarrow{d} \cdot \overrightarrow{e} | e \rangle$, $\overrightarrow{d}$ is the dipole moment $\overrightarrow{d} = q_e \overrightarrow{r}$ and $\{|g\rangle, |e\rangle\}$ are the ground and excited states

$$|g\rangle = \begin{pmatrix} 0 \\ 1 \end{pmatrix} \quad \text{and} \quad |e\rangle = \begin{pmatrix} 1 \\ 0 \end{pmatrix} \tag{8.9}$$

In the interaction picture the Hamiltonian reads

$$H_T = \hbar \begin{pmatrix} \delta_L & \Omega_L/2 \\ \Omega_L^*/2 & -\delta_L \end{pmatrix} \tag{8.10}$$

where $\delta_L = \omega_L - \omega_0$ is the so-called detuning. In order to take account of the spontaneous emission which results from the interaction of the two-level atom with the quantized transverse electromagnetic modes, it is usual [11] to write down a master equation in the Lindblad from:

$$\frac{d\rho}{dt} = \underbrace{-\frac{i}{\hbar}\left[\widehat{H},\rho\right]}_{\text{Schrodinger evolution}} - \underbrace{\frac{1}{2}\left(\widehat{L}^{\dagger}\widehat{L}\rho + \rho\widehat{L}^{\dagger}\widehat{L} - 2\,\widehat{L}\,\rho\widehat{L}^{\dagger}\right)}_{\text{Spontaneous emission: } \widehat{L}_{sp}} \tag{8.11}$$

where ρ is the 2×2 density matrix and $\widehat{L}$ is the Lindblad operator. In this case $\widehat{L}$ reads $\widehat{L} = \sqrt{\Gamma_0}\,\sigma^-$ where

$$\sigma^+ = \begin{pmatrix} 0 & 1 \\ 0 & 0 \end{pmatrix} \quad \text{and} \quad \sigma^- = \begin{pmatrix} 0 & 0 \\ 1 & 0 \end{pmatrix} \tag{8.12}$$

thus we get

$$\boxed{\widehat{L}_{sp} = -\Gamma_0 \begin{pmatrix} \rho_{ee} & \rho_{eg}/2 \\ \rho_{ge}/2 & -\rho_{ee} \end{pmatrix}} \tag{8.13}$$

8.1.6 Ergodic hypothesis

When the regime is stationary, it is possible to invoke the ergodic hypothesis to the extent that a large number of individual histories are considered. This allows us to write down, the expressions for the probabilities to find the atom in the excited (or ground) state as

$$\boxed{\rho_{ee} = \frac{1/\Gamma_0}{1/\Gamma_0 + 1/\Gamma_{\pm}}} \quad \text{and} \quad \boxed{\rho_{gg} = \frac{1/\Gamma_{\pm}}{1/\Gamma_0 + 1/\Gamma_{\pm}}} \tag{8.14}$$

The quantities ρ_{ee} and ρ_{gg} are the steady-state population of the excited and the ground level. Those probabilities do not depend on time, which means and are in one to one correspondence with the steady state solution of the master equation (8.11)

$$\rho_{ee} = \frac{\Omega^2/4}{\Omega^2/2 + \delta_L^2 + \Gamma_0^2/4}, \quad \text{and} \quad \rho_{gg} = 1 - \rho_{ee} \tag{8.15}$$

It is however necessary to take account of the Doppler effect. To do so let us consider the momentum and energy transfers that accompany the kick of a photon with the atom. The law of momentum conservation implies that

$$m\overrightarrow{v} + \hbar\overrightarrow{k_L} = m\overrightarrow{v_f} \tag{8.16}$$

where $\overrightarrow{v}$ (resp. $\overrightarrow{v_f}$) is the initial (resp. final) atomic velocity and $\hbar\overrightarrow{k_L}$ is the momentum carried by the photon. In addition, the energy conservation implies that

$$E_g + mv^2/2 + \hbar\,\omega_L = E_e + mv_f^2/2 \tag{8.17}$$

where E_g (resp. E_e) is the energy of the ground (resp. excited) state. Using these conservation equations lead to

$$\hbar\omega_L = \hbar\omega_0 + \hbar\,\overrightarrow{k}_L \cdot \overrightarrow{v} + \frac{\hbar^2 k_L^2}{2m} \tag{8.18}$$

The last term above is the recoil energy which in the regime considered here can be neglected [3]. Now let us write $\tilde{\omega_0} = \omega_0 + \overrightarrow{k_L} \cdot \overrightarrow{v}$, we see that an atom moving with velocity $\overrightarrow{v}$ will have a natural linewidth centered at $\tilde{\omega}_0$.

The steady-state population in the excited level is modified as follows:

$$\boxed{\rho_{ee} = \frac{\Omega_L^2/4}{(\omega_L - \tilde{\omega}_0)^2 + \Omega_L^2/2 + \Gamma_0^2/4} = \frac{\Omega_L^2/4}{(\delta_L - \overrightarrow{k}_L \cdot \overrightarrow{v})^2 + \Omega_L^2/2 + \Gamma_0^2/4}} \tag{8.19}$$

Now, the steady state is by definition reached when emission and absorption exactly compensate each other. This means that:

$$\rho_{ee}\,\Gamma_0 = \rho_{gg}\,\Gamma_\pm \tag{8.20}$$

Combining the constraints (8.14) and (8.20), and making use of the fact that, in the low intensity regime considered here, $1/\Gamma_0 + 1/\Gamma_\pm \approx 1/\Gamma_\pm$, we finally get

$$\Gamma_\pm \approx \Gamma_0\,\rho_{ee}. \tag{8.21}$$

Hence, it allows us to accurately estimate the value of the probability per unit of time Γ_- (resp. Γ_+) to absorb a photon originating from the laser in $-X$ (resp.$+X$) :

$$\boxed{\Gamma_{+/-} \approx \frac{\Omega_L^2/4}{(\omega_L - \tilde{\omega}_{0,+/-})^2 + \Omega_L^2/2 + \Gamma_0^2/4}\,\Gamma_0} \tag{8.22}$$

where $\tilde{\omega}_{0,+/-} = \omega_0 \pm k_L\,v$.

8.1.7 Monte-Carlo formulation of the cooling process

At this level, we have at our disposal enough information in order to simulate, in a Monte-Carlo approach, the individual histories undergone by an atom during Doppler cooling. Those histories are exemplified here by the code reproduced from the reference [17] (see figure 8.6 for more detail). This numerical scheme aimed at providing a microscopic description of the laser cooling process along one dimension (say X). In the present section we shall assume that, for what concerns the external degrees of freedom, the atom is "classical" ($T_C = T$, $T_Q = 0$), i.e. the atom is treated in the usual way.

In summary, the process illustrated in figure 8.6 goes as follows:

- If the atom is excited (left column), it can spontaneously de-excite to its ground state after a time of the order of $1/\Gamma_0$ and with a probability:

$$\boxed{\Gamma_0\,dt} \tag{8.23}$$

Thus if we write $k_0 = \omega_0/c$ then the magnitude of momentum transfer is equal to $\hbar k_0$. In the case of spontaneous emission, the direction of the emitted photon is randomly distributed. Let us denote by $R_0 = \hbar k_0$ the radius of a 3-D sphere over which the momentum of the photon can be distributed, and let us project this momentum along the axis of cooling (X).

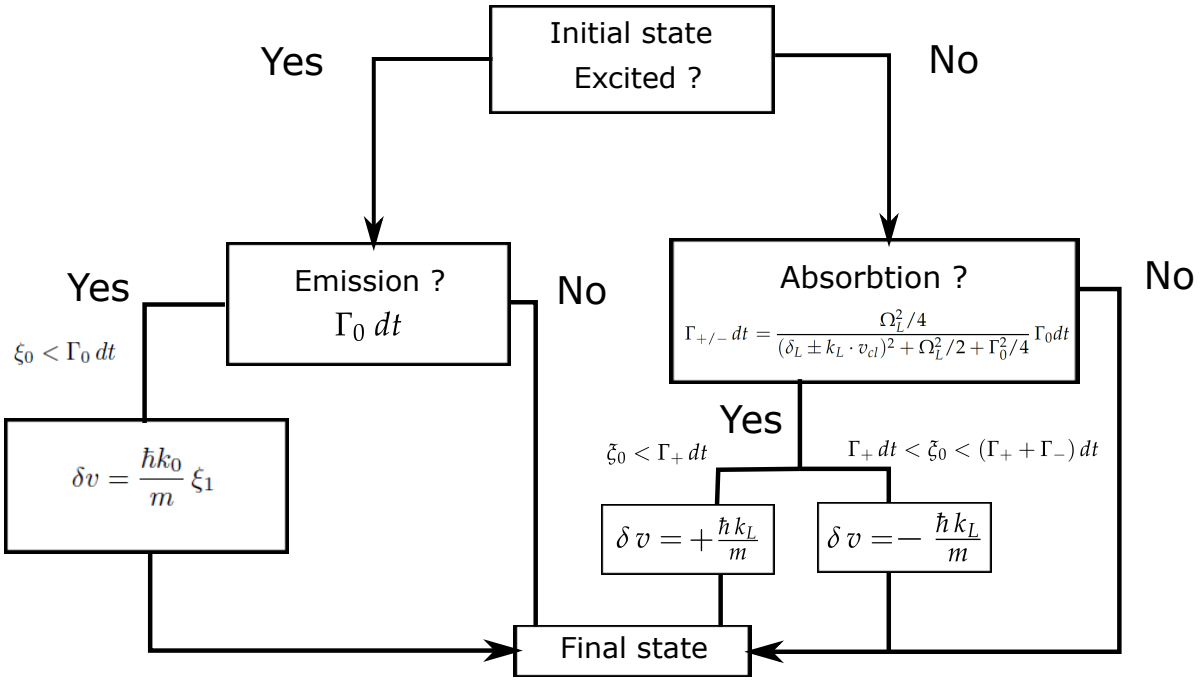

FIGURE 8.6: Numerical scheme of the cooling process [17]. Here we introduced two uniformly distributed random numbers, $\xi_0 \in [0,1]$ and $\xi_1 \in [-1,1]$. Note that stimulated emission practically never happens in the low intensity regime that we consider here. It is because its probability, which is equal to that of stimulated absorption, is very low as compared to that of spontaneous emission.

Denoting θ the angle between the $X-$axis and this momentum, we get that the probability that the projection of momentum lies in the interval $[R_0\, cos\theta, R_0\, cos(\theta + d\theta)]$ is equal to

$$\frac{1}{4\pi R_0^2}(2\pi R_0\, sin\theta)\cdot(R_0\, d\theta) = \frac{1}{2}d(cos\theta) = \frac{1}{2\,R_0}\cdot dx \tag{8.24}$$

where $x = R_0\, cos(\theta)$ varies from $-R_0$ to $+R_0$.

We conclude that the projection of the momentum of the photon on the axis X is uniformly distributed in the range $[-\hbar k_0, \hbar k_0]$ according to the uniform probability density

$$P_x = \frac{1}{2\,\hbar k_0}. \tag{8.25}$$

- Now if the atom is in the ground state (right column), the probability to absorb a photon of the laser at $\pm X$ in a time interval dt is given by the Lorentzian probability distribution (8.22) time dt

$$\boxed{\Gamma_{+/-}\, dt \approx \frac{\Omega_L^2/4}{(\delta_L \pm k_L \cdot v_{cl})^2 + \Omega_L^2/2 + \Gamma_0^2/4}\,\Gamma_0 dt} \tag{8.26}$$

At this level one might object that ergodicity is not applicable because the process is not stationary, due to the fact that ρ_{ee} varies in time during the cooling process, because of the Doppler shift which depends on time. However, many quantum jumps are necessary in order to significantly change the velocity of the atom, because the photon wind is very weak. Therefore, it makes sense to assume that a "local in time" condition of ergodicity is fulfilled.

8.1.8 Monte-Carlo simulation of the cooling process

Here we consider the cooling process of Calcium atoms with the lasers tuned to address the ground state $4^2\,S_{1/2}$ and the excited state $4^2\,P_{1/2}$. The associated resonant wavelength is $\lambda_0 = 397$ nm, while the line width is $\Gamma_0 = 143 \times 10^6\,\mathrm{s}^{-1}$ so that the lifetime of the excited state is $1/\Gamma_0 \approx 7$ ns. The mass of the calcium atom is $m = 40$ a.m.u. Based on experimental observations and on the domain of approximations discussed before, we chose the Rabi frequency to obey $\Omega_L = 0.1\Gamma_0/\sqrt{2}$, and imposed the detuning of the lasers to obey $\delta_L = -\Gamma_0/2$. In the numerical simulations we chose a time step $dt = \Gamma_0^{-1}/10 = 0.7$ ns.

The term describing the dipole is traditionally [18] taken to be of the order of

$$||\langle g|q_e\,\overrightarrow{r}\,|e\rangle\,|| = 2q_e a_0, \tag{8.27}$$

where q_e is the electron charge, and $a_0 = 5.29 \times 10^{-11}$ m is the Bohr radius. The Rabi frequency is by definition given by the following expression

$$\Omega_L = -\frac{E_0}{\hbar}\langle g|\,q_e r\cdot\hat{e}\,|e\rangle\,. \tag{8.28}$$

From the values ($\Gamma_0 = 143 \times 10^6 \mathrm{s}^{-1}$ and $\Omega_L = 0.1\,\Gamma_0/\sqrt{2}$), we find $E_0 \approx 60$ V/m, which corresponds to a laser power The spontaneous emission is an isotropic process, equivalent to a random walk (brownian motion) in the velocity space which consequently heats the atoms. The Doppler cooling limit is reached when the heating due to spontaneous emission compensates the cooling. The temperature limit also known as Doppler temperature T_D depends of course on the way we describe the random emission process. In [3] it is shown that the Doppler temperature obeys

$$T_D = \frac{\hbar\,\Gamma_0}{2k_B} = 0.544 \text{ mK in this case} \tag{8.29}$$

In figure 8.7, we illustrate the time evolution of the temperature obtained after performing the loop described here above for 1000 atoms, whose initial velocities are distributed according to a 1D Maxwell Boltzmann distribution. The initial velocities are generated using an initial temperature $T_0 = 1$ mK which corresponds to a mean velocity around 0.5 m/s. At any subsequent points of time, the velocity is modified by the process. The temperature is deduced using the equipartition theorem at 1D:

$$\boxed{T = \frac{m}{k_B}\,\langle v^2\rangle} \tag{8.30}$$

Our simulation shows that the temperature decreases gradually and then reaches a limit of 0.35 mK, which differs from the theoretical value (8.29), i.e. we found $T_\mathrm{f} \approx 2\,T_D/3$.

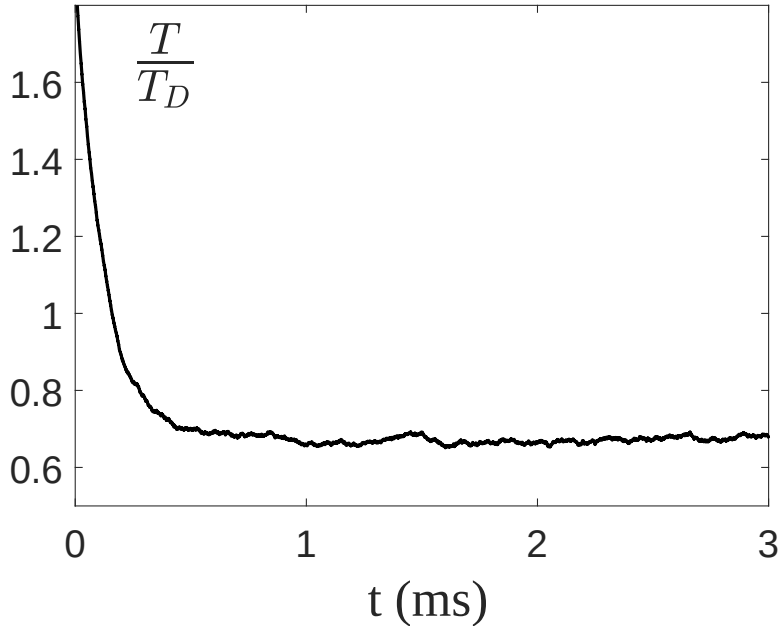

FIGURE 8.7: Here we illustrate the time evolution of the temperature of a gas made by 1000 atoms. The temperature is expressed in function of the Doppler temperature (8.29). Here we used an initial temperature of 1 mK. The temperature decreases and stabilizes close to the Doppler temperature, i.e. $T_{\mathrm{f}} \approx 2\,T_D/3$ where T_D.

It is not surprising because from (8.25) and because we consider two lasers it follows that

$$\hbar\,\langle k\rangle = 2\cdot\frac{1}{2\,\hbar k_0}\int_{-\hbar k_0}^{\hbar k_0} dx\,x = 0, \quad \text{and} \quad \hbar^2\,\langle\,k^2\,\rangle = 2\cdot\frac{1}{2\,\hbar k_0}\int_{-\hbar k_0}^{\hbar k_0} dx\,x^2 = \frac{2}{3}\,\hbar^2 k_0^2 \tag{8.31}$$

$$I = E_0^2\sqrt{\frac{\epsilon_0}{\mu_0}} = \frac{E_0^2}{377} \approx 10\ \mathrm{W/m^2}. \tag{8.32}$$

which explains the factor $2/3$.

A fine understanding of the process does not really matter actually because anyhow the Doppler cooling limit is not observed experimentally. The reason is that the model sketched here does not take account of extra-cooling mechanisms such as the Sysiphus mechanism which result in a substantial lowering of the cooling limit [19]. Practically the process reaches temperatures quite lower than the Doppler limit and it is ultimately limited from below by the recoil limit [3]

$$T_R = \frac{(\hbar\,k_L)^2}{k_B\,m} = 3\,\mu\mathrm{K} \text{ in this case where } k_L = 1.58\cdot 10^7 \text{ m and } m = 40 \text{ a.m.u} \tag{8.33}$$

At this level the model outlined above loses its relevance because it ought to be complemented by incorporating more complex effects of the Sysiphus type. In figure 8.8 we plot the temperature of one atom whose initial velocity is $v_0 = 10$ m/s and we plot in figure 8.9 the Doppler kicks the atom had undergone during its evolution.

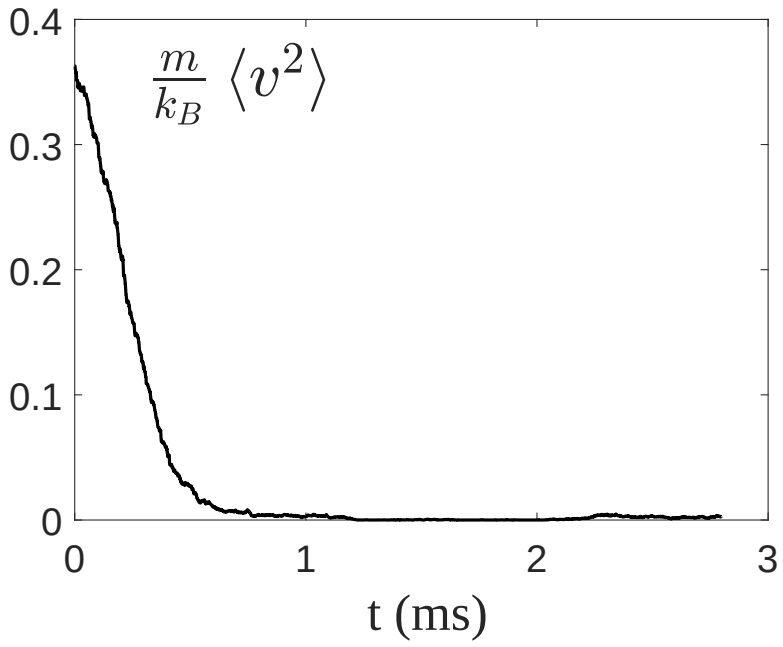

FIGURE 8.8: Temperature of one atom during the cooling process. We used an initial velocity of 10 m/s and an atomic mass $m = 40$ a.m.u.

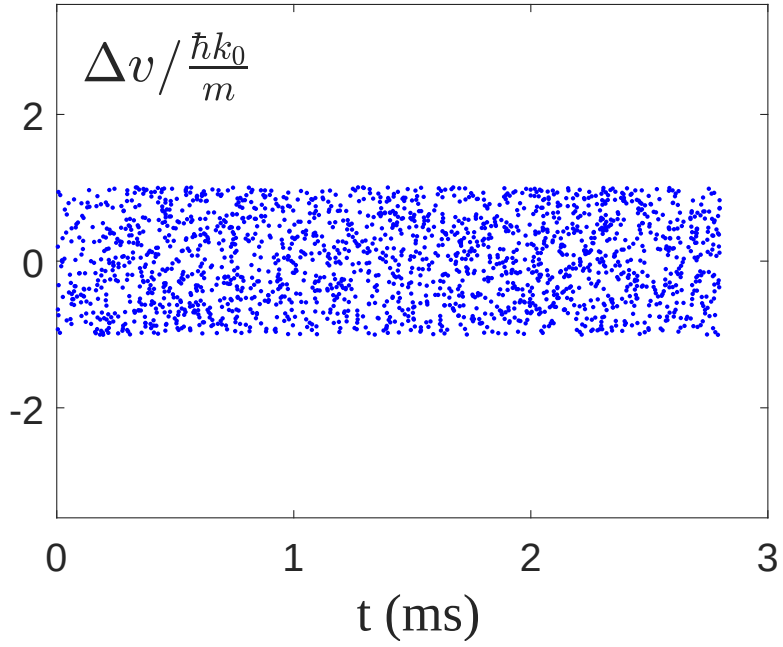

FIGURE 8.9: We plot here the Doppler kicks Δv due to spontaneous emissions. The kicks are uniformly distributed between $\pm \frac{\hbar k_0}{m}$.

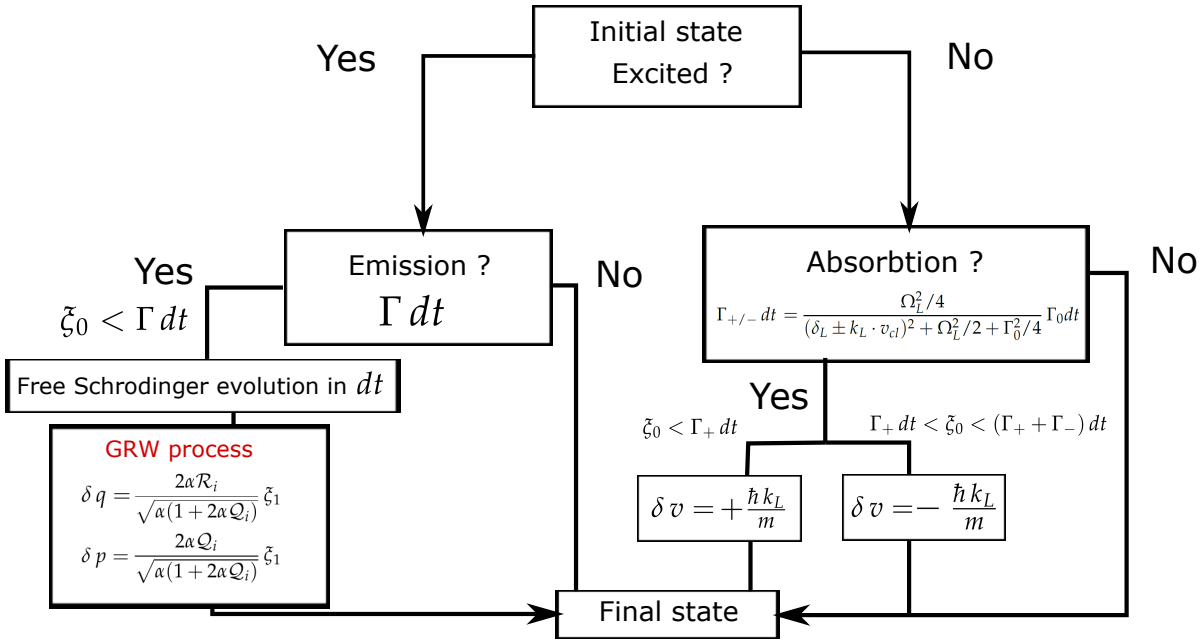

FIGURE 8.10: Here we consider a numerical scheme which combines GRW decoherence (7.80-7.81) and Doppler cooling. We introduced two random numbers, ξ_0 is uniformly distributed in $[0,1]$ and ξ_1 is normally distributed.

8.2 GRW and cooling

A last important step before to implement decoherence is to justify the choice of the two parameters characterizing the GRW model in this context. The physical justification is the following: at each spontaneous emission, the atom is instantaneously localized in space. This localization is accompanied by a quantum decoherence process that will be modeled by the GRW model. Therefore, it seems natural to use the decay rate Γ_0 as the decoherence frequency Γ.

Now we have to justify the choice of the second parameter α which is related to the spatial localization. A physical way to choose α is the following: as explained in the previous section, the Doppler limit (8.29) occurs when the effect of the cooling is compensated by the brownian motion in the velocity space. This Brownian motion which is due to spontaneous emission is accompanied by a heating which in this case [3] is equal to:

$$\left(\frac{d\langle p^2\rangle}{dt}\right)_{DC} = \hbar^2\,\Gamma_0\,\langle k^2\rangle \tag{8.34}$$

Now using (8.31) we get

$$\left(\frac{d\langle p^2\rangle}{dt}\right)_{DC} = \frac{\hbar^2\,\Gamma_0}{3}\,k_0^2 \tag{8.35}$$

Since the GRW model [2] is also characterized by a heating

$$\left(\frac{d\langle p^2\rangle}{dt}\right)_{GRW} = \frac{\hbar^2\,\Gamma_0\,\alpha}{2} \tag{8.36}$$

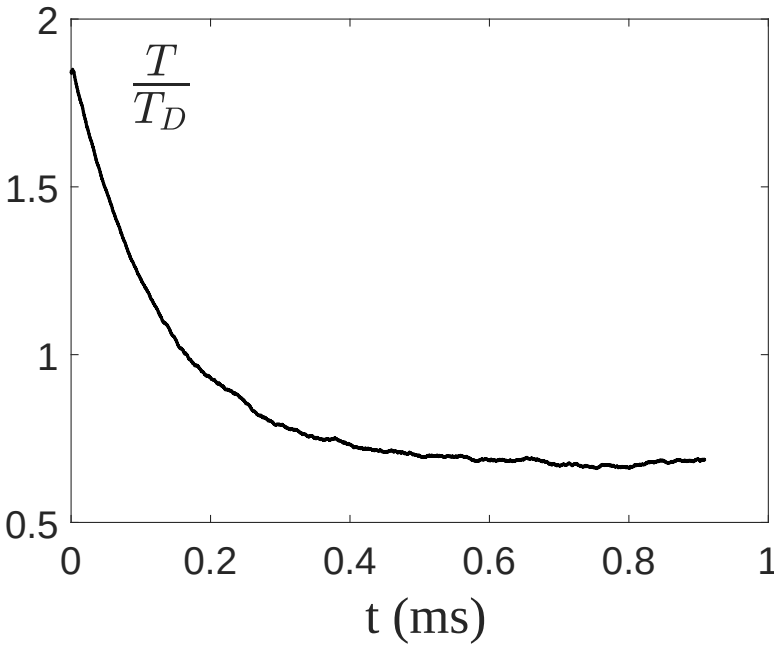

FIGURE 8.11: Here we plot the temperature of a gas made by 10^4 atoms when combining Doppler cooling and GRW decoherence. We chose an initial wavefunction spread $\sigma_{x,i,0} = 10^{-8}$ m. In this case, the temperature still stabilizes to $2\,T_D/3$ as if there is no decoherence (as in figure 8.7).

it seems natural to equalize both processes to deduce the value of α. Thus we finally get

$$\boxed{\alpha = \frac{2}{3}k_0^2} \tag{8.37}$$

Physically, it means that the decoherence localizes the atom in a region of space $1/\sqrt{\alpha}$ which is of the order of the photon wavelength λ_0.

8.2.1 Monte-Carlo simulation of the GRW process in the Doppler cooling

Similarly to the Monte-Carlo description of the cooling process presented in section 8.1.7, let us consider a numerical scheme in which the GRW model is implemented. To do so, we replace in the numerical scheme 8.6 the part of the code devoted to spontaneous emission by a GRW process (see figure 8.10). The GRW parameters were chosen as described in the previous section.

The resulting cooling process is plotted in figure 8.11. As can be seen in this figure, we obtain the same evolution of the temperature as the one obtained in figure 8.7 in accordance with (8.37). The figures 8.12-A and 8.12-B show the evolution of the spread in position and velocity averaged over 10^4 atoms. As confirmed numerically, those spreads remain gaussian distributed over time in agreement with the GRW model. We also plot in figure 8.13 the kicks in position Δq and in velocity Δv undergone by one atom during its evolution.

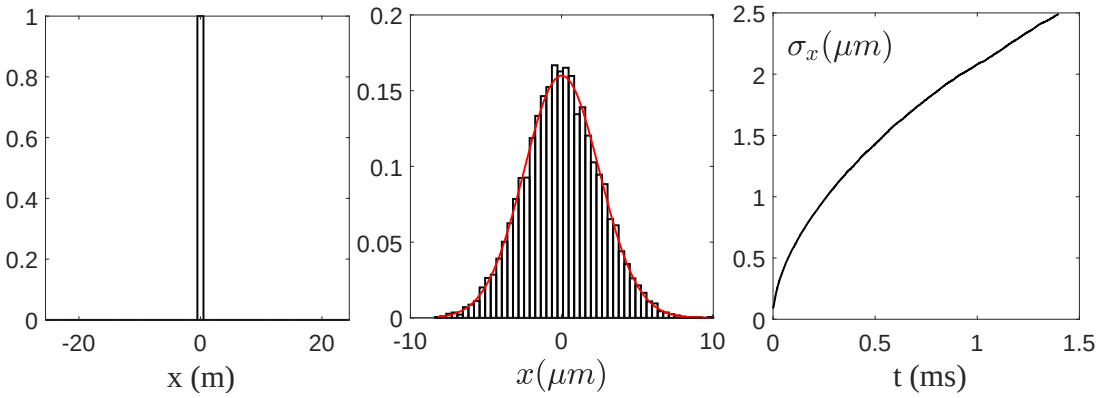

(A) Histogram of the positions at $t = 0$ (ms). (B) Histogram of the positions at $t = 1.4$ (ms). (C) Here we plot the time evolution of σ_x.

FIGURE 8.12A: The time evolution of the atomic positions are illustrated with histograms at time $t = 0$ and at $t = 1.4$ ms. The initial positions are all generated from the same source in $x = 0$. The continuous curve in (B) is a a gaussian fit traducing the fact that the positions are normally distributed according to $\mathcal{N}(0, \sigma_x)$. The gaussian width is plotted in figure (C). We started from $N = 10^4$ atomic initial positions at $x = 0$. We considered a sampling time step $\Delta t = 7.10^{-10}$ s.

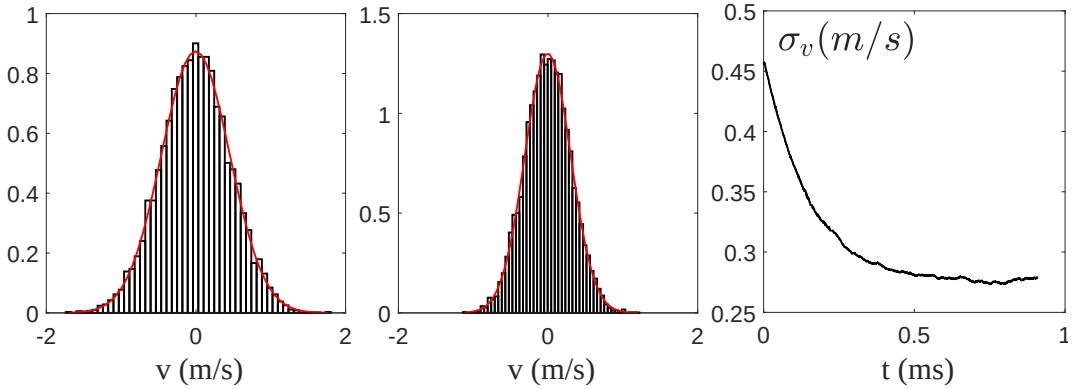

(D) Histogram of the velocities at $t = 0$ (ms). (E) Histogram of the velocities at $t = 1.4$ (ms). (F) Here we plot the time evolution of the spread σ_v.

FIGURE 8.12B: The time evolution of the atomic velocities are illustrated with histograms at time $t = 0$ and at $t = 1.4$ ms. The continuous curve in (D,E) is a a gaussian fit traducing the fact that the velocities are still normally distributed according to $\mathcal{N}(0, \sigma_v)$. The gaussian width is plotted in figure (F). We started from $N = 10^4$ atomic initial velocities distributed according to a Maxwell-Boltzmann velocity distribution for $T = 1$ mK and for a mass $m = 40$ a.m.u. We considered a sampling time step $\Delta t = 7.10^{-10}$ s.

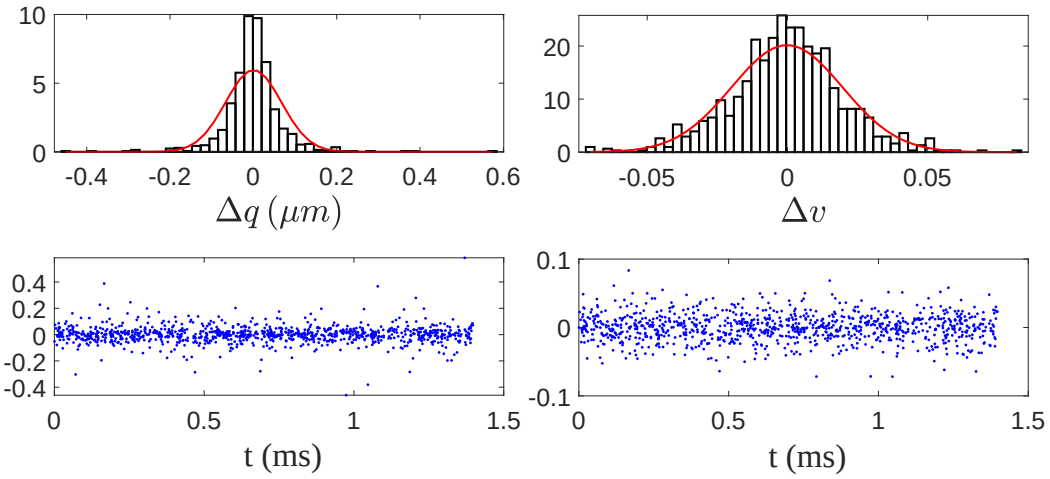

(A) Kicks in positions (B) Kicks in velocity

FIGURE 8.13: We plot here the kicks in position Δq and in velocity Δv undergone by one atom during its evolution. We also plot the corresponding histograms of those kicks. Here we chose $\sigma_{x,i,0} = 10^{-8}$ m.

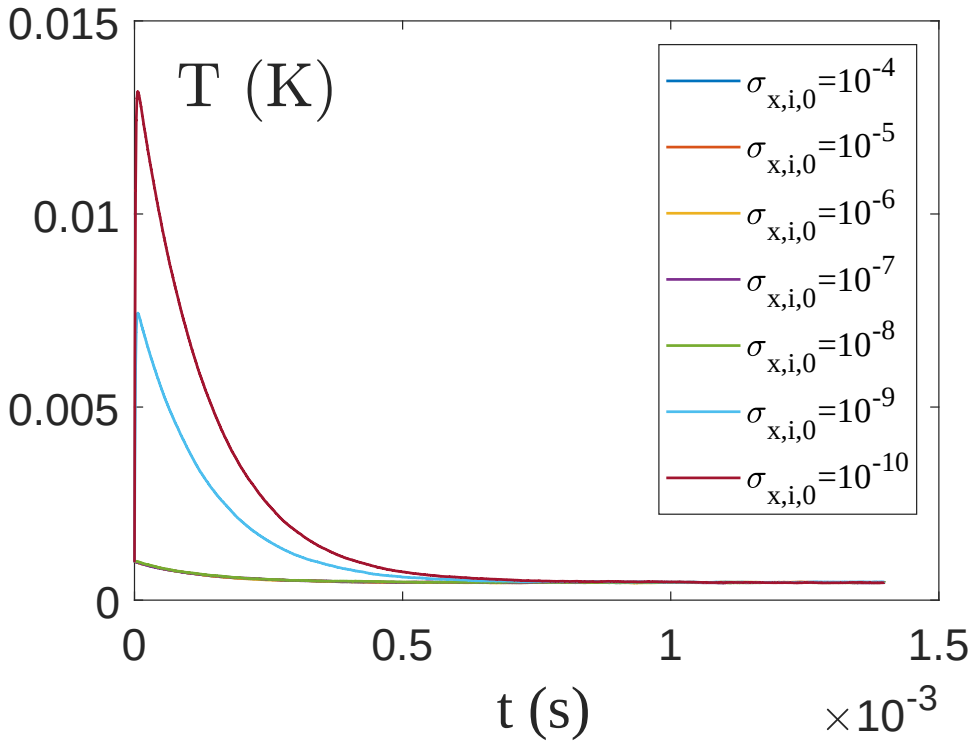

FIGURE 8.14: Here we plot the temperature of a gas of 10^4 atoms when combining Doppler cooling and GRW decoherence for different initial spreads $\sigma_{x,i,0}$ m. For $\sigma_{x,i,0} \geq 10^{-9}$, the classical temperature still stabilizes to $2\,T_D/3$ as if there is no decoherence (by comparison to figure 8.7). However, for $\sigma_{x,i,0} \leq 10^{-9}$ m, the temperature is dramatically affected and increases quickly before to stabilize after a relaxation process to $2\,T_D/3$. Here we used an initial temperature of 1 mK.

The key novelty here is that we have two new degrees of freedom in the description of the cooling which are the size of the individual atomic wave packets $\mathcal{Q}_i$ and their corresponding individual spread in velocity $\mathcal{P}_i$. In figure 8.14 we plot the temperature for various initial values of those individual spreads. For an initial spread $\sigma_{x,i,0} \geq 10^{-9}$ m, decoherence does not affect the stabilized temperature, it is still 0.35 mK exactly the same way as figure 8.7. However, a notable difference occurs beyond a critical value of the initial spread ($\sigma^c_{x,i,0} \approx 10^{-9}$ m) for which we can see that the temperature is dramatically affected. It quickly increases before to stabilize, after a relaxation process, around the Doppler temperature. In the one hand, it is reassuring to find the same temperature limit for all $\sigma_{x,i,0}$ while, on the other hand, it is surprising to see such a difference in the behavior of the temperature for $\sigma_{x,i,0} \leq 10^{-9}$ m.

We shall now give a theoretical justification of this increase and justify the critical value of the initial spread $\sigma^c_{x,i,0} \approx 10^{-9}$ m.

8.2.2 Momentum transfer from the quantum to the classical degrees of freedom

The first thing to note is that the increase of temperature occurs for small times, typically after the first few kicks. It is already confirmed by the numerical simulations as can be seen in figure 8.15 in which we used an initial spread $\sigma_{x,i,0} = 10^{-9}$ m. This figure provides a zoom of the transfer of momentum occurring between the quantum and the classical degrees of freedom during the process of decoherence.

In fact, as illustrated in figure 8.15, after some localizations, the individual spreads converge to the asymptotic spread predicted by the GRW model (for more details we refer the reader to section 7.E in which we introduced the parameter $\epsilon = \sqrt{\frac{\hbar\alpha}{m\Gamma}}$), i.e. here $\epsilon \approx 0.043$ so that the equilibrium spread is

$$\boxed{\sigma^*_{x,i} = \sqrt{\mathcal{Q}^*_i} = \left(\frac{\epsilon}{\sqrt{2}\,\alpha}\right)^{\frac{1}{2}} \approx 1.35 \cdot 10^{-8}\,\text{m}} \tag{8.38}$$

This means that the quantum degrees of freedom get frozen very quickly. Thus, the initial spread in position $\sigma_{x,i,0}$ typically transfers, in accordance with Heisenberg principle, a momentum contribution

$$\boxed{\sigma_{p,i,0} \approx \frac{\hbar}{2\,\sigma_{x,i,0}} \sim 5 \cdot 10^{-26}\ \text{kg.m/s}} \tag{8.39}$$

which corresponds to a temperature

$$\boxed{T_Q = \frac{\sigma^2_{p,i,0}}{m\,k_B} \approx 3\ \text{mK}} \tag{8.40}$$

This is almost the value of the heating peak observed in figure 8.14 for $\sigma_{x,i,0} = 10^{-9}$ m. The initial classical temperature was $Tc = 1$ mK which is less than T_Q so that it explains how the heating occurs.

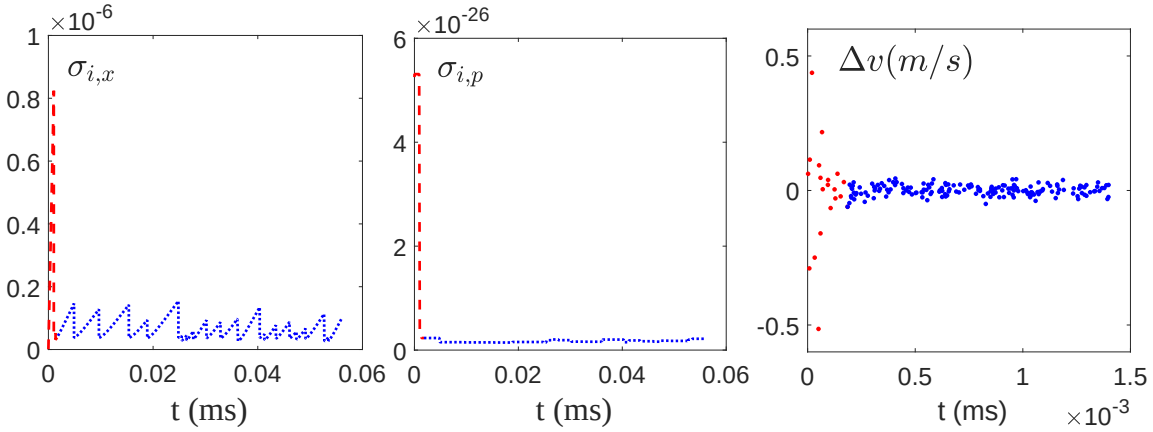

FIGURE 8.15: We plot here the individual quantum spreads in position $\sigma_{i,x}$ and in momentum $\sigma_{i,x}$ (for one atom). We also plot the statistical distribution of transfer of momentum which occurs during jumps corresponding to the photon kicks. We chose an initial position spread $\sigma_{i,x,0} = 10^{-9}$.

8.2.3 Violation of the momentum conservation ?

When the spread in position is small compared to a critical value (that we shall precise in this section), it follows that the exchange of momentum accompanying the first quantum jump is enormous compared to the momentum transferred by a photon. At first sight, when we numerically observed this feature we doubted about the validity of our code, but this property was confirmed by a detailed study of the momentum transfer as we shall see in the present subsection.

As has been shown in [2] (for more detail see appendix 7.D.0.2) , the change in momentum occurring during a GRW localization [2] is expressed as follows:

$$\delta p = p_f - p_i = \frac{2\alpha \mathcal{R}_i}{\sqrt{\alpha(1+2\alpha \mathcal{Q}_i)}}\,\xi \tag{8.41}$$

where ξ is a random number normally distributed. The parameter $\mathcal{R}$ is defined through

$$\mathcal{R} = \sqrt{QP - \hbar^2/4} = \frac{\hbar}{2}\frac{\text{Im } A}{\text{Re } A} \tag{8.42}$$

where A is the quadratic parameter of the Gaussian (see appendix 7.D.0.2 - (7.76)). In absence of collision (when the evolution is ruled by the free Schrödinger equation) it can be shown[3] that:

$$\mathcal{Q}(t) = \mathcal{Q}(0) + 2\mathcal{R}(0)t/m + \mathcal{P}(0)t^2/m^2, \quad \text{and} \quad \mathcal{R}(t) = \sqrt{\mathcal{Q}(0)\cdot\mathcal{P}(0) + (\mathcal{P}(0)t/m)^2 - \hbar^2/4} \tag{8.43}$$

In our simulations we always choose initial gaussian wave packets for which Im $A = 0$ so that

$$\mathcal{R}(0) = 0 \quad \text{and thus} \quad \mathcal{Q}(0)\cdot\mathcal{P}(0) = \hbar^2/4 \tag{8.44}$$

in virtue of the Heisenberg uncertainty relation.

[3] We refer the reader to the paper [2] in which the formulas are explicitly derived.

Let us now assume that at time $\tau = 1/\Gamma_0$ the first collision occurs. Thus from (8.43,8.44) we get

$$\mathcal{Q}(\tau) = \mathcal{Q}(0)\left[1 + \frac{\hbar^2}{4\,m^2\mathcal{Q}(0)}\tau^2/m^2\right] \quad \text{and} \quad \mathcal{R}(\tau) = \frac{\hbar^2}{4\,m\,\mathcal{Q}(0)^2}\,\tau \tag{8.45}$$

Finally, the transfer of momentum (8.41) occurring during the first kick is expressed as follows

$$\boxed{\delta p = \alpha^{\frac{1}{2}}\hbar\,\frac{\epsilon^2}{2\,x_0\,\left[1+2\,x_0\,\left(1+\frac{\epsilon^4}{4\,x_0^2}\right)\right]^{1/2}}} \tag{8.46}$$

where here ξ has been put to unity and where we introduce the dimensionless parameters $x_0 = \alpha\,\mathcal{Q}(0)$ and $\epsilon = \left(\frac{\alpha\hbar\tau}{m}\right)^{1/2}$ as in section 7.E. According to our choice of the parameter α we have in the prefactor of (8.46)

$$\alpha^{\frac{1}{2}}\hbar \sim \hbar\,k_0 \tag{8.47}$$

so that the violation of the momentum conservation occurs when the right-hand side is more than one. This occurs from the critical value $x_{0,c}$ which is found to be solution of

$$\frac{\epsilon^2}{2\,x_{0,c}\,\left[1+2\,x_{0,c}\,\left(1+\frac{\epsilon^4}{4\,x_{0,c}^2}\right)\right]^{1/2}} = 1 \tag{8.48}$$

The value of $x_{0,c}$ depends only on ϵ. Here $\epsilon \approx 0.043$ which corresponds to $x_{0,c} \sim 9.2\cdot 10^{-4}$.

Using the value of $\alpha = 1.67\cdot 10^{14}$ we finally get

$$\boxed{\sigma^c_{x,i,0} = \sqrt{\frac{x_{0,c}}{\alpha}} \approx 10^{-9}\,\mathrm{m}} \tag{8.49}$$

The theoretical value found here corroborates the one obtained in the simulations 8.14.

Note that in the limit of small ϵ, the critical individual spread in position $\sigma^c_{x,i,0}$ converges to the asymptotic solution x_2^* solution found in (7.100), i.e. $\lim_{\epsilon\to 0} x_{0,c} \sim \frac{\epsilon^2}{2}$. The interpretation is straightforward: if $x_{0,c} = x_2^*$ then $T_0^Q = T^Q_{asymptotic}$ and no transfer of quantum energy occurs. Apparent violation of momentum conservation occurs when $x_0 < x_{0,c}$ (then $T_0^Q > T^Q_{asymptotic}$ and the transfer is exothermic).

This property (which would be absent in the classical regime, when $T_Q << T_C$) sheds a new light on the exchange of energy between the quantum and classical reservoirs, in situations during which the quantum reservoir is quite hotter than the classical one.

8.2.4 Discussion and intuitive explanation

When the initial individual spread in position $\sigma_{x,i,0}$ gets smaller than $\sigma^c_{x,i,0}$, the usual approximation to which the atom wave function is a plane wave is no longer valid. The gedanken-experiment below helps to understand why, whenever the wave function is not a plane wave, apparent violations of momentum conservation are likely to occur.

Let us, for simplicity, consider a description at one dimension of space (say X) and let us consider an atom in the ground state.
Suppose that this atom is initially prepared in a state which is a 50/50 coherent superposition of a "slow" gaussian packet (i.e. with an average velocity taken to be equal to zero in first approximation) and of a "fast" gaussian wave packet (for which the average velocity is equal to V).

If now we send a photon in the direction of the atom, which is red shifted relatively to the transition frequency of the atom in such a way that the photon would certainly get captured (and reemitted) by the fast component of the wave function of the atom and be invisible to the slow one. What we get is thus a superposition of a photon reemitted along an arbitrary direction with the atom in the fast state and of a photon passing through the atom without getting deflected with the atom at rest.

If afterwards we measure the photon along X it means thus that the atom is at rest, otherwise the atom is moving fast at velocity V. We could conclude from this analysis that this process violates momentum conservation because the transfer of momentum is apparently equal to $\pm mV$ where m is the mass of the atom (we supposedly are in right to neglect here the photon momentum $\hbar k$). However the full wave function does not violate momentum conservation which is (still neglecting $\hbar k$) $mV/2$ before and after the passage of the photon. Apparent violation occurs only whenever we trace over the photonic degrees of freedom (here its direction of propagation after the interaction) and consider individual histories. Now, GRW formalism and more generally all models of decoherence are precisely aimed at tracing over the environment and considering individual histories of the quantum system of interest (here the atom). This simplified situation explains why momentum violation may appear to get violated in situations where the spread of momentum of the atom is large compared to the photon momentum $\hbar k$, which is precisely the situation for which the GRW approach predicts.

8.3 Conclusion

In conventional treatments of Doppler cooling the atom is treated as a classical point. Here we made a fundamental correction to this model: the state of the quantum system under interest (atom/bead) ought to be described by a Gaussian quantum wave function. Instead of considering only the "classical" position and velocity, which are associated to the first moments of the corresponding observables, we add their "quantum" counterpart, which is associated to the second moment of the respective distributions. We use the GRW model [2] to simulate the decoherence effect during the process of Doppler cooling [3]. The decoherence does not only affects the quantum degrees of freedom via the wavefunction spread but it also affects the classical degrees of freedom (average position and velocity).

Our simulations demonstrate that there occurs a transfer of energy between quantum and classical degrees of freedom. In particular, this transfer cannot be described in classical terms before equilibrium is established. We studied in detail the apparent violation of momentum conservation characterizing the transitory regime which occurs before the onset of equilibrium. Our results also establish that Doppler cooling is not affected by GRW decoherence when the initial wavefunction has a sufficiently large spread. However, when the initial spread is very small, we predict a heating due to this transfer of energy between quantum and classical degrees of freedom. This is so essentially because the variance of two cumulated gaussian distributions is the sum of their respective variances.

Moreover we noted that the asymptotic spread, predicted in the framework of GRW model, $\sigma^*_{x,i} \approx 1.35 \cdot 10^{-8}\,\mathrm{m}$ corresponds to a quantum temperature of the order of the recoil temperature. This justifies retrospectively why it is legitimate in the conventional treatment of Doppler cooling to neglect the influence of quantum degrees of freedom (because $T_D \gg T_R$). However, it could be that in the Sysiphus regime the quantum degrees of freedom associated to the spatial wave function of the atoms would well play an important role...

In the case of nanospheres (beads), the typical preparation procedure is such that we are in the quantum regime $T_Q >> T_C$ at time $t = 0$ [20]. Our analysis makes it possible to estimate the conditions required for effectively cooling a nanosphere during its time of flight, which opens interesting and challenging experimental possibilities.

Bibliography

[1] Samuel Colin, Thomas Durt, and Ralph Willox. Crucial tests of macrorealist and semiclassical gravity models with freely falling mesoscopic nanospheres. *Physical Review A*, 93(6):062102, 2016.

[2] Gian Carlo Ghirardi, Alberto Rimini, and Tullio Weber. Unified dynamics for microscopic and macroscopic systems. *Physical Review D*, 34(2):470, 1986.

[3] Paul D Lett, William D Phillips, SL Rolston, Carol E Tanner, RN Watts, and CI Westbrook. Optical molasses. *JOSA B*, 6(11):2084–2107, 1989.

[4] Alfred Kastler. Quelques suggestions concernant la production optique et la détection optique d'une inégalité de population des niveaux de quantifigation spatiale des atomes. application à l'expérience de stern et gerlach et à la résonance magnétique. *J. phys. radium*, 11(6):255–265, 1950.

[5] Jean Dalibard and Claude Cohen-Tannoudji. Laser cooling below the doppler limit by polarization gradients: simple theoretical models. *JOSA B*, 6(11):2023–2045, 1989.

[6] F Diedrich, JC Bergquist, Wayne M Itano, and DJ Wineland. Laser cooling to the zero-point energy of motion. *Physical Review Letters*, 62(4):403, 1989.

[7] P Jeffery Ungar, David S Weiss, Erling Riis, and Steven Chu. Optical molasses and multilevel atoms: theory. *JOSA B*, 6(11):2058–2071, 1989.

[8] Y Castin, H Wallis, and Jean Dalibard. Limit of doppler cooling. *JOSA B*, 6(11):2046–2057, 1989.

[9] Claude Cohen-Tannoudji and William D Phillips. New mechanisms for laser cooling. *Phys. Today*, 43(10):33–40, 1990.

[10] Y Castin and J Dalibard. Quantization of atomic motion in optical molasses. *EPL (Europhysics Letters)*, 14(8):761, 1991.

[11] J Dalibard and Y Castin. Laser cooling from the semi-classical to the quantum regime. *Frontiers in Laser Spectroscopy: Varenna on Lake Como, Villa Monastero*, 120:445–476, 1992.

[12] Theodor W Hänsch and Arthur L Schawlow. Cooling of gases by laser radiation. *Optics Communications*, 13(1):68–69, 1975.

[13] DJ Wineland and H Dehmelt. Proposed $1014\delta\nu/\nu$ laser fluorescence spectroscopy on tl+ mono-ion oscillator iii (side band cooling). *Bull. Am. Phys. Soc*, 20(4):637–637, 1975.

[14] R.P. Feynman and A.R. Hibbs. *Quantum Mechanics and Path Integral*. McGraw-Hill, New-York, 1965.

[15] C. Cohen Tannoudji. Leçons du collège de france : Interactions du champ éctromagnétique avec des atomes. 1974.

[16] Claude Cohen-Tannoudji, Jacques Dupont-Roc, and Gilbert Grynberg. *Processus d'interaction entre photons et atomes*. Edp Sciences, 2012.

[17] M. Marciante. *Dynamique d'ions en pieges radio-frequences*. PhD thesis.

[18] C. Champenois. Lecture notes, "trapped charged particles, chapter 6: Laser cooling techniques applicable to charged particles", pages 117-145. Technical report, 2016.

[19] Christopher J Foot et al. *Atomic physics*, volume 7. Oxford University Press, 2005.

[20] Dominik Windey, Carlos Gonzalez-Ballestero, Patrick Maurer, Lukas Novotny, Oriol Romero-Isart, and René Reimann. Cavity-based 3d cooling of a levitated nanoparticle via coherent scattering. *Physical review letters*, 122(12):123601, 2019.

Chapter 9

Conclusion and open questions

"Tout a une fin... sauf la saucisse qui en a deux"

Proverbe allemand

In the present work, we have explored several topics that naturally appear if we aim at giving a formulation of the quantum theory in which quantum systems are sharply localized in space throughout time and follow "real" trajectories [1, 2, 3, 4, 5].

The first topic, quantum equilibrium, naturally emerges if we wish to make the economy of a postulate [6], the Born rule, and try to derive the Born rule from the dynamics [7, 8, 8, 9, 10]. As is well-known, when the dynamics resumes to the guidance condition, it is possible to derive the Born rule provided some chaos [11, 12, 13] is present, at the price of introducing some coarse-graining. As has been shown elsewhere, chaos [11, 14, 12, 13] accompanies the passage of the trajectory in the vicinity of a zero of the wave function. We retrieved these results in our analysis (chapter 2 and chapter 3), and we put into evidence the role of microstructures and mixing (chapter 4). What we have shown could be formulated as follows: it makes sense to talk about equilibrium when mixing is such that microstructures disappear. From this point of view, the time necessary to reach equilibrium is not absolute, it depends on the size of the microstructure and of the Lyapunov exponent characterizing the dynamics. We also introduced a measure of mixing inspired by the analogy with thermodynamical mixing. This measure, that is independent of the coarse graining, uses as a tool the Bernoulli distribution. We enlarged our analysis in order to consider a dynamics *à la* Nelson (the BHN dynamics [15, 16, 17, 18, 19, 20, 21]) in which, supplementary to the guidance condition, some Brownian motion is present. This approach substantiates original ideas by Bohm and Vigier in the 50's [7]. The mixture of Brownian motion and guidance condition was labeled by de Broglie under the name "quantum hidden thermostat" [22]. Note that these ideas are congenital to the so-called stochastic electro-dynamics and other zero point field fluctuations realistic approaches to the quantum theory [23].

We derived in this context several H-theorems (chapter 3) showing that quantum equilibrium irreversibly occurs due to the presence of the Brownian noise/quantum stochasticity. These H-theorems are formulated in terms of various measures of the departure from equilibrium: $\mathcal{L}_1$ norm, $\mathcal{L}_2$ norm, $\mathcal{L}_f$ norm and also the Kullback-Leibler divergence. When the trajectories of the system are confined (as happened in our case where we considered a particle trapped in a 2D harmonic oscillator) equilibrium is de facto guaranteed, what is however not true in the case of free particles, as shows the Guerra counterexample [17, 18, 19]. We also studied the ergodicity of the dBB and the BHN dynamics, and we connected it to the uniformization properties of the bouncing oil droplets dynamics

(chapter 5). Our analysis allowed us to formulate quantitative tests [24] putting the degree of noise present in the dynamics in relation with the ergodicity. We also proposed simple models aimed at qualitatively mimicking the trajectories observed in the case of a droplet trapped in a 2D harmonic potential [25], motivated by the experimental observation [26, 27] according to which the droplets trajectories can be characterized in terms of the same quantum numbers as those which characterize the energy levels of an isotropic 2D harmonic oscillator. Finally we proposed an effective model for droplets dynamics in which the degree of noise is expressed by two real parameters, ϵ and ϵ', model which make it possible to continuously tune between the classical, dBB and BHN dynamics.

At this level we ignore whether the dBB and BHN dynamics deliver good candidates for simulating the droplets dynamics, but we are hopeful that our ideas will stimulate the experimentalists and contribute to better understand and quantify the analogies and discrepancies between the pilot wave dynamics and the droplets dynamics, which remain largely unexplored questions.

The second topic dealt with de Broglie double solution program [3, 28, 29] and a proposal to realize it by introducing a fundamental non-linearity at the level of Schrodinger equation (6). To some extent, our first result appeared to be negative: we proposed an ansatz, the factorization ansatz, in which the double solution consists of a product of the pilot wave with the wave of the particle and showed that this ansatz resulted into a generalized guidance equation to which the internal degrees of freedom of the particle also contribute. Moreover we showed by a well-chosen example that this internal contribution conspires to restore the classical dynamics. These results were elucidated in terms of a generalized Ehrenfest theorem [30, 31], valid for a very large class of non-linearities (comprising e.g. N-S equation and NLS equations as particular cases) which all respect Galilean invariance. It is worth noting that the Ehrenfest theorem is also valid even when the factorization ansatz is not satisfied, provided the quantum wave function is sharply enough peaked. It is thus a very general theorem. A possible way to escape the limitations imposed by Ehrenfest theorem consists of replacing the internal velocity by a brownian noise. It is still an open question to know whether we could relate this brownian noise to the relativistic Dirac-Heisenberg zitterbewegung, as has been done for instance in the context of stochastic electro-dynamics and actually a relativistically covariant formulation of de Broglie's double solution program has up to now be largely unadressed. In the meanwhile, even though we were not able to realize stricto sensu de Broglie's double solution program due to the limitations imposed by the aforementioned generalized Ehrenfest theorem, the same theorem implies that the S-N equation remains a valuable candidate for elucidating the quantum-classical transition. From that point of view, quantum microscopic systems would indeed remain delocalized at the quantum level (in agreement with the recent loophole free violation of Bell's inequalities achieved by experimentalists), but macroscopic systems would happen to spontaneously localize and to follow classical trajectories. This constitutes an interesting prediction in itself, justifying the interest of considering nonlinear generalizations of Schrodinger equation à la Schrodinger-Newton.

We proposed (chapter 7) thus two experimental tests aimed at putting into evidence the existence of a non-linear self-interaction à la Schrodinger-Newton [32, 33, 34, 35, 36, 37, 38, 39, 30].

The first one involved a humpty-dumpty Stern-Gerlach experiment [40]. Such an experiment has actually not yet been realized, due to limitations imposed by decoherence, but

hopefully it could be realized in a near future, being given the serious progresses realizing in the previous decades in trapping and cooling mesoscopic quantum systems in processes characterized by a very low degree of decoherence (very low temperatures and nearly perfect vacuum).

The second test implements the idea that decoherence can be used as a tool for controlling and tailoring the evolution of a quantum system [32, 33]. Moreover it incorporates the concept of mobility [41, 42], central in the derivation of Gisin's famous no-go theorem [43] about non-linearity [44], which related the presence of a non-linearity to the violation of quantum signaling. Mobility, as it was introduced by Mielnik [42] connects the presence of a nonlinearity in the dynamics to the possibility to differentiate non-orthogonal states, which ultimately makes it possible to differentiate two realizations of a same density matrix and thus two unravelings of a same master equation. Similar to the humpty-dumpty experiment [40], the conditions required for realizing the experiment proposed by us have not been realized yet in the practice, because they impose initial conditions on the quantum state of the mesoscopic system (bead) that are out of reach to experimentalists. These experimental proposals also require to use a satellite in order to obtain the very long times of free flight which [33] seriously menaces their potential realization. Obviously, what still remains to be done is to extrapolate our experimental proposal to the case of trapped systems which would largely enhance its practical implementability, because it could be realized in a terrestrial lab. Unfortunately we had no time to carry out this study during the relatively short time (three years) imposed to the completion of this work, but this program is worth being fulfilled.

Indirectly, the study of the feasibility of our experimental proposals brought us to study in depth the role of decoherence during Doppler cooling [45, 46] (chapter 8). By doing so, we emphasized the role played by external quantum degrees of freedom of a Gaussian state (these are the square root deviations of velocity and position) which, supplementary to the external classical degrees of freedom (average velocity and average position) contribute to the temperature of the considered quantum system. Making use of GRW [47] formalism we studied how exchanges occur between the classical and quantum contributions to the temperature, due to the localization process caused by the spontaneous emission of photons by the quantum system. Ultimately, we hope that these ideas could be exploited in order to exert quantum control and tailoring of the state of a quantum system undergoing laser cooling and/or Doppler cooling, in particular in the mesoscopic domain.

To conclude, the simple question raised by Louis de Broglie in 1927 which is *"... have we the right to assume that quantum systems are sharply localized at all times ... ?"* brought us to explore several topics:

- the onset of quantum equilibrium,
- realization of the wave particle duality at the macroscopic scale with oil droplets,
- self-gravitationally induced non-linear modifications of Schrodinger equation,
- tests of quantum coherence at the mesoscopic level
- interplay between decoherence and cooling.

Our study settled certain questions and raised new ones, still to explore. We hope that it will stimulate experimentalists and that it will benefit to our knowledge of the quantum theory, a monument of the 20th century physics, still unachieved, for our greatest satisfaction.

Bibliography

[1] Louis deBroglie. La mécanique ondulatoire et la structure atomique de la matière et du rayonnement. *J. Phys. Radium*, 8(5):225–241, 1927.

[2] Louis De Broglie. The wave nature of the electron. *Nobel lecture*, 12:244–56, 1929.

[3] Louis De Broglie. An introduction to the study of wave mechanics. 1930.

[4] David Bohm. A Suggested Interpretation of the Quantum Theory in Terms of "Hidden" Variables. I. *Phys. Rev.*, 85(2):166–179, 1952.

[5] David Bohm. A Suggested Interpretation of the Quantum Theory in Terms of "Hidden" Variables. II. *Phys. Rev.*, 85(2):180–193, 1952.

[6] Travis Norsen. On the explanation of born-rule statistics in the de broglie-bohm pilot-wave theory. *Entropy*, 20(6):422, 2018.

[7] David Bohm and Jean-Pierre Vigier. Model of the causal interpretation of quantum theory in terms of a fluid with irregular fluctuations. *Phys. Rev.*, 96(1):208, 1954.

[8] Antony Valentini. Signal locality, uncertainty and the subquantum H-theorem. I. *Phys. Lett. A*, 156:5–11, 1991.

[9] Antony Valentini. *On the pilot-wave theory of classical, quantum and subquantum physics.* PhD thesis, SISSA, 1992.

[10] Antony Valentini and Hans Westman. Dynamical origin of quantum probabilities. *Proc. R. Soc. A*, 461:253–272, 2005.

[11] C. Efthymiopoulos, C. Kalapotharakos, and G. Contopoulos. Origin of chaos near critical points of quantum flow. *Phys. Rev. E*, 79(3):036203, 2009.

[12] C. Efthymiopoulos, G. Contopoulos, and A. C. Tzemos. Chaos in de Broglie - Bohm quantum mechanics and the dynamics of quantum relaxation. *Ann. Fond. de Broglie*, 42:133, 2017.

[13] Athanasios C Tzemos, Christos Efthymiopoulos, and George Contopoulos. Origin of chaos near three-dimensional quantum vortices: A general bohmian theory. *Physical Review E*, 97(4):042201, 2018.

[14] G. Contopoulos, N. Delis, and C. Efthymiopoulos. Order in de Broglie - Bohm quantum mechanics. *J. Phys. A: Math. Theor.*, 45(16):165301, 2012.

[15] Edward Nelson. Derivation of the schrödinger equation from newtonian mechanics. *Physical review*, 150(4):1079, 1966.

[16] D. Bohm and B. Hiley. Non-locality and locality in the stochastic interpretation of quantum mechanics. *Physics Reports*, 172(3):93–122, 1989.

[17] Nicola Cufaro Petroni. Asymptotic behaviour of densities for Nelson processes. In *Quantum Communications and Measurement*, pages 43–52. Springer, 1995.

[18] F. Guerra. Introduction to Nelson stochastic mechanics as a model for quantum mechanics. In *The Foundations of Quantum Mechanics*, pages 339–355. Kluwer Academic Publishers, 1995.

[19] Nicola Cufaro Petroni and Francesco Guerra. Quantum Mechanical States as Attractors for Nelson Processes. *Found. Phys.*, 25(2):297–315, 1995.

[20] Guido Bacciagaluppi. Nelsonian mechanics revisited. *Foundations of Physics Letters*, 12(1):1–16, 1999.

[21] Guido Bacciagaluppi. A Conceptual Introduction to Nelson's Mechanics. In *Endophysics, time, quantum and the subjective*, pages 367–388. R. Buccheri, M. Saniga, A. Elitzur (eds), World Scientific, 2005.

[22] Louis De Broglie. La thermodynamique «cachée» des particules. In *Annales de l'IHP Physique théorique*, volume 1, pages 1–19, 1964.

[23] Gerhard Grössing. Sub-quantum thermodynamics as a basis of emergent quantum mechanics. *Entropy*, 12(9):1975–2044, 2010.

[24] Mohamed Hatifi, Ralph Willox, Samuel Colin, and Thomas Durt. Bouncing oil droplets, de broglie's quantum thermostat, and convergence to equilibrium. *Entropy*, 20(10):780, 2018.

[25] Matthieu Labousse, Anand U Oza, S. Perrard, and J. W.M. Bush. Pilot-wave dynamics in a harmonic potential: Quantization and stability of circular orbits. *Physical Review E*, 93(3):033122, 2016.

[26] Y. Couder and E. Fort. Single-particle diffraction and interference at a macroscopic scale. *Phys. Rev. Lett.*, 97:15410, 2006.

[27] John W M Bush. Pilot-wave hydrodynamics. *Annu. Rev. Fluid Mech.*, 47:269–292, 2015.

[28] Louis De Broglie. *Non-linear wave mechanics: A causal interpretation*. Elsevier Publishing Company, 1960.

[29] Louis de Broglie. Interpretation of quantum mechanics by the double solution theory. *Annales de la Fondation Louis de Broglie*, 12(4):1–23, 1987.

[30] Huan Yang, Haixing Miao, Da-Shin Lee, Bassam Helou, and Yanbei Chen. Macroscopic quantum mechanics in a classical spacetime. *Physical review letters*, 110(17):170401, 2013.

[31] M. Hatifi, C. Lopez-Fortin, and T. Durt. De Broglie's double solution: limitations of the self-gravity approach. *Annales de la Fondation Louis de Broglie*, 43:63, 2018.

[32] S. Colin, T. Durt, and R. Willox. Can quantum systems succumb to their own (gravitational) attraction? *Class. Quantum Grav.*, 31:245003, 2014.

[33] Samuel Colin, Thomas Durt, and Ralph Willox. Crucial tests of macrorealist and semiclassical gravity models with freely falling mesoscopic nanospheres. *Physical Review A*, 93(6):062102, 2016.

[34] L. Diósi. Gravitation and quantum-mechanical localization of macro-objects. *Physics Letters A*, 105(4):199 – 202, 1984.

[35] Domenico Giulini and André Großardt. The schrödinger–newton equation as a non-relativistic limit of self-gravitating klein–gordon and dirac fields. *Classical and Quantum Gravity*, 29(21):215010, 2012.

[36] KRW Jones. Newtonian quantum gravity. *Australian Journal of Physics*, 48(6):1055–1082, 1995.

[37] C Moller. The energy-momentum complex in general relativity and related problems. In *Colloq. Int. CNRS*, volume 91, pages 15–29, 1959.

[38] Roger Penrose. On gravity's role in quantum state reduction. *General relativity and gravitation*, 28(5):581–600, 1996.

[39] L. Rosenfeld. On quantization of fields. *Nuclear Physics*, 40:353 – 356, 1963.

[40] Marlan O Scully, Berthold-Georg Englert, and Julian Schwinger. Spin coherence and humpty-dumpty. iii. the effects of observation. *Physical Review A*, 40(4):1775, 1989.

[41] Marek Czachor. Mobility and non-separability. *Foundations of Physics Letters*, 4(4):351–361, 1991.

[42] Bogdan Mielnik. Phenomenon of mobility in non-linear theories. *Communications in Mathematical Physics*, 101(3):323–339, 1985.

[43] Nicolas Gisin. Weinberg's non-linear quantum mechanics and supraluminal communications. *Physics Letters A*, 143(1-2):1–2, 1990.

[44] Joseph Polchinski. Weinberg's nonlinear quantum mechanics and the einstein-podolsky-rosen paradox. *Physical Review Letters*, 66(4):397, 1991.

[45] Theodor W Hänsch and Arthur L Schawlow. Cooling of gases by laser radiation. *Optics Communications*, 13(1):68–69, 1975.

[46] DJ Wineland and H Dehmelt. Proposed 1014$\delta\nu/\nu$ laser fluorescence spectroscopy on tl+ mono-ion oscillator iii (side band cooling). *Bull. Am. Phys. Soc*, 20(4):637–637, 1975.

[47] Gian Carlo Ghirardi, Alberto Rimini, and Tullio Weber. Unified dynamics for microscopic and macroscopic systems. *Physical Review D*, 34(2):470, 1986.